TRANSPORTATION RESEARCH

RECORD

No. 1330

Soils, Geology, and Foundations

Behavior of Jointed Rock Masses and Reinforced Soil Structures 1991

A peer-reviewed publication of the Transportation Research Board

TRANSPORTATION RESEARCH BOARD
NATIONAL RESEARCH COUNCIL
WASHINGTON, D.C. 1991

Transportation Research Record 1330
Price: $21.00

Subscriber Category
IIIA soils, geology, and foundations

TRB Publications Staff
Director of Publications: Nancy A. Ackerman
Senior Editor: Naomi C. Kassabian
Associate Editor: Alison G. Tobias
Assistant Editors: Luanne Crayton, Norman Solomon
Graphics Coordinator: Diane L. Snell
Production Coordinator: Karen W. McClain
Office Manager: Phyllis D. Barber
Production Assistant: Betty L. Hawkins

Printed in the United States of America

Library of Congress Cataloging-in-Publication Data
National Research Council. Transportation Research Board.

Behavior of jointed rock masses and reinforced soil structures, 1991.
p. cm.—(Transportation research record ; 1330)
"A peer-reviewed publication of the Transportation Research Board."
ISBN 0-309-05169-X
1. Rock mechanics. 2. Soil mechanics. 3. Rock slopes. 4. Soil stabilization. I. National Research Council (U.S.). Transportation Research Board. II. Series.
TE7.H5 no. 1330
[TA706]
388 s—dc20
[624.1'513] 92-5447
CIP

Sponsorship of Transportation Research Record 1330

GROUP 2—DESIGN AND CONSTRUCTION OF TRANSPORTATION FACILITIES
Chairman: Raymond A. Forsyth, Sacramento, California

Soil Mechanics Section
Chairman: Michael G. Katona, Tyndall AFB

Committee on Mechanics of Earth Masses and Layered Systems
Chairman: Tien H. Wu, Ohio State University
Walter R. Barker, Richard D. Barksdale, Richard J. Bathurst, Joseph A. Caliendo, Umakant Dash, Deborah J. Goodings, John S. Horvath, Mary E. Hynes, Ilan Juran, Glen E. Miller, Gerald P. Raymond, Harry E. Stewart, Harvey E. Wahls, John L. Walkinshaw

Committee on Geosynthetics
Chairman: Verne C. McGuffey, New York State Department of Transportation
Richard D. Barksdale, Robert K. Barrett, Laurinda T. Bedingfield, John A. Bove, Calvin G. Burgess, Robert G. Carroll, Jr., Jerome A. DiMaggio, James B. Farris, Graham R. Ford, S. S. Dave Guram, Neil F. Hawks, Gary L. Hoffman, Robert D. Holtz, Thomas C. Kinney, Robert M. Koerner, Larry Lockett, James H. Long, R. Gordon McKeen, Bernard Myles, Malcolm L. Steinberg, John E. Steward, Harry H. Ulery, Jr., Dennis B. Wedding, David C. Wyant

Geology and Properties of Earth Materials Section
Chairman: Robert D. Holtz, University of Washington

Committee on Soil and Rock Properties
Chairman: Mehmet T. Tumay, National Science Foundation
Robert C. Bachus, S. S. Bandy, Roy H. Borden, Timothy D. Bowen, William H. Highter, Robert D. Holtz, Richard H. Howe, An-Bin Huang, Steven L. Kramer, Rodney W. Lentz, C. William Lovell, Kenneth L. McManis, Priscilla P. Nelson, Norman I. Norrish, Sibel Pamukcu, Gerald P. Raymond, James J. Schnabel, Kaare Senneset, Robert M. Smith, J. Allan Tice, Recep Yilmaz

G. P. Jayaprakash, Transportation Research Board staff

Sponsorship is indicated by a footnote at the end of each paper. The organizational units, officers, and members are as of December 31, 1990.

Transportation Research Record 1330

Contents

Foreword

The eleven papers in this Record are of interest to geotechnical engineers. The first three papers contain information on strength characterization and analysis of jointed rock masses for slope design. Lorig et al. describe the use of the distinct element method, a numerical technique, to investigate the stability of discontinuous rock slopes. McCreath summarizes the methods he used for stability evaluation and the results obtained, with particular reference to the selection of Barton and Hoek-Brown shear strength parameters for rock masses. Wood describes geomechanical and geotechnical rock mass classifications and ways to adapt them to obtain rock mass strength parameters.

The remaining papers address important issues related to design and construction of reinforced soil structures. Fishman et al. measured stresses in a reinforced soil wall and compared them to those used in the design. Wright and Duncan compared the results from several methods of stability analysis for reinforced soil slopes. All the methods employed limit equilibrium but used different assumptions to simplify the solution. Horvath used finite-element analysis to evaluate the reduction in earth pressure on a wall from a live load, where compressible material and geosynthetics were incorporated in the backfill. Leshchinsky and Lambert report on an investigation of failure surface development in geosynthetically reinforced steep slopes. They compare the observed results with those predicted by a limit equilibrium analysis. Yuan and Chua report the results of laboratory pullout box and uniaxial tension tests conducted to measure displacement, axial stiffness of reinforcement, interface shear stiffness, and reinforcement length that are needed to determine the pullout resistance.

The last three papers are about the technique of soil nailing. Results from the French research project CLOUTERRE are presented by Schlosser and Unterreiner and by Plumelle and Schlosser. Alston describes the design and construction of a soil nailing project in Canada.

Slope Stability Analysis of Jointed Rock Using Distinct Element Method

L. J. LORIG, R. D. HART, AND P. A. CUNDALL

The fundamental objective in designing most slopes is to achieve the steepest slope possible consistent with knowledge of material properties, site constraints, external loads, required safety factors, and so on. Most traditional design methods for slopes in jointed media involve two-dimensional limit equilibrium analyses. All limit equilibrium analyses are restricted to predefined failure modes and assume that failure occurs along the failure surface according to a perfectly plastic shear force law (i.e., shear force is independent of displacement). Such approaches may yield reasonable results for situations in which the failure mode is readily identifiable and involves only translation or rotation. However, for more complicated problems or problems in which displacement estimates are important, limit equilibrium methods may not be appropriate. For example, in analysis of slopes composed of distinct rock blocks, analysis based on the distinct element method may be more appropriate. The results of several slope stability analyses are presented, including one actual problem in which limit analysis falsely predicts stable equilibrium and a distinct element kinematic analysis correctly predicts instability. Such false predictions can arise from the assumption of an inappropriate failure mode in limit equilibrium analysis. The distinct element method was developed specifically to study the behavior of jointed rock. Failure modes are not prescribed using this method but evolve naturally as the solution progresses. The method models a rock mass as an assemblage of blocks, not as an equivalent continuum. Discontinuities are regarded as distinct interactions between blocks with joint behavior prescribed for these interactions. A description of the fundamentals of the distinct element method relevant to slope stability analysis is included. Extensions of the method that allow practically meaningful problems to be addressed are also described. All of the features are described through illustrative examples.

Because the behavior of many rock slopes is dominated by displacements induced along joints and discontinuities (i.e., faults, bedding planes, etc.), appropriate analysis methods must account for these displacements. Current analysis methods include limit equilibrium, continuum (i.e., finite element and finite difference), and discontinuum methods.

Limit equilibrium methods assume that failure occurs along predefined failure surfaces with a perfectly plastic shear force law. This means that the shear force on the failure surface is independent of displacement. Hence, shear forces all become known functions of normal forces, and the system becomes statically determinate, although assumptions about lines of action are usually necessary. Stability in the limit equilibrium method is usually determined by a comparison of forces (i.e., driving and resisting) for a particular failure mode. The limit equilibrium method, therefore, yields reasonable results for situations in which the failure mode is simple and readily identifiable. However, the method may be inadequate for more complicated problems or for problems in which displacements must be known (e.g., in designing reinforcement systems).

Continuum methods require that the rock mass be represented as a continuous body. Continuum methods account for the presence of discontinuities by an equivalent continuum representation. Now, equivalent continuum models can give only a limited representation for the behavior of jointed rock, that is, they cannot fully account for the various displacements associated with jointed media, such as sliding, separation, and rotation along joints. Attempts to overcome this restriction usually involve incorporating joint elements, slidelines, or interfaces to model discontinuities. However, these adaptations are usually limited by (a) the number of joints that may be considered, (b) the extent to which joints may intersect, (c) the amount of displacement that may be considered, or (d) computational inefficiencies resulting from the underlying assumption of continuum behavior.

Discontinuum methods are numerical techniques formulated specifically to analyze the behavior of discontinuous or particulate systems. The best-known and most-advanced discontinuum method is the distinct element method, which was conceived as a means to model the progressive failure of rock slopes (*1*). The distinct element method is not very different from other numerical methods, particularly when existing variations are considered, but three attributes are usually associated with it: first, the rock mass is composed of individual blocks that can undergo large rotation and large displacements relative to one another; second, interaction forces between blocks arise from changes in their relative geometrical configuration; and third, the solution scheme is explicit in time.

Because of these features, the distinct element method is particularly well suited to investigate problems that address the question of stability of discontinuous rock slopes. The important points of the distinct element formulation as it relates to rock slope stability are the following:

1. Both stability and instability are modeled (when a net force exists on a block, it accelerates and moves to a new position; if the forces on a block balance, it remains at rest or moves with constant velocity).
2. Forces arise between two blocks where they interact.
3. The calculation marches from one state to another in small (usually, fictitious) time increments. The "final solution" may be equilibrium, or it may be a state of continuing motion.

Itasca Consulting Group, Inc., 1313 Fifth Street S.E., Suite 210, Minneapolis, Minn. 55414.

The following problem illustrates the distinct element analysis of a slope failure mechanism that cannot be identified from traditional slope stability analyses. The rock slope shown in Figure 1 is 40 m high with bedding that dips at an angle of 76 degrees and has a 4-m spacing. Two nearly horizontal joints intersect the slope face at a dip angle of 2.5 degrees. The friction angle of all joints is assumed to be 6 degrees. On the basis of a conventional rock slope stability analysis, this slope would be considered stable. In fact, the slope fails in a reverse-toppling mode, as shown in Figure 1. A similar analysis was performed by Cundall (*2*) to explain an actual slope failure at the Valdez pipeline terminal in Alaska.

DISTINCT ELEMENT FORMULATION

The essential feature of the distinct element method is its ability to model the arbitrary motion of each block with respect to any other. Blocks may be rigid or deformable. Because most slope stability problems involve stresses that are relatively low compared with the block strength and deformability, the blocks are usually considered rigid. The description of the formulation that follows has been implemented in two computer programs: Universal Distinct Element Code (UDEC) is a two-dimensional distinct element code; 3-Dimensional Distinct Element Code (3DEC) is a three-dimensional distinct element code. A detailed description of UDEC is given elsewhere (*3*). Hart et al. (*4*) describe the 3DEC formulation. For simplicity, the following discussion is based on the two-dimensional formulation.

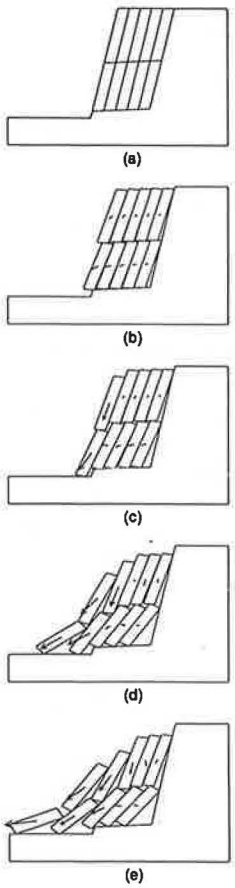

FIGURE 1 Stages in failure of slope by reverse toppling.

Calculation Cycle

The distinct element method is based on a dynamic (time domain) algorithm that solves the equations of motion of the block system by an explicit finite difference method. Cundall (*5*) demonstrates that such a solution scheme is better suited to indicate potential failure modes of discontinuous systems than schemes that ignore velocities and inertial forces. In the distinct element method, the motion laws and joint constitutive relations are applied at each time step. The integration of the motion law provides the new block positions and, therefore, the joint displacement increments (or velocities). Blocks are assumed to interact at discrete points referred to as "contacts." A force-displacement relation describing joint behavior at contacts is then used to obtain forces that are applied to the blocks at the next time step. The calculation cycles for rigid and deformable blocks are illustrated in Figure 2.

Block Motion

The equations of translational motion for one rigid block can be expressed as

$$\ddot{u}_i + \alpha \ddot{u}_i = \frac{\sum F_i}{m} + g_i \qquad (1)$$

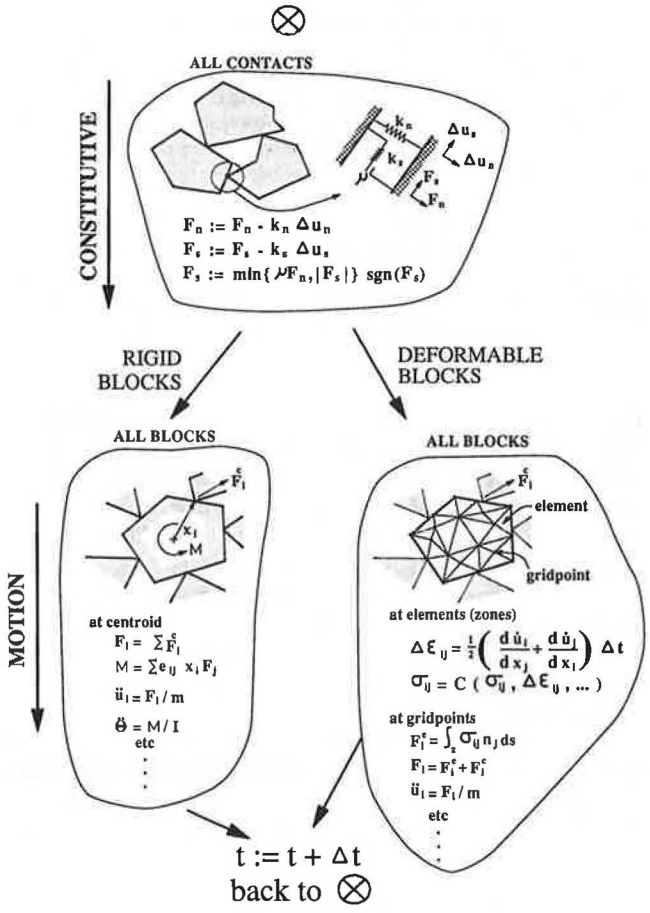

FIGURE 2 Calculation cycle used in distinct element method.

where

$\ddot{u}_i$ = acceleration of the block centroid,
α = viscous (mass-proportional) damping constant,
$\sum F_i$ = sum of forces acting on the block (from the block contacts and applied external forces),
m = block mass, and
g_i = gravitational acceleration.

Equation 1 is expressed in finite difference form as

$$\dot{u}_i^{(t+\Delta t/2)} = \left\{ D_1 \, \dot{u}_i^{(t-\Delta t/2)} + \left[\frac{\sum F_i^{(t)}}{m} + g_i \right] \Delta t \right\} D_2 \tag{2}$$

where

$$D_1 = 1 - \left(\alpha \frac{\Delta t}{2} \right),$$

$$D_2 = \frac{1}{1 + \left(\alpha \frac{\Delta t}{2} \right)}, \text{ and}$$

Δt = time step.

The equation of motion for rotation is given by

$$\dot{w}_i + \alpha w_i = \frac{M_i}{I} \tag{3}$$

where

w_i = rotational velocity,
M_i = total torque, and
I = moment of inertia.

The rotation equation is integrated by finite differences in exactly the same way as the translational equations.

Contact Force

The deformability and strength properties of joints are represented in the numerical model by spring-slider elements located at contact points between a block corner and an adjacent block edge. A simple force-displacement law relates normal forces directly to the amount of notional penetration—that is,

$$F_n = k_n u_n \tag{4}$$

where

F_n = normal force at the contact,
k_n = normal stiffness at a point, and
u_n = total normal penetration.

For most slope stability analyses (and all those reported here), it is assumed that the tensile strength of joints is zero.

Shear forces are considered to depend on load path. Incremental shear forces develop in proportion to incremental changes in relative shear displacement—that is,

$$\Delta F_s = k_s \Delta u_s \tag{5}$$

where

ΔF_s = change in shear force,
k_s = shear stiffness at a point, and
Δu_s = incremental shear displacement.

The maximum shear force is limited according to the Mohr-Coulomb criterion

$$|F_s| \leq c + F_n \tan \phi \tag{6}$$

where c is the cohesion and ϕ is the basic joint friction angle.

Shear failure occurs when the shear force reaches the maximum value. For the work described here, joint cohesion is assumed to be zero.

In addition to point contacts specified by force-displacement relations, edge contacts are important physically because they correspond to the case of an interface closed along its entire length. For such cases, the previous expressions are written in terms of stress rather than force and representative lengths are taken into account. Because the distinct element method is based on an explicit formulation, more-realistic joint constitutive relations may be introduced. In general, the joint constitutive relations must provide the stress increments as a function of displacement increments, current stresses, and possibly other state parameters.

$$\Delta\sigma_n, \Delta\sigma_s = f(\Delta u_n, \Delta u_s, \sigma_n\sigma_s, \ldots) \tag{7}$$

One such model is the continuously yielding joint model. This model, described by Cundall and Lemos (*6*) and Lemos (*7*) is intended to simulate the intrinsic mechanism of progressive damage of a joint under shear. The continuously yielding joint model is capable, therefore, of simulating a peak-residual type of behavior.

ROCK REINFORCEMENT

The function of rock reinforcement is to mobilize forces in the interior of the rock mass that act to resist deformation. Appropriate analysis of rock reinforcement must take into account the manner in which loads are mobilized in reinforcement elements by relative displacement between rock blocks and components of the rock reinforcement.

Several types of reinforcement are designed to operate effectively in a range of ground conditions. One type is represented by a reinforcing bar or bolt fully encapsulated in a strong, stiff resin or grout. This system is characterized by the relatively large axial resistance to extensions that can be developed over a relatively short length of the shank of the bolt and by the high resistance to shear that can be developed by an element penetrating a slipping joint. A second type of reinforcement system, represented by cement-grouted cables or tendons, offers little resistance to joint shear, and development of full-axial load may require deformation of the grout over a substantial length of the reinforcing element. These two types are identified, respectively, as local reinforcement and spatially extensive reinforcement.

Formulations representing both types of reinforcement and their implementations in explicit finite difference codes are described by Brady and Lorig (*8*). In this paper, only local reinforcement is described and demonstrated, although both have been implemented in the distinct element method.

Local Reinforcement at Joints

In the analysis of local reinforcement, attention is focused on the loads mobilized in the reinforcement element by slip and separation at a joint. The analysis involves deformation of an active length of the element, as shown in Figure 3, a procedure justified by the experimental observations of Bjurstrom (*9*) and Pells (*10*) that, in discontinuous rock, reinforcement deformation is concentrated near an active joint.

The conceptual model of the local operation of the active length is considered in terms of two springs: one parallel to the local axis of the element, and one perpendicular to it. When shear occurs at the joint, the axial spring remains parallel to the new orientation of the active length, and the shear spring is taken to remain perpendicular to the original axial orientation. Displacements normal to the joint are accompanied by analogous changes in the spring orientations.

Illustrative Example

To illustrate the use of the local reinforcement model in the distinct element method, the problem shown in Figure 1 is repeated with the reinforcement pattern shown in Figure 4 (*top*) installed. Figure 4 (*bottom*) shows that the specified reinforcement stabilizes the slope, and it shows the loads mobilized in the reinforcement, where it crosses a discontinuity.

HYDROMECHANICAL BEHAVIOR

Hydromechanical behavior of jointed rock masses involves complex interactions between joint deformation and effective stress, causing changes in aperture and thus hydraulic conductivity. Because most rocks have low permeability, the hydraulic behavior of any rock mass is mainly determined by

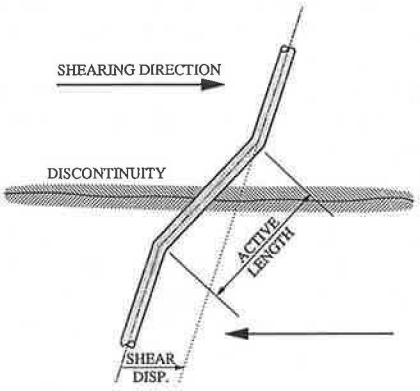

FIGURE 3 Local reinforcement deformation associated with active length of bolt.

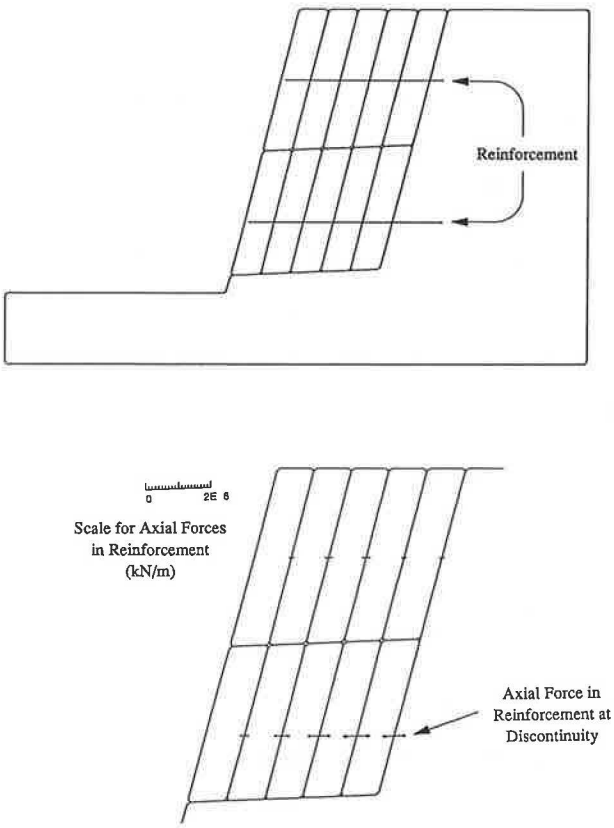

FIGURE 4 Stabilization of slope in Figure 1 by reinforcement: *top*, location; *bottom*, axial forces developed (maximum force = 830 kN).

the jointing pattern that introduces a strong directional conductivity. To the authors' knowledge, UDEC is the only general purpose distinct element code capable of performing a fully coupled mechanical-hydraulic analysis in which fracture conductivity is dependent on mechanical behavior.

Formulation

In UDEC, blocks are viewed as defining a network of interconnected voids and channels referred to as "domains." Referring to Figure 5, contacts are A–F and domains are 1–5. Domains 1, 3, and 4 represent joints, Domain 2 is located at the intersection of two joints, and Domain 5 is a void space. Flow is governed by the pressure differential (Δp) between adjacent domains. The flow rate (q) in joints is given by

$$q = ba^3 \frac{\Delta p}{l} \tag{8}$$

where

b = joint permeability factor (whose theoretical value is $1/12\mu$, μ being the dynamic viscosity of the fluid),
a = contact hydraulic aperture, and
l = length assigned to the contact between the domains.

At each time step, mechanical computations determine the geometry of the system, thus yielding new values of apertures

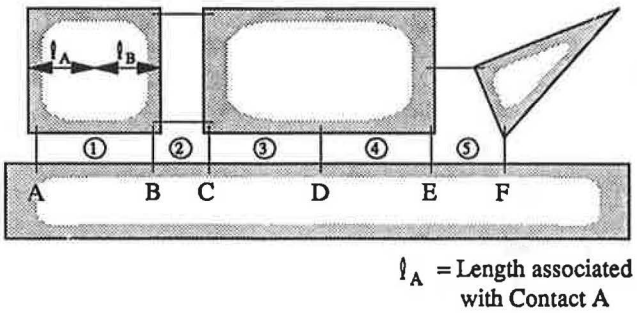

FIGURE 5 Definition of domains used in UDEC.

for all contacts and volumes of all domains. Flow rates through the contacts can then be calculated on the basis of the aforementioned formulas. Then domain pressures are updated, taking into account the net flow into the domain and possible changes in domain volume due to the incremental motion of the surrounding blocks. The new domain pressure (p) becomes

$$p = p_o + K_w Q \frac{\Delta t}{V} - K_w \frac{\Delta V}{V_m} \tag{9}$$

where

p_o = domain pressure in the preceding timestep,
Q = sum of flow rates in to the domain from all surrounding contacts,
K_w = bulk modulus of the fluid, and
$\Delta V = V - V_o$, $V_m = \dfrac{V + V_o}{2}$
where V and V_o are the new and old domain areas, respectively.

Given the new domain pressures, the forces exerted by the fluid on the edges of the surrounding blocks can be obtained. These forces are then added to the other forces to be applied to the block, such as the mechanical contact forces and external loads. As a consequence of this procedure, for deformable blocks, total stresses exist inside the impermeable (deformable) blocks, and effective normal stresses are obtained for the mechanical contacts.

Illustrative Example

In the example problem discussed here, the effect of various water levels behind a slope in regularly jointed rock (see Figure 6) is examined in terms of the stability of the slope. Initially, the problem is consolidated under gravity. Next, the water level at the right-hand side is raised to 6 m above the slope toe. The water level on the left-hand side is maintained at the level of the slope toe. With this right-hand water level, the slope is stable. The steady-state flow pattern for this condition is shown in Figure 7. Next, the right-hand water level is raised to 9 m. When the water level is raised, the slope remains stable. The steady-state flow condition for the 9-m water height is shown in Figure 8. Finally, the water level is raised to the top of the slope. The flow pattern for this case is shown in Figure 9. With the water level at 10 m, the lower portion of the slope slides, as shown in Figure 10. In Figures

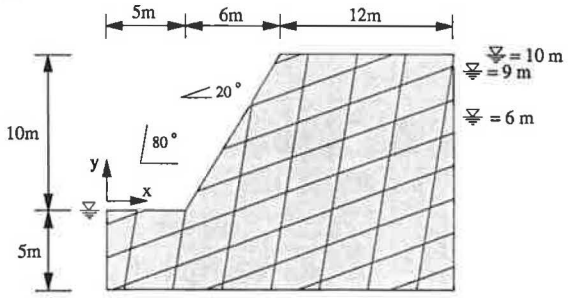

FIGURE 6 Problem geometry for example illustrating flow through jointed rock slope; ϕ = 25 degrees, c = 0, ρ = 2500 kg/m³.

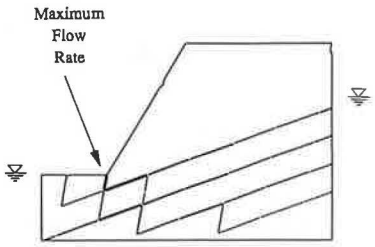

FIGURE 7 Calculated steady-state fluid flow rates for problem in Figure 5 for 6-m water level on right-hand side (maximum flow rate = 5.6e − 5 m³/sec).

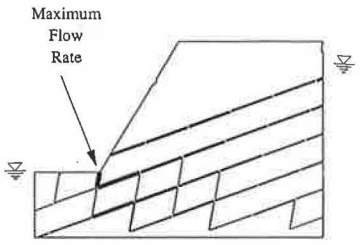

FIGURE 8 Calculated steady-state fluid flow rates for problem in Figure 5 for 9-m water level on right-hand side (maximum flow rate = 8.1e − 5 m³/sec).

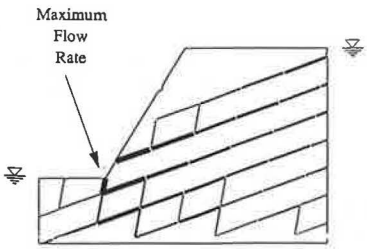

FIGURE 9 Calculated steady-state fluid flow rates for problem in Figure 5 for 10-m water level on right-hand side (maximum flow rate = 9.4e − 5 m³/sec).

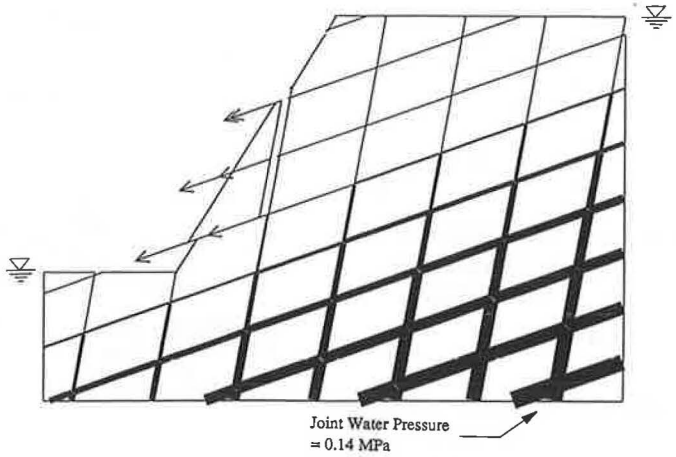

FIGURE 10 Failure of lower portion of slope when water level on right-hand side is 10 m.

7–9 the line thickness is proportional to the flow rates, and flow rates less than 1e − 5 m³/sec are not shown. In Figure 10 line thickness is proportional to calculated pore pressures in joints and the maximum joint water pressure is 0.14 MPa.

DYNAMIC ANALYSIS

The stability of rock slopes subjected to earthquake motion is frequently treated as a pseudostatic (actually, pseudodynamic) limit equilibrium problem with horizontal forces applied through the centers of gravity of potential sliding blocks. The magnitudes of the forces are equal to the product of the seismic coefficient and the weights of the sliding bodies. However, such approaches do not indicate the magnitude of displacements that may develop. Displacement estimates in the slope are often necessary to assess whether the relative displacements are sufficient to significantly reduce the shear strength along a discontinuity. The Newmark method of analysis (*11*) furnishes an estimate of displacement, but it is based on a single sliding block. More complicated slip patterns can be modeled by the distinct element method, which also accounts for the combined effect of horizontal and vertical seismic motion. Vertical motion can change joint normal stress and thereby influence sliding.

Dynamic analyses with the distinct element method are done with reduced or zero mass damping, but stiffness-proportional damping at contacts between blocks is usually present. Damping parameters are selected in an effort to reproduce the damping of natural materials at the correct level (about 2 to 5 percent) for the important frequencies in the problem. Input records of velocity are applied to the base of the model. Both horizontal and vertical motions may be prescribed, and all analyses are performed in the time domain. Detailed procedures for performing dynamic analyses are given by Lemos and Cundall (*12*). These authors present dynamic analysis of dam and jointed rock foundations subject to earthquake loading. They include results that quantify the damage on joint surfaces associated with repeated cyclic loading.

In the following example, the problem geometry shown in Figure 11 is used. Horizontal and vertical motion were specified for the base block and the slope response observed. The dynamic excitation used in all runs is that of an actual earthquake. The velocity records shown in Figures 12 and 13 were scaled to study the effect of different earthquake magnitudes. The slope configurations after 50 sec for scaling factors of 0.1, 0.5, and 0.6 are shown in Figure 14. Figure 14*a* shows that the slope is essentially stable for a scaling factor of 0.1, although small permanent deformations take place. Figure 14*b* shows more permanent deformation, and it shows that one block has fallen to the slope toe. Figure 14*c* shows the greatest displacement of slope blocks. Two of the blocks have moved outside the original problem window and are not shown.

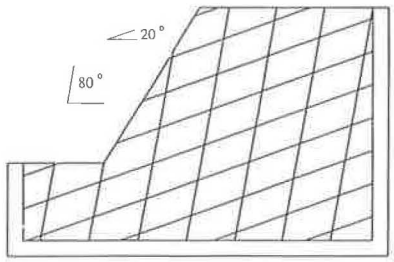

FIGURE 11 Problem geometry for example showing dynamic analysis (velocity input is specified for U-shaped base block); ϕ = 25 degrees, c = 0, ρ = 2500 kg/m³.

BLOCK DEFORMABILITY

Discussion so far has been limited to cases in which blocks can be assumed to be rigid. However, in some cases block deformability must be properly accounted for. The most obvious situations involve problems with high stresses relative to block strength. Another class of problems in which block deformability is important involves rock slopes or fills composed of many particles. Strictly speaking, their behavior on a small scale is that of a discontinuum. However, in cases in which particle size is small relative to critical dimensions of the problem, continuum behavior may be a reasonable ap-

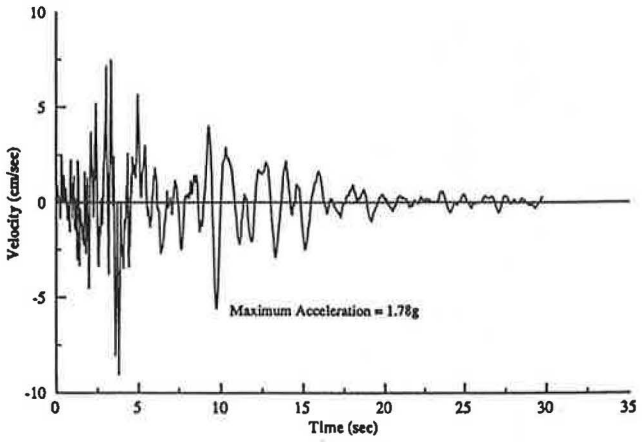

FIGURE 12 Earthquake velocity records applied to base block in Figure 11, vertical velocity input.

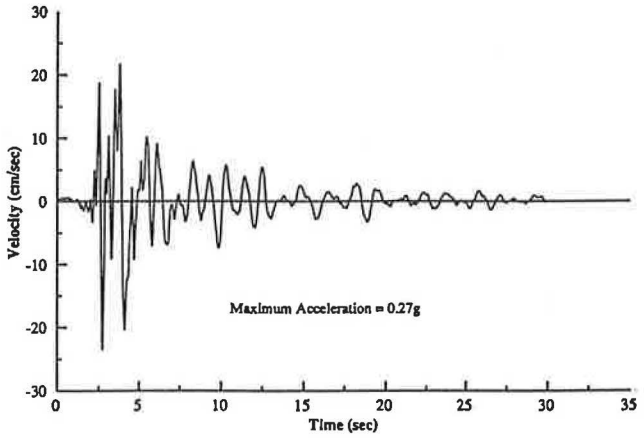

FIGURE 13 Earthquake velocity records applied to base block in Figure 11, horizontal velocity input.

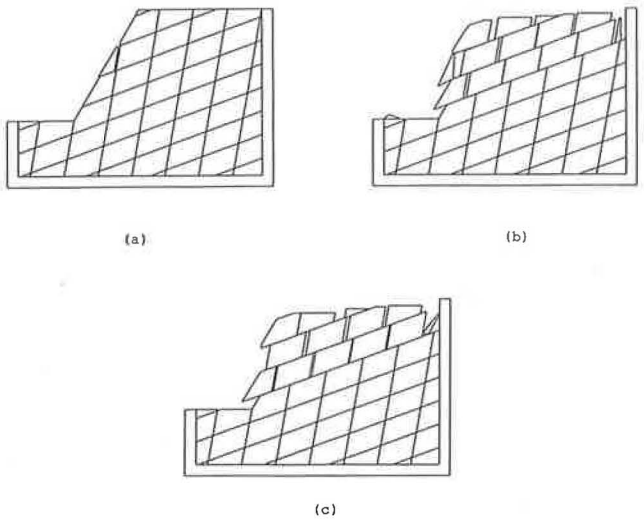

FIGURE 14 Equilibrium block positions 50 sec after earthquake: (a) scaling factor = 0.1, (b) scaling factor = 0.5, and (c) scaling factor = 0.6.

proximation. Response within each block can then be represented as a elastic-plastic material with failure defined by a Mohr-Coulomb criterion.

Formulation for Block Deformability

Fully deformable blocks are discretized into a mesh of triangular finite-difference zones, as in standard continuum modeling. Details of the formulation for fully deformable blocks are given in Board (*3*), Lemos (*7*), and elsewhere. The accuracy of the internal stress analysis corresponds to the degree of mesh refinement. Within each zone, a state of constant strain (stress) is assumed. Therefore, block boundaries remain defined by straight piecewise lines, permitting a simple determination of the relative displacements between adjacent blocks. Gridpoints are located at the vertices of each triangular zone. Their accelerations ($\ddot{u}_i$) are obtained from the equations of motion (no damping).

$$\ddot{u}_i = \frac{\int_S \sigma_{ij} n_j ds + F_i}{m} + g_i \tag{10}$$

where

S = Voronoi polygonal surface surrounding each gridpoint,
σ_{ij} = stress tensor,
n_j = components of the unit normal to S,
ds = incremental surface length,
m = mass lumped at each gridpoint, and
F_i = forces that include applied external loads and contact forces if gridpoints are located on a block boundary.

Illustrative Example

Rockeries (or rockery walls) are used to provide stability to otherwise oversteep-cut and embankment-filled slopes. They consist of large individual blocks stacked to form a retaining structure, as shown in Figure 15. Use of the distinct element method to analyze the capacity of such clopes is described by Lorig and Santurbano (*13*) and Santurbano (*14*).

Figure 16 shows the problem geometry used to idealize a bridge abutment similar to that shown in Figure 15. In Figure 16, the rockery is represented by five quadrilateral rigid blocks of regular shape. The footing is assumed to consist of a single rigid block. The base of the model, which is assumed to be a firm foundation, is also represented by a fixed rigid block. The rockfill is represented by five deformable blocks that have been internally discretized with four different element sizes, on the basis of their position. The smallest mesh size is under the footing; it was determined from sensitivity studies of a footing on a frictional material. The mesh size of the region just beneath was chosen from sensitivity studies of a slope in a frictional material. A coarser mesh was selected to represent the backfill because the stress and displacement gradient expected there are less. Finally, the position of the right-hand boundary was located at a distance remote enough to eliminate its influence on bearing capacity results.

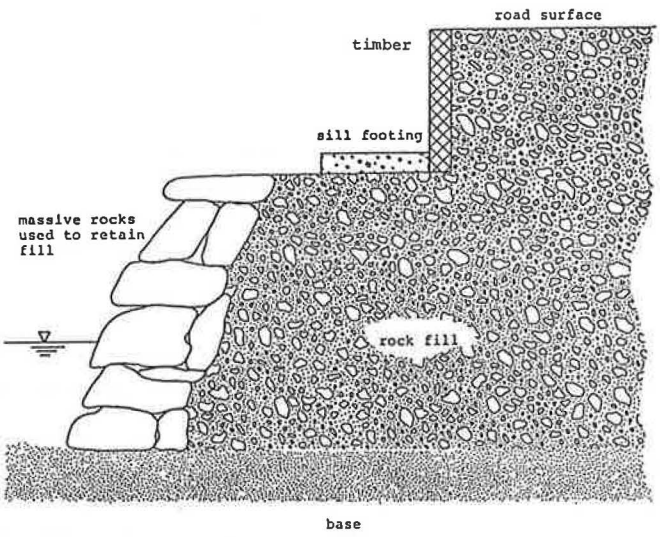

FIGURE 15 Composition of typical rockfill slope.

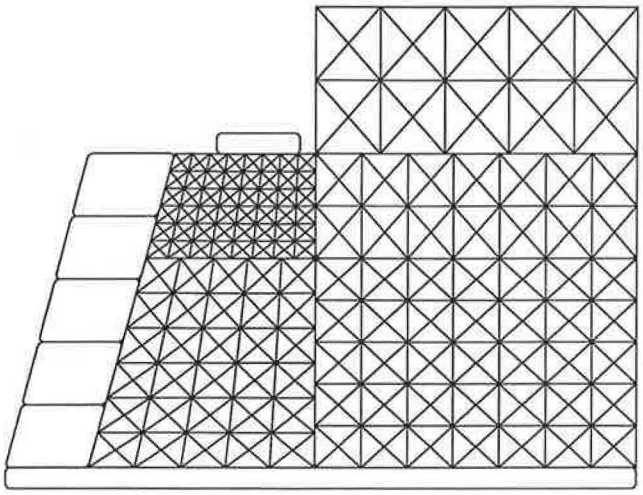

FIGURE 16 Idealization of typical bridge abutment (rockfill represented by constant strain triangular finite-difference zones).

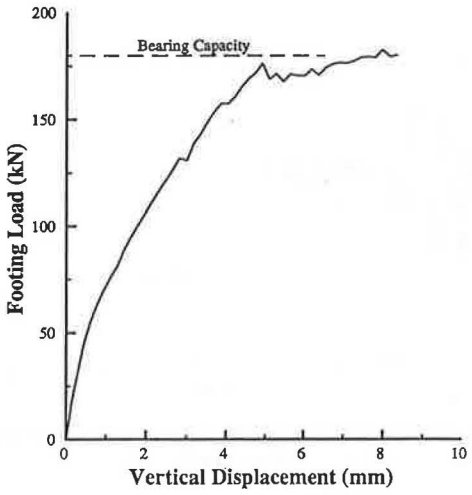

FIGURE 17 Footing load-displacement relation determined from distinct element analysis.

The footing load was simulated by applying a constant downward velocity to the rigid block representing the footing. The bearing capacity was determined by monitoring the force change beneath the footing. Figure 17 shows the relation of footing displacement and applied load. The velocity field shown in Figure 18 indicates that failure in this case results from rotation of the rock face about the base of the retaining structure; a different mode of failure, involving translational sliding, occurs for other combinations of parameters.

DISCUSSION OF RESULTS

The distinct element method provides a useful tool for understanding a wide range of problems involving the stability of slopes in jointed rock masses. The method requires specification of the usual problem parameters: geometry, joint strength properties, material density, and gravity. In addition, the

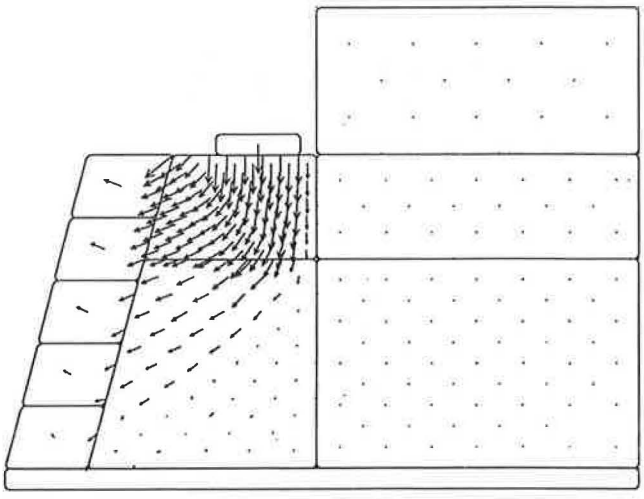

FIGURE 18 Velocity field at failure.

method uses joint stiffness properties that are difficult to determine. However, for nearly all problems, results of stability analysis are insensitive to the choice of joint stiffness. This is understandable, because stability depends primarily on strength, not on elastic properties. This paper has shown that the distinct element method overcomes the two main limitations of the limit equilibrium method, namely, the requirement to predefine the failure mode and the inability to compute displacements. The ability to estimate displacements has been shown to be particularly important for studying the behavior of rock reinforcement and rock slopes subjected to earthquake loading. Extensions of the method to include the presence of water in joints and block deformability have also been presented.

ACKNOWLEDGMENTS

The illustrative problem discussed under block deformability was studied under a contract administered by FHWA. The senior author expresses thanks to Carol Seitz of Region 10, U.S. Department of Agriculture, Forest Service, and to Al DiMillio of Office Engineering and Highway Operations R&D, FHWA, for enthusiastically sharing their time and suggestions during the course of this work.

REFERENCES

1. P. A. Cundall. A Computer Model for Simulating Progressive Large Scale Movements in Blocky Rock Systems. *Proc., Symposium of the International Society for Rock Mechanics*, Vol. 1, Nancy, France, 1971.
2. P. A. Cundall. Computer Interactive Graphics and the Distinct Element Method. *Proc., ASCE Speciality Conference*, Vol. II, Boulder, Colo., Aug. 1976.
3. M. Board. *UDEC Version ICG1.5.* Report NUREG/CR-5429, Vol. 1–3. U.S. Nuclear Regulatory Commission, Washington, D.C., Sept. 1989.
4. R. Hart, P. A. Cundall, and J. Lemos. Formulation of a Three-Dimensional Distinct Element Model—Part II: Mechanical Calculations for Motion and Interaction of a System Composed of Many Polyhedral Blocks. *International Journal of Rock Mechanics and Mining Sciences & Geomechanics Abstracts*, Vol. 25, 1988, pp. 117–126.
5. P. A. Cundall. Distinct Element Models of Rock and Soil Structure. *Analytical and Computational Methods in Engineering Rock Mechanics* (E. T. Brown, ed.). George Allen and Unwin, London, England, 1987, pp. 129–163.
6. P. A. Cundall and J. V. Lemos. Numerical Simulation of Fault Instabilities with a Continuously Yielding Joint Model. *Rockbursts and Seismicity in Mines* (C. Fairhurst, ed.). A. A. Balkema, London, England, 1990, pp. 147–152.
7. J. Lemos. *A Distinct Element Model for Dynamic Analysis of Jointed Rock with Application to Dam Foundations and Fault Motion.* Ph.D. thesis. University of Minnesota, Minneapolis/St. Paul, June 1987.
8. B. Brady and L. Lorig. Analysis of Rock Reinforcement Using Finite Difference Methods. *Computers and Geotechnics*, Vol. 5, No. 2, 1988, pp. 123–149.
9. S. Bjurstrom. Shear Strength of Hard Rock Joints Reinforced by Grouted Untensioned Bolts. *Proc., 3rd International Congress on Rock Mechanics*, Vol. 2, 1974, pp. 1,194–1,199.
10. P. J. N. Pells. The Behaviour of Fully Bonded Rock Bolts. *Proc., 3rd International Congress on Rock Mechanics*, Vol. 2, 1974, pp. 1,212–1,217.
11. N. M. Newmark. Fifth Rankine Lecture: Effects of Earthquakes on Dams and Embankments. *Geotechnique*, Vol. 15, No. 2, 1965, pp. 139–159.
12. J. V. Lemos and P. A. Cundall. Earthquake Analysis of Concrete Gravity Dams on Jointed Rock Foundations. *International Journal for Numerical and Analytical Methods in Geomechanics* (in preparation).
13. R. Santurbano and L. Lorig. An Improved Procedure for Design of Rockeries Using ESAC. *Rock Mechanics Contributions and Challenges*, A. A. Balkema, Rotterdam, the Netherlands, 1990, pp. 769–776.
14. R. Santurbano. *Development of a Computer-Aided Design Procedure for Massive Rock Slope Stability Analysis.* M.S. thesis. University of Minnesota, Minneapolis/St. Paul, 1990.

Publication of this paper sponsored by Committee on Soil and Rock Properties.

Use of Nonlinear Strength Criteria in Stability Analyses of Bridge Foundation on Jointed Rock

DOUGAL R. MCCREATH

During construction of a bridge project, it became important to check the stability of one of the bridge pier foundations. The spread-footing foundation was located at the crest of a 60-ft-deep bedrock channel formed by a series of steeply dipping joints. The overall slope of the channel face was about 50 degrees, and rock mass conditions exposed during construction prompted concerns about potential instability of the channel wall beneath the footing. As a consequence, the foundation was modified: a keyway was excavated beneath the footing and a series of long rock bolts designed to guard against possible sliding of the block of rock was installed beneath the footing. At the request of the owner, independent investigations and analyses were undertaken to evaluate the stability of the modified foundation. The approach used for the stability evaluation was first to assess which mechanisms of failure could be considered kinematically feasible on the basis of field investigations of geological conditions. Then, for each potential failure mechanism, appropriate strength parameters were assigned to the sliding surfaces involved. Finally, the stability of the system against each postulated failure mechanism was evaluated. In this process, the nonlinear Barton criterion for shear strength of a rough discontinuity was applied to a potential block sliding mechanism, and the nonlinear Hoek-Brown criterion for the strength of a pervasively jointed rock mass was applied to a potential circular failure surface passing beneath the footing. In the latter case, stability analysis methods developed by Bishop and Sarma were used, because the latter method allows specific geological structural features to be incorporated in the body of the slide mass with shear strength parameters that differ from those along the basal plane of sliding. This approach is considered to more closely reflect the actual conditions often present in a jointed rock mass. The methods used and the results obtained from the stability evaluation are summarized, with particular reference to the selection of Barton and Hoek-Brown shear strength parameters.

The structure considered in this paper is a bridge crossing of a 200-ft wide navigation channel. The bridge crosses the east-west channel in a north-south direction and has three interior piers in addition to its two end abutments (Figure 1). The navigation channel passes between the two most southerly interior piers, which are separated by a 390-ft span. The southern bank of the channel is formed by a steep bedrock face that rises to about 60 ft above the base of the channel (Figure 2). The lower 30 ft of this face are nearly vertical; it is separated by a 20-ft-wide bench from the upper 30 ft, which slope at 65 degrees to the north. Overall, the channel bank slopes at about 50 degrees to the north.

Golder Associates, Inc., 4104 148th Avenue N., Redmond, Wash. 98052. Current affiliation: School of Engineering, Laurentian University, Ramsey Lake Road, Sudbury, Ontario, Canada P3E 2C6.

The pier resting above the southern bank of the channel was designed to carry a total dead-plus-live load of 11,300 kips. The earthquake conditions assumed by the designers resulted in a lateral seismic loading equivalent to 0.3 times gravity. The foundation for this bridge pier was originally designed as a 34- × 46-ft spread footing bearing on a prepared horizontal rock surface. To develop the bearing surface, a rectangular box cut or sinking cut was planned; the depth of the cut varied from 12 ft at the northwest corner of the footing to 32 ft at the southeast corner because of the ground surface topography. During excavation of the cut, the contractor had some difficulties in maintaining this enclosed shape, and the front or northern face of the cut was lost. The resulting excavation was a bench with a flat floor at elevation 18 [elevations are given as feet above mean sea level (MSL)]. Inspection of the rock conditions exposed during this early stage of construction apparently aroused concern about the stability of the foundation. As a result, it was decided to strengthen the foundation area by cutting an 8-ft-deep "keyway" into the base of the excavation, installing thirty-one 150-kip-capacity rock bolts of various lengths and orientations and ultimately backfilling with reinforced concrete to the top of the footing at elevation 28. The final foundation geometry is shown in Figure 2.

In light of these experiences during construction and the various modifications made as a result, the owner wished to verify that the stability of the foundation was acceptable, and independent consultants were retained to do so. The geological conditions beneath the footing were investigated to identify what potential failure mechanisms, if any, could be considered kinematically feasible. On the basis of the investigation results, the relevant engineering properties of the foundation rock mass were assessed with particular regard to the shear strength available along significant preexisting discontinuities and the shear strength parameters governing the overall behavior of the jointed rock mass. These data were used as input to a series of analyses to evaluate the stability of the foundation under static and earthquake conditions, both with and without consideration of the rock bolts that had been installed.

SUMMARY OF POTENTIAL FAILURE MECHANISMS

For failure to occur through the rock mass underlying the footing, a failure mechanism that is kinematically possible

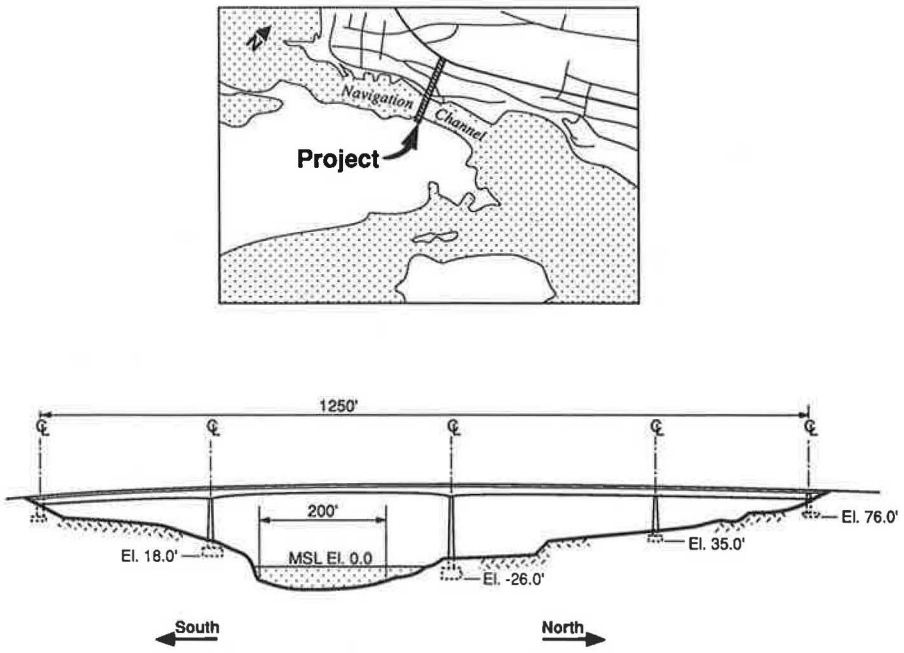

FIGURE 1 Project layout.

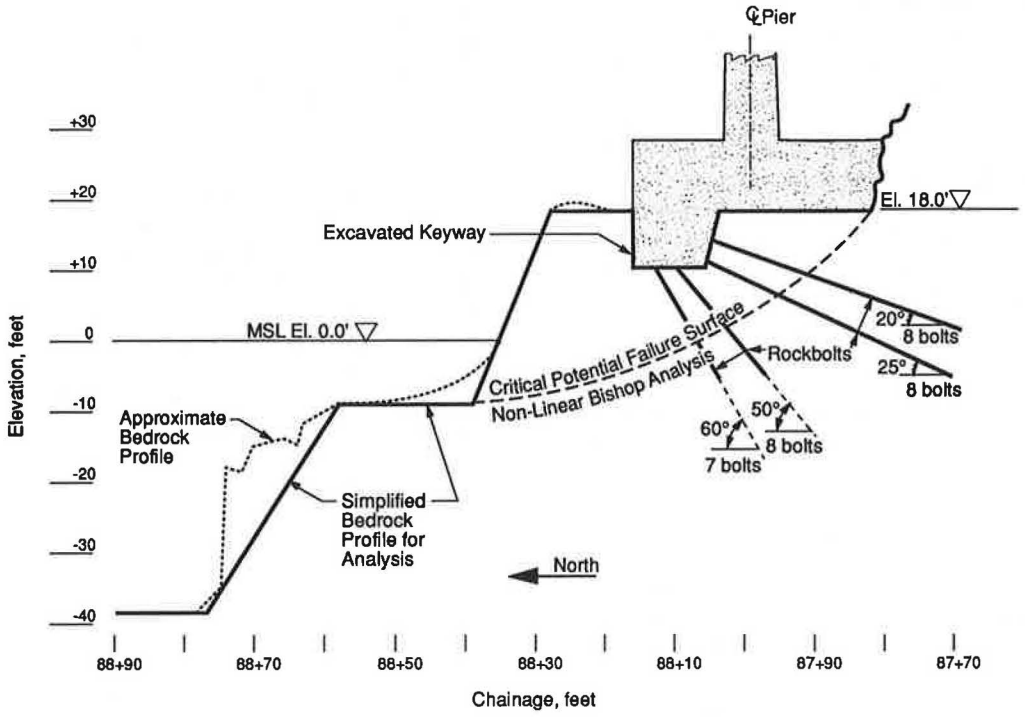

FIGURE 2 Pier foundation.

must be formed or it must preexist. Typical potential failure mechanisms have been presented by Hoek and Bray (*1*, p. 358), and the mechanisms relevant to the footing under consideration are shown in Figure 3. In general, there are two classes of such mechanisms: those that are controlled by preexisting discontinuities within the rock mass, or so-called structurally controlled failures, and those that require a new failure surface to form at some critical location, passing through the assemblage of jointed, blocky material that constitutes the overall rock mass; these are called general or overall failure mechanisms.

Structurally controlled mechanisms are governed by preexisting discontinuities within the rock mass, such as joints, faults, shear planes, or bedding planes, and the geometry of the potential sliding mass will be defined by these bounding planes. The stability of the mass will then be controlled by

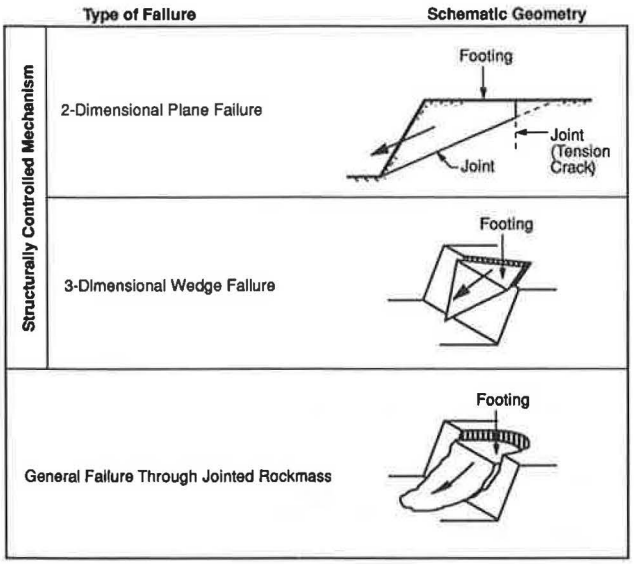

FIGURE 3 Potential failure mechanisms.

the shear strength that can be mobilized along these planes in comparison with the driving forces involved. For the foundation in question, two types of structurally controlled failure mechanism were potentially significant to the overall stability of the footing, these being a simple two-dimensional block sliding or planar failure mechanism and a three-dimensional wedge failure mechanism. In both cases, the potential for a kinematically feasible failure mechanism to form depends on whether the necessary bounding planes exist in the rock mass, that is, whether a failure geometry can be formed.

Thus, a primary objective of the geological investigation was to assess whether subsurface conditions existed giving rise to kinematically feasible, structurally controlled failure mechanisms, of either the planar or the wedge type, that might jeopardize the safety of the foundation. Hoek and Bray (*1*) have summarized the geometric conditions that must be met for these failure mechanisms to be kinematically possible, and these conditions were used as guidelines in assessing the potential for planar- or wedge-type failures to develop. For plane failure,

- The strike of the basal sliding plane must be within about ±20 degrees of the strike of the slope face;
- The dip of the base plane must be less than the dip of the slope face for the potential failure plane to daylight;
- Release planes must be present at the two ends of the potential failure mass;
- The dip of the base plane generally must be greater than the friction angle along the plane, in the absence of other disturbing forces; and
- The existence of a water-filled tension crack or joint forming a backscarp may significantly reduce stability.

For wedge failure,

- Two intersecting joint planes must exist, having a line of intersection plunging at less than the dip of the slope face in order to daylight;
- The direction of the line of intersection must be such that there is a plunge component out of the slope that meets the above criterion; and
- Truncation of the apex of the wedge by a water-filled joint or tension crack will reduce stability.

If the geometric conditions for planar sliding or wedge mechanisms are satisfied, then the potential for failure depends on the shear strength available along the bounding planes compared with the driving forces involved. Many authors have discussed the determination of reasonable shear strength parameters for discontinuities in rock, and these discussions are summarized in Hoek and Bray (*1*). For practical field applications, the relationship proposed by Barton (*2*) between the shear strength of a rough joint and the normal stress acting across the joint is particularly useful, and this approach was used for these investigations. Further detail is given later, in the discussion of engineering properties of the rock mass.

Besides the potential for structurally controlled failure mechanisms as noted, a general rotational failure surface may be formed through a rock mass that is closely or ubiquitously jointed relative to the scale of the foundation (Figure 3). In this situation, a failure surface may form anywhere within the rock mass, constrained only by the overall shear strength properties of the mass and the loads applied to it. In general the rock mass will comprise more or less interlocking blocks of essentially intact rock material separated by discontinuities, and the shear strength envelope of such a rock mass will generally be nonlinear because of the effects of dilation at the low normal stresses that commonly prevail in slope stability problems. For this reason, it was decided that the nonlinear strength envelope or failure criterion proposed by Hoek and Brown (*3*, p. 527) was most appropriate for application to any area of the foundation rock mass through which a general failure surface might develop because of its blocky, jointed nature. However, the problems of assessing the appropriate values of the strength parameters for such rock masses on the basis of theoretical or laboratory work are formidable. In recognition of this problem, a suggested method by which reasonable estimates of the strength of jointed rock masses can be made was the subject of Hoek's 1983 Rankine lecture (*4*). The method relies on characterizing the rock mass according to its lithology (i.e., the rock type) and its overall quality using the well-known Bieniawski (*5*) or Barton (*6*) classification systems. This characterization of the rock mass is then used to evaluate the necessary Hoek-Brown strength parameters. Further details are noted in the discussion of the engineering properties of the rock mass.

- Is it reasonable to assume that there are existing discontinuities in the foundation rock mass that could, on the scale of the footing, form the base plane for a two-dimensional planar sliding failure?
- Are there existing discontinuities in the rock mass that could, on the scale of the footing, fulfill the geometric requirements for a potential wedge failure?
- For either of those two cases, what geometric and strength parameters are reasonable to assign to the planes?

- What is the lithology and quality of the rock mass in the foundation, and do these factors vary for different domains across the footing area?
- What strength parameters are reasonable to assign to the jointed rock mass?

SUMMARY OF GEOLOGICAL CONDITIONS

When this stability evaluation was requested, construction had already progressed to the point that the footing concrete had been poured and crushed rock backfill placed over much of the site (Figure 4). Therefore, direct mapping of the rock mass immediately beneath the footing was no longer possible, and geologic description of the site conditions was accomplished through literature review, analysis of air photographs, detailed geologic mapping of adjacent areas, and the drilling of three coreholes through the footing into the underlying foundation rock mass. The relevant findings are briefly summarized in the following.

Geologic Units

The bridge pier under consideration is founded on an assemblage of sedimentary rocks thought to be weakly metamorphosed. On the basis of visual examination, these rocks were classified as interbedded metagreywackes and argillites. The metagreywacke is dark gray, with a grain size varying from fine sand to silt. It is classified mechanically as weak to medium-strong rock, according to International Society for Rock Mechanics standards. The grayish-black argillite usually occurs as interbeds of less than 4 in. thick. Slaty cleavage is developed locally, and in some cases "slate" may be a more appropriate rock name. The argillite is generally weaker than the metagreywacke, so joints, healed fractures, and drill breaks are frequently associated with the argillite interbeds.

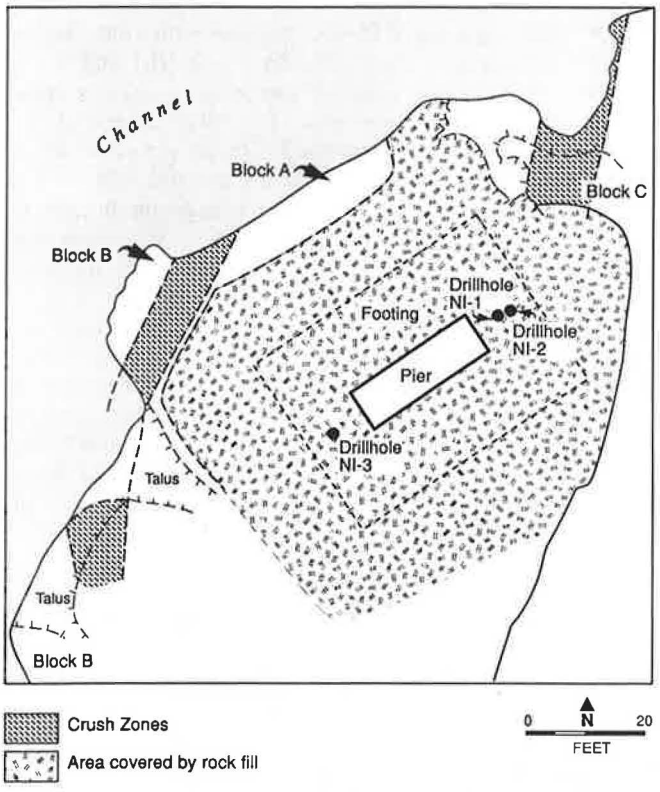

FIGURE 4 Rock mass domains in foundation area.

Rock Mass Domains

The rock mass near the pier footing was divided into three domains, designated Blocks A, B, and C, separated by crush zones or shear zones (Figure 4). The largest shear zone at the site lies to the east of Block A, separating it from Block C. As shown in Figure 4, this major crush zone appears in outcrop near the northeast corner of the footing and trends toward the pier location. On the basis of inference from the available outcrops and data from corehole drilling, it is probable that Block A rocks underlie approximately the western half of the footing area and shear zone or crush zone rocks underlie the eastern half. Projections of the trend of the major shear zone suggest that this proportion is likely, but the extent of the shear zone beneath the footing could not be located precisely because of masking by the coarse rockfill that had been placed over the footing. However, the overall width of the shear zone beneath the footing is constrained by the evidence from Borehole NI-3 to the west of the pier, which penetrates rocks interpreted as belonging to Block A and is clearly not within the much more fractured rocks of the shear zone.

The shear zone trends at an angle of about 45 degrees across the foundation and, within the shear zone itself, closely spaced vertical joints strike in a direction parallel to the overall trend of the zone. The rock within the shear zone comprises closely interlocked, vertically oriented slabs of hard, intact material, such that a significant amount of breakage of intact rock material would be required for any failure plane to cut across the grain of this shear zone. On the basis of geological evidence, the shear zone was not considered to represent a currently active fault.

The domain designated as Block A underlies at least the western part of the foundation. This block has consistent bedding with a strike of N23°E and a dip of 65 degrees south. The major slope face behind the footing and the channel face itself both have a strike of approximately N55°E and a dip of 55 degrees north, reflecting the presence of a general set of throughgoing, planar joints. Cross joints appear at intervals from 6 in. to 3 ft and are also planar but have a relatively rough surface. Persistence of the cross joints varies from 1 to 8 ft, and they tend to die out or be offset as they cross other joints or interbeds. The rock materials within Block A have considerable mechanical strength, as indicated by point-load tests that give strengths of about 20,000 psi. Jointing frequency in Block A is relatively low and rock quality designations (RQDs) of 100 percent were common in many of the core runs, with an average RQD value of 89 percent in Hole NI-3.

Structurally Controlled Potential Failure Mechanisms

Discontinuity orientation data were collected in areas adjacent to the bridge pier, and it was determined that these data were fully consistent with information on the regional structural geology. These data indicated that four discontinuity sets besides the previously noted shear zones were present in the general vicinity of the pier, as summarized below:

Discontinuity Set	*Strike/Dip*	*Description*
1	N55°E/55°N	Major joint set at site; forms channel wall
2	N30°W/75°N	Small number of joints in Block C
3	N20°E/65°S	Bedding in Block A
4	N65°E/70°S	Minor Block C joints
Crush (shear) zones	N15°E/90°	From few inches to several feet wide

These data were analyzed using stereographic projection to determine which failure mechanisms were kinematically feasible, as shown in Figure 5. This analysis indicated that although the steeply dipping Set 1 joints, lying parallel to the channel wall, were available to form the tension crack or backplane needed to release a planar failure, the necessary base sliding plane was absent from the data. In general, significant discontinuities with a northerly dip that could daylight out of the channel face were completely absent, not only from the immediate vicinity of the bridge pier but also from a much wider surrounding area. These surface observations were corroborated by the data from the carefully conducted drilling, which used triple-tube core barrel techniques to ensure full core recovery. No evidence was found of continuous planes that intersected the vertical coreholes at dip angles that could allow them to act as potential basal slide planes. The lack of any evidence of the existence of a potential basal slide plane effectively ruled out plane failure or two-dimensional block sliding as a mechanism that could jeopardize overall foundation stability. However, small, localized failures could still occur in the thin zone of rock lying between the north face of the footing and the channel wall, because of local variations in the dip of the Set 1 joints that directly control the shape of the channel wall.

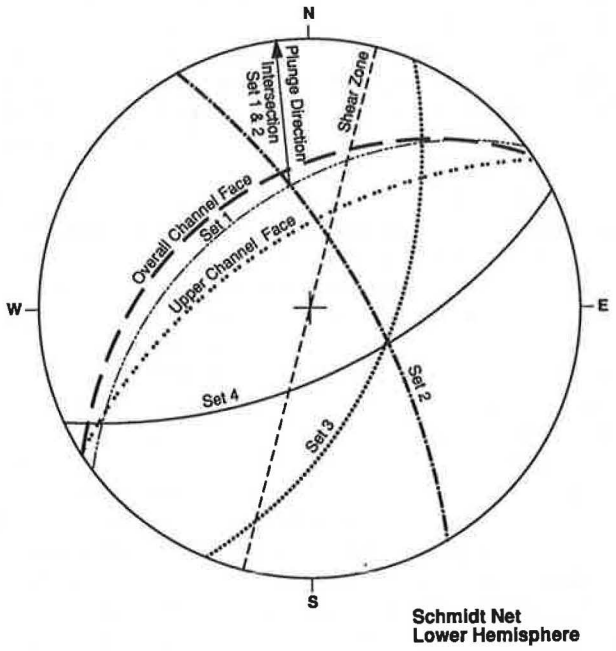

FIGURE 5 Summary of discontinuity orientations.

For wedge failures to be kinematically feasible and of significant concern, appropriate joint orientations must exist with respect to the free face (channel face), and the joints must be of sufficient persistence to allow sliding. As shown in Figure 5, only Joint Sets 1 and 2 could combine to form wedges that meet the necessary geometric criteria for potential failure. However, the Set 2 joints were mapped only within Block C, to the east of the actual footing area; some wedge failures were in fact evident in this Block C area, but they were of very minor extent, because the plunge of the line of intersection of the wedges is within a few degrees of the dip angle of the free face (Figure 5). On the basis of these factors, wedge failure was not considered to be a credible failure mode of significance with respect to the stability of the pier foundation.

General Rotational Failure

The development of a general slide plane through the foundation rock mass, along which an overall rotational failure could occur, depends on the presence of materials that are weak compared with the loads applied to them. In this regard, intensely jointed rocks are conceptually similar to granular soils with a very large grain size. Rock in the shear zone that underlies about half of the footing is the weakest material in the area of interest because of the intense jointing associated with the shearing to which the rock has been subjected. Within the major shear zone penetrated by Holes NI-1 and NI-2, fractures were so numerous that it was not possible to separate drill breaks from natural fractures. Naturally, the vertical orientation of the drillholes combined with the vertical attitude of the jointing within the shear zone, and therefore of the slabs or pods of intact rock, tended to exaggerate this effect, giving rise to particularly low RQD values. Nevertheless, the formation of a general slide surface in this material, not constrained by specific preexisting discontinuities, must be evaluated as a potentially credible failure mechanism. In undertaking this evaluation, it is important to keep in mind that the relative attitudes of the channel face, the shear zone, and the rock fabric within the shear zone are such that any new rotational sliding plane of failure that formed beneath the footing would be forced to cut across the grain of the intact rock fragments within the shear zone, requiring fracture of these intact rock materials.

In summary

- About half of the footing area (the western half) is founded on a block of relatively fresh, strong, interbedded greywackes and argillites (Block A) that has a fairly low joint frequency indicated by an average RQD of about 90 percent.
- Within Block A rocks, the steep channel face is controlled by a major joint set (Set 1) that could give rise to localized plane failures in front of the footing because of local variations in dip of the joints. No other planar failure or wedge failure mechanisms of significance were identified in Block A rocks.

- About half the footing area (the eastern half) is underlain by a major vertically oriented shear zone that strikes across the foundation at an angle of about 45 degrees.
- Within the shear zone, the closely spaced vertical jointing results in a fabric of vertically oriented interlocking pods or slivers of hard, intact rock material.
- Although development of a general surface of sliding across the shear zone rocks would require some fracturing of intact rock material, this potential failure mechanism must be further evaluated to determine if it threatens the stability of the foundation.

ENGINEERING PROPERTIES OF ROCK MASS

As noted, there are two geologically credible failure mechanisms that could affect the pier foundation. First, there is the possibility of local planar or block sliding occurring in front of the footing, along one of the preexisting Set 1 joint planes. Second, there is the potential for a general failure surface to develop through the rocks of the major shear zone that cuts across the foundation. In the first case, it is necessary to assign some appropriate shear strength parameters to the specific discontinuities on which sliding could occur. In the second case, it is necessary to evaluate the shear strength parameters for the overall rock mass material within the broad shear zone or crush zone beneath the footing.

In both cases, the shear strength envelopes of the rock materials are known to be nonlinear as a function of normal stress due to the effects of dilation, or volume increase that occurs as two rough surfaces are sheared past each other. Various investigators have proposed nonlinear strength envelopes for rock material in order to capture this effect (*1–3*), because ignoring this nonlinearity can result in seriously underestimating the shear strength of the material, particularly at the fairly low normal stress levels common in slope stability problems. However, many of the widely available slope stability analysis programs have been based on the use of linear strength envelopes for the materials, and it is therefore sometimes necessary or desirable to use equivalent linear strength parameters for these decidedly nonlinear materials. One way to do this is to first develop the nonlinear strength envelope that appears most appropriate for the material and then evaluate the approximate normal stress level that will be acting in the material and use this information to determine the slope angle (ϕ) and the cohesion intercept (c) of the tangent to the failure envelope at this specified level of normal stress. These parameters can be used as equivalent linear shear strength parameters, applicable to cases in which the normal stresses do not deviate too markedly from those assumed. Sometimes it may be more appropriate to use the slope of the secant to the nonlinear strength envelope at the normal stress level of interest. In this case the cohesion intercept would be zero and the equivalent linear shear strength would be defined by the single parameter of the overall friction angle (ϕ).

Shear Strength of Discontinuities

As previously summarized, the only significant discontinuities that are present in the rock mass and that could contribute to the formation of a structurally controlled failure in the foundation area are the joints that lie subparallel to the face of the channel and actually control the geometry of this face. These joints, referred to as Set 1, strike at about N55°E and dip generally between 50 and 70 degrees to the north. Such joints could form the base plane for a localized failure near the face of the channel; they could also form a tension crack or backscarp for a slide mass. In addition, these joints could form the interior slice boundaries within a general rotational slide mass. In each case, the shear strength available along these joints must be evaluated before meaningful stability analyses can be conducted.

To estimate the shear strength of cohesionless joint surfaces, the following relationship proposed by Barton (*2*) is particularly useful.

$$\tau = \sigma' \tan[\phi_b + \text{JRC} \log_{10}(\text{JCS}/\sigma')] \quad (1)$$

where

τ = shear strength,
σ' = effective normal stress across joint,
ϕ_b = basic friction angle of a planar discontinuity in the type of rock under consideration,
JRC = joint roughness coefficient, measured against standard profiles published by Barton and ranging in value from 5 for a smooth surface to 20 for a rough, undulating surface, and
JCS = joint wall compressive strength, which equals the uniaxial strength of the intact rock material for clean, unweathered joints.

On the basis of field investigations and index testing, such as point-load testing to assess comprehensive strength, the following parameters were selected for use in subsequent stability analyses:

- ϕ_b: The rock material is predominantly greywacke. On the basis of data published by Barton (*2*) and by Martin and Miller (*7*) on joint surfaces in moderately weathered greywacke, a value of ϕ_b between 25 and 30 degrees was considered appropriate.
- JRC: On the scale of the exposed joint faces visible in the field, to a maximum of 10 ft of continuity, values of JRC varied from 4 to 10 in a comparison with standard roughness profiles (*1*). However, on the scale of any failure mass large enough to significantly affect the integrity of the footing, the effect of undulations along the plane of the joint face must also be considered. Thus, a minimum value of 7 was considered to be conservative but reasonable.
- JCS: For the discontinuities under consideration, the wall rocks of the joints consist of unweathered to slightly weathered materials ranging in composition from siltstone to fine-grained sandstone. Point-load test results indicated uniaxial compressive strengths of the rock material in the order of 20,000 psi. For stability analyses a value of 7,500 psi was used to ensure that the results were conservative but realistic.

The normal stress acting across any specific joint plane (σ') will depend on the particular geometry involved, the loading conditions, and the joint water conditions or degree of saturation of the rock mass. For the conditions being considered,

the effective normal stresses lay in the range from 0 to 3,000 pounds/ft² (psf). On the basis of the parameters for Barton's Equation 1, Figure 6 shows a shear strength plot or Mohr envelope for these Set 1 joints. Note that this curvilinear envelope is only valid for cohesionless joints and does not apply to those conditions in which failure is forced to occur through bridges of intact rock. For such situations an additional allowance must be made for a cohesive component of the joint shear strength. As shown in Figure 6, the shear strength envelope is not very strongly curved in the region from $\sigma' = 0$ to 3,000 psf. At an effective normal stress level of $\sigma' = 1{,}000$ psf, the shear strength may be reasonably represented by an equivalent overall friction angle of $\phi = 50$ degrees and a cohesion of $c = 0$, which is the slope of the secant to the envelope at this normal stress level. This overall equivalent friction angle can then be used directly in stability analyses based on the well-known linear Mohr-Coulomb relationship

$$\tau = c + \sigma' \tan \phi \tag{2}$$

Shear Strength of Jointed Rock

As noted previously, there is a major shear zone or crush zone passing beneath the eastern half of the footing. Within this zone is a structure of vertically oriented interlocking angular fragments of generally unweathered greywacke and argillite. The overall attitude of the zone and of the long axes of the blocks of intact rock within the zone is close to vertical in dip, with the zone striking obliquely across the footing at an angle of about 45 degrees.

To provide a conservative but reasonable assessment of the stability of the foundation, it was assumed for analysis purposes that the entire rock mass beneath the footing consisted of one large shear zone. The logic behind this approach was that such a hypothesis would reflect the worst-case scenario that could reasonably be postulated within the constraints imposed by the geological framework of the site. If the calculated foundation stability were found to be acceptable under these postulated conditions, then there would be considerable confidence in the satisfactory performance of the actual foundation rock mass, which was predicted to comprise about equal proportions of Block A rock and shear zone rock.

To proceed with stability analyses incorporating general surfaces sliding through the crush zone or shear zone rocks underlying the footing, estimates were required for the shear strength of this jointed mass. Methods by which such estimates can be made have been outlined by Hoek (*4*). For this purpose, Hoek and Brown's empirical relationship between the major and minor principal stresses acting on an element of rock at failure is used (*3*):

$$\sigma_1 = \sigma_3 + (m\sigma_c\sigma_3 + s\sigma_c^2)^{1/2} \tag{3}$$

where

σ_1 = major principal stress at failure,
σ_3 = minor principal stress at failure,
σ_c = uniaxial compressive strength of intact rock particles within the jointed mass, and
m, s = empirical constants.

To evaluate the empirical constants m and s, the material is first classified according to its lithologic origin and then according to the overall quality of the rock mass (*4*). To characterize the overall quality of the rock mass, the widely known rock mass classification systems proposed by Barton (*6*) and Bieniawski (*5*) are used. In addition, in later publications Hoek (*8*) has considered whether or not the interlock of the blocks within the rock mass has been retained ("undisturbed rock mass") or lost ("disturbed rock mass"). Following these procedures in a conservative manner, the rock

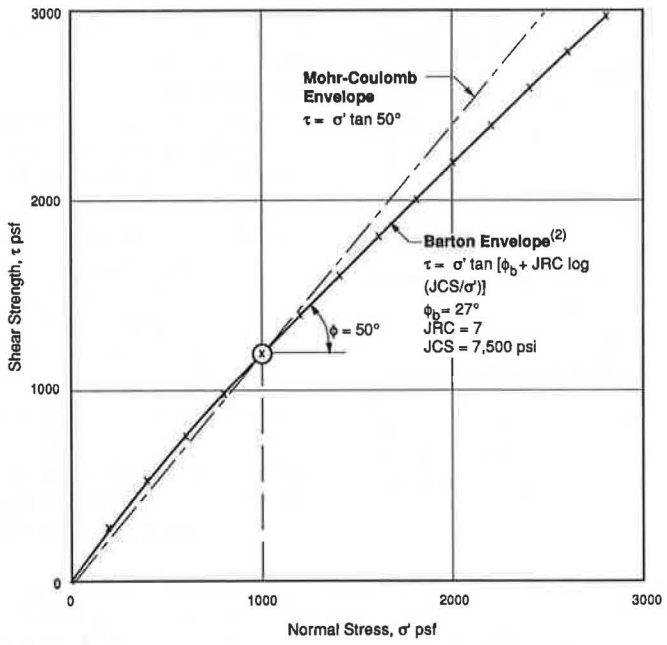

FIGURE 6 Estimated shear strength of Set 1 joints.

mass within the crush zone was considered to be disturbed, characterized as lithified argillaceous to arenaceous rocks of generally fair quality, locally ranging from good to poor quality, equivalent to a Rock Mass Rating of 25 to 50 (*5*). The unconfined strength of intact rock fragments is 7,500 psi.

For a rock mass so characterized, an appropriately conservative value of the empirical Hoek-Brown parameter m was selected as $m = 0.13$. The parameter s is generally considered to represent the degree of brokenness of the rock mass. The degree to which the shear zone rock mass should be considered as broken depends on the amount of intact material that would have to be sheared through in developing a sliding surface that cuts across the grain of the shear zone, as previously discussed. Therefore, it was decided to investigate the effect on stability of a range of values for the parameter s, from $s = 0.00005$ (more broken) to $s = 0.002$ (less broken).

On the basis of mathematical relationships (*4*), the Hoek-Brown failure criterion, which is expressed in terms of principal stresses, can be used to calculate envelopes of available shear strength (Mohr envelopes). Figure 7 shows the rock mass shear strength envelopes for the selected values of the Hoek-Brown parameters noted earlier. It is evident from the envelopes plotted on Figure 7 that the degree of brokenness of the rock mass, as expressed by the value of the parameter s, has a significant effect on the shear strength that can be mobilized along a potential general failure plane that passes through the rock mass. For the rock mass beneath the bridge pier, the fact that any general failure beneath the footing would be forced to cut across the structure of the rock within the shear zone is significant in this regard.

As shown schematically in Figure 7, at any selected point on the strength envelope defined by a specific normal stress the available shear strength may be defined by the values of instantaneous cohesion (c_i) and instantaneous friction (ϕ_i) determined from the cohesion intercept and slope of the tangent to the envelope at that value of normal stress.

PIER FOUNDATION STABILITY ANALYSES

The geometry of the rock profile beneath the bridge pier is shown in Figure 2. As indicated, a slightly simplified straight-line bedrock profile was used for analysis. A bearing pressure of 8 kips/ft^2 was assumed for the foundation loading, equivalent to a total vertical load of 12,500 kips on the 34- × 46-ft footing. This is slightly conservative, because the actual design

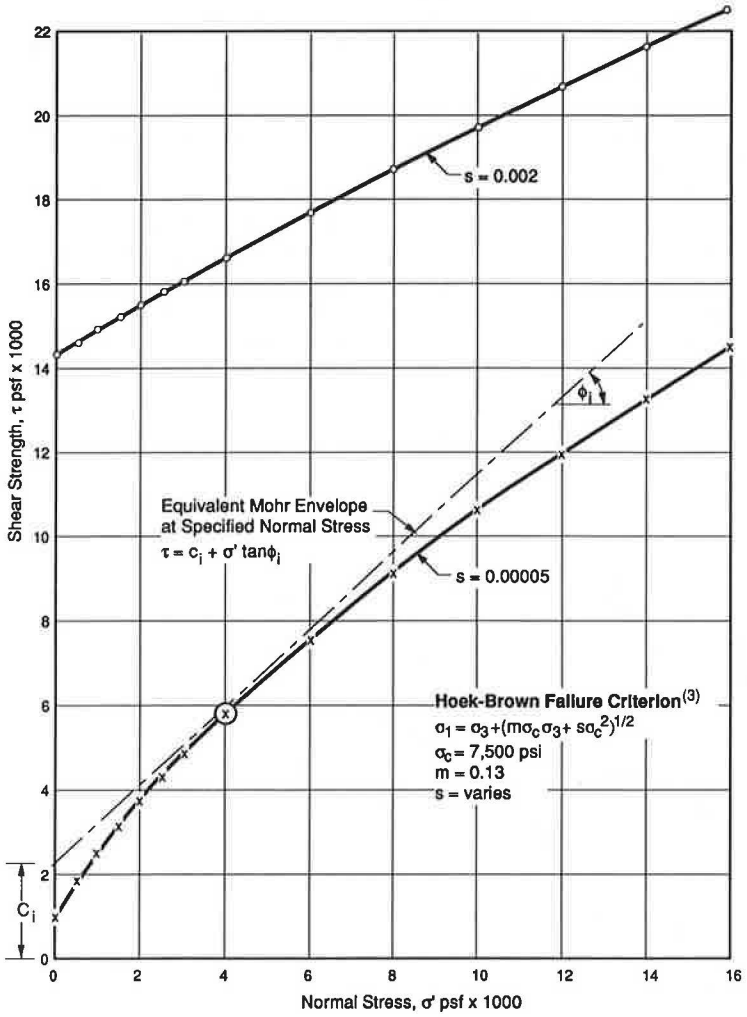

FIGURE 7 Estimated shear strength of crush zone rocks.

load is 11,300 kips. For earthquake conditions, a lateral acceleration of 0.3 times gravity was applied to the total vertical load on the foundation (12,500 kips), giving a lateral seismic load of 3,750 kips. For the rock itself, a lateral pseudostatic earthquake load was applied to the potential slide mass under consideration in each analysis, equal to 0.3 times the weight of the slide mass.

It is important to note that the simple pseudostatic approach that has been followed to assess the stability of the foundation under earthquake conditions is generally considered to be conservative (*9,10*). This method imposes a horizontal force of constant magnitude and direction on the foundation, whereas in reality this peak force is imposed only momentarily before decreasing and then reversing in direction. Although the method is conservative, it is nevertheless useful—if slopes can be shown to be stable under these assumed pseudostatic forces, then considerable confidence can be expressed in their actual performance under earthquake conditions. Seed (*9*) has suggested that if a factor of safety of about 1.15 against slope failure is obtained when using seismic acceleration coefficients of 0.1 *g* for magnitude $6^{1/2}$ earthquakes or 0.15 *g* for magnitude $8^{1/4}$ earthquakes, this should be sufficient "to ensure that displacements will be acceptably small." To be conservative, it was decided that this minimum factor of safety of 1.15 would be desirable, even though the seismic acceleration coefficient of 0.3 *g* that was used for analysis represented an acceleration of two to three times the values discussed by Seed.

As indicated in Figure 2, thirty-one 150-kip-capacity rock bolts had been installed in a staggered pattern from within the keyway excavation beneath the footing. Because these bolts were grouted, they act as a stiff, fully bonded system and the full yield capacity of the bolts will be mobilized with very small lateral displacement of any potential slide mass within the foundation, perhaps on the order of a few tenths of an inch. At yield, the bolts represent a total load capacity of 4,650 kips, or 101 kips/longitudinal-ft of the foundation, angled into the rock mass at inclinations varying from 20 to 60 degrees below the horizontal.

In general, all analyses were conducted assuming that the rock mass is fully saturated, clearly a conservative assumption under normal conditions. Unfortunately, however, a vertical grout curtain was apparently installed between the footing and the channel wall, and this curtain will tend to inhibit drainage and dissipation of joint water pressures within the foundation rock mass. Nevertheless, it is judged that the presence of the intense vertical jointing within the shear zone beneath the footing will permit some drainage of the rock mass, and any degree of drainage will make the foundation more stable than the analyses' assumption of full saturation.

Plane Failure

As previously noted, no geometric conditions were found that could give rise to a large-scale structurally controlled plane failure within the foundation rock beneath the footing. However, conditions may exist for a more localized potential failure to develop in front of the footing, as shown in Figure 8. The backscarp of such a failure would be defined by an existing Set 1 joint located along the face of the footing, with the base plane formed by a stepped series of Set 1 joints. However, because the dip of the Set 1 joints is generally greater than 50 degrees, formation of the flatter-lying stepped base plane would require some fracturing of bridges of intact material between the individual en echelon joints. Thus, the base plane could not be considered cohesionless and, in recognition of this, a modest cohesion value of 1,000 psf was assumed to exist along any potential base plane of sliding. An equivalent linear angle of friction for the Set 1 joints of 50 degrees was used for analysis, which was based on interpretation of Barton's nonlinear shear strength criterion.

Using these parameters, a series of simple block sliding analyses was done to determine the geometry of the most critical potential slide mass. For the fully saturated condition it was determined that the critical depth of a water-filled backscarp or tension crack was 11 ft and that the critical angle

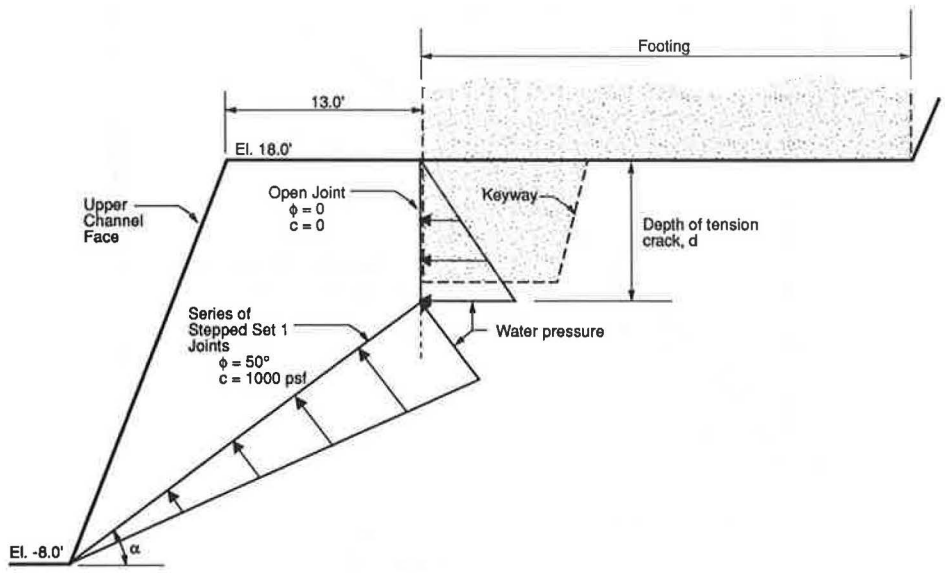

FIGURE 8 Potential plane failure in front of footing, for saturated conditions (α_{crit} = 35 degrees, d_{crit} = 11.0 ft).

of the base plane was a dip of 35 degrees, as shown in Figure 8. The computed factors of safety (FS) for this potential plane failure mechanism under fully saturated and fully drained conditions were as follows:

- Saturated conditions: $(FS)_{static} = 2.08$, and $(FS)_{seismic} = 1.39$.
- Drained conditions: $(FS)_{static} = 2.85$, and $(FS)_{seismic} = 1.90$.

A minimum factor of safety of approximately 1.4 is reached under conditions of full saturation and seismic (pseudostatic) loading, indicating that this postulated plane failure mechanism is not likely to occur. It was concluded that there were no significant plane failure mechanisms which could be realistically postulated in the vicinity of the pier footing.

General Rotational Failure

The Hoek-Brown strength parameters for the overall rock mass were based on the conservative assumption that the entire mass below the footing composes a major crush zone, as previously discussed. Using the nonlinear strength envelopes resulting from the Hoek-Brown criterion (Figure 7), a series of analyses was conducted to assess the stability of the footing against formation of a general rotational failure surface through the foundation.

Initial analyses were undertaken using the simplified Bishop method of slices, incorporating a nonlinear material strength criterion. The widely used Bishop limiting equilibrium method of slices assumes a circular failure surface, vertical boundaries for the interior slices, and interslice boundary forces equal to zero. Although these assumptions certainly are simplifications, the method is nevertheless useful for conducting initial stability analyses and searches to locate the critical potential failure surface. Resulting from these analyses, Figure 2 shows the location of the critical failure surface for the following assumptions:

- Parameters for Hoek-Brown failure criterion—$m = 0.13$, $s = 0.00005$, and $\sigma_c = 7{,}500$ psi;
- Fully saturated rock mass;
- Static analysis (no earthquake loading); and
- Rockbolt forces not included.

For these initial assumed conditions, the calculated factor of safety under static conditions was $(FS)_{static} = 2.17$.

For an actual potential slide mass, the boundaries of the interior slices would most likely be formed by preexisting joints belonging to Set 1, and in undertaking additional analyses it was desirable to model the fact that the shear strength available along these preexisting interslice boundaries would be different from that available within the main body of the rock mass, that is, along the basal planes of sliding. In addition, further parametric analyses were required to look into the effects of the 31 rock bolts that had been installed, the effects of earthquake loading, the effects of rock mass drainage, and the effects of variations in the estimated rock mass strength parameters—notably the parameter s, which reflects the relative degree of brokenness of the rock mass. For these purposes, the powerful limit equilibrium method of slices developed by Sarma (*4,11*) was used. This method allows consideration of a noncircular failure surface and incorporation of specific structural features as part of the potential slide mass, as well as including interslice forces, different strength parameters on different surfaces, and application of additional forces such as bolt forces or pseudostatic earthquake loading forces. However, Sarma analyses that used nonlinear shear strength criteria along the various surfaces of sliding were not widely available at the time, so it was decided to use an equivalent linear approach based on the instantaneous friction and the instantaneous cohesion values for the normal stress levels acting across the various surfaces. The effective normal stresses across each surface of sliding are calculated during the course of the Sarma analysis, and these values have been used to determine the appropriate values of instantaneous friction angle (ϕ_i) and instantaneous cohesion (c_i) along the basal surface of each slice.

On the basis of the initial Bishop analyses, a failure surface having the geometry shown in Figure 9 was then used for further analysis using the Sarma method. Because this geometry was based generally on the critical failure surface location as identified by the initial Bishop analyses, then for analyses including somewhat modified loading or strength assumptions, the location of the critical surface would be expected to change slightly. However, the changes would not be significant, except possibly in a case that indicated that stability was marginal. In such a case, additional searches were performed to confirm the location of the critical failure surface. As shown in Figure 10, equivalent linear or instantaneous values for the Mohr-Coulomb parameters of friction angle and cohesion were determined for the base of each of the three slices, on the basis of the nonlinear Hoek-Brown envelope and depending on the normal stress acting across each base plane respectively. The effects of the nonlinear shear strength behavior of the material, in terms of the changes in the values of friction angle and cohesion mobilized at different normal stress levels, are evident from the strength parameter values for the base of each slice as noted.

Base of Slice Number	*Normal Stress Across Base (psf)*	ϕ_i *(degrees)*	c_i *(psf)*
1	2,500	47	1,700
2	7,500	37	3,000
3	5,000	41	2,400

For the boundaries of the interior slices, formed by Set 1 joints, it was assumed that these joints were cohesionless with an instantaneous friction angle of $\phi_i = 50$ degrees, as previously discussed for Set 1 joints.

Using the same assumptions as those used in the Bishop analysis as noted above, the Sarma analysis gave a factor of safety under static conditions of $(FS)_{static} = 2.26$, which compares well with the computed Bishop value of 2.17.

Adding peak earthquake loading which is equivalent to a pseudostatic lateral load of $0.3\,g$, as previously discussed, gave $(FS)_{seismic} = 1.23$.

Because of the conservative nature of the assumptions incorporated in these analyses regarding rock mass strength, lack of drainage, no rock bolts, and a pseudostatic earthquake loading, these computed factors of safety indicated that the foundation stability was fully adequate.

The following computed factors of safety provide some measure of the sensitivity of these analysis results to the values of the input parameters assumed.

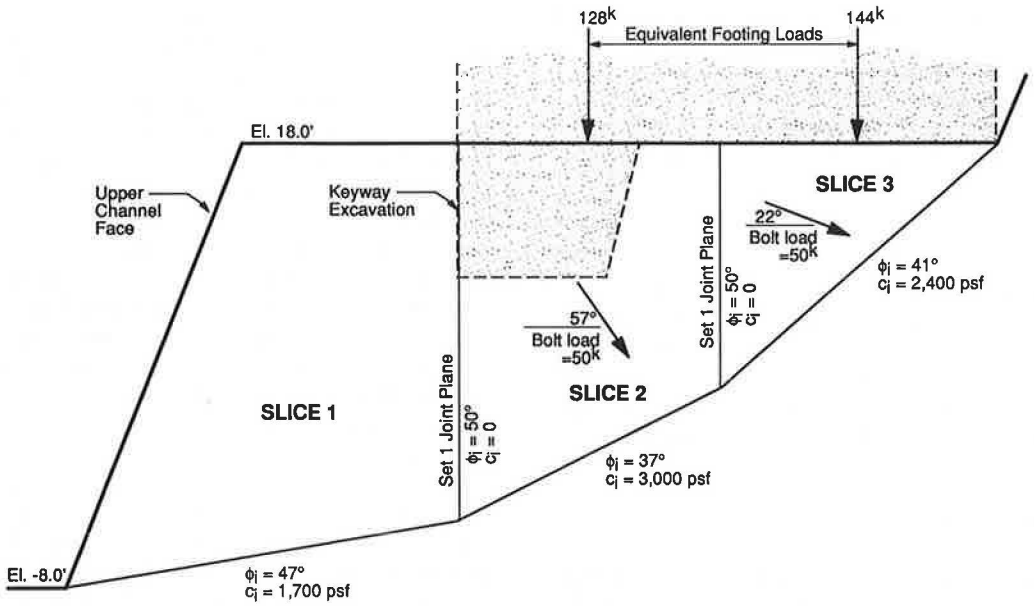

FIGURE 9 Conditions for Sarma analyses of potential general failure beneath footing (loads shown are for 1-ft-thick slice; Set 1 joint planes assumed as interior slip surfaces at 90-degree dip).

- For the assumed conditions as stated above, $(FS)_{static} = 2.26$ and $(FS)_{seismic} = 1.23$.
- For an increase in the Hoek-Brown strength parameter s from $s = 0.00005$ (equivalent to fair- to poor-quality rock) to $s = 0.002$ (equivalent to fair- to good-quality rock), $(FS)_{static} > 5.0$ and $(FS)_{seismic} = 3.40$.
- For initial assumed conditions plus the effect of the thirty-one 150-kip rock bolts installed during construction, $(FS)_{static} = 3.03$ and $(FS)_{seismic} = 1.94$.
- For initial assumed conditions but with the rock mass fully drained, $(FS)_{static} = 2.61$ and $(FS)_{seismic} = 1.48$.

CONCLUSIONS

During excavation of a bridge pier foundation and construction of the associated spread footing on rock, it had been postulated that the jointed and broken nature of the rock mass that was actually exposed could jeopardize the stability of the foundation. As a consequence, the footing design was modified to incorporate an excavated keyway, backfilled with reinforced concrete, from which long, grouted rockbolts were placed. Careful investigation of the site was later undertaken by independent consultants to confirm that the bridge pier foundation was indeed stable. The potential failure mechanisms identified as being kinematically possible included small-scale planar sliding of localized blocks formed in front of the footing by preexisting joint sets in the rock, and the development of a more generalized surface of rotation through the slabby, vertically oriented shear zone rocks found beneath a portion of the foundation. For analysis, it was assumed that the complete foundation was underlain by these shear zone rocks. Nonlinear strength criteria were used in the stability analyses, for the preexisting joints and for the shear zone rocks, because these criteria incorporate the important contribution to strength of the dilation that occurs when interlocking surfaces are sheared. This contribution is evident in

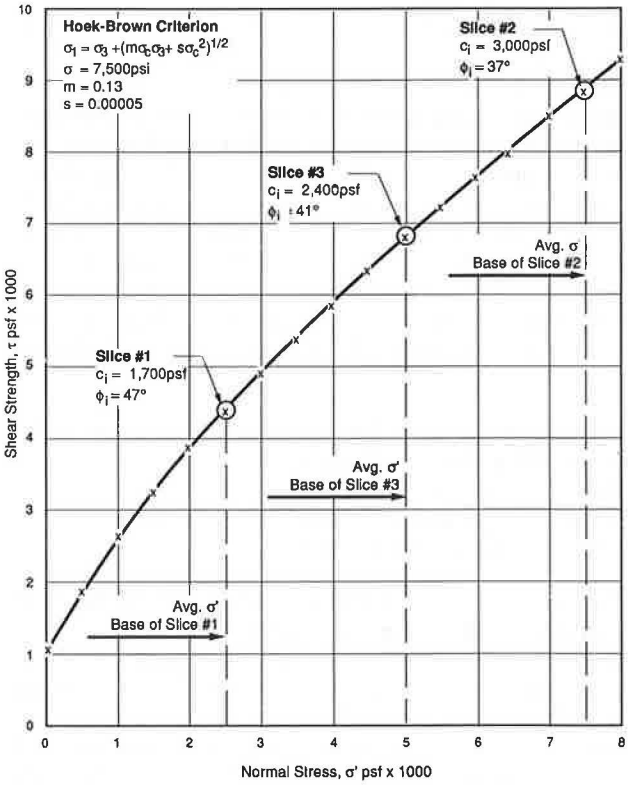

FIGURE 10 Equivalent linear Mohr-Coulomb parameters for Sarma analyses.

the high value of the instantaneous friction angle (ϕ_i) mobilized for such materials when sheared under low normal stresses. Where field investigation shows that there is a substantial degree of particle interlock in the fabric of the rock mass, along the direction of shearing necessary to cause failure, then ignoring this factor can result in significantly underestimating

the available shear strength along potential surfaces of sliding. The results of the investigations and analyses showed that the stability of the bridge foundation was fully acceptable. Although the addition of rock bolts increased the computed factors of safety, these factors were already well within the range of normally accepted design values.

ACKNOWLEDGMENTS

The work on this project of the author's colleagues at Golder Associates, Inc., is gratefully acknowledged. In particular, Bob Burk undertook all of the critically important geological investigations of the site and provided the interpretations of the engineering geology conditions that were essential to the analysis and understanding of the foundation stability.

REFERENCES

1. E. Hoek and J. W. Bray. *Rock Slope Engineering*, 3rd ed. Institution of Mining and Metallurgy, London, England, 1981.
2. N. R. Barton. Review of a New Shear Strength Criterion for Rock Joints. *Engineering Geology*, Vol. 7, 1973, pp. 287–332.
3. E. Hoek and E. T. Brown. *Underground Excavations in Rock*. Institution of Mining and Metallurgy, London, England, 1980.
4. E. Hoek. Strength of Jointed Rock Masses. *Geotechnique*, Vol. 33, No. 3, 1983, pp. 187–223.
5. Z. T. Bieniawski. Geomechanics Classification of Rock Masses and Its Application in Tunnelling. *Proc., 3rd International Congress on Rock Mechanics*, Denver, Colo., Vol. 11A, 1974, pp. 27–32.
6. N. Barton, R. Lien, and J. Lunde. Engineering Classification of Rock Masses for the Design of Tunnel Support. *Rock Mechanics*, Vol. 6, No. 4, 1974, pp. 189–236.
7. G. R. Martin and J. Miller. Joint Strength Characteristics of a Weathered Rock. *Proc., 3rd International Congress on Rock Mechanics*, Denver, Colo., Vol. 11A, 1974, pp. 263–270.
8. E. Hoek and E. T. Brown. The Hoek-Brown Failure Criterion—A 1988 Update. *Proc., 15th Canadian Rock Mechanics Symposium*, Toronto, 1988, pp. 31–38.
9. H. B. Seed. Considerations in Earthquake Resistant Design of Soil Slopes. *Geotechnique*, Vol. 29, No. 3, 1979, pp. 215–263.
10. N. M. Newmark. Effects of Earthquakes on Dams and Embankments. *Geotechnique*, Vol. 15, No. 2, 1965, pp. 139–160.
11. S. K. Sarma. Stability Analysis of Embankments and Slopes. *Journal of the Geotechnical Engineering Division*, ASCE, Vol. 105, No. GT12, 1979, pp. 1,511–1,524.

Publication of this paper sponsored by Committee on Soil and Rock Properties.

Estimating Hoek-Brown Rock Mass Strength Parameters from Rock Mass Classifications

DAVID F. WOOD

The use of rock mass classifications for designing support of underground excavations in rock has gained acceptance over the past 15 years to the extent that most geotechnical data collection programs now focus on the input parameters to the Norwegian Geotechnical Institute tunneling quality index (Q), the geomechanics classification rock mass rating (RMR), or both. In developing their empirical failure criterion for intact and heavily jointed rock masses, Hoek and Brown turned to rock mass classification schemes for the prediction of rock mass strength. The backgrounds of the two classifications used most frequently are reviewed, and ways in which they may be adapted to derive the Hoek-Brown rock mass strength parameters m, s, and σ_c are suggested. To incorporate the results of practical applications of the failure criterion under real engineering conditions, Hoek and Brown proposed equations to estimate rock mass strength parameters from classifications. These equations relate Bieniawski's RMR to m/m_i and s (where m_i is the Hoek-Brown parameter m for intact rock). The Barton et al. Q-index can also be used according to Bieniawski through a relationship between RMR and Q. The use of the complete quantitative rating or index from either classification is not recommended, and it is suggested that some components of the classification schemes are more appropriate than others in estimating the Hoek-Brown parameters. The proposed adaptations of Bieniawski's and Barton's work partially overcome the concern that classifications derived specifically for the estimation of tunnel support may not be appropriate for estimating rock mass strength.

The requirements of a characterization method developed for the design of tunnel support may be quite different from those needed for the estimation of rock mass strength parameters. Bieniawski (*1*) proposed that, in a tunneling application, a rock mass classification scheme has four purposes:

1. To divide a particular rock mass into groups of similar behaviour;
2. To provide a basis for understanding the characteristics of each group;
3. To yield quantitative data for the design of tunnel support; and
4. To provide a common basis for communication.

These principles led Bieniawski in his development of the geomechanics classification rock mass rating (RMR) (*1–6*).

The "quality" of the ground as an engineering medium is an intrinsic property that is spatially variable. It is a function of the strength of the intact material, the geometry of the rock mass fabric, and the character of the discontinuities that divide the intact rock into discrete blocks. Because the rock mass is used in engineering for civil or mining excavations, more variables are added to the behavioral character of the ground associated with excavation-induced effects. However, although properties such as induced stresses, excavation size, or water pressures are justifiably included in some classifications for designing tunnel support, rock mass strength is not a function of engineering use, and such parameters should not be considered in estimating strength parameters from a classification.

From field observations and discussions with practicing rock mechanics engineers, it appears that the behavior of better-quality rock masses is dominated by the geometry of the rock mass fabric, specifically block size and block shape; that of fair- to poor-quality rock masses, by the interblock shear strength and deformational characteristics; and that of worse-quality rock masses, by the low strength of the intact material. It is within this very broad generalization that developing Hoek-Brown rock mass strength parameters from rock mass classifications is considered.

BACKGROUND

The background of the Hoek-Brown failure criterion, Bieniawski RMR and the Norwegian Geotechnical Institute (NGI) tunneling quality index (Q) will be reviewed as it applies to this paper.

Hoek-Brown Failure Criterion

The most detailed description of the Hoek-Brown failure criterion is contained in the Rankine lecture by Hoek (*7*) that discusses the trial-and-error process of experimentally fitting triaxial test data with distorted parabolic curves to arrive at the following relationship:

$$\sigma_1' = \sigma_3' + \sqrt{m\sigma_c\sigma_3' + s\sigma_c^2} \quad (1)$$

where

σ_1' = major principal effective stress at failure,
σ_3' = minor principal effective stress or confining pressure,
m, s = material constants, and
σ_c = uniaxial compressive strength of the intact rock.

School of Engineering, Laurentian University, Ramsey Lake Road, Sudbury, Ontario, Canada P3E 5C6.

The Hoek-Brown empirical failure criterion contains three constants: m, s, and σ_c. In Hoek and Brown's words, m and s are "constants which depend on the properties of the rock and upon the extent to which it has been broken before being subjected to the [failure] stresses. . ." (*8*). All three constants are intrinsic or generic parameters and not related to any condition imposed by engineering.

"The manner in which fracture initiates and [failure] propagates . . . is reflected in the value of m. . ." (*8*). Hoek and Brown clearly indicate the way in which m is dependent on material properties, crystalline matrix, geological history, and so on. In the 1983 Rankine lecture, Hoek commented that m was "very approximately analogous to the angle of friction, ϕ', of the conventional Mohr-Coulomb criterion" (*7*). The same paper describes s as being very approximately analogous to the cohesive strength (c') of the Mohr-Coulomb criterion and goes on to discuss its bounds. Intact rock specimens with finite tensile strength have a maximum value of s equal to 1. Heavily jointed or broken rock in which the tensile strength, cohesive strength, and effective normal stress are zero is characterized by a minimum s-value of zero.

The main requirement of a classification to estimate rock mass strength parameters, then, is a close correspondence between the parameters included in the classification and the factors that affect the constants in the Hoek-Brown criterion. Parameters related to the geology and mineralogy of the rock mass, the degree to which the rock mass is broken, and the intact material strength should therefore be considered in deriving a relationship between rock mass strength and a classification.

Hoek and Brown (*9*) showed a plot of the parameter s and the ratio m/m_i against the NGI and adjusted RMR classification ratings (*4*) estimated for intact, undisturbed jointed and recompacted andesites in the initial publication on the empirical strength criterion for rock masses. The two classification schemes were scaled on the graph using Bieniawski's (*4*) correlation

$$\text{RMR} = 9 \log_e Q + 44 \tag{2}$$

Equations were derived from these plots by Priest and Brown (*10*), who related m/m_i and s directly to Bieniawski's RMR. These equations were modified by Hoek and Brown and published in the 1983 Rankine lecture (*7*). They were derived empirically from relatively few data points generated by extensive work on the Panguna andesites in Bougainville, Papua New Guinea. As the Hoek-Brown failure criterion has gained acceptance and has been used by the engineering community, it has been found that the values of m and s listed by Hoek (*7*) were somewhat conservative for practical engineering design. The values of the constants were then increased to model the behavior of "undisturbed or interlocked" rock masses by an arbitrary amount based on the experience of the authors.

Present correlations between the geomechanics classification and the Hoek-Brown failure criterion constants are given by Hoek and Brown (*11*) as

Disturbed rock masses:

$$\frac{m}{m_i} = \exp\left(\frac{\text{RMR} - 100}{14}\right) \tag{3}$$

$$s = \exp\left(\frac{\text{RMR} - 100}{6}\right) \tag{4}$$

Undisturbed or interlocked rock masses:

$$\frac{m}{m_i} = \exp\left(\frac{\text{RMR} - 100}{28}\right) \tag{5}$$

$$s = \exp\left(\frac{\text{RMR} - 100}{9}\right) \tag{6}$$

These equations were used to generate the values of m and s given in Table 1, which has been used extensively by the engineering community with a reasonable amount of success. However, experience in evaluating the behavior of underground excavations in civil and mining engineering projects shows that the values in Table 1 still underestimate the strength of rock masses at low confining stresses, that is, close to the boundary of an excavation. This is not too surprising in light of the meager data from which the relationships were derived and the difficulty in obtaining a complete suite of test results to "prove" the proposed criterion under a wide range of broken rock conditions. It must be remembered that the Hoek-Brown failure criterion was developed by curve-fitting the results of many triaxial compressive strength tests of intact rock and extended empirically to cover isotropic broken rock masses with little substantive correlation.

In the remainder of this paper, disturbed rock mass strength parameters will be discussed because they most closely represent the situation found in rock slope engineering. Increased rock mass strength parameters would be required if the engineering application were an underground excavation.

Geomechanics Classification

The geomechanics classification has been developed over the past 15 years by Bieniawski, who first proposed the RMR in 1973 and revised the scheme subsequently in 1974, 1975, 1976, 1979, and 1989. The RMR is the sum of a number of weighted parameters, and it is the number of parameters, the parameters themselves, and the weightings that have changed over the years. Table 2 shows the changes to the parameter ratings that have been suggested during the development of the geomechanics classification. The current recommendations use a basic RMR found by summing individual partial ratings [after Bieniawski (*5,6*)]:

Characteristic	*Rating*
Strength of intact rock (point load or compressive)	0–15
Drill core quality, Deere's RQD (*12*)	3–20
Spacing of discontinuities	5–20
Condition of discontinuities	0–30
Groundwater	0–15

In applying his classification to the estimation of support in tunnels, Bieniawski includes an adjustment for the orientation of predominant discontinuity sets relative to the orientation of the tunnel drive. This adjustment is inapplicable in the estimation of rock mass strength and will not be considered further in this paper.

TABLE 1 APPROXIMATE RELATIONSHIP BETWEEN ROCK MASS QUALITY AND MATERIAL CONSTANTS

		CARBONATE ROCKS WITH WELL DEVELOPED CRYSTAL CLEAVAGE *dolomite, limestone and marble*	LITHIFIED ARGILLACEOUS ROCKS *mudstone, siltstone, shale and slate (normal to cleavage)*	ARENACEOUS ROCKS WITH STRONG CRYSTALS AND POORLY DEVELOPED CRYSTAL CLEAVAGE *sandstone and quartzite*	FINE GRAINED POLYMINERALLIC IGNEOUS CRYSTALLINE ROCKS *andesite, dolerite, diabase and rhyolite*	COARSE GRAINED POLYMINERALLIC IGNEOUS & METAMORPHIC CRYSTALLINE ROCKS – *amphibolite, gabbro gneiss, granite, norite, quartz-diorite*
INTACT ROCK SAMPLES						
Laboratory size specimens free	m	7.00	10.00	15.00	17.00	25.00
from discontinuities	s	1.00	1.00	1.00	1.00	1.00
CSIR rating: RMR = 100	*m*	*7.00*	*10.00*	*15.00*	*17.00*	*25.00*
NGI rating: Q = 500	*s*	*1.00*	*1.00*	*1.00*	*1.00*	*1.00*
VERY GOOD QUALITY ROCK MASS						
Tightly interlocking undisturbed rock	m	2.40	3.43	5.14	5.82	8.56
with unweathered joints at 1 to 3m.	s	0.082	0.082	0.082	0.082	0.082
CSIR rating: RMR = 85	*m*	*4.10*	*5.85*	*8.78*	*9.95*	*14.63*
NGI rating: Q = 100	*s*	*0.189*	*0.189*	*0.189*	*0.189*	*0.189*
GOOD QUALITY ROCK MASS						
Fresh to slightly weathered rock, slightly	m	0.575	0.821	1.231	1.395	2.052
disturbed with joints at 1 to 3m.	s	0.00293	0.00293	0.00293	0.00293	0.00293
CSIR rating: RMR = 65	*m*	*2.006*	*2.865*	*4.298*	*4.871*	*7.163*
NGI rating: Q = 10	*s*	*0.0205*	*0.0205*	*0.0205*	*0.0205*	*0.0205*
FAIR QUALITY ROCK MASS						
Several sets of moderately weathered	m	0.128	0.183	0.275	0.311	0.458
joints spaced at 0.3 to 1m.	s	0.00009	0.00009	0.00009	0.00009	0.00009
CSIR rating: RMR = 44	*m*	*0.947*	*1.353*	*2.030*	*2.301*	*3.383*
NGI rating: Q = 1	*s*	*0.00198*	*0.00198*	*0.00198*	*0.00198*	*0.00198*
POOR QUALITY ROCK MASS						
Numerous weathered joints at 30-500mm,	m	0.029	0.041	0.061	0.069	0.102
some gouge. Clean compacted waste rock	s	0.000003	0.000003	0.000003	0.000003	0.000003
CSIR rating: RMR = 23	*m*	*0.447*	*0.639*	*0.959*	*1.087*	*1.598*
NGI rating: Q = 0.1	*s*	*0.00019*	*0.00019*	*0.00019*	*0.00019*	*0.00019*
VERY POOR QUALITY ROCK MASS						
Numerous heavily weathered joints spaced	m	0.007	0.010	0.015	0.017	0.025
<50mm with gouge. Waste rock with fines.	s	0.0000001	0.0000001	0.0000001	0.0000001	0.0000001
CSIR rating: RMR = 3	*m*	*0.219*	*0.313*	*0.469*	*0.532*	*0.782*
NGI rating: Q = 0.01	*s*	*0.00002*	*0.00002*	*0.00002*	*0.00002*	*0.00002*

NOTE: m and s are values for disturbed rock mass; *m* and *s* are values for undisturbed rock mass.

TABLE 2 CHANGES TO BIENIAWSKI'S RATINGS SINCE FIRST PUBLICATION

Year	Strength	RQD	Spacing	Condition	Groundwater	Comment
1973	0–10	3–16	5–30	2–19	2–10	Orient. +ve
1974	0–10	3–20	5–30	0–15	2–10	Orient. +ve
1975	0–15	3–20	5–30	0–25	0–10	Orient. –ve
1976	0–15	3–20	5–30	0–25	0–10	Interpretn.
1979	0–15	3–20	5–20	0–30	0–15	Interpretn.
1989	0–15	3–20	5–20	0–30	0–15	Interpretn.

Note: Other modifications have been made in the interpretations of RMR values, including new class ranges, alterations in stand-up time, Mohr–Coulomb rock mass strength parameters.

Although the geomechanics classification can yield RMR values anywhere between 0 and 100, Bieniawski recommends consideration of only five rock mass classes in order to design support. However, he suggests that the exact basic RMR be used to estimate m/m_i and s parameters from Equations 3–6 (*6*). Thus, the classification required for estimating support need not be as sensitive or accurate as that required for estimating rock mass strength parameters.

The characteristics that affect the behavior of an excavation in rock are a combination of generic parameters and engineering-induced effects. The geomechanics classification combines both, and this may be justified in the design of support. In contrast, a classification for rock mass strength should contain only generic parameters. These two observations are the main reasons that a refinement of the classification—into RMRm, RMRs, and intact uniaxial compressive strength—

is proposed for the estimation of Hoek-Brown parameters. Because the Hoek-Brown criterion is stated in effective stress terms, the influence of groundwater pore pressure is also explicitly considered.

The remainder of this section is devoted to determining rock mass strength parameters from the partial ratings RMRm and RMRs.

Geomechanics Classification m *Parameter: RMRm*

Bieniawski's basic RMR incorporates strength of intact rock material, drill core quality, spacing of discontinuities, condition of discontinuities, and groundwater. Underground excavation experience suggests that the way in which failure would propagate through a rock mass would be very sensitive to the condition of discontinuities. It is proposed that the partial rating for Bieniawski's discontinuity condition term be referred to as "RMRm" and that it be related to the Hoek-Brown parameter m. In developing a relationship between RMRm and m, reference will be made to the parameter m either as m_b for broken rock or as m_i for intact rock.

Plotting the values of m_b/m_i against Bieniawski's discontinuity condition (RMRm) originally calculated by Hoek and Brown (*8*) for the Panguna andesites gives curves with a poor visual fit to the data. One reason for this is that the early assessment used the incremental rating values given by Bieniawski (*4*), which proceed from 0 to 10, 20, 25, and 30 and incorporate three earlier terms used by Bieniawski (*2*): state of weathering, separation of joints, and continuity of joints.

Bieniawski eliminated the weathering term in 1974 because it was considered to be included in uniaxial compressive strength and discontinuity condition. In the current assessment, however, the Hoek-Brown constant σ_c refers to the uniaxial compressive strength of the intact rock material and does not, therefore, include an allowance for weathering. The author considers that weathering is one of the important factors in rock mass strength, because interblock shear is dominated by the presence or absence of weathering products caused by the passage of groundwater through discontinuities. Bieniawski (*6*) reintroduced weathering, along with roughness and infilling, in an amplified classification chart given in Table 3. It is this chart, extended to include intact rock, that is used to derive RMRm.

Intact rock, without discontinuities, relates to the initiation of fracture and has been evaluated by extrapolating discontinuity length, separation, and roughness in Table 3. It is proposed that Bieniawski's rating table be extended to include intact rock with a rating of 40. Table 3 has been used to refine the Panguna andesite data given by Hoek and Brown (*8*) and Jaeger (*13*). The rock mass strength values from triaxial testing and the interpreted RMRm ratings are shown in Table 4.

TABLE 3 RMRm = Σ (DISCONTINUITY CONDITION RATINGS) (*6*)

Parameter	Ranges of Values				
Trace Length	>1 m	1–3 m	3–10 m	10–20 m	<20 m
Rating	6	4	2	1	0
Separation	None	<0.1 mm	0.1–1 mm	1–5 mm	>5 mm
Rating	6	5	4	1	0
Roughness	Very rough	Rough	Smooth	Polished	Slickensided
Rating	6	5	3	1	0
	Hard filling			*Soft filling*	
Infilling	None	<5 mm	>5 mm	<5 mm	>5 mm
Rating	6	4	2	2	0
Weathering	Fresh	Slight	Moderate	High	Complete
Rating	6	5	3	1	0
Intact	Rating enhanced by 10				

Figure 1 shows a plot of RMRm against m_b/m_i for the revised data. This figure may be used as a design chart to estimate m_i/m_b from RMRm; alternatively, the following correlation may be used:

$$\frac{m_b}{m_i} = \exp\left(\frac{\text{RMRm} - 40}{5}\right) \tag{7}$$

Geomechanics Classification s *Parameter: RMRs*

Although there may be some overlap in the two parameters, Bieniawski's drill core quality and the spacing of discontinuities together make up the geometry of the rock mass. It is proposed that the sum of the partial ratings for drill core quality and spacing of discontinuities be referred to as "RMRs" and that it be related to the Hoek-Brown parameter s (see Table 5).

The maximum ratings for rock quality designation (RQD) and discontinuity spacing are 20 each (*6*). It is proposed that Bieniawski's spacing table be extended to include a rating of 25 for unjointed rock without discontinuities. This would give intact rock a combined partial sum of RMRs = 45. The minimum value of RMRs is 8 (minimum RQD rating of 3 plus minimum spacing rating of 5), which Hoek and Brown applied

TABLE 4 RMRs = RQD RATING AND SPACING RATING (*6*)

Intact Rock	$m_i = 18.9$		$s = 1$		$\sigma_c = 265MPa$	
Ratio m_b/m_i	1.0	0.0147	0.0061	0.0021	0.0016	0.0006
s	1.0	0.0002	0	0	0	0
Rock Mass	Intact	Undist	Recomp	Fresh	ModWeath	HiWeath
RMRm from Table 3, after Bieniawski [6]						
Length	6	1	0	0	0	0
Separation	6	4	1	1	1	1
Roughness	6	5	5	3	3	1
Infilling	6	4	4	2	2	1
Weathering	6	6	6	5	3	1
Intact	10					
Total RMRm	40	20	16	11	9	4

Note: Rock mass terms used by Hoek and Brown are: intact, undisturbed, recompacted, fresh, moderately weathered and highly weathered.

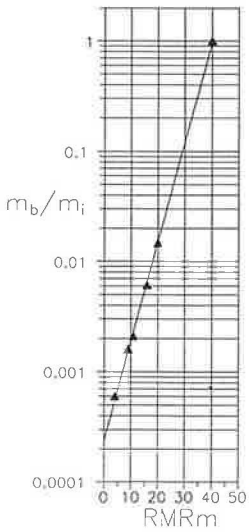

FIGURE 1 Correlation of RMRm with Hoek-Brown parameters.

TABLE 5 ROCK MASS STRENGTHS AND RMRm VALUES FOR PANGUNA ANDESITES (*9*)

Parameter	Ranges of Values				
Drill quality (RQD)	90–100%	75–90%	50–75%	25–50%	<25%
Rating	20	17	13	8	5
Joint spacing	>2 m	0.6–2 m	0.2–0.6 m	60–200 mm	<60 mm
Rating	20	15	10	8	5
Intact rock	Rating enhanced by 5				

to the rock mass conditions for undisturbed core samples of the Panguna andesites. This limits the ability to predict s from RMRs, although allowing RMRs to tend to zero as the rock mass becomes more broken may be warranted.

In their evaluation of the rock mass strength envelopes for the Panguna andesties, Hoek and Brown assumed that a value of $s = 0$ applied to the recompacted and weathered specimens. The only data points that can be derived in a plot of RMRs against s are for intact rock, $s = 1$, and undisturbed rock, $s = 0.0002$. The relationship between these s values and their respective RMRs values (45 and 8) is shown in Figure 2. Because there are only two points, a straight line relationship on the semilog plot has been inferred. This design envelope is obviously more tenuous than the one drawn for m_b/m_i, although it is considered as valid as the original presented by Hoek and Brown (*9*). The equation of the line is given by

$$s = \exp\left(\frac{\text{RMRs} - 45}{4.5}\right) \tag{8}$$

Other Geomechanics Classification Parameters

The strength of intact rock is obviously identical to the Hoek-Brown parameter σ_c and should be used directly rather than by ascribing a rating value. The ranges of strength values currently used in the geomechanics classification follow International Society for Rock Mechanics (ISRM) recommendations (*14*), and each rock strength group is assigned a rating value. It should be noted that the other two Hoek-Brown rock mass strength parameters, m and s, are dimensionless. The introduction of a dimensioned parameter (σ_c) becomes critical in establishing the input parameters for design analyses. It is therefore suggested that considerable care be taken in evaluating material strength of the intact rock.

Groundwater conditions are directly associated with the engineering structure to be created or the engineering role that the rock mass is required to play. Although an assessment of water conditions is undoubtedly important in the design of rock mass support, it should not be included in an evaluation of rock mass strength parameters that are generic in origin and not a function of the engineering project in question. It is again noted that the Hoek-Brown failure criterion is expressed in effective stress terms, and groundwater pore pressure is therefore explicitly considered.

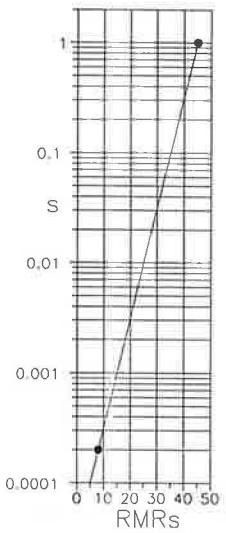

FIGURE 2 Correlation of RMRs with Hoek-Brown parameters.

NGI Tunneling Quality Index

Barton et al. (*15*) proposed a guide for estimating tunnel support requirements using a classification index. The original document, first published as an internal NGI report, contains a wealth of background information that forms the basis of the present discussion. It should be noted that the rating system selected by Barton et al. has not changed since the first publication. As with Bieniawski's RMR, a relationship between the classification index and rock mass strength parameters was not proposed, although various components of rock mechanics behavior are mentioned—for example, support pressure, approximate joint residual friction angles, and the effective shear strength of the rock mass. A review of the classification parameters follows.

The rock mass Q-index is derived from six parameters (*15*):

- Degree of jointing of the rock, in terms of RQD,
- Number of joint sets (J_n),
- Roughness and degree of planarity of the joints (J_r),
- Alteration of filling along the joints (J_a),
- Water inflow (J_w), and
- Rock load (SRF).

The complete index is found by multiplying the three quotients shown in Equation 9.

$$Q = \frac{\text{RQD}}{J_n} \times \frac{J_r}{J_a} \times \frac{J_w}{\text{SRF}} \tag{9}$$

The numerical value of the index varies from 0.001 for exceptionally poor quality rock conditions to 1,000 for exceptionally good quality, intact rock. Each quotient represents a different rock mass characteristic [Barton et al. (*15*)]. The first quotient, RQD/J_n, represents the structure of the rock mass and is a crude measure of the block or particle size. This would suggest a possible relationship with the Hoek-Brown parameter s. The second quotient, J_r/J_a, represents the frictional characteristics of the joint walls or infillings. Barton et al. report that $\tan^{-1}(J_r/J_a)$ approximates rock mass shear strength, and this suggests a possible relationship with the Hoek-Brown parameter m. The third quotient, J_w/SRF, comprises two stress parameters associated with water pressure and rock load. It is therefore design-dependent and will not be considered further.

The rock mass strength data reported for the Panguna andesites by Hoek and Brown (*8*), are shown in Table 6 along with the proposed NGI parameters. Figure 3 shows a plot of the natural logarithms of the quotient J_r/J_a against m_b/m_i and RQD/J_n against s for these data. The triangular data points give a good visual fit to the correlation:

$$\log_e\left(\frac{m_b}{m_i}\right) = 2\log_e\left(\frac{J_r}{J_a}\right) - 3.35 \qquad (10)$$

Again, the relationship between RQD/J_n and s is tenuous. Not only is it based on only two data points, but selection of the minimum NGI value of RQD = 10 percent constrains the location of one of the data points with an uncertain error margin. A suggested correlation is

$$\log_e s = 2\log_e\left(\frac{\text{RQD}}{J_n}\right) - 9.2 \qquad (11)$$

It is interesting to note that in Table 6, "block size" quotients RQD/$J_n < 1$ are all associated with interpreted s values from triaxial testing of zero. The significance of this may be seen from a comment by Barton et al. (*15*): "If the quotient is interpreted in units of centimetres, the . . . particle sizes . . . are seen to be crude but fairly realistic approximations." A rock mass with individual particles or blocks only 10 mm (1 cm) across represents a condition in which the tensile strength and cohesive strength would be zero. Hoek and Brown (*11*) suggest that such a rock mass be characterized by a minimum value of $s = 0$. The triaxial work on the Panguna andesites was clearly in this range; however, extrapolation of block sizes for low values of RQD/J_n to the scale of a real rock mass may not be realistic.

TABLE 6 NGI PARAMETERS FOR PANGUNA ANDESITES (*9*)

Rock Mass	Intact	Undist	Recomp	Fresh	ModWeath	HiWeath
Ratio m/m_i	1.0	0.0147	0.0061	0.0021	0.0016	0.0006
s	1.0	0.0002	0	0	0	0
RQD	100	10	10	10	10	10
J_n	1	9	12	15	18	20
RQD/J_n	100	1.11	0.833	0.667	0.555	0.5
J_r	4	2*	1.5	1	1	1
J_a	0.75	3*	4	4	6	8
J_r/J_a	5.33	0.63	0.375	0.25	0.167	0.125

All values of NGI parameters taken from Hoek and Brown [9] except those marked *, which have been re-assessed after reviewing the original publication of this data in Jaeger [13].

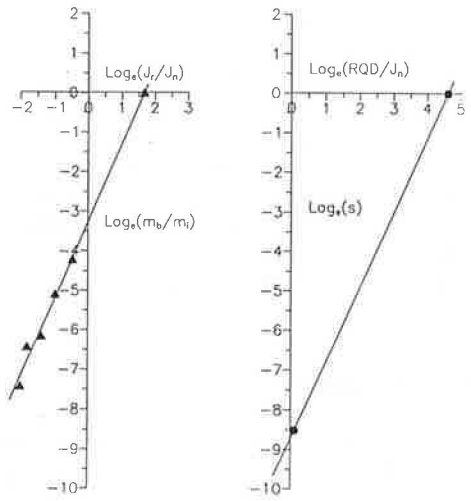

FIGURE 3 Correlations between NGI quotients and Hoek-Brown parameters.

ESTIMATING HOEK-BROWN PARAMETERS

The process of deriving the complete Hoek-Brown parameter set is described and followed by a worked example.

The relationships established between rock mass strength and classifications are all in terms of the ratio m_b/m_i and s. It follows that a value of m_i is required in order to calculate m_b. The complete parameter set thus includes m_i, for intact rock; m_b/m_i, from one or more classification; s, from a classification; and σ_c, preferably from laboratory testing.

On certain projects it may be justifiable to set out a complete rock mechanics testing program and generate a full suite of triaxial results for the prototype rocks on a particular site. In general, however, only a limited amount of testing is likely, probably restricted to uniaxial compressive strength and point-load index.

In the absence of site-specific data on intact rock material strength, a field approximation can be used, such as that presented in Table 7, based on the proposals of ISRM (*14*). Under these circumstances, tabulated values for m_i must be used. Table 8 shows values of the constant m_i taken from published results of triaxial testing by Hoek and Brown (*8*), Jaeger (*13*), and Jackson et al. (*16*). Other published works have not been directly concerned with rock mass strength, and interpretations of m_i have not been made. The various rock types tested were grouped according to mineralogy and grain size within the geological classification of sedimentary, metamorphic, and igneous rocks. It was found that values of m_i decrease with grain size for any particular group, with up to a 50 percent reduction from coarse to very fine grained.

TABLE 7 APPROXIMATION OF UNIAXIAL COMPRESSIVE STRENGTH

Uniaxial Compressive Strength, σ_c (MPa)	Point Load Index, I_s (MPa)	Term	Field Estimate of Strength	Examples*
> 250	> 10	Very Strong	Requires many blows of geological hammer to break intact rock specimen	Basalt, chert, diabase, quartzite
100 – 250	4 – 10	Strong	Hand held specimen broken by single blow of geological hammer	Amphibolite, basalt, gneiss dolomite, gabbro, granite, limestone, marble, tuff
50 – 100	2 – 4	Mod. Strong	Knife cannot scrape surface, shallow indentations under firm blows of pick	Andesite, limestone, marble phyllite, sandstone, schist, shale, slate
25 – 50	1 – 2	Mod. Weak	Firm blow with geological pick indents rock to 5mm, knife just scrapes surface	Claystone, coal, concrete, schist, shale, siltstone
5 – 25	**	Weak	Knife cuts material, but too hard to shape into triaxial specimen	Chalk, rocksalt, potash
1 – 5	**	Very Weak	Material crumbles under firm blows of geological pick, can be shaped with a knife	Highly weathered or altered rock, fault zone

* All rock types exhibit a broad range of uniaxial compressive strengths which reflects heterogeneity in composition and anisotropy in structure. Stronger rocks are characterized by well interlocked crystal fabric and few voids.

** Rocks with a uniaxial compressive strength below 25MPa are likely to yield highly ambiguous results under point load testing.

This table developed after ISRM, [14].

TABLE 8 PARAMETER m_i BY ROCK GROUP

Grain size	Sedimentary		Metamorphic		Igneous		
	Calcic	Silica	Calcic	Acidic	Acid	Basic	Basic
Coarse	Dolomite 6.8	(Conglom.)	Marble 10.6	Gneiss 24.5	Granite 29.2	Gabbro 23.9	Norite 23.2
Medium	Limest. 5.4	Sandstone 14.3		Amphibolite 25.1		Dolerite 15.2	
Fine	(Micrite)	(Siltstone)		Quartzite 16.8	(Rhyolite)	Andesite 18.9	(Basalt)
V.Fine	(Chalk)	Mudstone 7.3		Slate 12.5	(Obsidian)		

Values shown were derived from curve fitting routines to triaxial data for each rock type. Rock names in parentheses have not yet been assessed for m_i.

Rocks with a high calcite content have lower m_i-values than corresponding rocks with a high silica content, and coarse-grained polymineral rocks (including foliated metamorphic gneisses) have similar values of m_i regardless of exact mineralogy.

The use of partial classification parameters RMRm or J_r/J_a is recommended in establishing a value for m_b/m_i in accordance with design charts such as those presented in Figures 1–3 or Equations 7 and 10. A design value for the broken rock parameter m_b can then be found by multiplying m_i from Table 8 by m_b/m_i.

A design value for s can be derived in a similar way using RMRs or RQD/J_n and Figures 1–3 or Equations 8 and 11.

The following illustrates the determination of rock mass strength parameters for a blocky sandstone rock mass. It is described in engineering geological terms as slightly weathered, moderately widely bedded, pale gray, fine to medium grained, moderately strong sandstone with two orthogonal sets of joints creating tight blocks 0.1 to 0.2 m across; surfaces are planar and rough. No laboratory tests have been carried out, so Tables 7 and 8 are used to determine σ_c = 75 MPa and m_i = 14.3.

Using the geomechanics classification, RMRm and RMRs can be found by reference to Tables 3 and 5.

Characteristic	*Value*	*Rating*
Discontinuity length	1–3 m	4
Separation	None	6
Roughness	Rough	5
Infilling	None	6
Weathering	Slight	5
Total RMRm		26

Equation 7 gives $m_b/m_i = \exp(\text{RMRm} - 40/5)$, from which, m_b/m_i = 0.061, or m_b = 0.87.

RQD, as defined by Deere (*12*), is a measure of jointing in rock core. To estimate a value of RQD from surface mapping, a relationship first proposed by Palmström in the paper by Barton et al. (*15*) is often used.

$$\text{RQD} = 115 - 3.3J_v \quad (12)$$

where J_v is the joint volume and is the sum of the number of discontinuities per cubic meter of rock. In this case, with bedding at 60 to 200 mm, and two sets of jointing at 100 to 200 mm, it may be expected that there would be about 23 discontinuities/m^3, giving an RQD of 39 percent. Table 5 shows an RQD rating of 8 and a spacing rating of 8, giving an RMRs value of 16.

Equation 8 gives $s = \exp[(\text{RMRs} - 45)/4.5]$, from which s = 0.0016.

Using the NGI classification, the first two quotients will be used to derive values of the Hoek-Brown parameters:

Parameter	*Value*	*Quotient*
RQD	39%	
J_n	Three sets—9	RQD/J_n = 4.33
J_r	Rough, planar—1.5	
J_a	Surface staining—1.0	J_r/J_a = 1.5

Equation 10 gives $\log_e(m_b/m_i) = 2\log_e(J_r/J_a) - 3.35$, from which m_b/m_i = 0.079, or m_b = 1.13. Equation 11 gives $\log_e s = 2\log_e(\text{RQD}/J_n) - 9.2$, from which s = 0.0019.

It can be seen that the two methods give comparable results. However, one of the classification methods may be easier to derive on a particular project and more confidence may be obtained in the output. It is suggested that both methods be attempted and that the final Hoek-Brown parameter set be selected depending on the confidence level of the data set. Although this example used Equations 7, 8, 10, and 11, the design charts given in Figures 1–3 may also be used. It should be remembered that these rock mass strength values are appropriate for design in rock slope engineering. Further modifications may be required to extrapolate these values to underground excavations in rock.

CONCLUSIONS AND RECOMMENDATIONS

The rock mass classifications proposed by Barton et al. (*15*) and Bieniawski (*1–6*) can be used to estimate the rock mass strength parameters proposed by Hoek and Brown (*7–9*). However, it is recommended that only partial ratings be used because the complete index or rating comprises characteristics associated with engineering design in addition to the generic rock mass features on which rock mass strength is dependent. The possibilities of introducing errors in the use of empirical relationships should be borne in mind, especially in attempts to relate different parameters derived for different purposes. In the context of this paper, it appears that both Barton et al.'s tunneling quality index quotient J_r/J_a, and Bieniawski's RMRm can be used to estimate a value of the rock mass strength parameter m_b, although most published work has concentrated on a relationship between RMR and the Hoek-Brown parameters. The data base is too small to compare the correlations between the two partial classifications and s.

The limitations that exist in classification methods for tunnel support design should be considered in attempts to estimate rock mass strength parameters, as should the limitations in rock mass conditions under which the Hoek-Brown failure criterion itself is considered valid. Figure 4 shows different scales of rock mass geometries relative to the size of a design excavation for which the Hoek-Brown criterion is considered valid. Scale factors associated with size of the prototype design excavation to the host rock mass geometry or block size should be considered to ensure that the Hoek-Brown parameters estimated are to be used in a valid constitutive model in which truly jointed rock mass conditions prevail.

ACKNOWLEDGMENTS

The research presented in this paper was carried out under the Industrial Research Chair in Rock Engineering established in the Department of Civil Engineering at the University of Toronto. The chair is held by Evert Hoek and funded jointly by the Natural Sciences and Engineering Research Council of Canada and the Campbell Red Lake Mines. The

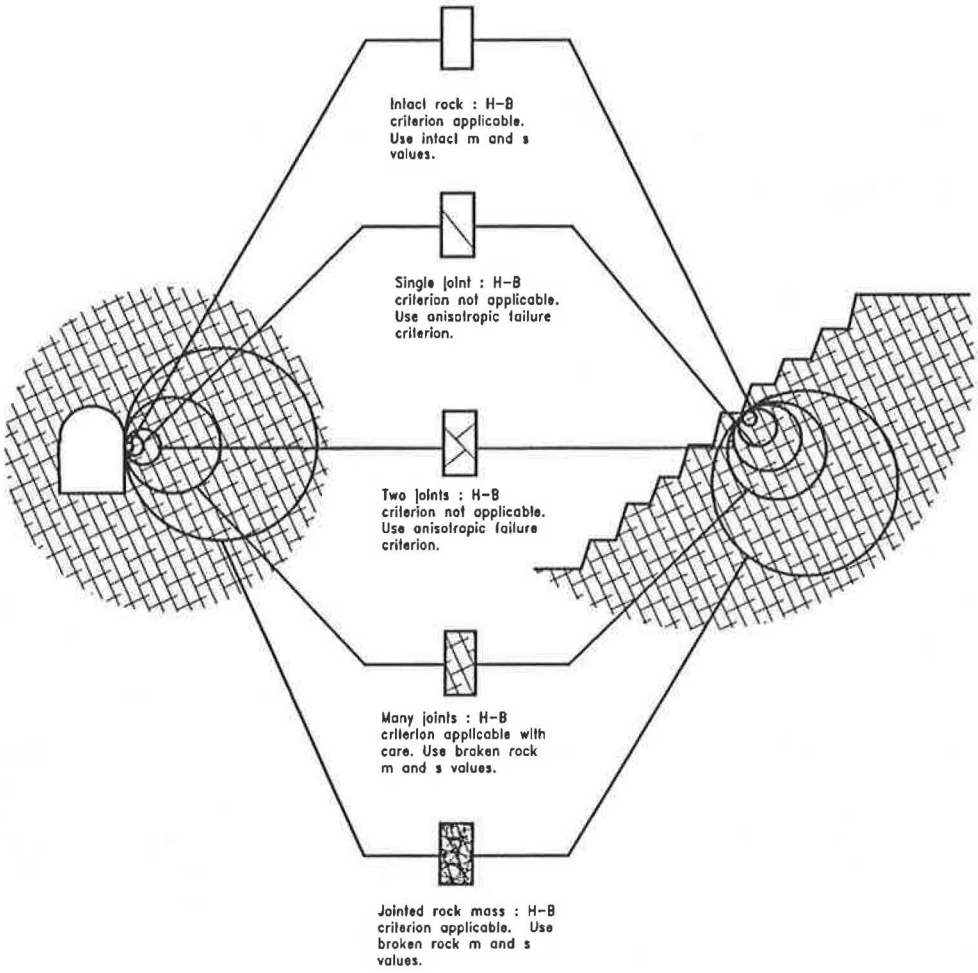

FIGURE 4 Applicability of Hoek-Brown failure criterion.

fundamental research activities supported in this program are concerned with the development of methods for estimating the strength and deformation characteristics of rock masses. The stimulating environment created by the research group involved is highly appreciated.

REFERENCES

1. Z. T. Bieniawski. Estimating the Strength of Rock Materials. *Journal of South African Institute Mining and Metallurgy*, Vol. 74, No. 8, 1974, pp. 312–320.
2. Z. T. Bieniawski. Engineering Classification of Jointed Rock Masses. *Transactions of the South African Institution of Civil Engineers*, Vol. 15, 1973, pp. 335–344.
3. Z. T. Bieniawski. Case Studies: Prediction of Rock Mass Behavior by the Geomechanics Classification. *Proc., 2nd Australia–New Zealand Conference on Geomechanics*, Brisbane, Australia, 1975, pp. 36–41.
4. Z. T. Bieniawski. Rock Mass Classifications in Rock Engineering. In *Exploration for Rock Engineering*. Z. T. Bieniawski, ed., A. A. Balkema, Johannesburg, South Africa, 1976, pp. 97–106.
5. Z. T. Bieniawski. The Geomechanics Classification in Rock Engineering Applications. *Proc., 4th International Congress on Rock Mechanics*, International Society for Rock Mechanics, Montreaux, Switzerland, Vol. 2, 1979, pp. 41–48.
6. Z. T. Bieniawski. *Engineering Rock Mass Classifications*. John Wiley & Sons, New York, N.Y., 1989.
7. E. Hoek. Strength of Jointed Rock Masses. *Geotechnique*, Vol. 33, No. 3, 1983, pp. 187–223.
8. E. Hoek and E. T. Brown. *Underground Excavations in Rock*. Institute of Mining and Metallurgy, London, England.
9. E. Hoek and E. T. Brown. Empirical Strength Criterion for Rock Masses. *Journal of the Geotechnical Engineering Division*, ASCE, Vol. 106, No. GT9, 1980, pp. 1,013–1,035.
10. S. D. Priest and E. T. Brown. Probabilistic Stability Analysis of Variable Rock Slopes. *Transactions of the Institution of Mining and Metallurgy, Section A*, Vol. 92, 1983, pp. A1–A12.
11. E. Hoek and E. T. Brown. The Hoek-Brown Failure Criterion—A 1988 Update. *Proc., 15th Canadian Rock Mechanics Symposium*, University of Toronto, 1988, pp. 31–38.
12. D. U. Deere. Technical Description of Rock Cores for Engineering Purposes. *Rock Mechanics and Engineering Geology*, Vol. 1, No. 1, 1963, pp. 16–22.
13. J. C. Jaeger. Behavior of Closely Jointed Rock. *Proc., 11th Symposium on Rock Mechanics*, Berkeley, Calif., 1970, pp. 57–68.
14. International Society for Rock Mechanics. *Rock Characterization, Testing and Monitoring—ISRM Suggested Methods*. Pergamon, London, England, 1981.
15. N. R. Barton, J. Lunde, and R. Lien. Engineering Classification of Rock Masses for the Design of Tunnel Support. *Rock Mechanics*, Vol. 6, No. 4, 1974, pp. 189–236.
16. R. Jackson, J. S. O. Lau, and A. Annor. Mechanical, Thermo-Mechanical and Joint Properties of Rock Samples from the Site of AECL's Underground Research Laboratory, Lac du Bonnet, Manitoba. *Proc., 42nd Canadian Geotechnics Conference*, Winnipeg, Manitoba, 1989, pp. 41–49.

Publication of this paper sponsored by Committee on Soil and Rock Properties.

Geosynthetic-Reinforced Soil Wall: 4-Year History

K. L. FISHMAN, C. S. DESAI, AND R. R. BERG

A geogrid-reinforced earth-retaining wall using full-height precast concrete wall facing was instrumented in Tucson, Arizona. Construction on the wall was completed in October 1985. Instruments were monitored during construction, at intervals during the year after construction, and once a year thereafter. Tensile strains measured during construction indicate that during compaction of the wall fill, a tension force was induced in the geogrids that is low in comparison with safe working loads. Measurements of tension in the geogrids are compared with tensions computed by limit equilibrium analysis. In general, this comparison is satisfactory. In addition, a study of measured geogrid response over a 4-year period reveals that rates of creep strain are not appreciable.

A geogrid-reinforced earth-retaining wall using full-height precast concrete wall facing was instrumented in Tucson, Arizona. The purpose of the instrumentation was to study the response of the wall system and compare it with design assumptions and calculations applied to wall systems using strip reinforcements and articulated wall facing. Instruments were placed to measure geogrid strains, lateral earth pressure transferred to the wall face, strains in the reinforced wall fill, vertical stress, and the distribution of temperature within the reinforced wall fill.

Construction on the wall was completed in October 1985. Instruments were monitored during construction at intervals during the year after construction and once a year thereafter. Readings taken during 1990 represent the sixth year of the wall-monitoring program, but these data are not available for presentation. The purpose of this paper is to present measurements taken since initial construction of the wall through the end of 1988. In this manner the performance of the geogrid-reinforced wall system over a long period of time may be discussed. The presentation in this paper is derived from various previous publications (*1–4*).

DESCRIPTION OF WALL SYSTEM

The wall system serves as a grade separation for a highway project; it was considered as an alternative to a conventional cantilevered retaining-wall system or a mechanically stabilized earth wall system using steel strips as reinforcement. Schematics of the instrumented earth-reinforced retaining wall are shown in Figures 1 and 2, which refer to separate wall panels that were instrumented. In this paper "height" refers to the vertical elevation and "depth," to the horizontal distances into the fill measured from the wall face. The instrumented wall panels were 15.5 ft (4.72 m) high. Wall facing consisted of precast concrete panels 6 in. (15.24 cm) thick and 10 ft (3.05 m) wide. Geogrids were mechanically connected to the concrete facing panels (Figure 3) at the elevations shown and extended to a depth of 12 ft (3.66 m). On the top of the wall fill, a pavement structure was constructed that consisted of a 4-in. (10.16-cm) base course covered by 9.5 in. (24.13 cm) of portland cement concrete.

The specified soil reinforcement was Tensar's SR2 geogrid, which is made of extruded high-density polyethylene, uniaxially oriented to obtain a high tensile strength equivalent to that of mild steel. It is reported to be resistant to chemical substances normally existing in soils. The geogrids have a maximum tensile strength of 5,400 lb/ft (79 kN/m) and a tension modulus at 2 percent elongation determined from unconfined "quick" (2 percent strain/min) tension tests of 75,000 lb/ft (1094 kN/m). A long-term allowable tensile strength of 1,986 lb/ft (29 kN/m) based on extensive creep testing has been reported. This value was reduced by an overall factor of safety equal to 1.5 to compute a long-term design tensile strength of 1,324 lb/ft (19 kN/m) for use in design.

Construction Methods

Construction methods can have a major impact on the performance of the wall system. The construction procedures used on this project are discussed in detail elsewhere (*1,2,4*). Brief details are given in the following.

Full-height precast concrete wall facing panels were hoisted and set vertically on a leveling pad. The panels were stabilized with struts so that they were initially battered inward.

As placement proceeded, geogrids were secured to the wall face at proper elevations and stretched to take up the slack. Fill was placed and spread onto the geogrid with a front-end loader. The fill was placed up to the next geogrid elevation and compacted. Compaction near the wall face was performed using a jumping jack; further from the wall face, however, a self-propelled vibratory compacter was used. As the height of the wall increased, struts on the outside of the wall were loosened, allowing the load to be transferred to the geogrids. This process was repeated for each geogrid level until the top of the wall was reached.

K. L. Fishman, State University of New York at Buffalo, 244 Ketter Hall, Buffalo, N.Y. 14260. C. S. Desai, Department of Civil Engineering and Engineering Mechanics, University of Arizona, Tucson, Ariz. 85721. R. R. Berg, Ryan R. Berg and Associates, 7501 South 80th Street, Cottage Grove, Minn. 55016.

Description of Instrumentation

The instrumentation program was designed to measure

1. Movements of wall faces by surveying the fronts of the concrete facing panels,
2. Strains in the reinforcement by resistance strain gages and inductance coils fastened to the geogrid reinforcement,
3. Horizontal and vertical strains in the soil with inductance coils placed in the reinforced wall fill,
4. Lateral earth pressure against the wall face and the distribution of vertical stresses along a geogrid with pressure cells installed in the reinforced wall fill, and
5. Distribution of temperature within the reinforced soil mass with resistance thermometers.

Locations of instruments are shown in Figures 1 and 2. All elevations referred to in this section are with respect to the base of the wall. The instrumented wall panels were 10 ft apart; they are denoted as 26-30 and 26-32. In general, instrument locations in the two walls were similar, to provide a cross-check; some differences in instrument layout allowed for acquiring additional information, such as geogrid strains at different elevations or the measurement of vertical stress and lateral earth pressures against the wall facing.

Details of instrument calibration, performance, and installation can be found in a preliminary instrumentation report (*1*).

DESIGN EQUATIONS

The wall was designed in accordance with available reinforced-soil methodology (*5*). A value engineering study performed by Dames and Moore (*6*) provides a detailed description of the design for this particular project. A summary of parameters used in the analysis is presented in Table 1.

Considering the internal stability of a soil wall constructed with frictional fill, as was the case with the instrumented wall

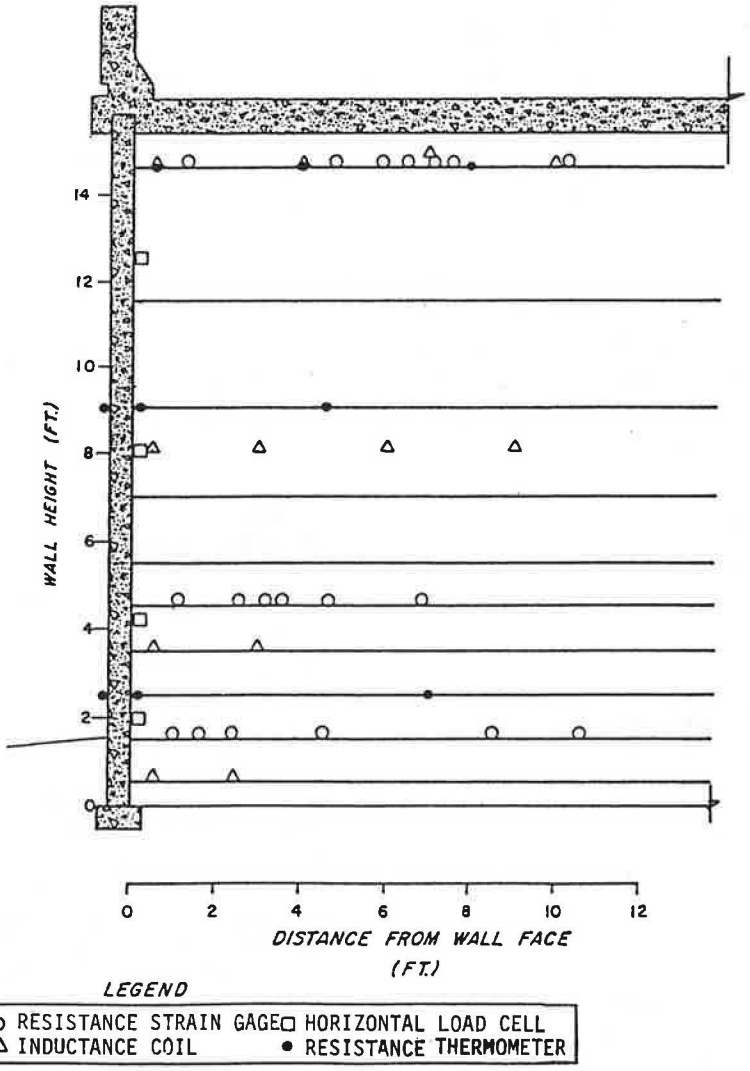

FIGURE 1 Schematic of instrumented earth reinforced retaining wall, Wall 26-30.

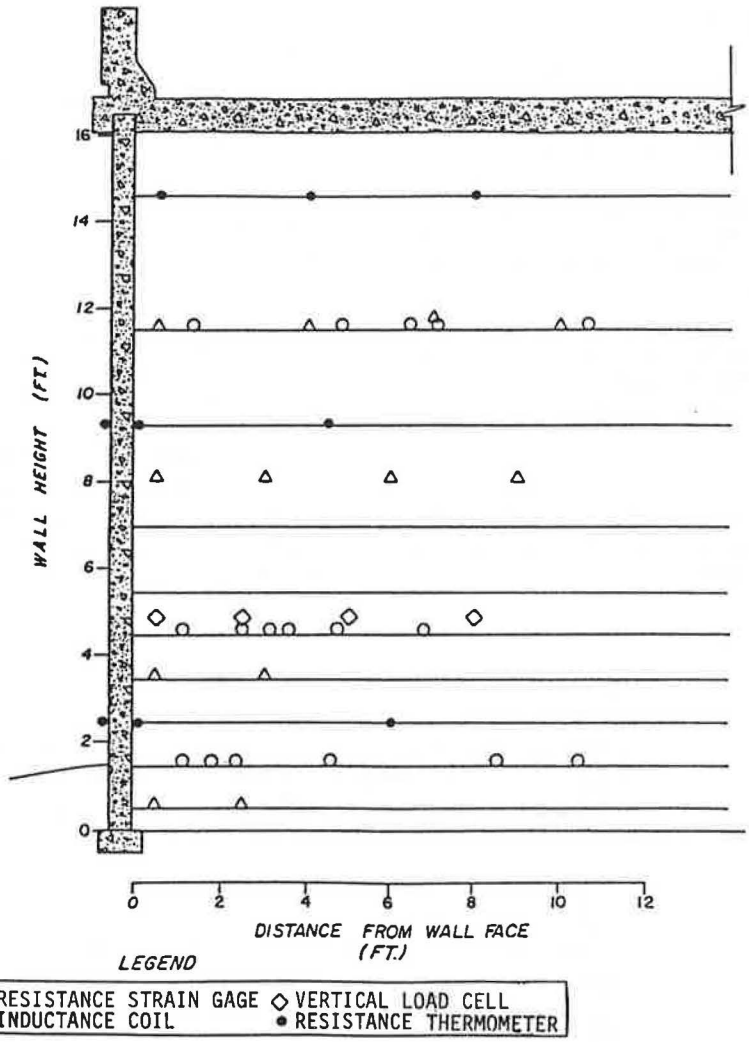

FIGURE 2 Schematic of instrumented earth reinforced retaining wall, Wall 26-32.

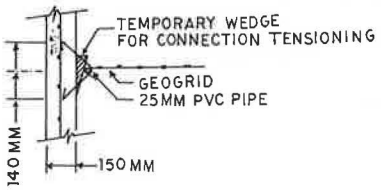

FIGURE 3 Measurements of strain in connection between geogrids and wall facing.

panels, the tensile force in the geogrid at level i (T_i) per unit width of wall is given by

$$T_i = K_{aw}\,\sigma_{vi}\,V_i \quad (1)$$

where

V_i = vertical spacing of the geogrids,
σ_{vi} = maximum vertical stress at level i obtained by assuming a linear variation of vertical stress (*5*), and
K_{aw} = Rankine coefficient of active earth pressure for the wall fill.

COMPARISON BETWEEN MEASUREMENTS AND DESIGN QUANTITIES

In general, good agreement was obtained between maximum tensions in the geogrids computed with Equation 1 and those obtained from measurements with gages attached to the grids. Measured strains were converted to geogrid loads using a stiffness modulus considering both the time-dependent stress-strain response of the viscoelastic polymer composing the geogrid and the increased stiffness that results from in-service soil confinement. Isochronous tension strain curves for Tensar SR2 geogrid (*5*) indicate that for the low levels of strain realized in this project, most time-dependent deformation occurred within the first 100 hr after load application. The 100-hr isochronous modulus relating strain to load in the geogrid is about one-third of the modulus determined from a "quick" tension test performed on the material. However, this reduction in stiffness is counteracted by the tendency of in-service soil confinement to increase the stiffness modulus. Results from tension tests performed on model plastic geogrids reported by Juran and Christopher (*7*) indicate that the confined stiffness modulus is about three times the unconfined

TABLE 1 SUMMARY OF PARAMETERS USED IN ANALYSIS

Parameter	Material		
	Wallfill	Backfill	Geogrid
Internal Friction	34°	30°	---
Cohesion	0	0	---
Unit Weight, lb/ft^3	125	115	---
(kN/m^3)	(19.6)	(18.0)	
Longterm Allowable Tension, lb/ft			1986
(kN/m)			(29.0)
Longterm Design Tension, lb/ft			1324
(kN/m)			(19.3)

stiffness modulus. When effects of both time and soil confinement were considered coincidentally, the stiffness modulus determined from unconfined quick tension testing was used to convert strains measured in the field to geogrid loads. However, further study is required to better establish confined behavior of in-service materials.

Measurements indicate that tensile strains in the geogrids are in the range of 0.3 to 0.8 percent, corresponding to a load of 225 to 600 lb/ft (3.28 to 8.75 kN/m) in the geogrids. Comparing this load with the ultimate tensile strength of the geogrids, which is 5,400 lb/ft (79.0 kN/m), the grids are loaded to between only 4 and 11 percent of the ultimate load level. At this low load level, significant creep is not expected.

Maximum tensions in the geogrids computed with Equation 1 and measurements from instrumented geogrids are compared in Figures 4–8. Tensile strain is depicted in these figures, and Equation 1 is used to compute the maximum tensile forces in the geogrids, which are then converted to strains. Results are presented for geogrids at elevations of 0.5, 1.5, 3.5, 4.5, and 11.5 ft (0.15, 0.46, 1.07, 1.37, and 3.51 m). Development of strain in the geogrids due to successive placement of lifts over the grids, indicated by fill placement height, is displayed. Results are presented for wall panels 26-30 and 26-32 when measurements from both walls are available, and in general, the results from the two wall sections are consistent.

Measurements include strains induced during compaction of the first lift of fill over the geogrid (with compaction) and measurements that do not include compaction strains (post compaction). Compaction strains are not shown for measurements made with inductance coils at elevations of 0.5, 3.5, and 11.5 ft (0.15, 1.07, and 3.51 m), because these measurements were deemed to be unreliable at such low strains. It appears that compaction did induce some additional tensile strain, roughly between 0.1 and 0.2 percent. These strain levels correspond to a tension load between 75 and 150 lb/ft (1.1 and 2.2 kN/m), which is considered small when compared with the design working load level of 1,324 lb/ft (19.4 kN/m).

Results presented for geogrids at the lower elevations of 0.5 and 1.5 ft (0.15 and 0.46 m) are shown in Figures 4 and 5. Strain measurements taken during the early part of construction when the height of fill over the grids was low are relatively close to those predicted by Equation 1. As construction proceeded and the height of fill over the geogrids increased, strains predicted by Equation 1 became higher than those that were measured. Results for geogrids located at higher elevations are shown in Figures 6–8. Here, strain measurements appear to be in good agreement with predicted strains throughout the construction process, indicating closer agreement between Equation 1 and measurements with respect to geogrids at these higher elevations.

A possible explanation for the response of the lower geogrids is related to the pinned connection between the precast concrete wall facing and a strip footing at the base of the wall. The connection may have allowed a small amount of initial translation between the wall facing and footing while the first few lifts of backfill were placed. Displacements were such that load transfer between the soil and geogrid reinforcement was possible. Further displacement at the bottom of the wall facing was restricted by the pinned connection, so load transfer to

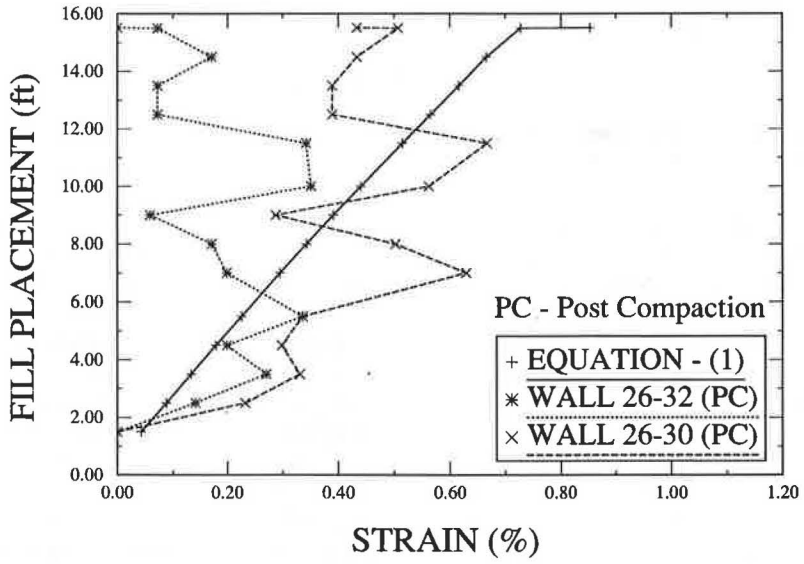

FIGURE 4 Maximum tensile strain during construction in geogrid at elevation 0.5 ft (0.15 m).

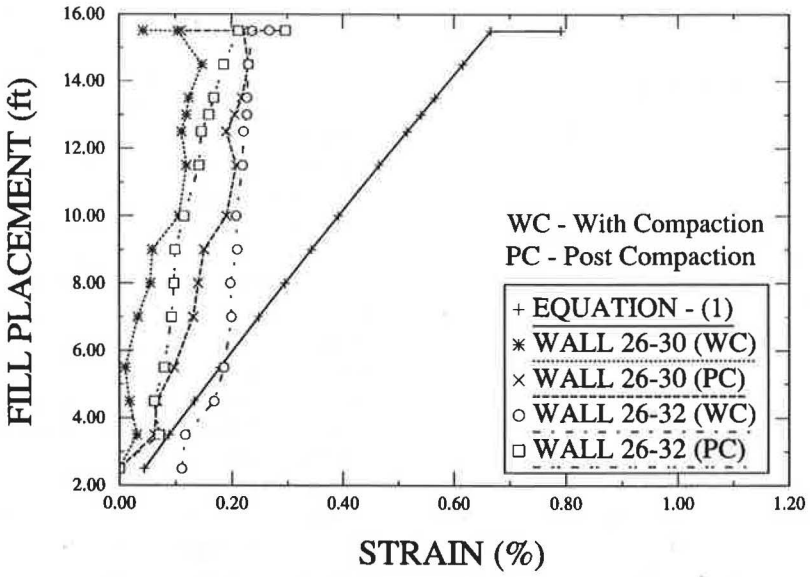

FIGURE 5 Maximum tensile strain during construction in geogrid at elevation 1.5 ft (0.46 m).

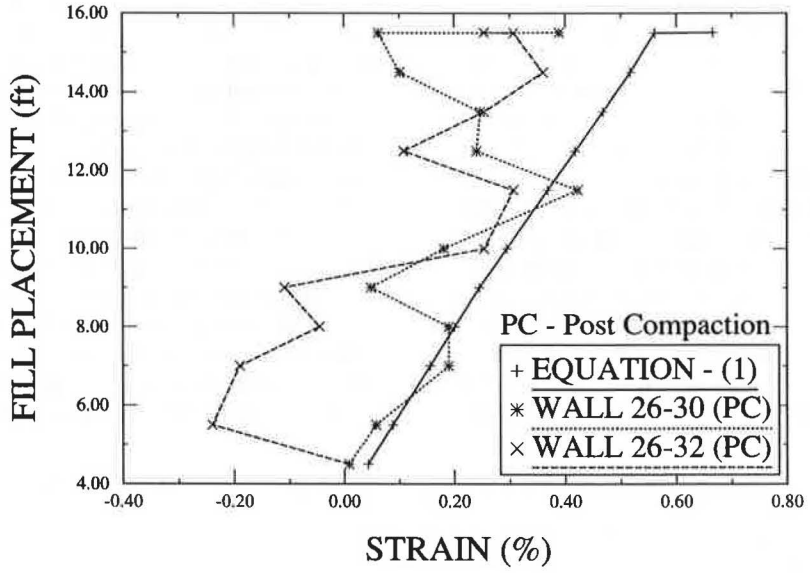

FIGURE 6 Maximum tensile strain during construction in geogrid at elevation 3.5 ft (1.07 m).

the geogrids was not possible while backfill was being placed at higher elevations. Perhaps increased lateral earth pressure was then applied to the wall face, as indicated by pressure measurements at the wall face.

LONG-TERM BEHAVIOR

Fluctuations in readings from pressure cells and inductance coils throughout the first year after construction of the wall appear to well represent the seasonal temperature fluctuations within the reinforced soil mass. These fluctuations may be due to the temperature effects on the wall sytem or to the effect of temperature on the instruments. Temperature compensation was provided for resistance strain gages, and no significant or consistent fluctuations with temperature variation throughout the year were observed.

Creep effects were not apparent for the year during which readings were taken. The effects of the creep may have been masked by temperature effects. However, the level of tension in the geogrids may be so low that creep effects are insignificant.

Figures 9–14 present results of geogrid strain measurements taken with resistance strain gages along the length of grids at elevations of 1.5, 4.5, 11.5, and 14.5 ft (0.46, 1.37, 3.51, and 4.42 m). Readings acquired at the end of construction of the wall (October 1985) are compared with readings taken annually in 1986, 1987, and 1988. Data from resistance strain gages were not obtained during 1989 because of equip-

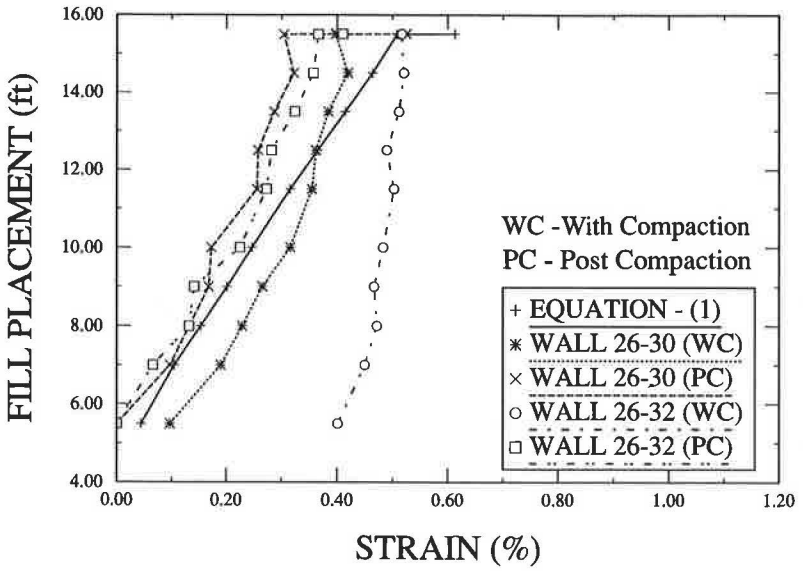

FIGURE 7 Maximum tensile strain during construction in geogrid at elevation 4.5 ft (1.37 m).

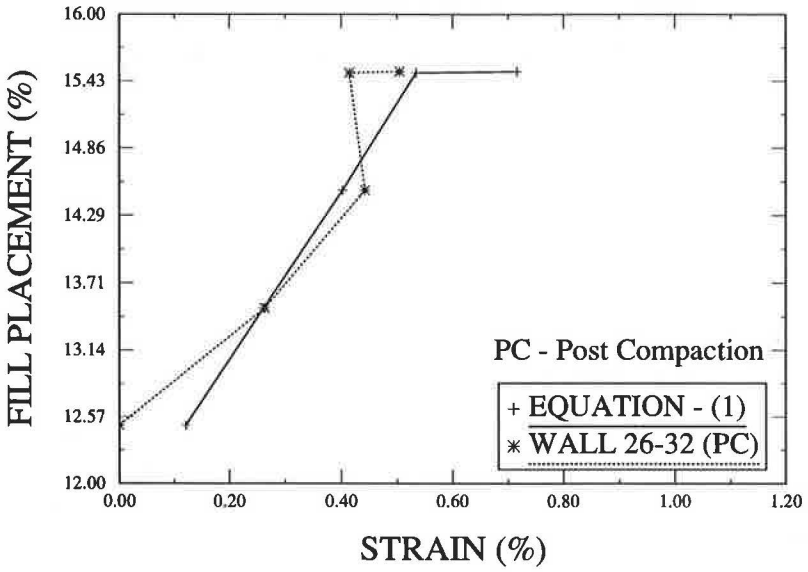

FIGURE 8 Maximum tensile strain during construction in geogrid at elevation 11.5 ft (3.51 m).

ment difficulties. Information shown in Figures 9–14 reveals that subsequent readings display little change from previous readings and no consistent pattern. Creep or a change in strain with time is not indicated.

Figure 15 shows results from measurements of strain in the connection between geogrids and the full-height precast concrete wall facing. The connection consists of pieces of geogrid embedded in the precast concrete wall panels to form a loop through which the ends of geogrids are inserted. The connection is illustrated in Figure 3. Measurements are from resistance strain gages mounted to the top portion of the loops. A small increase in strain over time is revealed from measurements taken with gages mounted on loops at elevations 0.5, 1.5, and 3.5 ft (0.15, 0.46, and 1.07 m). The small increase in strain, which may be due to settlements that occurred in the wall fill, appears to have stabilized between 1987 and 1988. The decrease in strain recorded from measurements taken at elevation 11.5 ft is most likely due to a loss of bond between the strain gage and the geogrid material.

CONCLUSIONS

This study is unique in its focus on field measurements of geogrid-reinforced retaining walls with full-height precast concrete facing. Tensile strains measured during construction of the wall indicate that during compaction of the wall fill, a tension force was induced in the geogrids that is low when

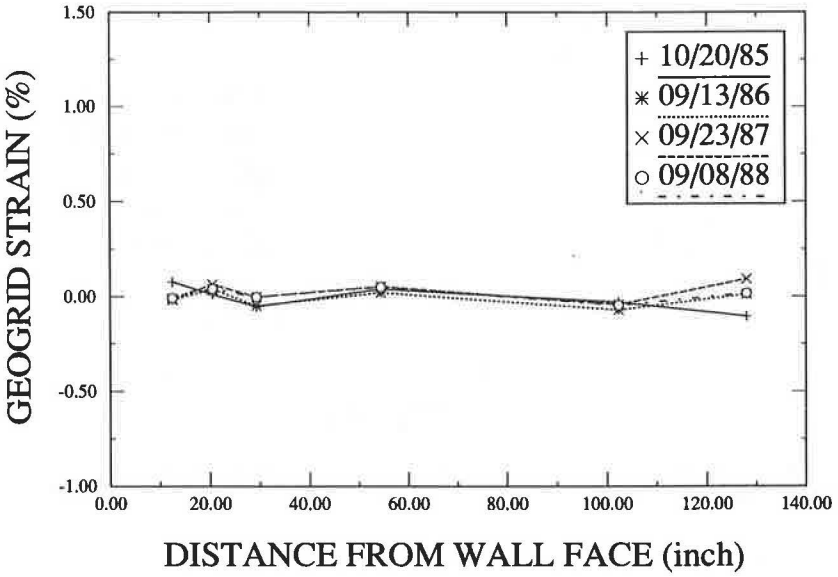

FIGURE 9 Annual measurements of strain along geogrid at elevation 1.5 ft (0.46 m), Wall 26-30.

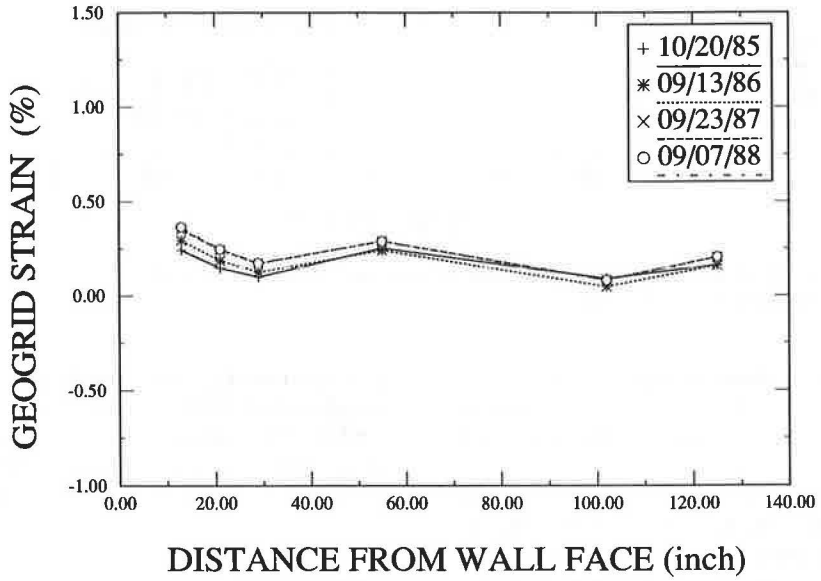

FIGURE 10 Annual measurements of strain along geogrid at elevation 1.5 ft (0.46 m), Wall 26-32.

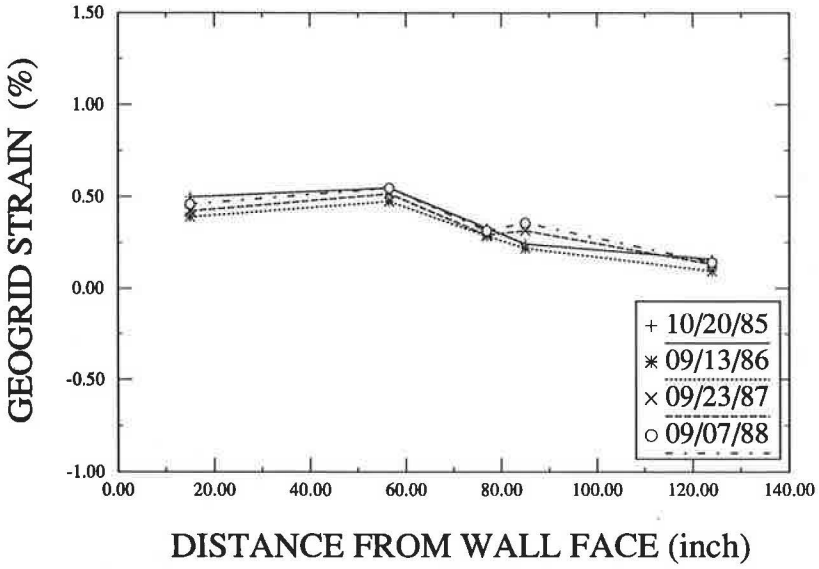

FIGURE 13 Annual measurements of strain along geogrid at elevation 11.5 ft (3.51 m), Wall 26-32.

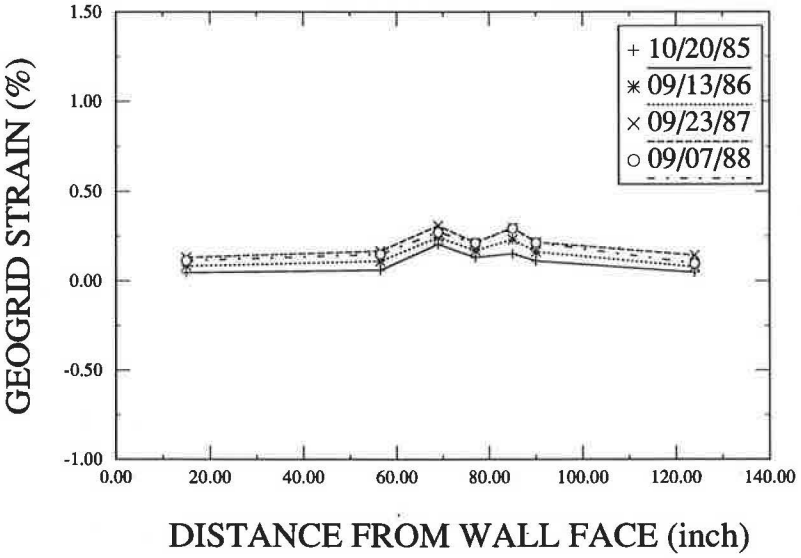

FIGURE 14 Annual measurements of strain along geogrid at elevation 14.5 ft (4.42 m), Wall 26-30.

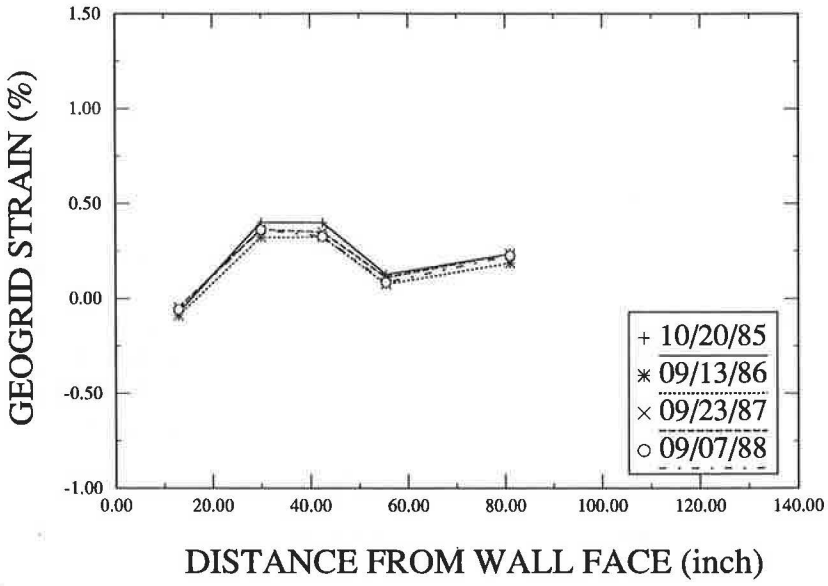

FIGURE 11 Annual measurements of strain along geogrid at elevation 4.5 ft (1.37 m), Wall 26-30.

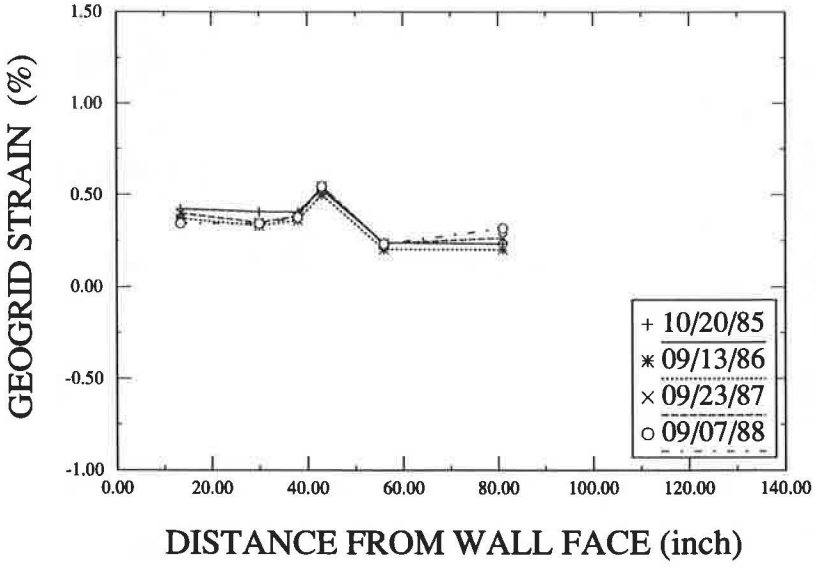

FIGURE 12 Annual measurements of strain along geogrid at elevation 4.5 ft (1.37 m), Wall 26-32.

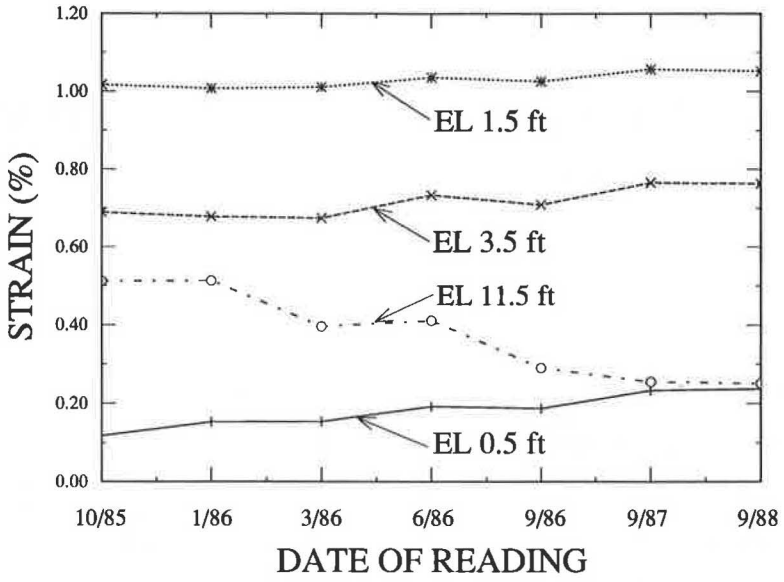

FIGURE 15 Detail of connection between geogrids and wall facing (*8*).

compared with safe working loads. Geogrid strains measured during and after construction demonstrate that the computation of maximum tension in the reinforcement using Equation 1 was in general satisfactory.

In addition, this project is especially important because of its duration. Survivability of the instruments installed in this project has allowed the observation of the long-term behavior of geogrids in service. Data obtained so far indicate that appreciable rates of creep strain are not evident. Although this conclusion lends credibility to the use of strain-hardened polyethylene materials for long-term applications, it should be noted that the level of tension that prevailed in the geogrids was far below the design tensile strength. Future studies should focus on the behavior of geogrids installed in systems such that the geogrids are loaded to working stress levels.

ACKNOWLEDGMENTS

The research study was conducted for Pima County Department of Transportation and Flood Control District (PCDOT & FCD) on two reinforced retaining walls at the Tanque Verde–Wrightstown–Pantano Project in Tucson, Arizona. The walls were built by M. M. Sundt Construction Company. Funding for the study was provided by FHWA and the Tensar Corporation. The instrumentation project was conceived by Barry Berkovitz, who was a staff engineer for PCDOT & FCD and is now with FHWA, and John Walkinshaw, who is also with FHWA. Administration was conducted by the project manager, Ali I. Fermawi of PCDOT & FCD. The research study was contracted with Desert Earth Engineering with active participation of personnel from the Department of Civil Engineering and Engineering Mechanics at the University of Arizona in Tucson. Calibration and testing of the instruments were performed in the department's Constitutive Modeling Laboratory.

REFERENCES

1. Desert Earth Engineering. *Tensar Earth-Reinforcement Wall Monitoring at Tanque Verde–Wrightstown–Pantano Roads, Tucson, Arizona*. Preliminary report to Pima County Department of Transportation and Flood Control District, Tucson, Ariz., 1986.
2. Desert Earth Engineering. *Tensar Earth-Reinforcement Wall Monitoring at Tanque Verde–Wrightstown–Pantano Roads, Tucson, Arizona*. Final report to Pima County Department of Transportation and Flood Control District, Tucson, Ariz., 1987.
3. K. L. Fishman, C. S. Desai, and R. L. Sogge. Field Behavior of Instrumented Geogrid Soil Reinforced Wall. *Journal of the Geotechnical Engineering Division*, ASCE, submitted March 1990.
4. *Tensar Geogrid Reinforced Soil Wall*. Experimental Project 1, Ground Modification Techniques. FHWA-EP-90-001-005. FHWA, U.S. Department of Transportation, Jan. 1989.
5. *Guidelines for the Design and Construction of Reinforced Walls Using Tensar Geogrids*. Netlon Ltd., Blackburn, England, 1984.
6. Dames and Moore. *Tensar SR2 Reinforced Retaining Walls for Tanque Verde Road, Tucson, Arizona*. Study for Pima County Department of Transportation and Flood Control District, Tucson, Ariz., 1984.
7. I. Juran and B. Christopher. Laboratory Model Study on Geosynthetic Reinforced Soil Retaining Walls. *Journal of the Geotechnical Engineering Division*, ASCE, Vol. 115, No. 7, July 1989.
8. R. R. Berg, R. Bonaparte, R. P. Anderson, and V. E. Chouery. Design, Construction, and Performance of Two Geogrid Reinforced Soil Retaining Walls. *Proc., 3rd International Conference on Geotextiles*, Vienna, Austria, 1986.

Publication of this paper sponsored by Committee on Mechanics of Earth Masses and Layered Systems.

Limit Equilibrium Stability Analyses for Reinforced Slopes

STEPHEN G. WRIGHT AND J. M. DUNCAN

Limit equilibrium slope stability analysis procedures have been successfully adapted and used for analyses of reinforced slopes. A potential source of inaccuracy in these analyses is the limit equilibrium procedure used, specifically the assumptions that are made to satisfy static equilibrium and the equilibrium conditions that are satisfied. A second possible source of inaccuracy is related to the manner in which the reinforcement forces are assumed to be distributed in the soil mass and the direction in which they are assumed to act. Stability computations have been performed using the logarithmic spiral, Bishop simplified, Spencer's, and force equilibrium procedures to evaluate the magnitudes of these inaccuracies. Methods that satisfy complete static equilibrium (logarithmic spiral and Spencer's) were found to result in essentially the same values for the factor of safety. Bishop's simplified procedure also produces very nearly the same values for the factor of safety, although the procedure does not satisfy complete static equilibrium. Force equilibrium procedures produce factors of safety that are sensitive to assumptions made about the inclination of side forces between slices.

Geotextiles, geogrids, and steel reinforcing elements are being used with increasing frequency to reinforce slopes and embankments, making possible construction of steeper slopes and higher embankments. Design of these slopes and embankments is usually based on equilibrium stability analyses. The reinforcing elements are represented in the analyses as stabilizing forces of known magnitude, and the necessary amount and distribution of reinforcement within the slope is determined by trial and error.

Although equilibrium analyses have been used successfully for designing many slopes and for developing design charts for reinforced slopes and embankments, two possible sources of potential inaccuracy are not well understood:

1. How are the factors of safety for reinforced slopes affected by whether or not the method satisfies all conditions of equilibrium and by the assumptions involved in the method? For example, Bishop's simplified procedure does not satisfy horizontal equilibrium, and it assumes that there are no vertical side forces. Are the factors of safety calculated using this method accurate or not?
2. How are the factors of safety for reinforced slopes affected by the way in which the reinforcement forces are represented in the analyses? Reinforcement forces have been represented as concentrated forces on the base of single slices, as concentrated forces at the face of the slope, and as forces distributed within the reinforced soil mass. Do these methods lead to the same value of safety factor or to different values; if different values, which is more correct?

This paper answers these questions through comparative analyses of reinforced slopes and embankments using the logarithmic spiral procedure of analysis, Bishop's simplified procedure, Spencer's procedure, and a force equilibrium procedure of slope stability analysis.

S. G. Wright, Department of Civil Engineering, University of Texas, Austin, Tex. 78712. J. M. Duncan, Department of Civil Engineering, 104 Patton Hall, Virginia Polytechnic Institute and State University, Blacksburg, Va. 24061.

ADAPTATION OF LIMIT EQUILIBRIUM PROCEDURES

All limit equilibrium analysis procedures are based on solving one or more static equilibrium equations for one or more unknowns, including the factor of safety, or F. The factor of safety is defined with respect to soil shear strength as

$$F = \frac{\text{available shear strength}}{\text{shear strength required for equilibrium}}$$

The number of unknowns must be equal to the number of equations to achieve a statically determinant solution. Various assumptions regarding the unknowns are made to achieve a balance between equations and unknowns. The number of equilibrium conditions satisfied also varies, depending on which limit equilibrium procedure is used.

When reinforcement is introduced into an analysis, it presents little in the way of additional complexity. Because the reinforcement force is considered to be known and is prescribed for purposes of the analysis, it introduces no additional unknowns. The reinforcement forces are additional known forces that are included in the appropriate equilibrium equations.

Four limit equilibrium procedures are considered in this paper. The first is the logarithmic spiral procedure. This procedure satisfies all conditions of equilibrium for a free-body consisting of the soil mass bounded by the shear surface and the surface of the slope. The three remaining procedures are procedures of slices: the Bishop's simplified (*1*), Spencer's (*2*), and force equilibrium procedures. The force equilibrium procedure satisfies equilibrium of forces only; equilibrium of moments is not considered.

Logarithmic Spiral Procedure

The logarithmic spiral procedure assumes that the shear surface is a logarithmic spiral. The spiral is defined by its center point and a radius (r) of the form

$$r = r_o \exp(\Theta \tan \Phi_m)$$

where

r_o = radius to some prescribed reference point (often the toe of the slope),
Θ = angle between the reference radius and the radius r at some other point on the spiral, and
Φ_m = "mobilized" friction angle ($\tan \Phi_m = \tan \Phi / F$).

Summation of moments about the center of the spiral results in an equilibrium equation that involves only one unknown, Φ_m (that is, the factor of safety). The moment equilibrium equation is solved for the factor of safety.

When reinforcement is included in an analysis, the moments about the center of the spiral include moments due to the reinforcement as well as moments due to the weight of the soil mass and any pore water pressures or cohesive component of shear strength. The moments due to these forces can be computed from the known conditions and an assumed factor of safety. A trial-and-error procedure is used to determine the factor of safety that produces static equilibrium.

Unlike the procedures of slices, the logarithmic spiral procedure requires no assumptions about the internal forces. Accordingly, it provides a useful independent check of the validity of the procedures of slices.

Bishop's Simplified Procedure

The Bishop's simplified procedure is based on equilibrium of moments about the center of a circular shear surface and equilibrium of forces in the vertical direction. Equilibrium of moments is considered only for the entire free-body composed of all slices; vertical force equilibrium is considered for individual slices. Horizontal reinforcement forces contribute to the equation of moment equilibrium but do not directly enter or affect the equilibrium equation for forces in the vertical direction. Inclined reinforcement forces affect equilibrium of moments and equilibrium of forces in the vertical direction. In some cases the effect of inclined reinforcement on vertical force equilibrium has been ignored (*3*,*4*). For the analyses in this paper, the contribution of inclined reinforcement to both moments and vertical force equilibrium has been accounted for.

Spencer's Procedure

Spencer's procedure assumes that the side forces are parallel, that is, that all side forces have the same inclination. Complete static equilibrium of moments and forces is satisfied. The solution involves evaluating the factor of safety, the inclination of the side forces, and the other unknown forces and their locations. Reinforcement forces contribute to the moments on slices and to the forces in the vertical and horizontal directions.

Force Equilibrium Procedure

Several force equilibrium procedures differ with regard to the assumption made concerning the inclination of forces between slices. The force equilibrium procedure chosen for the present analyses is based on the assumption that the side forces are horizontal, that there is no shear between slices. This assumption is sometimes referred to as the "simplified Janbu" assumption; it was chosen because of its simplicity and because it has been found to give relatively low, conservative values for the factor of safety.

EXAMPLE PROBLEMS

Two example problems are considered to illustrate the differences among the various procedures. The first example consists of a cohesionless fill slope constructed on a firm foundation; any potential for failure is assumed to be restricted to the slope itself. The second example consists of a cohesionless fill slope constructed on a very weak foundation where the foundation governs the stability and necessitates reinforcement. These examples represent two of the most common slope conditions in which reinforcement is likely to be employed.

Example 1

The first example slope is a 1:1 (45-degree) slope, 38 ft high, as shown in Figure 1. The soil is cohesionless and has an angle of internal friction of 32 degrees and a total unit weight of 120 pcf. The slope contains 17 layers of reinforcement, varying from 23.9 to 29.2 ft long and spaced vertically as shown in Figure 1.

This example was taken from Tensar (*5*). The original example presented by Tensar had a surcharge of 240 psf, equivalent to about 2 ft of additional slope height, which was neglected for the current analyses.

Each layer of reinforcement has an axial force of 1,000 lb. Although the force would actually decrease to zero near the embedded ends of the reinforcement, the force was assumed to be constant along the entire length of the reinforcement for the current stability computations.

The computed factors of safety for the first example slope are summarized in Table 1. Factors of safety were computed for the reinforcement force acting in two directions. In the first case the reinforcement force acted horizontally; in the second case it was assumed that the reinforcement had rotated such that the force acted tangentially to the shear surface.

The critical shear surface producing the minimum factor of safety was located for each case and for each of the limit

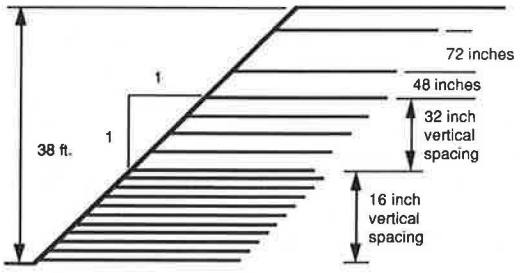

FIGURE 1 Example slope 1.

TABLE 1 COMPARISON OF FACTORS OF SAFETY COMPUTED FOR EXAMPLE 1 WITH REINFORCEMENT FORCES HORIZONTAL AND TANGENT TO SHEAR SURFACE

Analysis Procedure	Horizontal Reinforcement	Reinforcement Tangent to Shear Surface
Spencer	1.44	1.42
Simplified Bishop	1.45	1.44
Force Equilibrium	1.30	1.29
Logarithmic Spiral	1.46	1.46

equilibrium analysis procedures. Although Spencer's procedure and the force equilibrium procedure can accommodate noncircular shear surfaces, only circular shear surfaces were considered to permit comparisons to be made with the Bishop's simplified procedure and the logarithmic spiral procedure. Experience has shown that the most critical logarithmic spiral shear surface is very similar to the most critical circle and, thus, circles and logarithmic spirals can be considered comparable shapes.

The factors of safety computed by the four limit equilibrium procedures are summarized in Table 1. The three procedures that satisfy moment equilibrium (Bishop simplified, Spencer's and logarithmic spiral) produced factors of safety that agree within approximately 2 percent.

The force equilibrium procedure produced factors of safety that were approximately 10 percent lower than the values that the others produced. These lower values are consistent with what the authors have often found using the force equilibrium procedure for unreinforced slopes; they indicate the conservative nature of the procedure in this instance.

The differences between the factors of safety computed for horizontal reinforcement forces as compared to forces tangent to the shear surface were in all cases negligible. This observation is contrary to results of Low and Duncan (*6*), who found that the factor of safety with the reinforcement force tangent to the shear surface was always larger than the factor of safety with the reinforcement force horizontal. However, the analyses performed by Low and Duncan did not include the vertical component of the reinforcement force in the equations of vertical equilibrium, and this is believed to be the cause of the differences in the results shown in Table 1 and the findings of Low and Duncan.

An inclined force tends to produce a larger moment than a horizontal force, but it has a smaller contribution to the normal forces (and shear strength) along the shear surface. The two effects tend to compensate for each other and the net effect is thus small.

The remarkably close similarity between the factors of safety computed by the Bishop's simplified, Spencer's, and logarithmic spiral procedures was unexpected. In particular, the close agreement between the factors of safety computed by procedures satisfying complete equilibrium and the Bishop's simplified procedure was surprising, because the Bishop's simplified procedure ignores forces in the horizontal direction, which is the direction of all or much of the reinforcement force, depending on its inclination.

The close agreement between the Bishop's simplified and complete equilibrium procedures apparently stems from the fact that moment equilibrium is considered and force equilibrium is satisfied in at least one direction by all three methods. This can be seen by first considering the illustration in Figure 2. Equilibrium of moments involves the known moments due to the weight of the soil and the reinforcement force. The only other moment is produced by the shear stresses along the shear surface. Because the weight and reinforcement produce a given, known moment, the average shear stress along the shear surface is fixed, regardless of any assumptions made in the procedures of slices that satisfy moment equilibrium. Now considering the equilibrium of forces in the vertical direction and the illustration in Figure 3, equilibrium of forces in the vertical direction involves the weight (W), the shear stresses (τ), and the normal stresses (σ) along the shear surface. The weight is fixed and, as discussed earlier, the average shear stress is fixed by the requirement of moment equilibrium. The normal stress is the only remaining quantity contributing to vertical equilibrium. Accordingly, the normal stress is also, for practical purposes, fixed—at least in an average sense. The shear and normal stresses may vary in different ways along the shear surface, depending on the specific limit equilibrium procedures used; however, if the procedures satisfy moment equilibrium and, at least in the vertical direction, equilibrium of forces, the average shear and the average normal stresses must be about the same. For this reason the factor of safety, which depends on the stresses along the shear surface, is apparently almost independent of the assumptions made in limit equilibrium procedures, such as Spencer's and the Bishop's simplified, that satisfy moment equilibrium and force equilibrium in at least one direction. Only the force equilibrium procedure, which does not satisfy moment equilibrium, produces results that are not in agreement with the other procedures.

Example 2

The second example consists of a 10-ft-high cohesionless fill resting on a 10-ft layer of saturated ($\Phi = 0$) clay, as shown

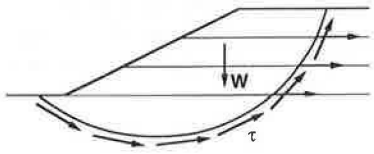

FIGURE 2 Forces and stresses contributing to equilibrium of moments for reinforced slope.

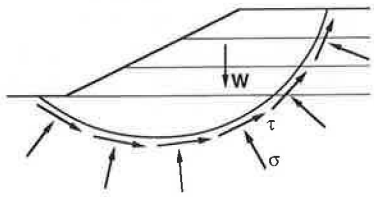

FIGURE 3 Forces and stresses contributing to equilibrium of forces in vertical direction for reinforced slope.

in Figure 4. Much stronger soils are assumed to exist below the clay. The fill has an angle of internal friction (Φ) of 35 degrees and a total unit weight of 105 pcf. The clay has a uniform undrained shear strength of 200 psf.

One layer of reinforcement is placed at the base of the fill on the surface of the clay. The reinforcement carries a constant force of 3,000 lb/linear-ft of slope. The factor of safety of the unreinforced slope is approximately 1.1; reinforcement was selected to increase the value to an acceptable level.

Two slightly different locations of the reinforcement were examined. First, the reinforcement shown in Figure 4 is considered to be located just above the clay so that it crosses the shear surface in the sand. The reinforcing force is thus applied to a slice with an entirely frictional strength, where normal stresses and the contribution of the reinforcement to the normal stresses would be expected to have the greatest influence. Second, the reinforcement shown in Figure 4 is considered to be located just below the top surface of the clay. In this case the reinforcement crosses the shear surface in the clay. The reinforcement force is thus applied to a slice with a purely cohesive strength, where normal stresses on the shear surface have no affect on the shear strength and computed factor of safety. The two positions for the reinforcement were selected because they were expected to illustrate the maximum effect of treating the reinforcement force as a concentrated force. In one case, in which the reinforcement is in the clay, the concentrated force is applied to a slice where the strength is independent of the normal stress on the shear surface; in the other case the force is applied to a slice where the shear strength is directly proportional to the normal forces on the shear surface.

The factors of safety for the second example slope were computed by the Bishop simplified, Spencer's, and force equilibrium procedures for horizontal reinforcement forces and forces tangent to the shear surface. The logarithmic spiral is, for practical purposes, restricted to homogeneous slopes (Φ = constant), so it could not be used for this second example.

The factors of safety for horizontal reinforcement forces are summarized in Table 2. It can again be seen that the computed factors of safety differ very little. The extreme range in the values computed was less than 2 percent. The force equilibrium procedure produced factors of safety almost identical to the ones computed by the other procedures for this case, because the side force inclination satisfying moment equilibrium, 2 to 3 degrees, is very close to horizontal. Thus, the force equilibrium procedure, which assumed horizontal side forces, gave results in close agreement with Spencer's procedure, which determined as part of the solution that the side forces are close to horizontal for this case.

The factors of safety for reinforcement forces that are tangent to the shear surface are summarized in Table 3. The values for the reinforcement located in the sand agree closely

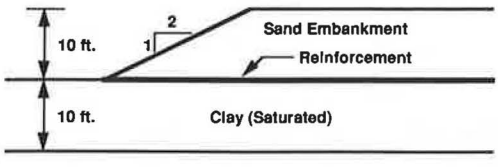

FIGURE 4 Example slope 2.

TABLE 2 COMPARISON OF FACTORS OF SAFETY COMPUTED FOR EXAMPLE 2 WITH REINFORCEMENT FORCES HORIZONTAL

Analysis Procedure	Reinforcement in Sand	Reinforcement in Clay
Spencer	1.37	1.36
Simplified Bishop	1.36	1.37
Force Equilibrium	1.35	1.35

TABLE 3 COMPARISON OF FACTORS OF SAFETY COMPUTED FOR EXAMPLE 2 WITH REINFORCEMENT FORCES TANGENT TO SHEAR SURFACE

Analysis Procedure	Reinforcement in Sand	Reinforcement in Clay
Spencer	1.36	1.57
Simplified Bishop	1.36	1.58
Force Equilibrium	1.33	1.52

with those computed for horizontal reinforcement, shown in Table 2. This reflects the compensating effects of the inclined reinforcement forces on the moments and the normal stresses (shear strength) in the sand, similar to what was shown for Example 1.

The factors of safety for the reinforcement in the clay are significantly higher when the reinforcement forces are tangent to the shear surface. This indicates that the reinforcement has approximately twice the stabilizing effect: the factor of safety increased from approximately 1.1 to 1.57 with the reinforcement forces tangent to the shear surface as compared with an increase from 1.1 to 1.35 for horizontal reinforcement. The higher factors of safety are due to the added effect of the reinforcement on the moment, when the forces are tangent to the shear surface rather than horizontal. The reinforcement forces had no effect on the shear strength when the reinforcement was assumed to be located in the clay because Φ was equal to zero.

The effects of the inclination of the reinforcement forces can be significant when $\Phi = 0$ because compensating effects on strength and moment do not exist. However, it seems unlikely that such a case could exist in practice. There is no practical way to install the reinforcement below the surface of the saturated clay. Reinforcement is usually placed on the surface of a sand or gravel pad on top of the clay and is thus embedded in cohesionless material.

INTERNAL DISTRIBUTION OF FORCES

All the stability computations and procedures discussed up to this point have been based on the assumption that each layer of reinforcement can be represented by a concentrated force applied to the base of the slice. Although the reinforcement also creates internal forces between slices, the internal forces were not considered directly. In procedures such as Spencer's and force equilibrium, the side forces, which are evaluated as unknowns, include the forces transmitted through the soil as well as the force in the reinforcement where it crosses the slice boundary. The assumptions that are made and counted on in the limit equilibrium procedures to properly handle the

forces between slices must also be counted on to properly handle the reinforcement forces between slices.

In reality, the forces in reinforcement are developed and transferred to the soil along the length of the reinforcement. The forces that are actually transferred to individual slices represent the difference between the force at the left and right sides where the reinforcement crosses the slice. Depending on how the reinforcement forces are developed and transferred to the soil, the forces on each slide will vary in magnitude and direction. For example, if the forces gradually increase and decrease along the length of the reinforcement as shown in Figure 5 (*top*), they will be distributed to individual slices as represented by the net forces on each slice in Figure 5 (*bottom*).

A realistic way of applying the forces to slices in a limit equilibrium analysis is, thus, to apply the net reinforcement force to each slice. This is done by applying the reinforcement force not only where the reinforcement crosses the shear surface, but also where it crosses the boundaries between slices. Such a set of applied forces is illustrated schematically in Figure 6. The internal reinforcement forces between slices have no net effect on the overall equilibrium of the soil mass; equal and opposite forces on each internal slice boundary of adjacent slices simply cancel. However, the internal reinforcement forces (the differences in reinforcement force on the left and right sides of each slice) do have an effect on the distribution of forces among individual slices, including the distribution of shear and normal stresses along the shear surface.

To examine the effect of the way in which reinforcement forces are applied to the soil mass, another series of stability

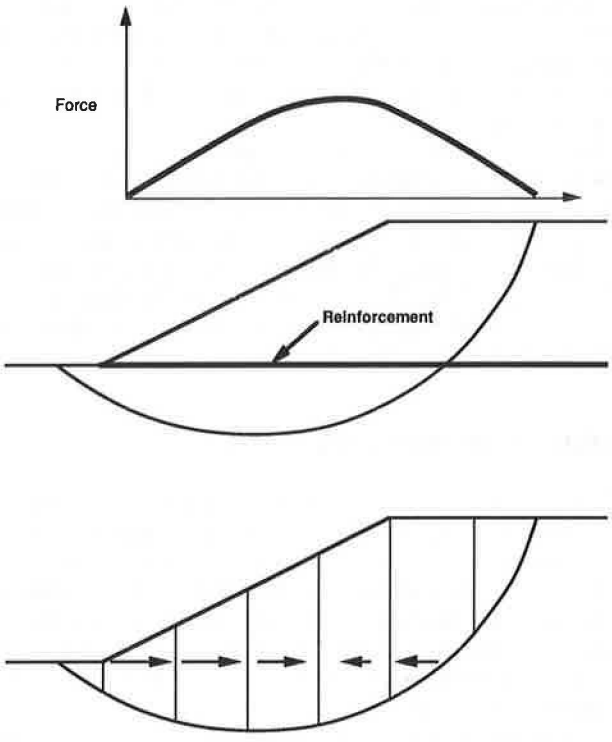

FIGURE 5 Net forces applied to individual slices when force varies along length of reinforcement.

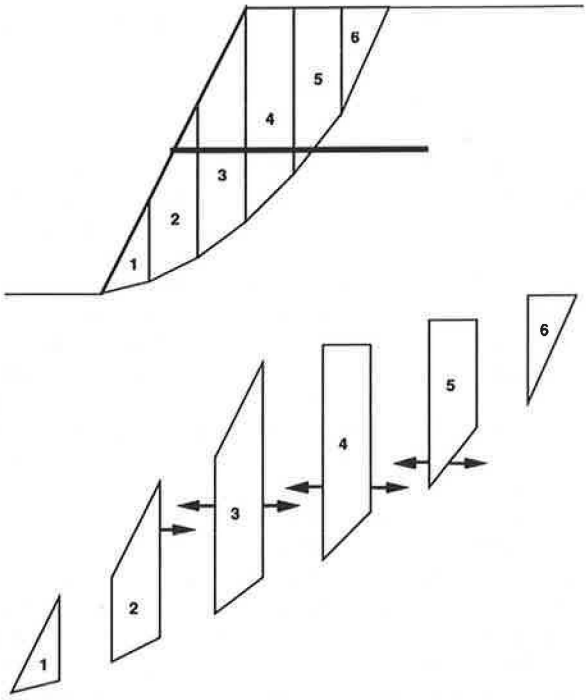

FIGURE 6 Internal and external forces applied to slices to represent reinforcement.

computations was performed. In these analyses the reinforcement force was considered to be constant along the length of the reinforcement, and internal as well as external forces were applied. The consequence of assuming a constant force was to make the net reinforcement force zero wherever the reinforcement crosses two boundaries of a slice (including the shear surface). The net force is equal to the reinforcement force at the point where the reinforcement terminates. Each layer of reinforcement that is intersected by the shear surface causes a single force to be applied to the face of the slope where the reinforcement is terminated (Layers 1, 2, and 3 in Figure 7).

Reinforcement that does not cross the shear surface and is contained entirely within the soil mass causes two forces of equal magnitude but opposite direction to be applied at the two points at which the reinforcement is terminated (Layers 4, 5, and 6 in Figure 7).

The assumption of a constant force in the reinforcement for the current computations is not considered to be realistic.

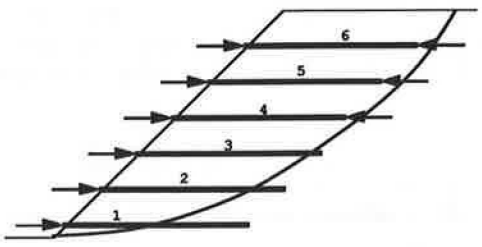

FIGURE 7 Forces applied to slices when reinforcement force is constant along length of reinforcement.

TABLE 4 COMPARISON OF FACTORS OF SAFETY COMPUTED FOR EXAMPLE 1 WITH REINFORCEMENT FORCES APPLIED TO SHEAR SURFACE ONLY AND BOTH TO SHEAR SURFACE AND INTERNALLY

Analysis Procedure	Forces Applied to Shear Surface Only	Forces Applied Internally and at Shear Surface
Spencer	1.44	1.44
Simplified Bishop	1.45	1.45
Force Equilibrium	1.30	1.28

TABLE 5 COMPARISON OF FACTORS OF SAFETY COMPUTED FOR EXAMPLE 2 WITH REINFORCEMENT FORCES APPLIED TO SHEAR SURFACE ONLY AND BOTH TO SHEAR SURFACE AND INTERNALLY

Analysis Procedure	Forces Applied to Shear Surface Only	Forces Applied Internally and at Shear Surface
Spencer	1.37	1.36
Simplified Bishop	1.36	1.36
Force Equilibrium	1.35	1.35

However, it provides an extreme case for comparison with the case in which the reinforcement forces were applied as concentrated forces at the shear surface, as described earlier.

Factors of safety were computed for both of the example slopes. The values are shown in Tables 4 and 5. Values are shown for the reinforcement forces distributed internally as well as for the reinforcement force applied as a concentrated force at the shear surface. It can be seen from the results in these two tables that the manner in which the reinforcement force is applied has virtually no effect on the computed factor of safety for either slope. Had the reinforcement forces been assumed to vary along the length of the reinforcement, the differences between the factors of safety computed with the concentrated force applied to the shear surface and those computed as described earlier in this section would have been even smaller.

CONCLUSIONS

The analyses described in the preceding sections provide a basis for some important conclusions concerning the use of equilibrium methods for analysis of the stability of reinforced slopes:

1. Methods that satisfy all conditions of equilibrium result in essentially the same value of factor of safety regardless of the assumptions they may involve. This conclusion is illustrated by the close similarity between the values of factor of safety calculated using the logarithmic spiral procedure and Spencer's procedure of analysis.
2. Bishop's simplified method, although it does not satisfy all conditions of equilibrium, results in values of safety factor that are essentially the same as values calculated using methods that do satisfy all conditions of equilibrium. This is true for steep reinforced slopes on firm foundations and for embankments on weak foundations. The key to its accuracy appears to be the fact that it satisfies moment equilibrium.
3. Factors of safety calculated using force equilibrium procedures (which do not satisfy moment equilibrium and which require assumption of the inclination of the side force inclination) result in factors of safety that are sensitive to the assumed orientation of the side forces. If the assumed inclination is close to the one that satisfies moment equilibrium, the computed factor of safety is close to the value calculated using methods that satisfy all conditions of equilibrium. If the assumed side force inclination is far different from the one that satisfies moment equilibrium, the factor of safety will be different also. Calculating accurate values of factor of safety using force equilibrium methods is thus largely a matter of choosing the correct side force inclination. This is unnecessary if a method of analysis is used that satisfies all conditions of equilibrium. Spencer's procedure is such a method; it applies to either circular or noncircular (wedge-type) failure surfaces. Alternatively, if only circular shear surfaces are to be analyzed, Bishop's simplified method can be used with equally accurate results.
4. The manner in which the reinforcement force is distributed along the length of the reinforcement has no significant effect on the calculated values of factor of safety. Whether the force is applied as a concentrated force acting at the base of the slice through which it crosses the slip surface or as a concentrated force at the surface of the slope where it terminates, the calculated factor of safety is for all practical purposes the same. These two points of application represent the extremes possible, and it can thus be inferred that any other reasonable method of representing the reinforcement force will also lead to the same value of safety factor.
5. Whether the reinforcement force is applied horizontally or parallel to the shear surface, the calculated factor of safety is essentially the same, provided that the method of analysis includes the horizontal and vertical components of the reinforcement force in the equations of force equilibrium as well as the equation (or equations) of moment equilibrium and provided that Φ is not equal to zero. Reinforcement would almost always be located in a material in which Φ is not zero, so the effects of inclination can usually be ignored.
6. In Bishop's simplified procedure, which satisfies vertical force equilibrium, the vertical components of the reinforcement forces should be included in the equations of vertical equilibrium. In Spencer's procedure, which satisfies both horizontal and vertical equilibrium, both horizontal and vertical reinforcement forces should be included in the force equilibrium equations.
7. The studies described in this paper are concerned with factors of safety with respect to sliding along curved surfaces (log spirals or circular arcs). When the frictional resistance to sliding between the reinforcement and the soil is smaller than the shearing resistance for sliding through the soil mass, slip surfaces with a planar portion that coincides with the soil and reinforcement interface may be more critical than continuously curved surfaces, and they should be studied.

REFERENCES

1. A. W. Bishop. The Use of the Slip Circle in the Stability Analysis of Slopes. *Geotechnique*, Vol. 5, No. 1, March 1955, pp. 7–17.

2. E. Spencer. A Method of Analysis of the Stability of Embankments Assuming Parallel Inter-Slice Forces. *Geotechnique*, Vol. 17, No. 1, March 1967, pp. 11–26.
3. J. M. Duncan, B. K. Low, and V. R. Schaefer. *STABGM: A Computer Program for Slope Stability Analysis of Reinforced Embankments and Slopes—Microcomputer Version*. Department of Civil Engineering, Virginia Polytechnic Institute and State University, Blacksburg, Sept. 1985.
4. D. N. Humphrey and R. D. Holtz. *STABL6 with Reinforcing Option—User's Manual*. Report FHWA/IN/JHRP-86-18. Purdue University, West Lafayette, Ind., Oct. 1986.
5. *Slope Reinforcement with Tensar Geogrids—Design and Construction Guideline*. Tensar Technical Note TTN:SR1. Tensar Corporation, Morrow, Ga., May 1986.
6. B. K. Low and J. M. Duncan. *Analysis of the Behavior of Reinforced Embankments on Weak Foundations*. Report VPI/CE-GT-85-11. Department of Civil Engineering, Virginia Polytechnic Institute and State University, Blacksburg, 1985.

Publication of this paper sponsored by Committee on Mechanics of Earth Masses and Layered Systems.

Using Geosynthetics To Reduce Surcharge-Induced Stresses on Rigid Earth-Retaining Structures

JOHN S. HORVATH

Results of a finite-element study are presented that indicate that it is possible to achieve significant reductions in surcharge-induced horizontal stresses on rigid earth-retaining structures (retaining walls, bridge abutments, etc.). This is achieved by using a new type of geosynthetic, called a geoinclusion, that is placed between the structure and retained soil. The geoinclusion functions as a relatively compressible inclusion that allows the retained soil to undergo controlled yielding to mobilize its inherent strength. In doing so, the soil resists a significant portion of the surcharge-induced stress increment rather than merely transmitting it to the wall. If, in addition to the geoinclusion, relatively stiff tensile reinforcement such as polymer geogrid or steel is placed within the retained soil, even greater reductions in surcharge-induced horizontal stresses can be achieved. These conclusions are consistent with previous studies that included both finite-element modeling and physical testing of the use of geoinclusions, either alone or with tensile reinforcement, under gravity-induced earth loads only.

A new application of geosynthetics that is attracting increasing attention from both practitioners and researchers is the reduction of horizontal earth pressures acting on relatively rigid retaining structures (basement and retaining walls, bridge abutments, navigation locks, etc.) to levels significantly below the at-rest pressure state (or greater, if compaction-induced stresses are considered) that would normally be used in the design of such structures. The author calls this the reduced earth pressure (REP)-wall concept. The element necessary to achieve this behavior is a new type of geosynthetic, called a geoinclusion, that is placed along the interior (soil-side) face of the structure. Some authors have referred to this material as "geoboard" (*1*,*2*). The primary function of the geoinclusion is to act as a relatively compressible inclusion that allows the retained soil to deform laterally without significant resistance. This movement simultaneously mobilizes the shear strength of the soil and reduces lateral earth pressures. The overall phenomenon is referred to as "controlled yielding." Both numerical (finite-element) modeling and physical testing, as well as limited application in practice, have verified this concept (*1*,*3*–*8*). It is also possible, and in most cases desirable, to incorporate additional functions into the geoinclusion, such as drainage, thermal insulation, and possibly the attenuation of noise and vibration. Therefore, for most applications the geoinclusion will be a geocomposite consisting of a highly compressible solid panel of variable thickness that is bonded to a thinner, permeable panel with nonwoven geotextile covering for drainage.

Carrying this concept further, the incorporation of horizontal layers of tensile reinforcement into the retained soil allows the horizontal earth pressures to be reduced even more (*5*,*7*). This is because tensile forces in the reinforcement are mobilized as the geoinclusion compresses and the retained soil undergoes controlled yielding. As a result, the retained soil is transformed into an otherwise conventional mechanically stabilized earth mass that is essentially independent of the rigid retaining structure. The author terms this application of combined geosynthetics (geoinclusion plus reinforcement) the zero earth pressure (ZEP)-wall concept, because lateral earth pressures approaching zero can be achieved using reinforcement of suitable stiffness. The use of a geoinclusion to allow the relatively unrestricted movement necessary to activate the tensile reinforcement is better than leaving a void behind the wall for this purpose. A void of the necessary width can be difficult to create during construction and might result in maintenance or other operational problems after the wall is in service (*9*). In addition, the geoinclusion can—and in most cases would—be designed to provide one or more additional functions, as in the REP-wall application.

PURPOSE AND SCOPE

In many situations, particularly in the transportation field, it is desirable to add or significantly increase a surface surcharge load adjacent to a wall. In transportation applications, in which a surface surcharge is generally used to simulate the effect of a live load, this might involve loads from motor vehicles, aircraft, or trains adjacent to a bridge abutment or retaining wall that are significantly in excess of the original design loads. Retrofitting a wall structurally for such increased loads can be expensive and difficult, as would be totally replacing it. The study summarized in this paper was undertaken to investigate if the REP- and ZEP-wall concepts could be used to limit the horizontal stress increase on rigid earth-retaining structures due to surface surcharges.

METHOD OF ANALYSIS

The research performed for this study consisted of finite-element modeling of a simple, hypothetical problem. The computer code used was SSTIPNH, a microcomputer con-

Manhattan College, Civil Engineering Department, Manhattan College Parkway, Bronx, N.Y. 10471.

version by the author of the well-known mainframe program SSTIPN. The general capabilities of SSTIPN are discussed in its user's manual (*10*), and the specific capabilities of SSTIPNH are discussed by Horvath (*11*).

PROBLEM STUDIED

Geometry

Figure 1 shows the overall geometry of the problem studied and the finite-element discretization used. Both the retained soil and geoinclusion (if present) were modeled using rectangular solid elements. Because a perfectly rigid wall was assumed, it was not necessary to model the wall explicitly. Instead, the nodes on the left side of the modeled continuum were simply fixed against movement. The reinforcement (if present) was modeled using zero-thickness linear springs, which will be discussed in more detail subsequently. Not shown, because of space limitations, are the one-dimensional interface elements that were used above and below each layer of reinforcement to simulate the frictional interface between soil and reinforcement.

SSTIPNH allows for the simulation of incremental construction. In this study, the geoinclusion (if present) was placed full-height on the wall, followed by the repetitive placement of 1-ft-thick layers of retained soil and a sheet of reinforcement (if present).

Surface Surcharge

The simulated surcharge is also shown in Figure 1; it was an infinite strip load parallel to the wall that approximated a Cooper E-80 railroad loading assumed to be uniformly distributed over the bottom of an 8-ft-wide tie. In the computer simulation, this load was applied in two increments of equal magnitude.

Soil Properties

SSTIPNH allows for nonlinear stress-strain behavior of solid elements using the familiar hyperbolic model for both Young's modulus and the bulk modulus, with Poisson's ratio calculated from these two parameters. Elastoplastic one-dimensional elements are also available to model the interface between dissimilar materials. The various model parameter values used in this study were based on data from Clough and Duncan (*12*), Duncan et al. (*13*), and other sources. Values are given in Tables 1 and 2 for the soil and soil-concrete interface for the free-field case of no geoinclusion or reinforcement. To approximate the effect of soil compaction during placement, each layer was assumed to be overconsolidated with a $K_o = 1$ immediately after placement. This is not a rigorous simulation of the compaction process [see papers by Duncan and Seed (*14*) and Seed and Duncan (*15*) for thorough discussion of this topic], but it was judged to be a reasonable approximation that was within the capabilities of SSTIPNH.

Geosynthetic Properties

The geoinclusion was modeled as a linear-elastic solid. The Young's modulus was based primarily on the test data reported by Partos and Kazaniwsky (*1*). The values of the hyperbolic-model parameters used to approximate this behavior are given in Tables 3 and 4. It was assumed that the geoinclusion composite was covered with a nonwoven geotextile on the field (soil) side. The soil-nonwoven geotextile interface was modeled using one-dimensional interface elements with the values given in Tables 3 and 4. These values were based primarily on ones given by Koerner (*16*).

The three types of reinforcement evaluated [woven geotextile, polymer grid (geogrid), and steel] were each modeled as chains of linear-elastic spring elements of zero thickness using what are called nodal link elements in SSTIPNH. The nodal link spring stiffness can have a transverse component

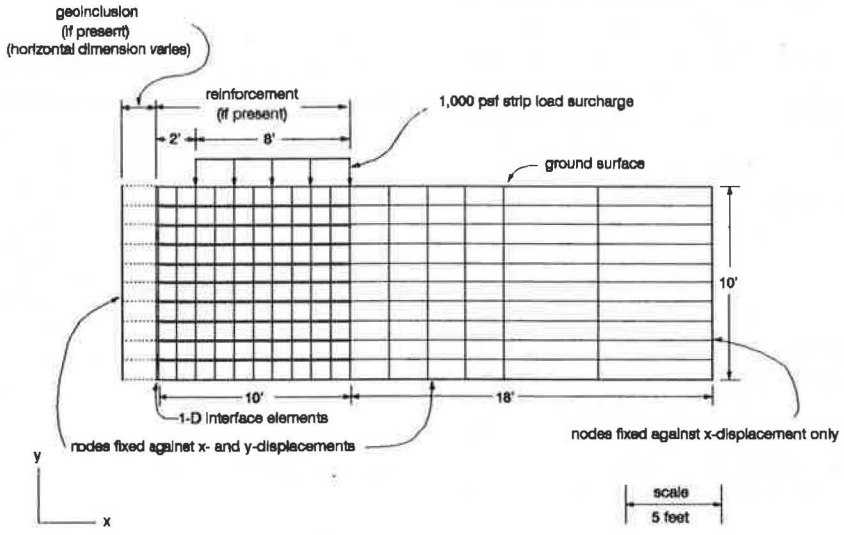

FIGURE 1 Problem geometry and finite-element mesh.

TABLE 1 SOIL AND SOIL-CONCRETE INTERFACE PROPERTIES, SOLID ELEMENTS

material	γ_t (pcf)	c (psf)	ϕ (deg)	$\Delta\phi$ (deg)	K_0	K	n	R_f	K_b	m
sand	115	0	40	0	1	1000	0.5	0.8	300	0.25

TABLE 2 SOIL AND SOIL-CONCRETE INTERFACE PROPERTIES, INTERFACE ELEMENTS

material	c_a (psf)	δ (deg)	$\Delta\delta$ (deg)	K_n	K_s	K_{sur}	n	R_f
concrete	0	32	0	$1x10^9$	$4x10^4$	$6x10^4$	1	0.9

TABLE 3 GEOINCLUSION AND SOIL-GEOSYNTHETIC INTERFACE PROPERTIES, SOLID ELEMENTS

material	γ_t (pcf)	c (psf)	ϕ (deg)	$\Delta\phi$ (deg)	K_0	K	n	R_f	K_b	m
geoinclusion	1	1	0	0	0	2.17	0	0	0.72	0

TABLE 4 GEOINCLUSION AND SOIL-GEOSYNTHETIC INTERFACE PROPERTIES, INTERFACE ELEMENTS

material	c_a (psf)	δ (deg)	$\Delta\delta$ (deg)	K_n	K_s	K_{sur}	n	R_f
nonwoven geotextile	0	36	0	$1x10^6$	$1x10^3$	$1.5x10^3$	1	0.9
woven geotextile	0	32	0	$1x10^6$	$1x10^3$	$1.5x10^3$	1	0.9
polymer geogrid	0	25	3	$1x10^6$	$1x10^3$	$1.5x10^3$	1	0.9
steel	0	40	0	$1x10^9$	$4x10^4$	$6x10^4$	1	0.9

as well as an axial (longitudinal) component. The transverse component was used in this analysis to approximate the tension that develops in reinforcement as a result of differential vertical deflection (*17*). The values used for reinforcement stiffness are given in Table 5. They were derived from typical moduli reported in the manufacturer's literature around early 1989, when this study was begun, and rounded off for simplicity. The goal here was to approximate the stiffness of generic types of reinforcement rather than duplicate specific products. It is recognized that the relative difference in stiffness between geogrids and some woven geotextiles may be less than the 10:1 ratio assumed.

The frictional interface between reinforcement and soil was modeled using one-dimensional interface elements, with separate interfaces above and below each layer of reinforcement. For the geogrid and steel, a technique suggested by Human et al. (*17*) was used to account for the fact that there is at least partial continuity of soil through the reinforcement. This was accomplished by forcing the nodes of the solid soil elements immediately above and below the reinforcement to have the same horizontal displacement. This was not done with the woven geotextile, because it was assumed to behave as an effective separator between soil above and below it. Thus, there could be relatively lateral displacement between the soil above and below the geotextile. Values for the interface-model parameters are given in Table 2; they were adapted from Koerner's (*16*) for the woven geotextile, those of Human et al. (*17*) for the geogrid, and the author's assumptions for the steel.

TABLE 5 REINFORCEMENT STIFFNESS PARAMETERS

Reinforcement	Spring Stiffness (lb/ft/ft of wall)	
	Longitudinal	Transverse
woven geotextile	2,000	1
polymer geogrid	20,000	10
steel	2,000,000	1,000

DISCUSSION OF RESULTS

General Comments

The primary results of interest discussed in this section are the stress increases on the wall caused by application of the surcharge. These results are plotted in a dimensionless form, with the vertical axis being the relative depth below the top of the wall (actual depth divided by the wall height of 10 ft) and the horizontal axis being the actual horizontal stress increase divided by the 1,000-psf vertical surcharge.

Free-Field

Initially, a "free-field" analysis was made to investigate the stresses acting on the wall in the absence of any geoinclusion or reinforcement. The increase in horizontal stress on the wall caused by the surcharge is shown in Figure 2. The results are relatively insensitive to the assumed soil-wall friction. Normally, friction effects with rigid earth-retaining structures are ignored in design practice because it is assumed that soil-wall friction cannot develop in the absence of any wall movement. However, as discussed by Horvath (*11*) and Duncan et al. (*18*), significant levels of soil-wall friction can develop as a result of even slight (fraction of 1 in.) settlement of the retained soil that will occur during the soil placement and compaction process. The rapid decrease in calculated stresses near the bottom of the wall is the result of the perfectly rough boundary condition that was assumed in the finite-element model. Also shown is the theoretical stress increased based on the usual design method of doubling the solution for a homogeneous, isotropic elastic half-space. The rationale behind this approach is discussed in detail by Tschebotarioff (*19*). The actual solution used was taken from work by Poulos and Davis (*20*). Identical results were obtained using the solution in the PILE BUCK Design Manual (*21*). The difference between calculated and theoretical results is consistent with observed behavior (*22*).

Geosynthetics

Analyses were performed using the geoinclusion alone (REP wall) as well as combined geosynthetics, that is, geoinclusion plus reinforcement (ZEP wall). The results of these analyses are summarized in Figures 3, 4, and 5, each of which shows, for a different type of reinforcement, the increase in horizontal stress on the wall caused by the surcharge, both without and with reinforcement, with the frictional free-field results for comparison. In Figure 3, the explanation of the unex-

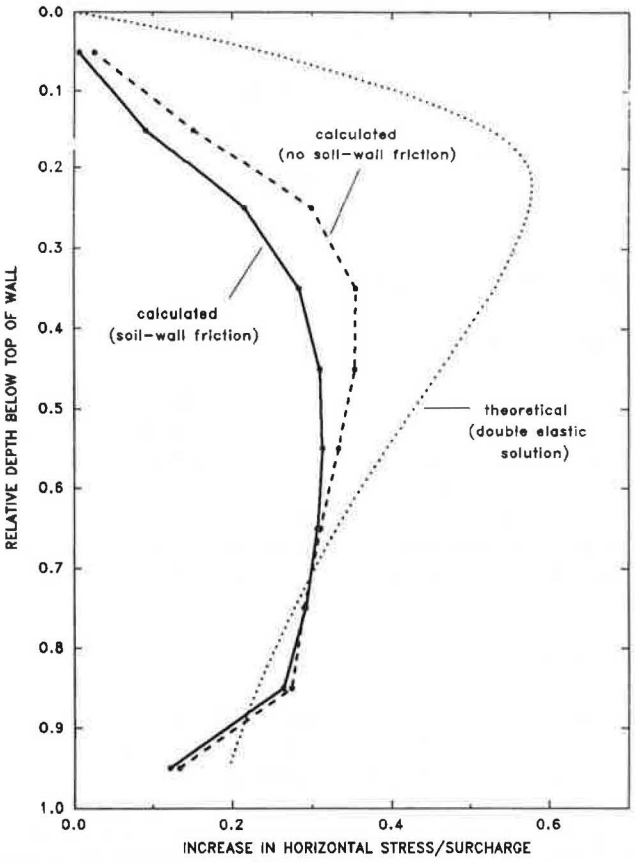

FIGURE 2 Horizontal stress increase on wall caused by surcharge under free-field conditions—no geoinclusion or reinforcement.

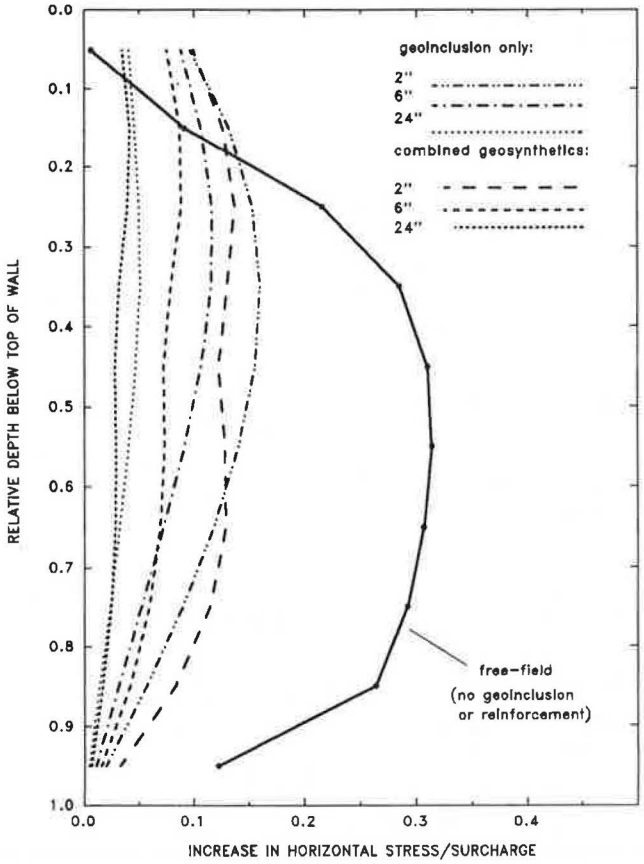

FIGURE 3 Horizontal stress increase on wall caused by surcharge—geotextile reinforcement.

pected result of slightly greater stresses near the bottom of the wall using woven geotextile reinforcement as opposed to no reinforcement is not readily apparent.

To provide some idea of the horizontal deformations that occur, the horizontal compression of the 24-in. geoinclusion for the cases studied is shown in Figure 6. Note that this shows the total compression of the geoinclusion under combined earth plus surcharge loads.

The reductions in horizontal stress increase achieved using geosynthetics are summarized in Figure 7. This shows the percentage reduction of the peak horizontal stress increase caused by the surcharge, using the frictional free-field results as the basis of comparison (i.e., 100 percent). It should be noted that the relative depth at which the peak stress occurs differs between the free-field condition and when geosynthetics are used (the depths are always shallower in the geosynthetics cases). However, the results plotted in Figure 7 do provide some insight into the effectiveness of geosynthetics in achieving stress reductions.

CONCLUSIONS

The conclusions drawn from these results are as follows:

1. The use of even a relatively thin geoinclusion alone provides a significant reduction in the increase in horizontal stress on the wall caused by the surcharge.
2. The use of woven geotextile reinforcement of the stiffness assumed provides slight improvement over the geoinclusion alone. The relative improvement would be greater for a stiffer geotextile.
3. The geogrid reinforcement produces more significant reductions in horizontal stresses than the geoinclusion alone.
4. The steel reinforcement produces dramatic reductions in the horizontal stress increase in comparison with the geoinclusion alone and effectively achieves a condition of a zero earth pressure increase.

In all cases, the trends are the same as those observed for the behavior under earth loading alone (*5*,*7*).

RECOMMENDATIONS

Applications

Potential applications of the REP- and ZEP-wall concepts to situations in which surcharge loading is involved include new construction and existing structures. In new construction, sometimes it is not desirable or economical to design the retaining structure for soil plus surcharge loads, particularly if the surcharge load might exist only for a limited time—for example, during construction that is of short duration compared with the design life of the structure.

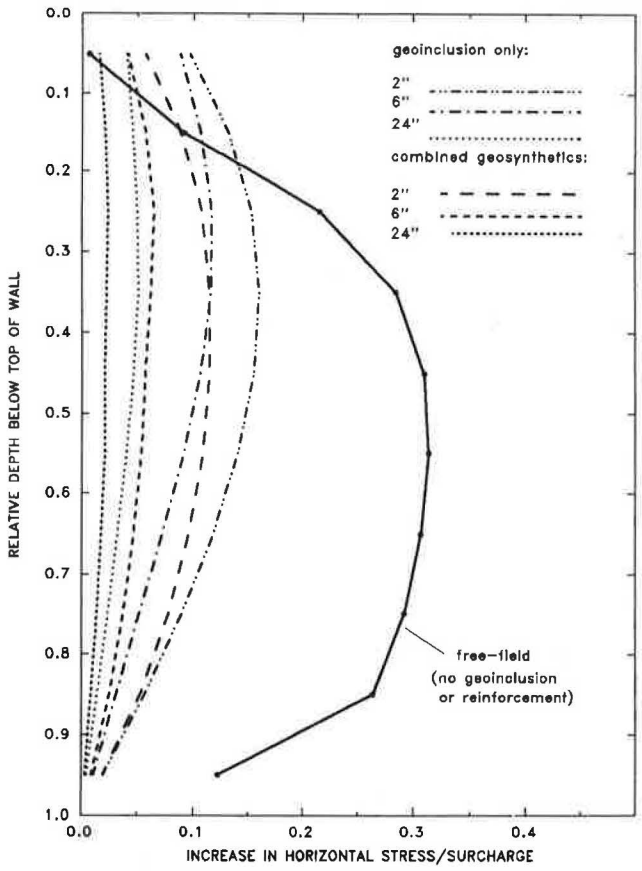

FIGURE 4 Horizontal stress increase on wall caused by surcharge—polymer geogrid reinforcement.

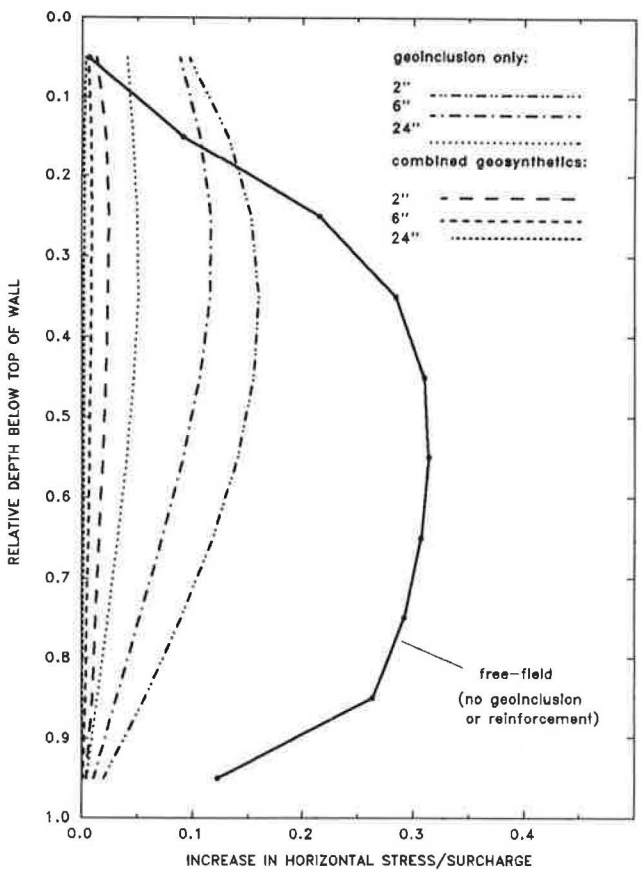

FIGURE 5 Horizontal stress increase on wall caused by surcharge—steel reinforcement.

As far as existing structures, typical situations in which a structure is subjected to surcharge stresses that exceed its allowable capacity were mentioned earlier in this paper. It may be more economical to reduce these stresses permanently using geosynthetics than to strengthen the wall structurally or replace it.

Future Study

At this point in the development of the use of geoinclusions, either large-scale model or full-scale field testing is required to verify the theoretical results presented in this paper. The primary area of investigation with regard to surcharge loading is evaluating the effect on the surcharge-induced stresses of long-term creep, modulus changes, and nonrecoverable deformation of the geosynthetics, particularly the geoinclusion, and nonrecoverable deformations of the retained soil when subjected to many cycles of live load. Testing reported by Sherif and Mackey (*22*) indicates that horizontal stresses caused by a surcharge can increase significantly after many load cycles even without geosynthetics.

SUMMARY

Numerical modeling suggests that it is possible to achieve significant, even total, reduction in surcharge-induced horizontal stresses on rigid earth-retaining structures. This is done by using either a new type of geosynthetic called a geoinclusion or a combination of geoinclusion and synthetic reinforcement of the retained soil. These are referred to as the REP- and ZEP-wall concepts, respectively. Although it appears that a geoinclusion alone will produce significant benefits, physical testing is required to investigate whether its effectiveness may be diminished as a result of nonrecoverable deformations and modulus increase after many cycles of surcharge applications that would occur in most actual installations. It may be that the use of synthetic reinforcement is necessary to sustain the effectiveness of the stress reductions. The nonrecoverable and creep deformations of polymer reinforcement (woven geotextiles and geogrids) also must be studied. However, these issues are design details and should not detract from this interesting advancement and application of geosynthetics technology.

ACKNOWLEDGMENTS

A portion of the time spent performing the research described in this paper was supported by Manhattan College under its 1990 summer grants program for faculty research. Computer hardware and software were provided by the Manhattan College Civil Engineering Department, chaired by Nicholas F. Morris, and by Horvath Engineering, P.C. The author is grateful to all concerned for this support.

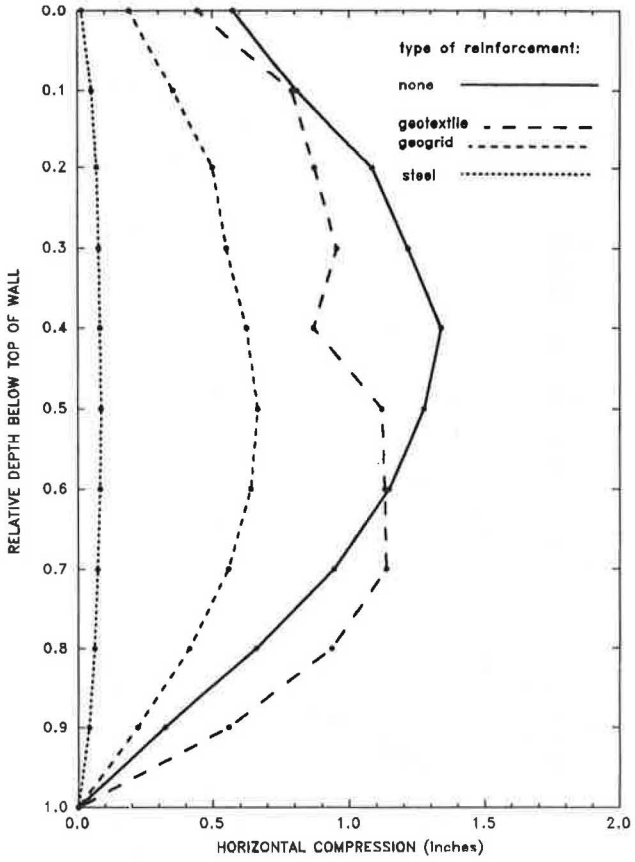

FIGURE 6 Total compression of 25-in. geoinclusion after application of surcharge.

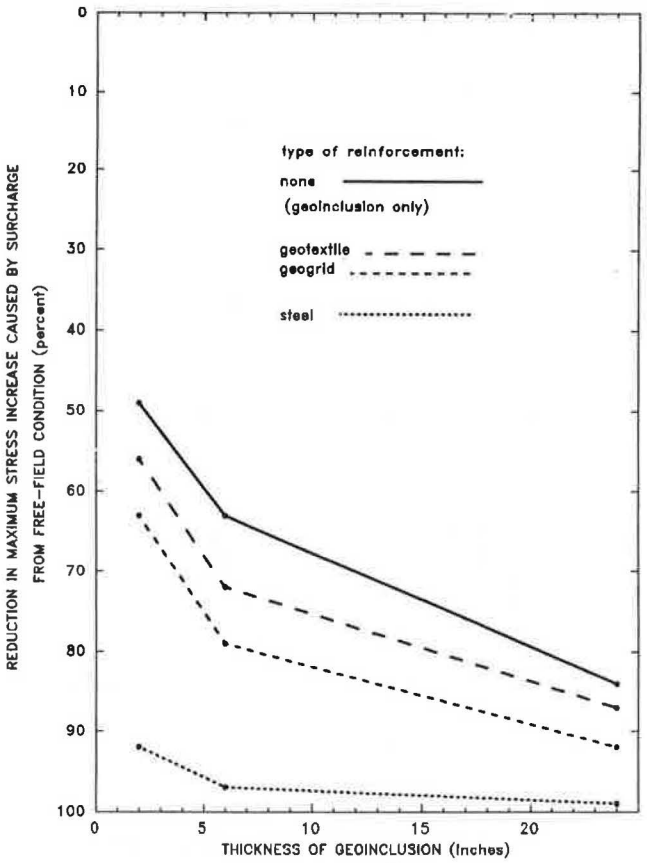

FIGURE 7 Effectiveness of geosynthetics in reducing horizontal stress increase caused by surcharge.

REFERENCES

1. A. M. Partos and P. M. Kazaniwsky. Geoboard Reduces Lateral Earth Pressures. *Proc., Geosynthetics '87*, Industrial Fabrics Association International, St. Paul, Minn., 1987, pp. 628–639.
2. J. P. Gnaedinger and S. A. Gill. Geogrid Reinforced Soil-Cement Arch Over Accelerator Ring. *Proc., Geosynthetics '91*, Industrial Fabrics Association International, St. Paul, Minn., 1991, pp. 917–933.
3. A. McGown, R. T. Murray, and K. Z. Andrawes. *Influence of Wall Yielding on Lateral Stresses in Unreinforced and Reinforced Fills*. Research Report 113. U.K. Transport and Road Research Laboratory, Crowthorne, Berkshire, 1987.
4. A. McGown, K. Z. Andrawes, and R. T. Murray. Controlled Yielding of the Lateral Boundaries of Soil Retaining Structures. In *Geosynthetics for Soil Improvement*, Geotechnical Special Publication 18, ASCE, New York, N.Y., 1988, pp. 193–210.
5. J. S. Horvath. *The Use of Geosynthetics to Reduce Lateral Earth Pressures on Rigid Walls; Phase I: Concept Evaluation*. Research Report CE/GE-90-2. Manhattan College, Bronx, N.Y., 1990.
6. K. Z. Andrawes, K. H. Loke, and K. C. Yeo. Application of Boundary Yielding Concept to Full-Scale Reinforced and Unreinforced Soil Walls. Presented at International Reinforced Soil Conference, British Geotechnical Society, Glasgow, Scotland, 1990.
7. J. S. Horvath. Using Geosynthetics to Reduce Earth Loads On Rigid Retaining Structures. *Proc., Geosynthetics '91*, Industrial Fabrics Association International, St. Paul, Minn., 1991, pp. 409–423.
8. R. Karpurapu and R. J. Bathurst. Numerical Investigation of Controlled Yielding of Soil Retaining Wall Structures. *Geotextiles and Geomembranes* (in press).
9. T. V. Edgar, J. A. Puckett, and R. B. D'Spain. Effects of Geotextiles on Lateral Pressure and Deformation in Highway Embankments. *Geotextiles and Geomembranes*, Vol. 8, No. 4, 1989, pp. 275–292.
10. *User's Guide for SSTIPN*. Virginia Polytechnic Institute and State University, Blacksburg, 1979.
11. J. S. Horvath. *A Study of Some Miscellaneous Wall Problems*. Research Report CE/GE-90-1. Manhattan College, Bronx, N.Y., 1990.
12. G. W. Clough and J. M. Duncan. Finite Element Analysis of Retaining Wall Behavior. *Journal of the Soil Mechanics and Foundations Division*, ASCE, Vol. 97, No. 12, Dec. 1971, pp. 1,657–1,673.
13. J. M. Duncan, P. Byrne, K. S. Wong, and P. Mabry. *Strength, Stress-Strain and Bulk Modulus Parameters for Finite Element Analyses of Stresses and Movements in Soil Masses*. Report UCB/GT/80-01. University of California, Berkeley, 1980.
14. J. M. Duncan and R. B. Seed. Compaction-Induced Earth Pressures Under K_o-Conditions. *Journal of the Geotechnical Engineering Division*, ASCE, Vol. 112, No. 1, Jan. 1986, pp. 1–22.
15. R. B. Seed and J. M. Duncan. FE Analyses: Compaction-Induced Stresses and Deformations. *Journal of the Geotechnical Engineering Division*, ASCE, Vol. 112, No. 1, Jan. 1986, pp. 23–43.
16. R. M. Koerner. *Designing with Geosynthetics*, 1st ed. Prentice-Hall, Englewood Cliffs, N.J., 1986.

17. C. A. Human, R. B. Seed, J. K. Mitchell, and R. I. Borja. Predicted Behavior of the Stanstead Abbotts Trial Embankment. *Proc., Prediction Symposium on a Reinforced Embankment on Soft Ground*, King's College, London, England, 1986.
18. J. M. Duncan, G. W. Clough, and R. M. Ebeling. Behavior and Design of Gravity Earth Retaining Structures. *Proc., Conference on Design and Performance of Earth Retaining Structures*, Geotechnical Special Publication 25, ASCE, 1990, pp. 251–277.
19. G. P. Tschebotarioff. *Foundations, Retaining and Earth Structures: The Art of Design and Construction and Its Scientific Basis in Soil Mechanics*. McGraw-Hill, New York, N.Y., 1973.
20. H. G. Poulos and E. H. Davis. *Elastic Solutions for Soil and Rock Mechanics*. John Wiley & Sons, New York, N.Y., 1974.
21. *PILE BUCK™ Steel Sheet Piling Design Manual*. Pile Buck, Inc., Jupiter, Fla., 1987.
22. M. M. Sherif and R. D. Mackey. Pressures on Retaining Walls with Repeated Loading. *Journal of the Geotechnical Engineering Division*, ASCE, Vol. 103, No. 11, Nov. 1977, pp. 1,341–1,345.

Publication of this paper sponsored by Committee on Mechanics of Earth Masses and Layered Systems.

Failure of Cohesionless Model Slopes Reinforced with Flexible and Extensible Inclusions

DOV LESHCHINSKY AND GREG LAMBERT

The objectives of the reported work were (a) to identify the failure surfaces developing in geosynthetically reinforced steep slopes and (b) to compare the observed critical results with those predicted by a limit equilibrium analysis. Failure surfaces were induced through all reinforcing strips (i.e., internal failure) by the backfill self-weight in 60-, 75-, and 90-degree small-scale slopes. The backfill material consisted of an assembly of steel pins, which exhibited a constant internal angle of friction of 37.4 degrees under stresses in the models. Its performance corresponded to plane strain conditions, and its uniform geometry enabled one to construct slopes repeatedly with ease and to nearly perfect specifications. The reinforcement material used was aluminum foil having a tensile modulus and elongation at failure that are typical of values specified for geosynthetics in design. All slip surfaces initiated at the lowest reinforcement layer and rapidly propagated upward. For 90-degree slopes, the slip surface appeared to be nearly planar, whereas for flatter slopes, it was curved. The test results were compared with predictions by a rigorous limit equilibrium analysis that uses a log spiral failure surface. The analysis indicates that this surface degenerates to a plane for 90-degree slopes. When the reinforcement's tensile force is assumed to be orthogonal to the radius vector defining it rather than to remain horizontal as installed, the predictions of the analysis correspond better to the test results in terms of both trace of slip surface and collapse height. Generally, it appears that the limit equilibrium analysis reasonably predicts the critical conditions for cohesionless slopes reinforced with extensible inclusions.

Geosynthetically reinforced steep slopes are increasingly being constructed because of their cost-effectiveness. In the design of reinforced slopes, the required tensile resistance and the layout of the geosynthetic sheets must be specified. This is typically done by using a limit equilibrium analysis that has been modified to deal with the reinforcement effects. However, because there are rarely fully documented failures due to the internal collapse of a geosynthetically reinforced earth structure, the predictive potential of this analysis has not yet been extensively assessed. If the predictive capacity of a limit equilibrium analysis is to be properly evaluated, it should be compared with a case in which the state of global collapse is just about to occur (i.e., a slope in which all failure-resisting strengths are fully mobilized having a safety factor of 1). Specifically, the predicted location of the slip surface and the reinforcement's required tensile resistance should be compared at the verge of failure.

D. Leshchinsky, Department of Civil Engineering, University of Delaware, 130 Du Pont Hall, Newark, Del. 19716. G. Lambert, U. S. Army Corps of Engineers, Custom House, Second and Chestnut Streets, Philadelphia, Pa. 19106.

This paper attempts to provide much-needed experimental data for reinforced steep slopes founded on a firm foundation at the onset of failure. It also compares the predictions of a typical, but rigorous, limit equilibrium analysis with these experimental results, considering two extreme values for the inclination of tensile resistance. For reasons detailed in the paper, however, aluminum foil, rather than geosynthetics, is used. This reinforcement behaves as an extensible material, thus exhibiting structural response comparable with that of geosynthetically reinforced slopes without the overcomplications of factors such as creep that may introduce an element of speculation when the results are interpreted for comparison with limit equilibrium analysis predictions.

TEST PROCEDURE

Testing Facilities

Model Frame

The frame supporting the model was assembled of steel channel 125 mm wide (Figure 1). The base and height of the frame measured 1 m each. An additional steel channel 125 mm wide supported the slope facing during construction. This support was hinged at the top of the frame and could rotate outward by the use of a screw jack. The entire frame was placed in a special steel fixture so that the facing and its support could be inclined at any angle. When the frame was rotated in the fixture, a section of steel channel was positioned at the base to ensure a horizontal foundation (i.e., base) in the model, as would be expected in the case of an embankment over a firm foundation. Steel pins were used as the backfill material, so no side panels were necessary for support. Subsequently, end effects typical to soil backfill were avoided.

Facing

The slope facing was made of smooth Plexiglas panels, as shown in the inset in Figure 1. Two triangular wedges were glued to the outer side of each panel. These wedges rested against the steel channel support during construction (see Figure 1), producing a terraced slope with a desired average inclination. When a 90-degree slope was constructed, no wedge supports were used. The need to use a "stepped" slope face

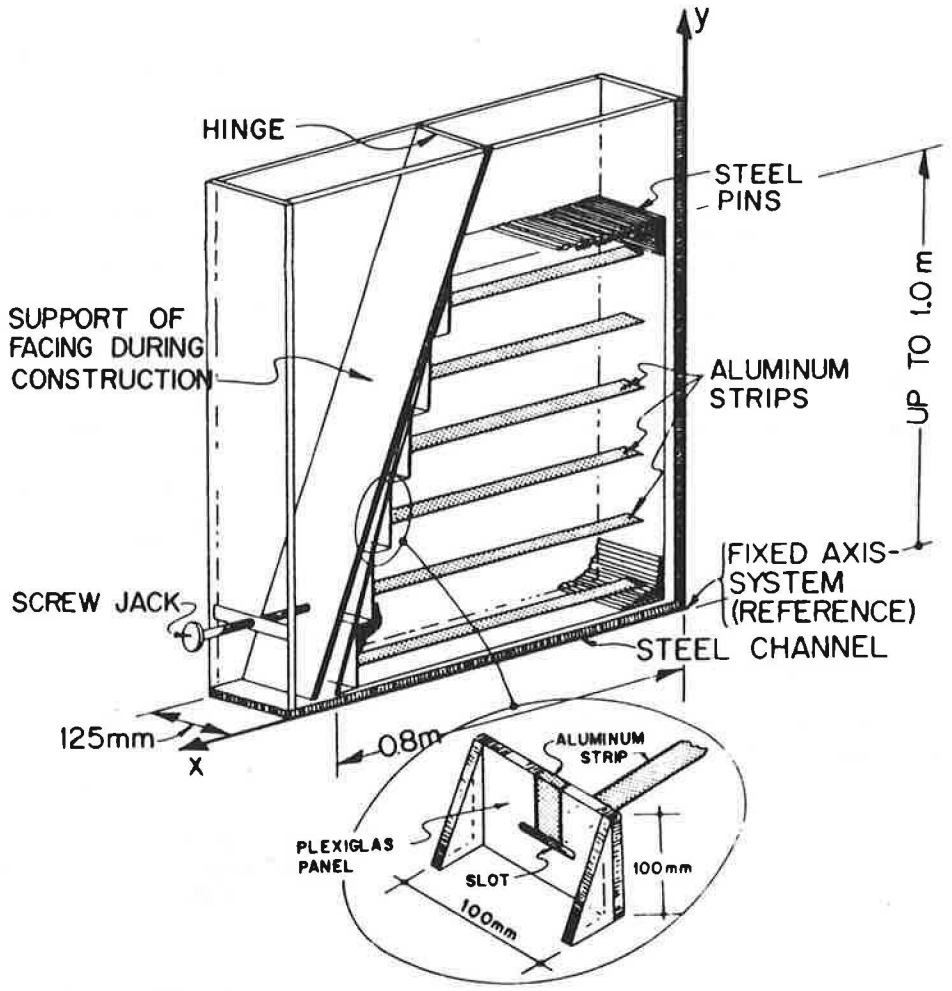

FIGURE 1 Model setup.

rather than a smooth one was recognized when the backfill material could not be placed in a uniform density immediately behind the facings when nonvertical slopes were constructed.

Materials

Flexible Inclusions

Ideally, geosynthetics would have been used directly in the experiments. However, reduction of data to verify analysis corresponding to a limit state requires the consideration of such complicated factors as creep and effects of overburden pressure on geosynthetics response. Furthermore, inducing failure in small-scale models requires the use of geosynthetics that have unrealistically low strength and stiffness factors that may complicate the interpretation of results. To avoid such uncertainties, an aluminum foil was used as a reasonable substitute for geosynthetics. Manufactured by Reynolds Metal Company, it was made of Alloy 8111 and had a thickness of 23.9 ± 5 percent μm, an ultimate tensile strength per unit width of 2.06 ± 8 percent kN/m, and an elongation at failure of 5.5 to 6.25 percent. This elongation classifies the foil as extensible reinforcement (*1*), having the same order as a typical permissible value in design when geosynthetics are used (i.e., to develop such strain in the reinforcement that the soil will most likely reach failure with a complete slip surface extending between crest and toe). In fact, using Young's modulus of aluminum (70×10^6 to 75×10^6 kPa), the thickness of the foil, and the widths of strips relative to the net breadth of the tested slopes (102 mm), one can calculate the equivalent tensile modulus of the foil in the elastic range (i.e., similar to the wide-width modulus defined in ASTM D 4595: the tensile force at a given strain divided by the specimen's width) to be about 200 to 800 kN/m, depending on the width of the strip in each test (see results with Figures 2–10 and Table 1 for widths used). This range of tensile modulus pertains to an equivalent material, such as geosynthetic sheets, that has continuous width rather than to strips narrower than the backfill breadth of 102 mm. This range falls well within typical values for geosynthetics used for reinforcement. Hence, in terms of stiffness, the aluminum foil in its elastic range can generally be considered as a reasonable model for geosynthetics.

A sharp knife was used to cut the aluminum foil strips, and metal templates were used to ensure a consistent and precise width and therefore attain an exact prescribed tensile strength. Special care was taken to avoid any small tears and creases

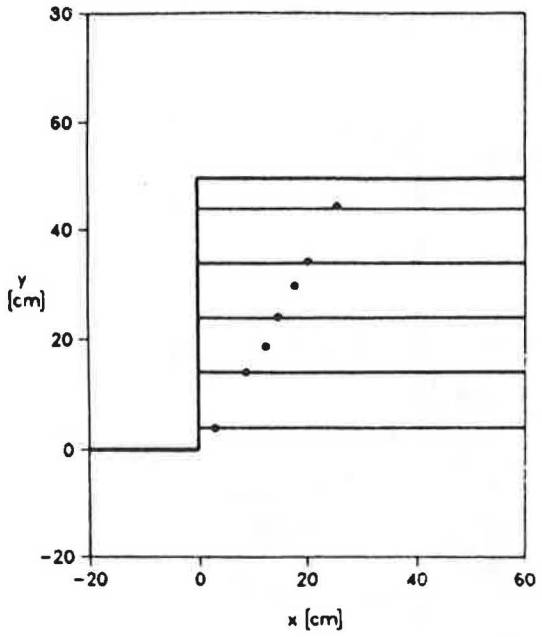

FIGURE 2 Data points defining slip surface for 90-degree slope: failure height = 49.7 cm; five reinforcement strips.

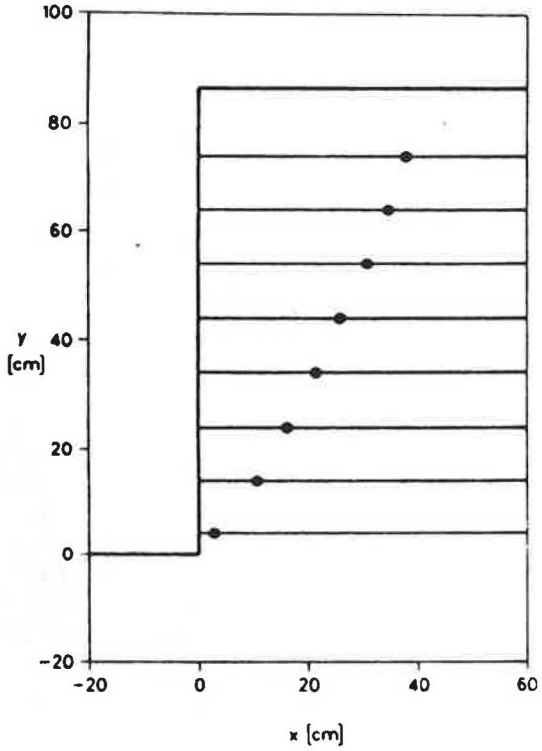

FIGURE 4 Data points defining slip surface for 90-degree slope: failure height = 86.5 cm; eight reinforcement strips.

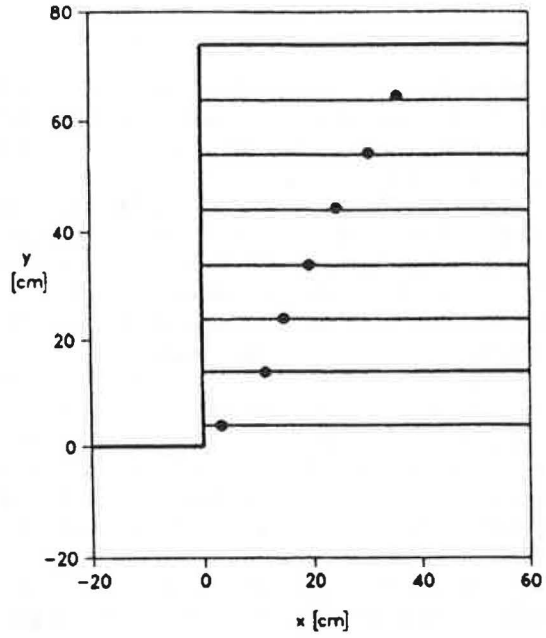

FIGURE 3 Data points defining slip surface for 90-degree slope: failure height = 74.0 cm; seven reinforcement strips.

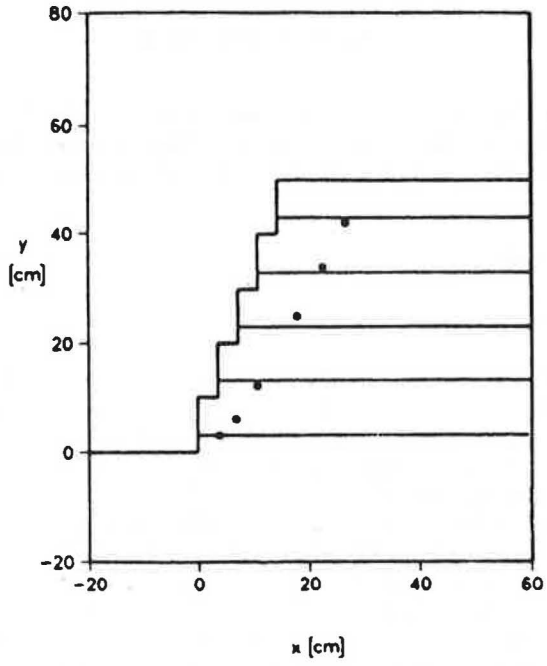

FIGURE 5 Data points defining slip surface for 75-degree slope: failure height = 50.0 cm; five reinforcement strips.

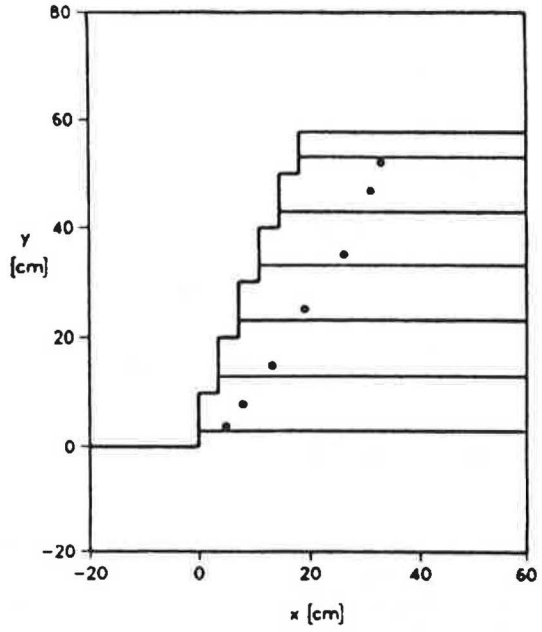

FIGURE 6 Data points defining slip surface for 75-degree slope: failure height = 57.7 cm; six reinforcement strips.

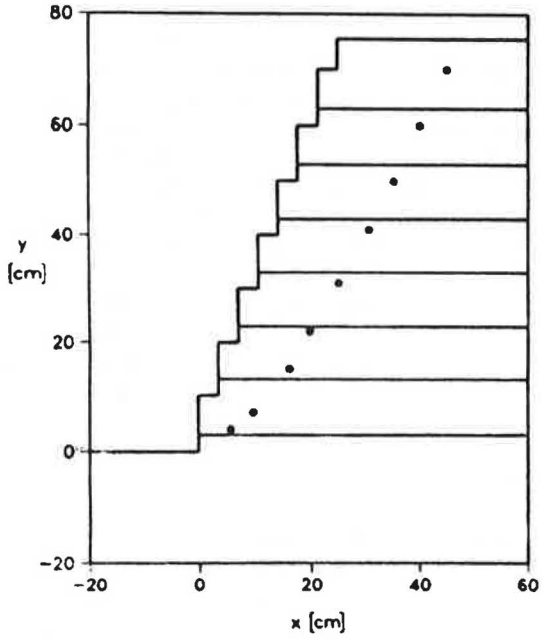

FIGURE 7 Data points defining slip surface for 75-degree slope: failure height = 75.5 cm; seven reinforcement strips.

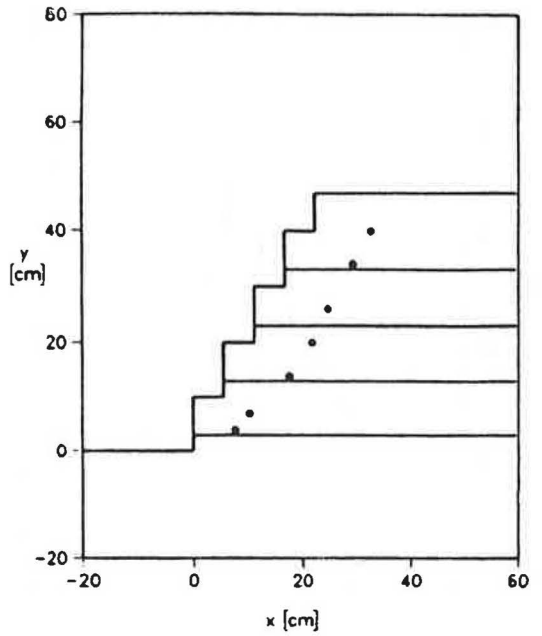

FIGURE 8 Data points defining slip surface for 60-degree slope: failure height = 47.0 cm; four reinforcement strips.

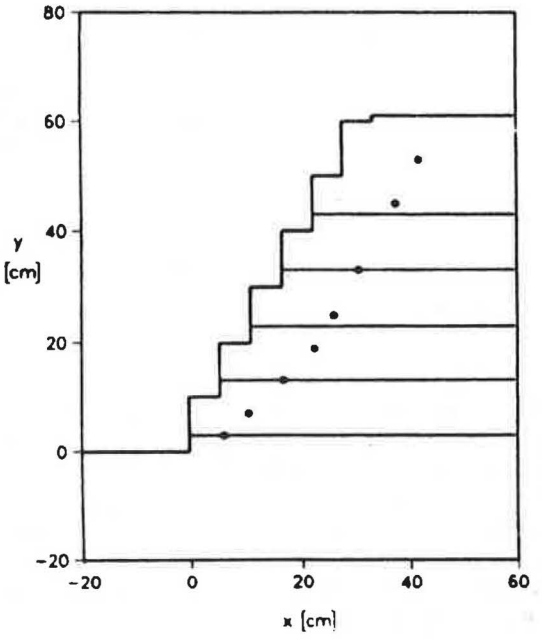

FIGURE 9 Data points defining slip surface for 60-degree slope: failure height = 61.0 cm; five reinforcement strips.

that might locally decrease the strength and cause premature and unexplained (i.e., inconsistent) failure.

Backfill

Steel pins 3.18 mm in diameter and 102 mm long were used as backfill in all experiments. The assembly of steel pins is known as the Schneebeli model (*2*). The shear behavior of this assembly resembles that of a dense cohesionless soil under plane strain conditions. The peak angle of internal friction, as determined from direct shear tests under normal stresses up to 40 kPa, was $\phi = 37.4$ degrees. It should be noted that the direct shear data points defined a nearly perfect straight-line envelope passing through the origin. This is unlike cohesionless soils, which typically exhibit much higher ϕ under

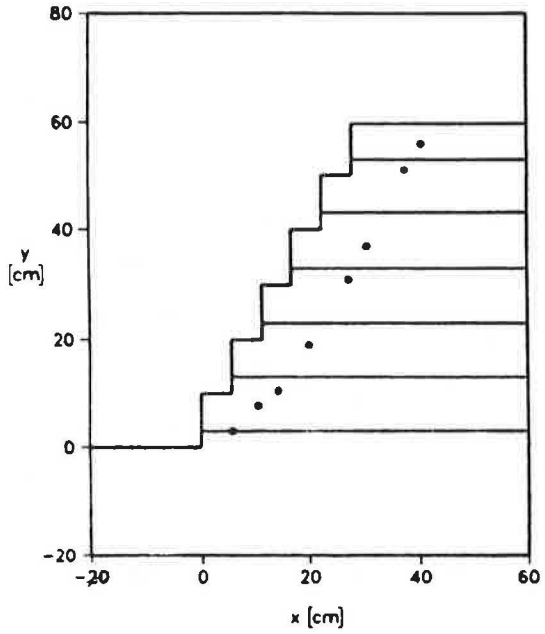

FIGURE 10 Data points defining slip surface for 60-degree slope: failure height = 59.8 cm; six reinforcement strips.

TABLE 1 VALUES FOR FIGURES 2–10

Figure	w (cm)	t (kN/m)	y_1 (cm)
2	3.02	0.615	4.0
3	4.62	0.942	4.0
4	5.72	1.164	4.0
5	2.01	0.412	3.0
6	2.46	0.502	3.0
7	3.33	0.677	3.0
8	1.14	0.233	3.0
9	1.63	0.332	3.0
10	1.47	0.300	3.0

NOTE: Values for t are ±8 percent.

low normal stress. Consequently, interpretation of results obtained from tests on small-scale models using steel pins in the context of limit equilibrium (i.e., at failure where ϕ is a prime input) is simple compared with cohesionless small-scale soil models, if one is to extrapolate results to realistic structures.

A preliminary verification of the suitability of the steel-pin assembly to model soil in studying failure mechanisms was conducted. Two unreinforced walls were constructed to failure, using the frame shown in Figure 1, to determine whether the resulting failure surfaces corresponded to those predicted by Rankine's theory (i.e., 45 degrees + $\phi/2$). To comply closely with Rankine's assumptions, the vertical wall facing was greased and then covered by a layer of latex membrane to minimize interface friction. Once the backfill was placed to a desired height, the hinged support constituting the wall facing was rotated outward using the screw jack shown in Figure 1 until a clearly visible slip surface developed. The coordinates of points on the trace of the slip surface were measured relative to a fixed axis system defined by the testing frame shown in Figure 1. Figure 11 presents the results, showing a nearly perfect agreement with Rankine's surface. Because the validity of Rankine's surface for unreinforced walls

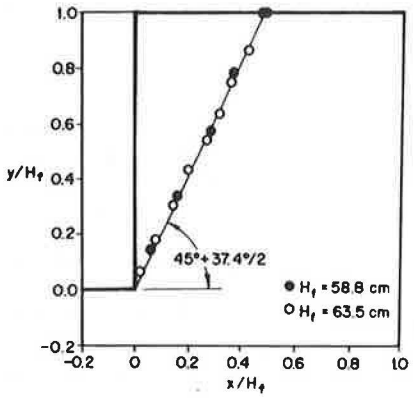

FIGURE 11 Failure surface developed in unreinforced wall.

is well established, it was believed that although the steel-pin assembly represents an idealized material, it can be used as an adequate substitute for cohesionless soils in the investigation of slip surfaces, especially in conjunction with a simple limit state analysis.

Attaining a uniform and consistent bulk density throughout each model required minimal effort because of the uniformity of the pins. The bulk density of the steel-pin assembly was $\gamma = 63$ kN/m^3 in all tests. This γ is three or four times the density of a typical backfill soil. Thus, a slope constructed to a height of 1 m using the steel pins would effectively simulate pressures existing in a 3- to 4-m prototype soil slope.

It should be pointed out that limit equilibrium analyses used in designing reinforced slopes are two-dimensional. Subsequently, experimental verification of these analyses requires essentially plane strain conditions in the tested models if one is to draw safe conclusions about the analyses. Using this steel-pin assembly ensures the existence of plane strain conditions because no sidewalls were necessary to support this backfill. Such ideal conditions are difficult to attain when soil is used in small-scale and narrow models because of the end effects of the model box sidewalls containing the soil.

Construction of Model

The first facing panel was wedged against the support shown in Figure 1. Steel pins were then placed in thin layers up to the elevation of the first aluminum strip. The strip was placed down on the pins' leveled surface to the end of the frame structure. Additional steel pins were placed gently on the aluminum strip up to the same level as the top of the panel (i.e., step). To release the facing support without jerking the system, the screw jack was turned, thus allowing the reinforced layer to carry the load and deformations to develop fully. Next, the facing support was adjusted so that it just touched the top of the panel, and construction of the second layer proceeded similarly to the first step. The same procedure was repeated for each additional layer, as Figure 12 shows for the third and fourth layers.

After attaining the height at which the factor of safety was presumably slightly larger than 1, the facing support (now supporting only the top panel) was moved slightly outward

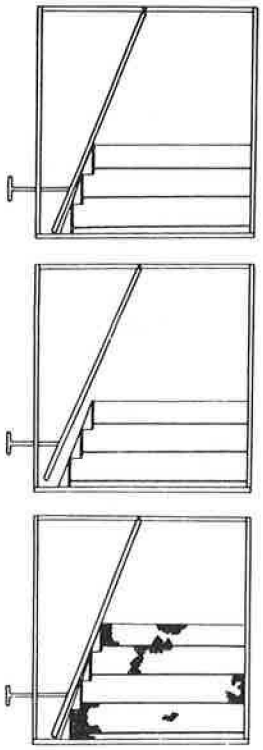

FIGURE 12 Construction sequence: *top*, completion of third layer; *middle*, release of facing support; *bottom*, construction of fourth layer.

to allow the structure to be completely self-supporting. More steel pins were then laid carefully and evenly in thin layers on top until failure. Failure occurred with the breakage of the lower aluminum strips after some visibly significant deformations developed at the lower zone. The clearly defined trace of failure surface and the final height of the backfill were recorded. Because the facing support was only a few millimeters from the slope face at the instant of failure, the collapsed structure leaned against this support. Subsequently, it prevented any significant postfailure propagation of slip surface. This postfailure stabilization "froze" the slip surface that had developed at the onset of failure. Thus, the failure of interest in design and in the framework of limit equilibrium could be traced. It should be pointed out that if failure had been allowed to propagate, the trivial case of a slope at its angle of repose would have been attained.

RESULTS

Three tests were performed for each slope inclined at 60, 75, and 90 degrees to establish a consistent characteristic behavior representing a variety of numbers of reinforcing strips and therefore a variety of tensile strengths. Because of intentional excessive embedment length of reinforcement, failure was always due to reinforcement breakage rather than to pullout. In all tests the lowest aluminum strip broke first, instigating a sudden collapse of the structure. The failure surface initiated at the location of breakage of the lowest strip and immediately propagated upward to form a surface extending between the crest and the toe.

It should be pointed out that the tensile force distribution along each reinforcing strip was not measured, although such information would have been useful. This measurement was not done because it was believed that (a) loads mobilized in the strips before failure are too small, especially in upper layers, to be measured accurately using inexpensive techniques; (b) common and inexpensive load-measuring devices (typically a calibrated strain gage) may locally alter the strip properties, including stiffness and strength, potentially affecting the model performance; and (c) wiring required to monitor the sensors may introduce additional reinforcement, also affecting the small-scale structure performance.

To facilitate the presentation of results, the following notation is introduced:

w = width of each aluminum strip (mm);
t = [(ultimate tensile strength of aluminum foil = 2.06 kN/m) × w/(breadth of tested slope = 102 mm)] = tensile strength per unit width of an equivalent reinforcing sheet that is continuously wide (as typically specified for geosynthetics; e.g., ASTM D 4595), equivalent to the strength of the aluminum strip used in the test, which had a width of w;
y_1 = elevation of lowest strip, measured relative to the toe;
d = spacing between two adjacent strips;
n = number of equally spaced strips; and
H_f = measured failure height of slope.

Figures 2–10 represent the results obtained for the 90-, 75-, and 60-degree slopes. In all figures, the strip elevations, the slope facing, and the crest elevation at the actual failure height are illustrated. In all figures, d is 10.0 cm; the rest of the information pertinent to the reinforcement is given in Table 1. Points defining the trace of the slip surface, recorded immediately after collapse, are superimposed on the figures.

It should be pointed out that attempts to conduct tests on 45-degree slopes (ϕ = 37.4 degrees) were unsuccessful mainly because the required w (or, alternatively, t), considering the maximum feasible height of slope possible to attain with the testing frame (i.e., less than 1 m for 45-degree inclination), was too narrow to be cut accurately and provide reliable results.

COMPARISON OF ANALYSIS WITH TEST RESULTS

An objective of this work was to compare the results of the experimental work with the predictions of a rigorous limit equilibrium analysis. It was convenient and instructive to use the analysis of Leshchinsky and Boedeker (*3*). Considering the measured (i.e., the nonspeculative) data, the comparison is limited to the location of slip surface and the height of the slope at failure.

Leshchinsky and Boedeker used a log spiral failure mechanism to obtain the minimum factor of safety for the reinforced structure while satisfying all three global limiting equi-

librium equations. In their analysis (termed "internal stability"), it was implicitly assumed that the critical slip surface is passing through all sheets on the basis of the tieback analogy. Furthermore, it was explicitly assumed that at the verge of failure the distribution of tensile resistance mobilized is linear with depth, proportional to the overburden pressure, with a maximum value at the toe elevation and, if no surcharge is applied, zero at the crest. Although their formulation was presented in a framework of pullout mode of failure, the final layout of the reinforcement, considering external stability and practical constraints that lead to specification of sheets of equal length, is such that breakage of lower layers due to excessive embedment occurs at failure, as was imposed on the models tested here. Leshchinsky and Boedeker considered two possible extreme inclinations of the reinforcement's tensile resistance force at the slip surface: horizontal (i.e., as installed) and orthogonal to the radius vector of the log spiral (i.e., the most efficient contribution). Figures 13–16 show typical distributions of tensile resistance for the critical cases of horizontal and orthogonal reinforcement force inclinations. Leshchinsky and Perry (*4*) provide a physical explanation of how the reinforcement can reorient itself in the orthogonal direction, as well as show explicitly the simple governing equations obtained for vertical slopes in which case the log spiral degenerates to a plane. Leshchinsky and his colleagues have concluded that for cohesionless soils, the required tensile resistance for the horizontal case is slightly larger than for the orthogonal one (typically less than 10 percent difference). However, the required embedment length for the orthogonal case is longer; somewhat deeper slip surfaces are predicted. Subsequently, the information provided by the experimental work reported here should be useful for studying the extent of slip surfaces as well as critical heights of steep slopes. Note that critical slope height is directly related to the available tensile strength

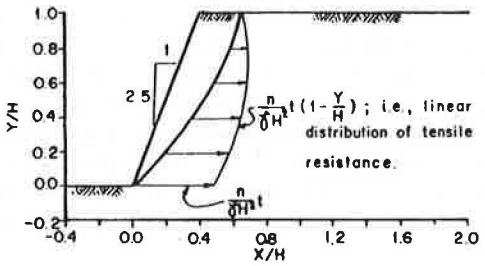

FIGURE 13 Calculated horizontal tensile force distribution, ϕ = 40 degrees.

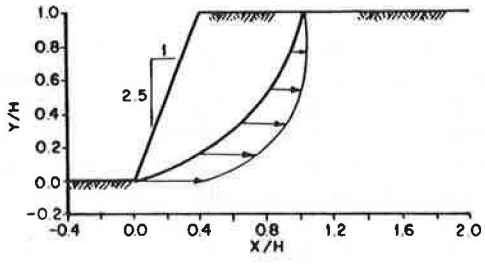

FIGURE 14 Calculated horizontal tensile force distribution, ϕ = 15 degrees.

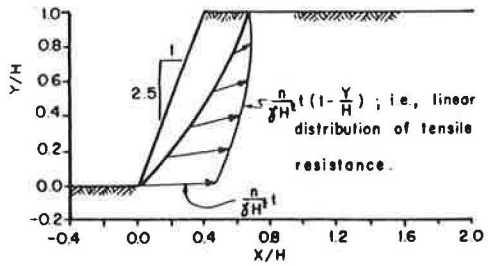

FIGURE 15 Calculated orthogonal tensile force distribution, ϕ = 40 degrees.

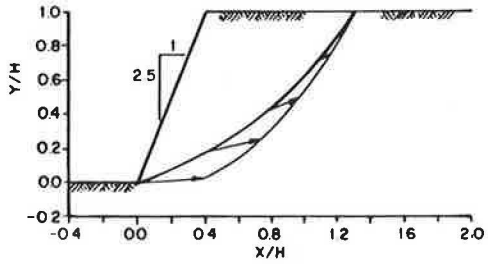

FIGURE 16 Calculated orthogonal tensile force distribution, ϕ = 15 degrees.

of the reinforcement when the factor of safety is unity. To provide an accurate comparison of results, Lambert (*5*) modified the original formulation to deal with a stepped slope face, simulating the models tested.

Figure 17 shows the trace of the predicted slip surface for the 90-degree slope and for the assumed horizontal and orthogonal inclinations of the reinforcement tensile resistance. Superimposed on this figure are the experimental data points shown also in Figures 2–4. To condense the results presentation, the axes are normalized, that is, x/H and y/H are introduced. In each respective test, the measured H_f was used instead of H in the normalization. In the analytically predicted surface, H_{cr} was used instead of H where H_{cr} represents the predicted collapse height. Similarly to Figure 17, Figures 18 and 19 represent the predicted versus the measured surfaces for the 75- and 60-degree slopes, respectively.

Figure 20 shows the actual failure heights versus the predicted ones for the horizontal case; Figure 21 shows them for the orthogonal case. Note in these figures that if a data point lies on a 45-degree line passing through the origin, the prediction is perfect. However, if this point lies above the line, the predicted failure height is lower than actual (i.e., conservative prediction). Conversely, if it is below, the predicted failure height is higher than actual. Also note that the predicted height is signified by a range of values accounting for potential manufacturing variability in tensile strength of the aluminum foil (i.e., ± 8 percent). Table 2 summarizes the results of the actual and predicted failure heights for all models tested and provides pertinent information about each test.

From this comparison, it appears that the predicted slip surfaces for the orthogonal case are closer to the observed ones, especially when steeper slopes are considered. Because in practice the reinforcement embedment length is determined by the location of potential slip surfaces, the results

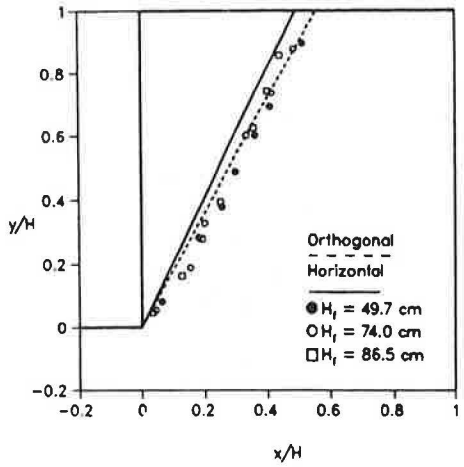

FIGURE 17 Predicted and measured slip surface, 90-degree slope (*3*).

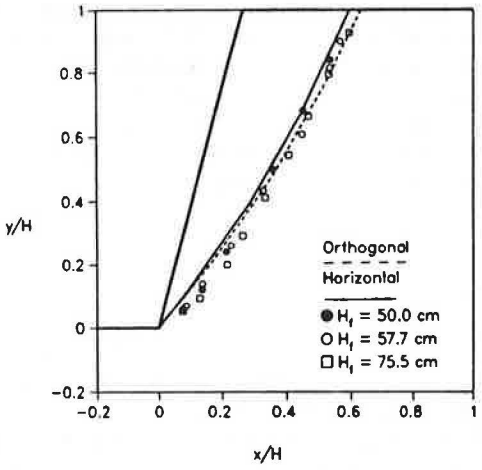

FIGURE 18 Predicted and measured slip surface, 75-degree slope (*3*).

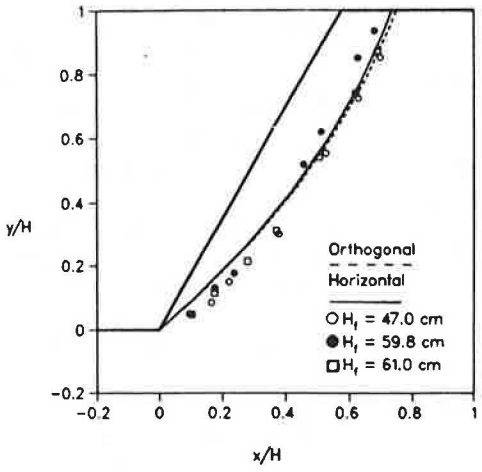

FIGURE 19 Predicted and measured slip surface, 60-degree slope (*3*).

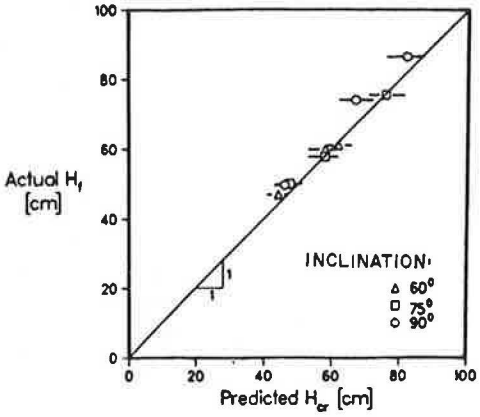

FIGURE 20 Predicted versus actual failure heights, horizontal tensile force.

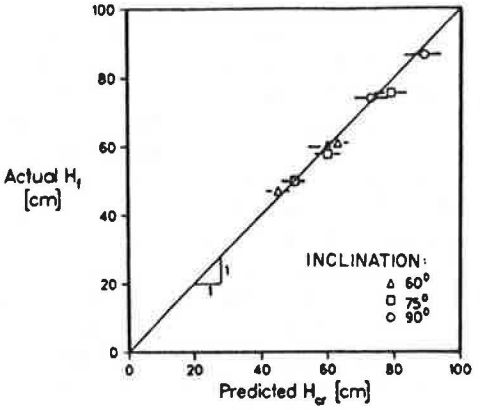

FIGURE 21 Predicted versus actual failure heights, orthogonal tensile force.

reported here suggest that in design this length should be determined using orthogonal inclination of tensile force in the stability analysis. Furthermore, the analysis using orthogonal inclination accurately predicts the range of failure heights whereas the horizontal case slightly underestimates it (i.e., it is slightly conservative with respect to tensile strength).

Although an assembly of steel pins resembles the shear behavior of a granular soil under plane strain conditions and although its behavior in modeling the Rankine's wedge in retaining walls is satisfactory (Figure 11), there is a question as to its suitability for simulating the failure mechanism of geosynthetically reinforced earth structures, especially when aluminum foil is used as a substitute. Unfortunately, relevant published information about internal failures of large-scale (or even small-scale) geosynthetically reinforced steep slopes—those less than 90 degrees—is, at best, limited. Therefore, full comparison of model performance is not possible now. However, good-quality data for large-scale geogrid-reinforced walls at failure were generated by Bathurst et al. (*6*) and Bathurst and Benjamin (*7*). Figure 22 shows data points along the trace of the slip surface as measured by Bathurst and

TABLE 2 SUMMARY OF ACTUAL AND PREDICTED FAILURE HEIGHTS

Test #	Slope	Reinforcement Strength, t (kN/m)	1st Sheet Elevation, $y(cm)$	Total Number of Sheets n	Spacing d(cm)	Failure Height, H_f (cm)	Predicted Failure Height H_{cr} (cm)	
							Orthogonal	Horizontal
1	90°	0.615(± 8%)	4.0	5	10.0	49.7	50.0(46.0,53.0)(*)	46.0(43.0,49.0)(*)
2	90°	0.942(± 8%)	4.0	7	10.0	74.0	73.0(68.0,78.0)	67.0(62.0,72.0)
3	90°	1.164(± 8%)	4.0	8	10.0	86.5	89.0(83.0,94.0)	82.0(76.0,87.0)
4	75°	0.412(± 8%)	3.0	5	10.0	50.0	50.0(46.0,53.5)	47.5(44.0,51.0)
5	75°	0.502(± 8%)	3.0	6	10.0	57.7	60.0(56.0,64.0)	58.0(53.0,62.0)
6	75°	0.677(± 8%)	3.0	7	10.0	75.5	79.0(74.0,84.0)	76.0(72.0,81.5)
7	60°	0.233(± 8%)	3.0	4	10.0	47.0	45.0(41.5,48.5)	44.0(41.0,47.0)
8	60°	0.332(± 8%)	3.0	5	10.0	61.0	63.0(59.0,66.5)	62.0(58.0,66.0)
9	60°	0.300(± 8%)	3.0	6	10.0	59.8	60.0(54.0,63.5)	58.0(53.0,62.0)

(*) First number in parentheses corresponds to (t − 8%).
Second number in parentheses corresponds to (t + 8%).

Benjamin (*7*). When comparing these points with the results obtained in this work (Figure 17), one sees a similar trend: the actual slip surface is better described by the orthogonal case. Because ϕ in Figure 17 (37.4 degrees) and Figure 22 (53 degrees) was different, a direct comparison of measured data points, in a normalized style similar to Figure 17, is not possible. However, this consistency in trend of failure surface exhibited when referenced to the same analysis is encouraging and, it is hoped, increases the confidence in this work's observations as applied to geosynthetically reinforced steep slopes.

It should be pointed out that although Bathurst and Benjamin report the strain distribution developing in the geogrid sheets at the verge of failure, the authors do not have sufficient information to convert these data to the corresponding tensile force distribution (e.g., reported strains include a significant component of creep and the strains intensity signifies highly nonlinear behavior for which their reported secant modulus is not applicable). Subsequently, full comparison is not possible. However, a comparison of similar nature has been conducted by Leshchinsky and Perry (*4*) with Bathurst et al. (*6*) showing closer agreement between the orthogonal case and experimental results with regard to tensile force distribution (or, alternatively, collapse height).

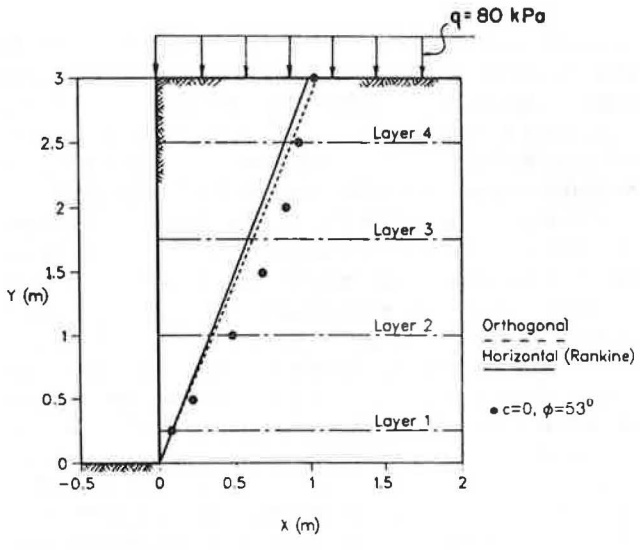

FIGURE 22 Predicted versus actual full-scale test results, slip surfaces (*3,7*).

CONCLUSIONS

The results of an experimental study on the failure surfaces developing in reinforced cohesionless slopes are presented. An assembly of steel pins was used as a two-dimensional model for granular soil. The internal angle of friction of this assembly is nearly constant and independent of confining pressures, thus simplifying interpretation of results and making it suitable for small-scale models, especially if the performance is to be compared with the predictions of a limit equilibrium analysis in which this angle is a prime input. Aluminum foil was used as reinforcement. This foil is extensible and can be considered as a reasonable substitute for geosynthetics in the small-scale models. For 90-degree slopes, the slip surface exhibits a similar trend to the one obtained from a full-scale test on a wall reinforced with a geogrid. This is a positive indication about the relevance of the tested models. The observed slip surfaces were curved for nonvertical slopes and nearly planar for the 90-degree slope.

The test results were compared with predictions by a typical limit equilibrium analysis. It was observed that when the reinforcement tensile force is assumed to be orthogonal to the radius defining it, rather than being assumed to remain horizontal as installed, the analysis's predictions correspond better to the test results in terms of both trace of slip surface and collapse height (or required tensile strength of reinforcement). Generally, it appears that limit equilibrium analysis predicts fairly well the critical conditions for cohesionless slopes reinforced with extensible inclusions.

REFERENCES

1. R. A. Jewell. Strength and Deformation in Reinforced Soil Design. *Proc., 4th International Conference on Geotextiles, Geomembranes and Related Products*, the Hague, the Netherlands, May 1990.
2. G. Schneebeli. A Mechanical Analogy for the Study of the Stability of Two-Dimensional Earth Structures. *Proc., 4th International Conference on Soil Mechanics and Foundation Engineering*, Vol. 2, London, England, pp. 228–232.
3. D. Leshchinsky and R. H. Boedeker. Geosynthetic Reinforced Soil Structures. *Journal of the Geotechnical Engineering Division*, ASCE, Vol. 115, No. 10, 1989, pp. 1,459–1,478.
4. D. Leshchinsky and E. B. Perry. On the Design of Geosynthetic-Reinforced Walls. *Geotextiles and Geomembranes*, Vol. 8, No. 4, 1989, pp. 311–323.
5. G. Lambert. Cohesionless Slopes Reinforced with Flexible Inclusions. M.S. thesis. Department of Civil Engineering, University of Delaware, Newark, May 1990.
6. R. J. Bathurst, D. J. Benjamin, and P. M. Jarrett. Laboratory Study of Geogrid Reinforced Soil Walls. In *Geosynthetics for Soil Improvement*, Geotechnical Special Publication 18 (R. D. Holtz, ed.), ASCE, 1988, pp. 178–192.
7. R. J. Bathurst and D. J. Benjamin. Failure of a Geogrid Reinforced Soil Wall. In *Transportation Research Record 1288*, TRB, National Research Council, Washington, D.C., 1990.

Publication of this paper sponsored by Committee on Geosynthetics.

Analytical Model for Pullout of Soil Reinforcement

ZEHONG YUAN AND KOON MENG CHUA

A closed-form solution for describing the pullout behavior of reinforcements embedded in soils is presented. The solution shows that pullout resistance is an explicit function of pullout displacement, reinforcement axial stiffness, interface shear stiffness, and reinforcement length. Laboratory pullout box tests as well as uniaxial tension tests were performed to obtain these parameters. The laboratory results of pullout versus displacement of a geogrid and a geotextile in sand are compared with the assumptions found in the current state of the practice. An example problem involving a geotextile and a geogrid in sand is used to illustrate the interaction among the four variables. The analytical solution shows that the shear stress is not uniform along the length of the reinforcement. The effective reinforcement length at which tension is nonzero is shown to vary with the two stiffness values as well as with the magnitude of the pullout force. Practical applications of this new analytical model are proposed.

The maximum force required to cause a pullout of reinforcement from a soil mass is of major concern to engineers designing reinforced earth structures. These reinforcements may be in the form of galvinized steel strips or geosynthetics such as geogrids or geotextiles. One of the more popular methods for determining pullout resistance and soil-reinforcement interactions properties is the pullout box method. The pullout box test essentially consists of pulling a piece of reinforcement through a slit or gap, away from the soil mass in which it is embedded. The applied force and the corresponding displacement are measured during the test. The pullout force is usually expressed in terms of per unit width of reinforcing material and is commonly referred to as the "pullout resistance." The apparent shear stress is calculated by dividing the pullout resistance by twice the plan area of the embedded reinforcement.

At present, laboratory test results obtained from the pullout box and the direct shear box are interpreted in the manner just described, that is, assuming a uniform shear stress distribution over the exposed area of the embedded reinforcement material (*1–6*). As such, the apparent soil-reinforcement interaction properties are based on an average stress. In reality, the shear stress distribution is not uniform, and it is obvious that the stress will approach zero at some distance from the pullout end if the embedded reinforcement is long enough. In other words, for that applied force magnitude, there will be an "effective" reinforcement length beyond which it is redundant. To date, little attention has been given to describing this stress distribution profile. This paper presents an analytical solution that explicitly relates the pullout resistance as a function of pullout displacement, soil-reinforcement interface properties, reinforcement stiffness, and reinforcement length.

This theoretical relationship will be shown to be very helpful in understanding the pullout phenomenon, in interpreting experimental pullout test results, and in improving the accuracy of design methods.

Department of Civil Engineering, University of New Mexico, Albuquerque, N.Mex., 87131.

DESIGNING REINFORCED EARTH STRUCTURES: CURRENT PRACTICE

Soil reinforcement essentially involves introducing elements that can take tension into the soil mass and as a result increase the stability of the earth structure. This concept was first recognized by Henri Vidal in the 1950s. In his investigation he concluded that when a dry granular soil is combined with a rough flexible material having tensile strength, the resulting "reinforced earth" is stronger than soil alone (*7*).

Reinforced earth technology has found wide application in geotechnical engineering in the past decade. Reinforced earth walls and reinforced slopes are examples of these applications. Figure 1 shows the components in a typical reinforced earth structure, in this case a reinforced earth wall. The reinforcement layers are usually embedded some distance away from the slope face or the front facing, if any.

Typical Design Approach

The conventional method for analyzing and designing these types of structures is by using the limit equilibrium approach. Basically, the steps involved are

1. Assume a failure surface,
2. Check equilibrium of the reinforced soil mass above that surface and calculate the safety factor, and
3. Repeat Steps 1 and 2 until a minimum safety factor is found.

Referring again to Figure 1, the potential failure surface refers to the surface intersecting the different reinforcement layers at their respective points of maximum tensile force. The maximum tensile force line separates two zones, namely, an active zone behind the wall facing where the shear stresses from the soil are directed outward, causing the reinforcements to be in tension, and a resistant zone where shear stresses are mobilized from the soil to resist the slipping of the reinforcements.

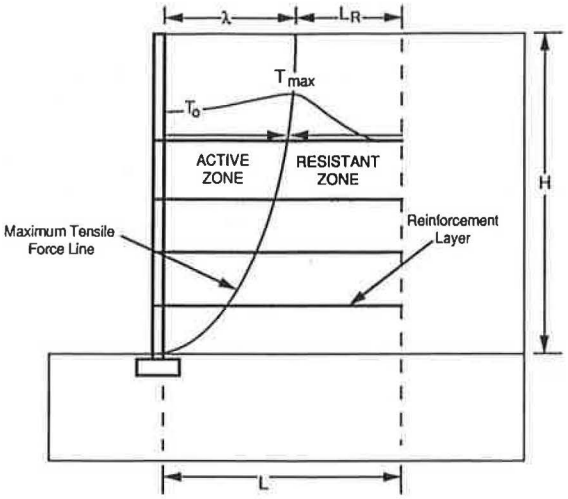

FIGURE 1 Design considerations in typical reinforced earth structure.

In most practical design procedures, Step 3, which involves assuming new failure surfaces, is not performed because the maximum tensile force line can be reasonably estimated. According to Schlosser et al. (*1*), the location of the line may be conservatively approximated in the following manner: at the upper part of the wall, the maximum tensile force is located along a vertical line at a distance (λ) of one-third of the wall height (H) from the wall facing. At the lower part of the wall, the maximum tension force is located on a line that is inclined at an angle of 45 degrees to the horizontal and that passes through the toe of the wall.

Determining Required Reinforcement Length

The total length (L) of each reinforcing layer is divided into two parts, namely, the active length (λ) and the resistant length (L_R). The reinforcement at each level of the earth structure must be of an adequate length to resist the pullout force anticipated at that level. This can be calculated by

$$L_R = \frac{T_m}{2b\, f^*\, \sigma_n} \tag{1}$$

where

b = width of reinforcement,
f^* = apparent coefficient of friction (value 0–1),
σ_n = overburden pressure, and
T_m = maximum tensile force in reinforcement.

Additionally, Schlosser et al. (*1*) suggested that the reinforcement length should be adequate to provide a factor of safety of 1.5 or greater with respect to the anticipated maximum pullout force or

$$\frac{L - \lambda}{L_R} \geq 1.5 \tag{2}$$

Substituting Equation 1 into Equation 2 yields

$$L \geq 1.5\left(\frac{T_m}{2bf^*\,\sigma_n}\right) + \lambda \tag{3}$$

Equation 3 is used to calculate the total length of the reinforcement at each reinforcement level.

Determining Apparent Friction Coefficient

The apparent friction coefficient (f^*) is an interaction property that is dependent on the type of reinforcement and the soil properties. Thus, to be accurate, it should be obtained by laboratory testing using the proposed reinforcement and the soil under the expected field conditions from the project site.

DEVELOPING NEW PULLOUT EQUATION

The following sections show the development of the closed-form solution describing the pullout behavior of reinforcements.

Figure 2 shows the schematic diagram of a pullout of a reinforcement at the point of maximum tensile force. The interface shear stress at Point x distance along the x-axis is related to the tensile force in the reinforcement at that point by

$$\tau(x) = \frac{1}{2}\left[\frac{\partial T(x)}{\partial x}\right] \tag{4}$$

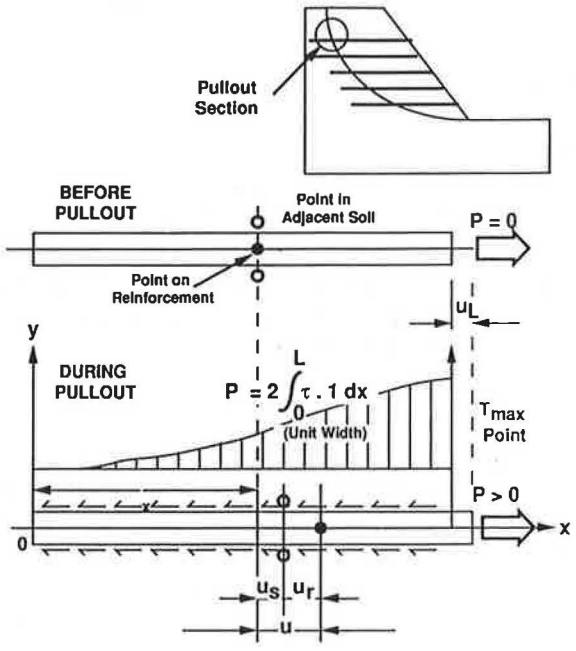

FIGURE 2 Relative displacement between soil and reinforcement.

where

x = longitudinal coordinate,
$\tau(x)$ = interface shear stress at x, and
$T(x)$ = tensile force at x in the reinforcement.

In addition, $T(x)$ is also related to tensile strain in the reinforcement in the following manner:

$$T(x) = k_a \varepsilon(x) = k_a \frac{\partial u(x)}{\partial x} \quad (5)$$

where

k_a = reinforcement stiffness,
$\varepsilon(x)$ = tensile strain of reinforcement at x, and
$u(x)$ = displacement of reinforcement at x.

The shear stress is related to the relative shear displacement and described by the following equation:

$$\tau(x) = k_s u_r \quad (6)$$

where k_s is the interface shear stiffness and u_r is the relative shear displacement. The relative shear displacement is the difference between displacement of a point in the reinforcement and a point in the adjacent soil mass as a result of pullout. These two points in the original configuration should have the same x-coordinates and a very small difference in the y-coordinates. The shear displacement (u_r) can be then expressed as

$$u_r(x) = u(x) - u_s(x) \quad (7)$$

where u_s is the displacement in soil adjacent to reinforcement in the x-direction, as illustrated in Figure 2. Following the definition of engineering strain, the shear strain developed in soils adjacent to the reinforcement can be defined as

$$\gamma_s = \frac{\partial u_s}{\partial y} + \frac{\partial v_s}{\partial x} \quad (8)$$

where

γ_s = engineering shear strain of soil,
v_s = vertical displacement of the adjacent soil, and
y = vertical coordinate.

The compatibility of interface shear stress requires that the shear stress acting on reinforcement and in the adjacent soil to be equal in magnitude, that is,

$$k_s u_r = G_s \gamma_s \quad (9)$$

where G_s is the shear modulus of the adjacent soil. Substituting Equations 5 and 6 into Equation 4 and Equation 9 into Equation 8 yields the following governing equations describing the pullout phenomenon of a reinforcement in soil:

$$k_a \frac{\partial^2 u}{\partial x^2} = 2k_s u_r \quad (10)$$

$$k_s u_r = G_s \left(\frac{\partial u_s}{\partial y} + \frac{\partial v_s}{\partial x} \right) \quad (11)$$

SOLVING GOVERNING EQUATIONS

To solve the previous two simultaneous partial differential equations analytically, it is necessary to assume that the soil displacement (u_s) is very small in comparison with the reinforcement displacement (u). In other words, shear strain is allowed and translation of the adjacent soil element is not. As a result, Equation 7 can be reduced to

$$u_r(x) = u(x) \quad (12)$$

The pullout phenomenon can now be described by one differential equation:

$$k_a \frac{\partial^2 u}{\partial x^2} = 2\, k_s u \quad (13)$$

The boundary conditions associated with Equation 13 are as follows:

$$T(0) = k_a \left(\frac{\partial u}{\partial x} \right)_{x=0} = 0 \quad (14)$$

$$T(L) = k_a \left(\frac{\partial u}{\partial x} \right)_{x=L} = P \quad (15)$$

where P is the applied pullout force per unit width of the reinforcement. The general solution to Equation 13 for displacement u is

$$u = C_1 e^{\alpha x} + C_2 e^{-\alpha x} \quad (16)$$

and

$$\alpha = \sqrt{\frac{2k_s}{k_a}} \quad (17)$$

Using the boundary conditions from Equations 14 and 15, C_1 and C_2 are found to be

$$C_1 = C_2 = \frac{P}{\alpha k_a (e^{\alpha L} - e^{-\alpha L})} \quad (18)$$

Substituting Equation 18 into Equation 16 yields the following:

$$u = \frac{P}{\alpha k_a (e^{\alpha L} - e^{-\alpha L})} (e^{\alpha x} + e^{-\alpha x}) \quad (19)$$

or

$$u = \frac{P \cosh(\alpha x)}{\sqrt{2k_a k_s} \sinh(\alpha L)} \quad (20)$$

From Equations 5 and 20, the distribution of tensile force along a reinforcement is

$$T = \frac{P \sinh(\alpha x)}{\sinh(\alpha L)} \quad (21)$$

From Equations 4 and 20, the distribution of interface shear stress is

$$\tau = \frac{1}{2} P\alpha \frac{\cosh(\alpha x)}{\sinh(\alpha L)} \tag{22}$$

Because the pullout response is usually described by the relationship of the applied pullout force (P) versus the pullout displacement (u) measured at the end where the force is applied, Equation 20 can be rewritten as

$$P = \sqrt{2k_s k_a} \tanh(\alpha L)\, u \tag{23}$$

Equations 20, 21, 22, and 23 are exact if the assumption that the soil displacement (u_s) is negligible when compared with the reinforcement displacement (u) is accurate. This assumption is acceptable because the soil will only move when the soil reinforcement system becomes globally unstable.

DETERMINING STIFFNESS PARAMETERS IN LABORATORY

To show the relationships between parameters in the new solution, pullout tests were performed for a geotextile (Geolon 200) and a geogrid (Tensar UX1100) in a fine, well-graded sand. The unit weight of the sand is 108 pcf and the relative density is about 70 percent. Results from conventional triaxial tests indicate the angle of internal resistance of 42 degrees.

Pullout Box Test

The pullout box at the University of New Mexico was designed and built in 1985 for the New Mexico State Highway and Transportation Department (NMSHTD) and is described in detail by Carney (*8*). The internal dimensions of the steel box are 30 in. long, 28 in. wide, and 24 in. deep. The loading system consists of three 20-ton-capacity hydraulic jacks, one of which is used to apply the vertical load and the others for the pullout. Strain-gage type load cells are used to measure applied loads. The applied vertical load is transmitted to the soil by an assemblage of thick wooden blocks, and it is assumed to be uniformly distributed in the soil mass before the pullout force is applied. The reinforcement is usually pulled at a constant rate after the vertical pressure is applied and the pullout distance is measured by linear variable differential transducers (LVDTs).

Axial Stiffness

The axial stiffnesses of a geogrid and a geotextile were obtained by uniaxial tension tests (without soil). The specimens were 48 in. long and 18 in. wide. Figure 3 shows the relationship of the tensile force and the strain of the two specimens, respectively. Figure 4 shows the axial stiffness of the specimens. The axial stiffness, or the membrane stiffness, is measured in pounds per inch and refers to the slope of the tensile force versus strain curve. Referring again to Figure 3, because the specimens are 48 in. long, a 1 percent strain will

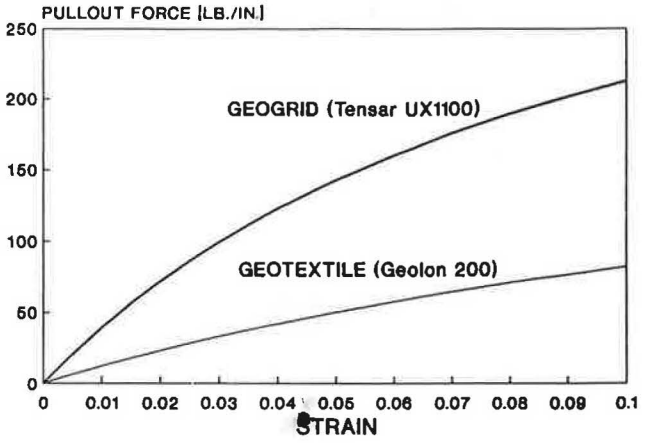

FIGURE 3 Results of uniaxial tension test with geotextile and geogrid for specimen 48 in. long.

be about ½ in. of displacement. At this displacement, it can be seen from Figure 4 that the axial stiffnesses of the Geolon 200 and Tensar UX1100 are reduced by about 10 and 20 percent, respectively. However, in practice this amount of extension over the entire length will not occur because much of the load is transferred to the soil.

Shear Stiffness

Figures 5 and 6 show the plots of pullout force versus displacement for Geolon 200 and Tensar UX1100 in sand, respectively. The pullout force (in pounds per inch width) is for a 30-in.-long reinforcing member that is in contact with the soil.

Yuan and Chua (*9*) argued that it is incorrect to assume that the shear stress is simply the pullout force divided by the area of reinforcing element in contact with the soil. This is because first, the shear stress distribution is not uniform, and second, the entire length of the embedded reinforcement need not be effective, as will be shown in the last section. It was proposed that the shear stress can be described as

$$\tau = \frac{u}{a + bu} \tag{24}$$

and the shear stiffness is obtained as

$$k_s = \frac{a}{(a + bu)^2} \tag{25}$$

where a and b are values dependent only on the applied vertical pressure for that particular interface and u is the pullout displacement at that point on the interface.

The shear stiffness curves shown in Figures 7 and 8 were obtained by trial and error using a finite element program called GEOT2D that was developed by the authors. GEOT2D (Geotechnical Engineering Two-Dimensional Analysis) uses nonlinear soil properties in simulating the continuum elements, and it also uses nonlinear interface elements and membrane elements to model the reinforced earth structure. Large deformation is allowed through the updated Lagrangian for-

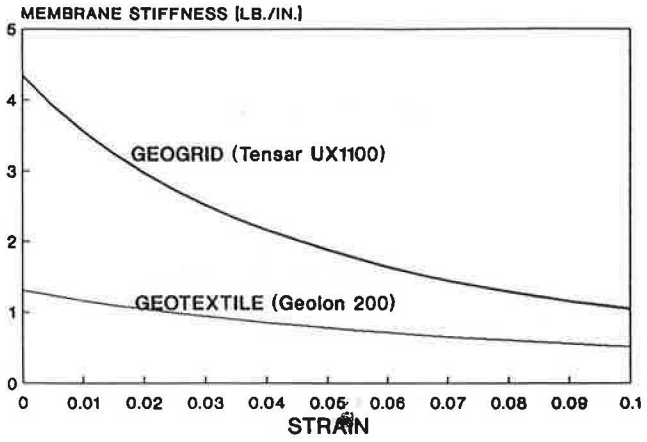

FIGURE 4 Axial stiffnesses of geotextile and geogrid for specimen 48 in. long.

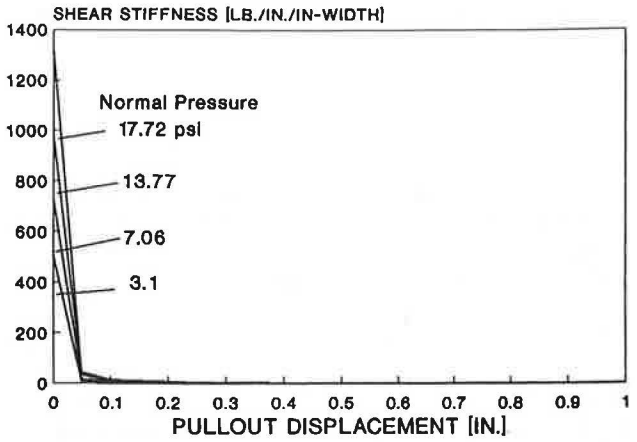

FIGURE 7 Interpreted shear stiffness of geotextile (Geolon 200) in sand.

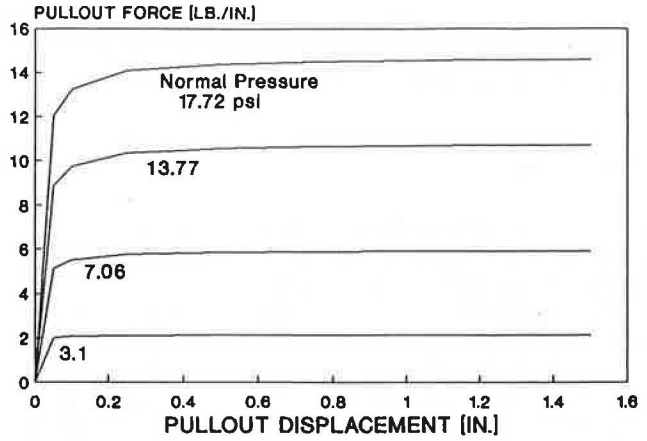

FIGURE 5 Results of pullout box test with geotextile (Geolon 200) in sand.

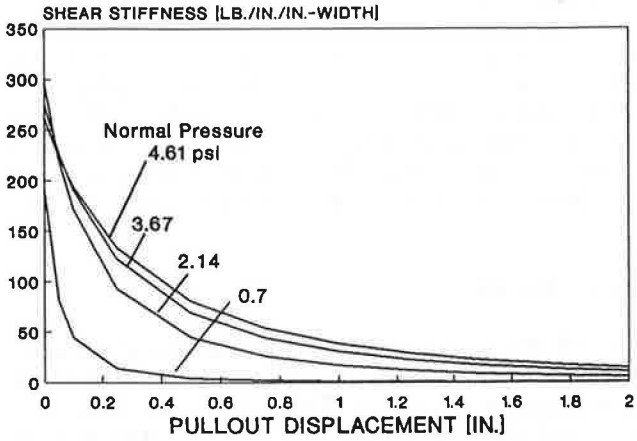

FIGURE 8 Interpreted shear stiffness of geogrid (Tensar UX1100) in sand.

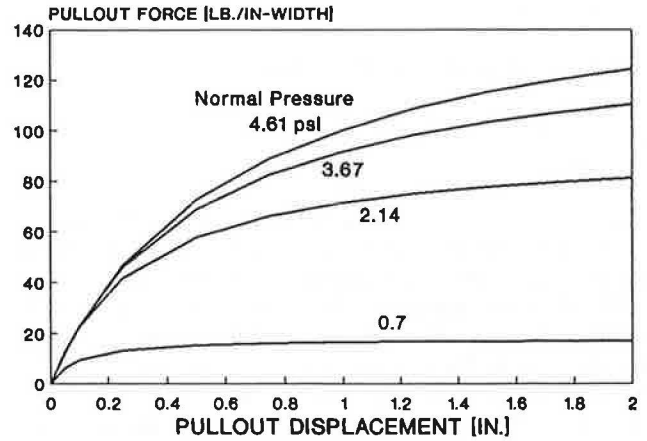

FIGURE 6 Results of pullout box test with geogrid (Tensar UX1100) in sand.

mulation. The shear stiffness parameters, a and b, are changed until the predicted pullout characteristics match those shown in Figures 5 and 6, respectively. This approach, which is discussed in Yuan and Chua (*9*), seems complicated, but it is not difficult. The results serve to explain what actually occurs at soil-reinforcement interfaces. It can be seen from Figures 7 and 8 that the shear stiffness of the sand-geotextile interface reduces more rapidly than that of sand-geogrid interface with pullout displacement.

Summary

The nonlinear responses seen in Figures 5–8 suggest that soil-reinforcement interaction is more complicated than usually assumed and that the pullout behavior of reinforcing materials is not uniform through the entire embedded length. The finite

element approach is convenient for some to use, but it may be unavailable as well as too costly for practicing engineers. In view of this, it will be shown that the analytical solution proposed earlier can to a large extent model the "real" soil-reinforcement interface.

ANALYTICAL MODELING: EXAMPLE PROBLEM

For this problem, assume that pullout tests are performed and the results shown in Figure 3 (pullout force versus strain) and Figures 5 and 6 (pullout versus displacement for Geolon 200 and Tensar UX1100, respectively) are obtained. The axial stiffnesses for Geolon 200 and Tensar UX1100 can be estimated from Figure 3 and are found to be about 1,300 and 4,350 lb/in.-width, respectively. Consider the reinforcing materials to be buried horizontally under 4 ft of sand at about 2 psi of vertical pressure. Referring to Figures 6 and 7, at some nonzero pullout displacement (say 0.05 in. to avoid the initial slope, which is reasonable because some movement will always occur), the slopes of the curves for a 2-psi normal pressure are 3 and 80 lb/in.-width for Geolon 200 and Tensar UX110, respectively. These slopes are the shear stiffnesses for the two reinforcing materials in that particular sand. Although the finite element approach of determining the shear stiffnesses is more accurate, this method of estimating the stiffness values is more convenient. It will also be an improvement over the assumption that the shear stress distribution is always uniform. These stiffness values will be used in the following discussions.

Pullout Displacements

Figure 9 shows curves of pullout displacements versus distance from the maximum tension line for the geotextile and geogrid under pullout forces of 2, 5, and 10 lb/in.-width. It can be seen that for the geogrid, very little displacement occurs beyond 2 ft from the maximum tension line. The length of the geotextile that is actually resisting the pullout can be seen to be only about 7 ft. This implies that even if the embedded reinforcement length is 40 ft beyond the maximum tension line, most of the material will be redundant. Unfortunately, this is often ignored and the state of the practice continues to assume that the entire embedded length is effective in resisting pullout.

The pullout resistance (P) is also seen to increase with an increasing pullout displacement (u), and this is consistent with pullout test results. Figure 9 shows this. This suggests that for an earth reinforcement to work, lateral movement is inevitable.

Reinforcement Tension

Figure 10 shows the distribution of the tensile force in the reinforcement along the length of the reinforcement for the geotextile and the geogrid at various pullout force levels. Again it can be seen that the tensile force in the reinforcement reduced very rapidly with distance from the maximum tension line.

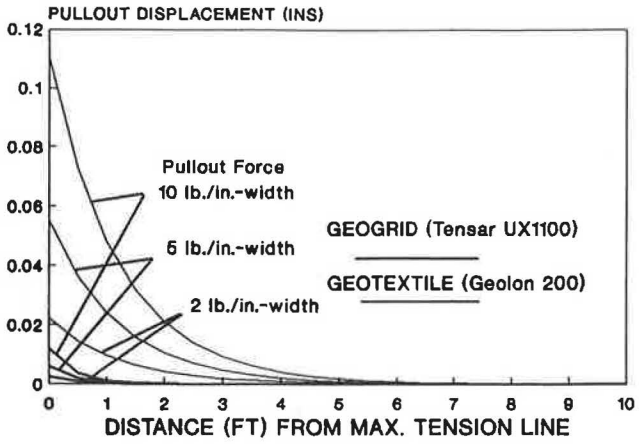

FIGURE 9 Computed pullout displacements along a long reinforcement (normal pressure 2 psi or 4 ft of sand).

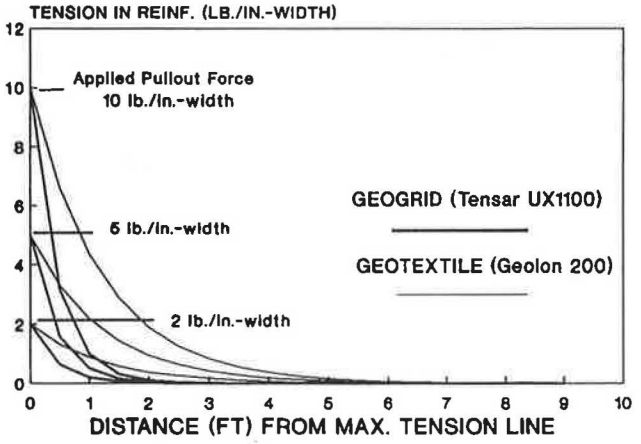

FIGURE 10 Computed tension along a long reinforcement (normal pressure 2 psi or 4 ft of sand).

Shear Stress Distribution

Figure 11 shows the shear stress distributions for the two reinforcing materials at different pullout force levels. The stress level reduces more rapidly in the stiffer reinforcement (Tensar UX1100) than in the geotextile.

Reinforcement Length

Figures 12–14 show the results obtained using the proposed solution for a 12-in.-long reinforcement. It can be seen from Figure 12 that the whole geotextile is being pulled about 0.13 in. through the soil when a 10 lb/in.-width pullout force is applied. The geogrid is seen to be holding fast to the soil. Figure 13 shows that both reinforcement types are completely in tension. The tension at the free end is zero, which is consistent with the principle of equilibrium because no tension

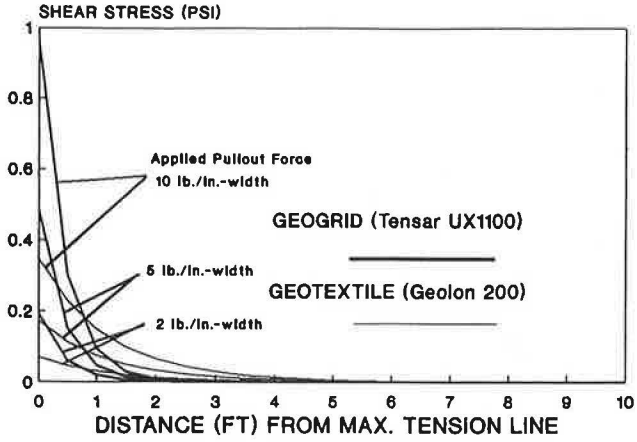

FIGURE 11 Computed shear stresses along a long reinforcement (normal pressure 2 psi or 4 ft of sand).

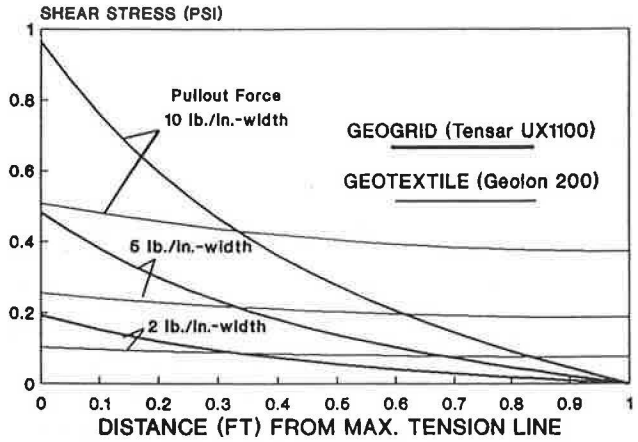

FIGURE 14 Computed shear stresses along a short reinforcement (normal pressure 2 psi or 4 ft of sand).

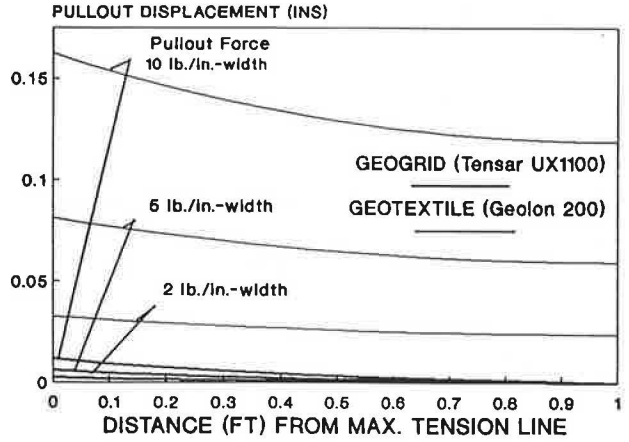

FIGURE 12 Computed pullout displacements along a short reinforcement (normal pressure 2 psi or 4 ft of sand).

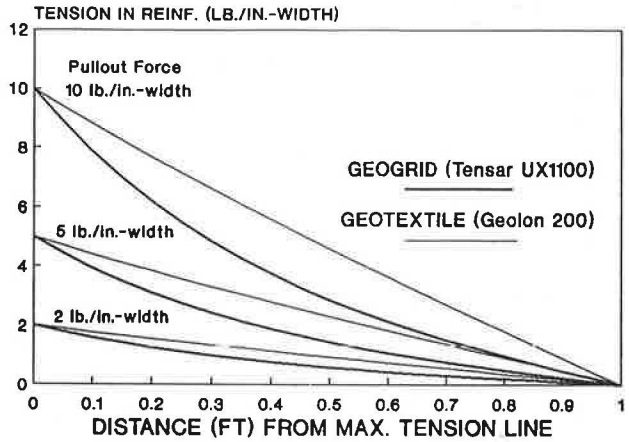

FIGURE 13 Computed tension along a short reinforcement (normal pressure 2 psi or 4 ft of sand).

can be derived from the soil. It is interesting to note in Figure 14 that the shear stresses at the free ends of the geotextiles are not zeros whereas those in the geogrid are.

It can be seen that the reinforcement length is an important consideration in determining the available pullout resistance. The pullout forces assumed here are relatively small. The force levels in the field will be much larger. The increase in vertical pressure will also give a stiffer shearing interface, which will cause the effective length of the reinforcement to increase.

CONCLUSIONS AND RECOMMENDATIONS

A closed-form solution for describing the pullout behavior of reinforcements in soils is presented here. It is shown that the pullout resistance (P) is an explicit function of four variables: pullout displacement (u), interface shear stiffness (k_s), reinforcement stiffness (k_a), and reinforcement length (L). The characteristics of the axial and shear stiffnesses are discussed. The proposed solution has practical merits that can be seen from the following recommendations for implementation.

1. The current design methods for reinforced earth walls and reinforced earth slopes do not consider pullout to be directly affected by reinforcement length. It seems that this factor can be easily incorporated into the current design practice if a minimum reinforcement length is specified on the basis of the axial and shear stiffnesses and the anticipated pullout force level. In recognizing that the effective length varies as a function of pullout, it may be possible to eliminate the otherwise redundant materials beyond the effective zone and be more cost-effective. Conversely, the solution can also be used to determine whether an available embedded length is adequate.

2. The shear stress at the soil reinforcement interface and the tensile stress in the reinforcement predicted by the analytical solution for the field condition can be compared with pullout test results to determine if slippage will occur at the

interface for that particular length of reinforcement. Because the length is included in the solution and shear stresses are correctly described as being nonuniform, the question as to whether the longitudinal dimension of any pullout box will affect laboratory pullout properties will not arise.

3. The pullout characteristics are affected by the ratio between the axial and the shear stiffness, so it may be possible to match reinforcement stiffnesses with different types of soil to optimize the design. It can be shown using the proposed solution that the tensile stresses in the reinforcement will be distributed more uniformly if the reinforcement stiffness is more compliant with the soil. This is an appreciable feature because the stresses will be less concentrated.

4. The proposed analytical model can be easily incorporated into existing slope stability analysis codes. This will give the added flexibility of allowing the pullout resistance to vary with depth as well as with reinforcement length. The axial stiffness and shear stiffness can be easily determined in the laboratory. Eventually, these determinations may be made from a data base.

5. It will also be possible to use the proposed solution to estimate the maximum pullout force at different reinforcement levels from observed lateral movement of a reinforced earth structure. This can provide a useful indication of the critical condition of any in-place reinforced earth structure.

REFERENCES

1. F. Schlosser and V. Elias. Friction in Reinforced Earth. *Proc., ASCE National Convention*, Pittsburgh, Pa., April 1978, pp. 735–763.
2. R. W. Lentz and J. N. Patt. Pull-Out Resistance of Geogrids in Sand. In *Transportation Research Record 1188*, TRB, National Research Council, Washington, D.C., 1988, pp. 48–55.
3. C. Bonczkiewicz, B. R. Christopher, and D. K. Atmatzidis. Evaluation of Soil-Reinforcement Interaction by Large-Scale Pull-Out Tests. In *Transportation Research Record 1188*, TRB, National Research Council, Washington, D.C., 1988, pp. 1–18.
4. R. K. Rowe, S. K. Ho, and D. G. Fisher. Determination of Soil-Geotextile Interface Shear Strength Properties. *Proc., 2nd Canadian Symposium on Geotextiles*, 1985, pp. 25–34.
5. A. Collios, P. Delmas, J. P. Gourc, and J. P. Giroud. Experiments on Soil Reinforcement with Geotextiles. *Proc., ASCE National Convention*, Portland, Oreg., 1980, pp. 53–73.
6. R. D. Holtz. Laboratory Studies of Reinforced Earth Using a Woven Polyester Fabric. *International Conference on the Use of Fabrics in Geotechnics*, Paris, France, 1977, pp. 149–154.
7. M. H. Vidal. The Development and Future of Reinforced Earth. *Proc., ASCE National Convention*, Pittsburgh, Pa., April 1978, pp. 1–61.
8. J. B. Carney. *A Test Chamber for the Determination of the Pullout Resistance of Soil Reinforcing Elements*. Report CE-76 (86) NMSHD-000757. Department of Civil Engineering, University of New Mexico, Albuquerque, March 1986.
9. Z. Yuan and K. M. Chua. Numerical Evaluation of the Pullout Box Method of Studying Soil-Reinforcement Interactions. In *Transportation Research Record 1278*, TRB, National Research Council, Washington, D.C., 1990, pp. 116–124.

Publication of this paper sponsored by Committee on Geosynthetics.

Soil Nailing in France: Research and Practice

F. SCHLOSSER AND P. UNTERREINER

In 1986 a 4-year, $4 million research project named CLOUTERRE was initiated in France by the French Minister of Transport. The main objective was to develop recommendations on soil nailing for temporary and permanent nailed soil walls in excavation, with special emphasis on safety and durability. The results and the subsequent recommendations for seven selected important topics are presented. The behavior of a nailed soil wall during construction, in service, and near failure was studied on three full-scale experimental walls pushed to failure according to three modes of failure. A design method based on Schlosser's multicriterion is recommended to account for all possible modes of failure. The classical definition of the global factor of safety is abandoned, and a new procedure using partial safety factors and weighing factors is recommended. A new method is proposed to design the facing thickness as a function of the nail spacings. More than 450 in situ pullout tests were collected to create a unique data base allowing correlations between the nail and soil types and the soil-nail interface frictional resistance. Detailed recommendations are developed to calculate the extra thickness of steel required in permanent nailed soil structures depending on the characteristics of the soil. Limitations of soil nailing are clearly defined for different situations. CLOUTERRE recommendations are a major contribution to the status of knowledge on soil nailing in excavation. They will allow the increasing use of soil nailing for temporary and permanent structures.

Soil nailing is a technique that consists of reinforcing in-place soils with bars or structural members called nails, which can be either driven or installed and grouted in drilled holes. When used in excavation, the nails are horizontally placed and able to withstand primarily tensile forces, making possible the construction of nailed soil retaining walls. The construction procedure is simple; it consists of the following steps (Figure 1): (a) excavation of the in-place soil, (b) installation of the nails, and (c) construction or installation of the facing.

The first nailed soil retaining wall was built in France in 1972–1973 at Versailles to retain a cut for rail tracks (Figure 2). Since then, soil nailing has been used extensively in France and abroad for temporary retaining structures in excavation because of its many advantages. Compared with traditional techniques, soil nailing requires limited labor and only light construction equipment, and the wall can be finished while the soil is being excavated. In addition, this technique can be adapted to any type of site downtown or in the mountains and to most types of soil. This makes a time- and cost-effective technique, which explains the rapid worldwide success of soil nailing. However, because of this rapid success, the state of the practice was ahead of the state of knowledge. Moreover, until recently soil nailing was used primarily for temporary retaining structures because of the lack of knowledge about the longtime behavior of such structures. Therefore, in 1986 a 4-year, $4 million national research program, CLOUTERRE, was initiated by the French Minister of Transport. Twenty-one organizations, including private companies and public research laboratories, participated directly in the project.

The main objectives of CLOUTERRE were to promote soil nailing in France for temporary as well as permanent retaining structures in excavation by improving the current status of knowledge and developing recommendations for temporary and permanent nailed soil walls. The objective of this paper is to present the main results of the research and the subsequent recommendations for seven important topics: (a) behavior of a nailed soil wall during construction, in service, and near failure; (b) design methods; (c) safety considerations; (d) facing design; (e) pullout tests; (f) durability; and (g) limitations.

BEHAVIOR OF A NAILED SOIL WALL

One of the major contributions of CLOUTERRE to the status of knowledge is the monitoring of three full-scale experimental walls from construction to failure through service by Plumelle and Schlosser (discussed in another paper in this Record). In the following section the main mechanisms involved in a nailed soil wall will be summarized and the design methods will be described.

Deformations

A nailed soil wall is constructed from the top to the bottom by alternating excavation with the installation of the nails and the facing. At each excavation step, the excavated soil remains exposed for some time before being nailed. This situation results in the vertical settlement and lateral decompression of the bottom soil, which generate horizontal and vertical outward displacements of the top of the wall. The top bends outward a bit more at each new excavation step (Figure 3) and ends up with vertical displacements of the same order as the horizontal displacements (Figure 4). All the measurements performed within CLOUTERRE (nine instrumented nailed soil walls) confirm that the ratio of horizontal displacement of the top of the wall (δ_H) over height of the wall (H) varies between 1/1,000 and 3/1,000 for walls built with a reasonable factor of safety (Figure 5). Moreover, the ratio of

F. Schlosser, TERRASOL, Tour Horizon, 52 quai de Dion Bouton, 92806 Puteaux Cédex, France. P. Unterreiner, Ecole Nationale des Ponts et Chaussées, CERMES, La Courtine, 93167 Noisy-le-Grand Cédex, France.

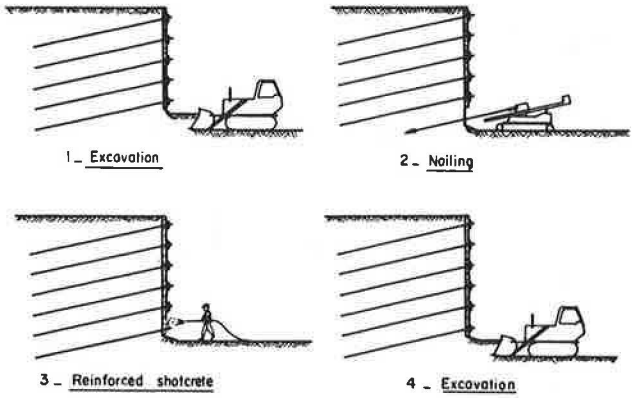

FIGURE 1 Steps in constructing nailed soil wall.

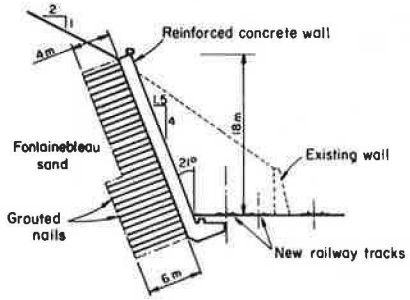

FIGURE 2 First nailed soil wall, in Versailles (*13*).

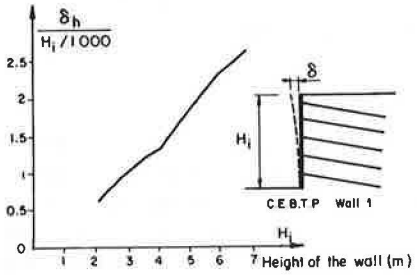

FIGURE 3 Evolution of horizontal displacements at top of nailed soil wall during construction.

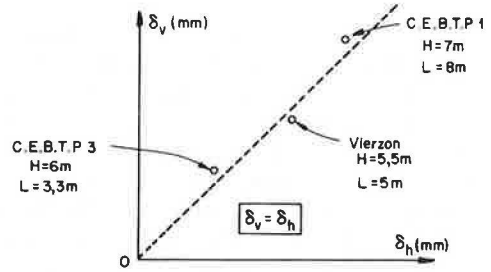

FIGURE 4 Observation of nailed soil wall displacements.

horizontal displacement at the surface right above the ends of the nails (δ_o) over H varies between 4/10,000 and 5/10,000 (Figure 6).

Soil-Nail Interaction

During construction, nails are loaded essentially in tension because of the lateral decompression of the soil. The transfer of stresses between the soil and the reinforcements involves a basic mechanism, namely, frictional resistance (*1*). The shear stress τ at the interface is limited in value by q_s, interface frictional resistance. In soil nailing where reinforcements are installed in in-place soils, the phenomenon of restrained dilatancy has been observed. This phenomenon, first described by Schlosser and Elias in 1978 (*2*) for reinforced earth, was observed for soil nailing by Cartier and Gigan (*3*) and confirmed by field and laboratory experiments in CLOUTERRE (*4*) (Figure 7). As a result, q_s is a function only of the soil, nail, and soil-nail interaction properties. Therefore, correlations have been developed between q_s and in situ testing measurements, typically the limit pressuremeter pressure, p_l (Figure 8). However, because of the high dispersion of such correlations, q_s is usually determined more precisely with pullout tests.

Distribution of Tension Forces in Nails

At each new excavation step, because of the horizontal lateral decompression of the soil, nails are activated essentially in

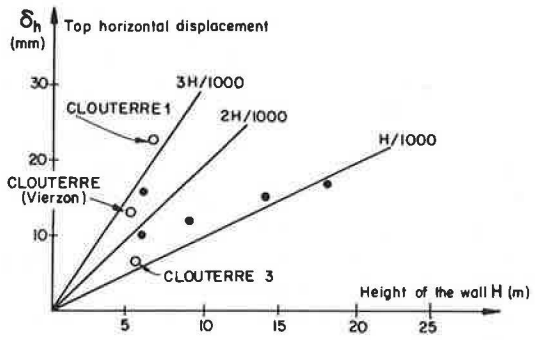

FIGURE 5 Horizontal displacements of nailed soil wall.

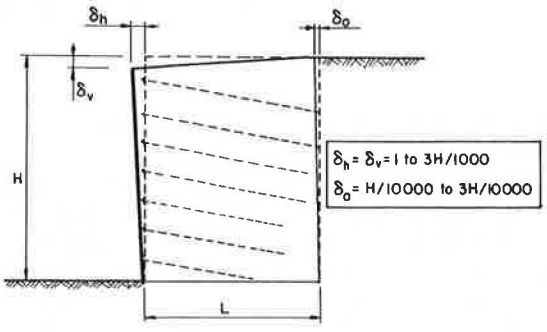

FIGURE 6 Deformation of nailed soil wall.

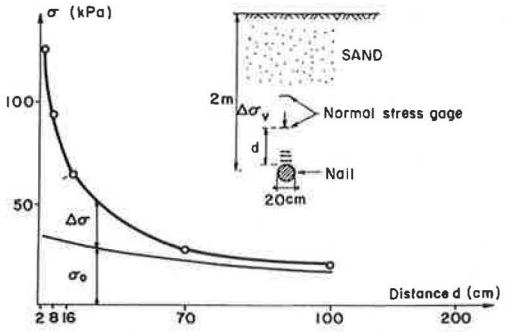

FIGURE 7 Increase in normal stress due to restrained dilatancy around nail.

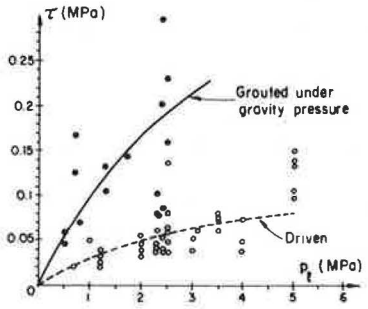

FIGURE 8 Correlations between limit frictional shear stress and limit pressure obtained from pressuremeter test (*12*).

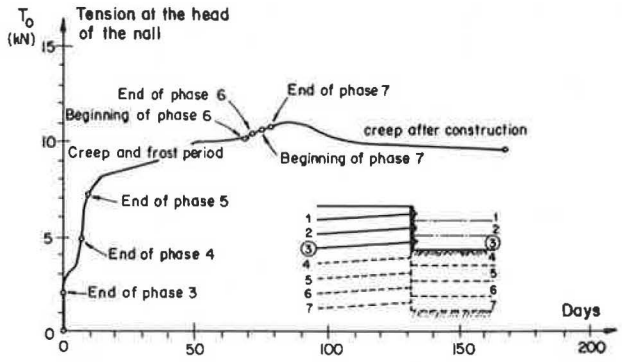

FIGURE 9 Variations of tension in nail head during excavation, Wall 1.

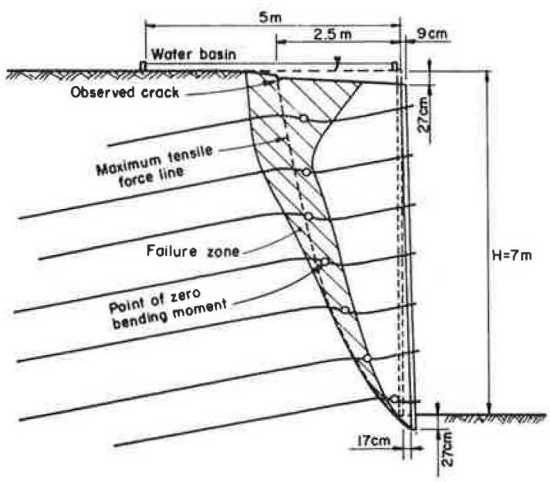

FIGURE 10 Failure zone developed in full-scale experiment on nailed soil wall.

tension. The progressive increase of nail tension was monitored in CLOUTERRE for several full-scale walls from construction to failure through service (Figure 9). The distribution of tension in the nails at the end of construction, that is, in service, is very similar in principle to the distributions that have been observed for other reinforcement techniques, such as reinforced earth. The maximum tension in the nails occurs at a certain distance from the facing and not at the facing. The locus of the points at which the tension T is maximum (T_{max}) defines a surface that divides the reinforced soil mass into two zones: the active zone and the passive zone. In the active zone, which is behind the facing, the shear stress acting on the nails is pointing outside the wall; in the passive zone it is pointing inside. At the top of a wall with a vertical facing and horizontal top, the locus of T_{max} is almost vertical; at the base it is inclined and goes through the toe of the wall (Figure 10).

Mobilization of Shear Force and Bending Moment

As far as the forces (tension or shear force) and moments (bending moment) that can be developed in a nail are concerned, a clear distinction among construction, service, and failure conditions must be made. During construction and in service, nails are essentially loaded in tension. Locally near the facing, small shear forces and bending moments may be generated during construction but only in extreme cases in which the facing is hanging on the nails. But near and at failure, significant shear forces and bending moments will appear along the failure surface. Concerning this point, the full-scale experimental wall—Wall 1—is of major interest. The 7-m-high nailed soil wall was pushed to failure as the sandy soil behind the facing was saturated. After failure, the deformed shape of the failed wall was investigated. Around the potential failure surface, represented by the locus of maximum tension, a wide zone of shear and distortion developed. Within this zone nails underwent distorsions of about 20 degrees (Figure 10). The importance of the shear force (T_c) compared with the tensile force (T_n) has been investigated by Marchal (*5*) with the direct shear box on soil samples reinforced with steel bars (Figures 11 and 12). The ratio T_c/T_n depends on the orientation of the reinforcing bar relative to the shear plane. However, for inclinations of about 70 to 90 degrees, the ratio T_c/T_n can be as high as 15 percent. Therefore, limit equilibrium design methods should be able to take into account this benefit of the shear forces and bending moment in the stability analysis. This is what will be developed in the next section with the multicriterion.

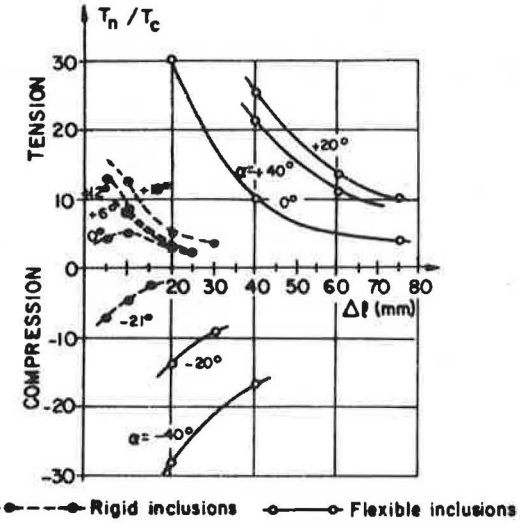

FIGURE 11 Evolution of ratio of tensile force to shear force as a function of displacement (α = inclination of bar with vertical) (*5*).

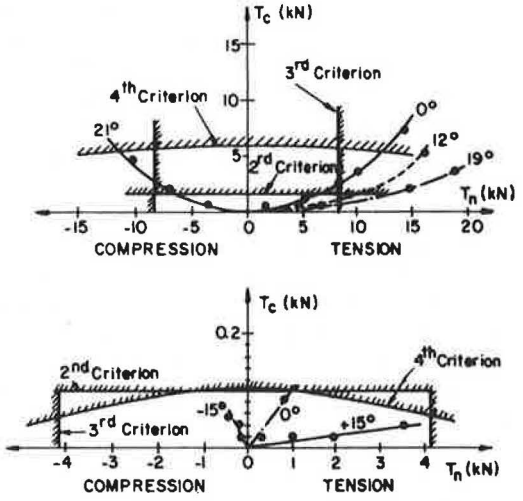

FIGURE 12 Evolution of limit values of tensile and shear forces: *top*, rigid inclusions (σ = 350 kPa); *bottom*, flexible inclusions (σ = 300 kPa) (*5*).

DESIGN METHOD

Until now, it has not been possible to develop effective design methods calculating both deformations and efforts in the nails in service. Only limit equilibrium design methods are available and used for design purposes. A suitable limit equilibrium design method should be able to (a) analyze the different failure modes—external, mixed, and internal—and (b) take into account the contribution (positive or negative) of the nail tension and compression for flexible nails; for nails with a sufficient bending stiffness, shear forces and bending moments should be taken into account as well.

Types of Failure

Three types of failure must be considered: external, mixed, and internal. In an external failure mode, the failure surface does not intersect the nailed soil mass, which is considered as a monolithic block. For this type of failure, classical limit equilibrium methods are sufficient for design purposes. A failure is said to be internal or mixed when the failure surface is totally or partially within the nailed soil volume. For the latter two failure modes, classical limit equilibrium methods are not sufficient. Internal failures of nailed soil walls are due to either the breakage of the nails or the lack of frictional resistance. Both types of internal failure have been realized on full-scale experimental walls (Walls 1 and 3, respectively).

Internal Failure by Breakage

In an internal failure by breakage, nails can break in tension or in tension and shear if the bending stiffness is high enough. The failure surface that develops in the wall from the toe to the top is very close to the locus of maximum tension. When nails have some bending stiffness, a shear zone rather than a clear failure surface develops around the locus of maximum tension. The rupture is less rapid and more progressive than it is with flexible nails because large shear deformations develop before the wall reaches complete failure. This point is important in the field because there is time to prevent a complete failure.

Failure by Pullout

In contrast to failure by breakage, failure by pullout is less common and had never really been studied before CLOUTERRE. This type of failure occurs when nails are not long enough or when the interface friction resistance is not sufficient to balance the maximum tension. Wall 3 of CLOUTERRE was induced to failure by reducing the length of the nails (Figure 13).

Multicriterion

It has been shown that the role of nails in the structure is quite complex and that different types of internal failure can occur. A suitable analysis should take into account all possible modes of failure and treat them in a simple way. This is what the multicriterion is all about. Limit equilibrium methods consider the equilibrium of a soil mass at a limit state. In the equations of equilibrium, only the tensions and compressions (T_n) and the shear forces (T_c) of the nails at the intersection with the potential failure surface play a role. For a given potential failure surface, (T_n, T_c) must be determined for each nail depending on the orientation of the nail with the failure surface and on the mode of failure that is most probable for the given surface. Four failure criteria must be considered to take into account all the possible failure conditions of a nail. Each criterion will be written in terms of (T_n, T_c), the values of the axial and shear forces in the nail at the point of intersection with the potential failure surface.

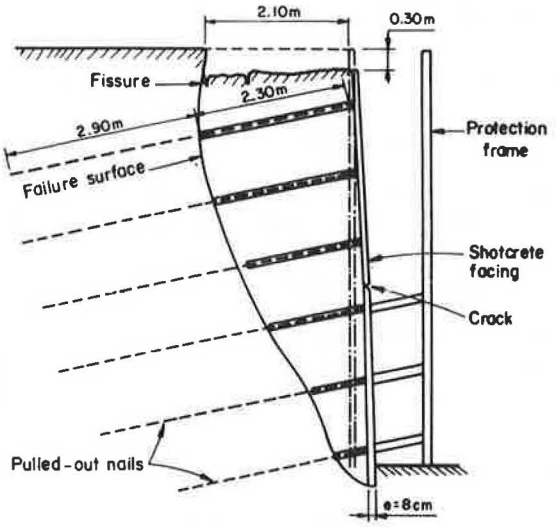

FIGURE 13 Postfailure investigation of Wall 3 (Fountainebleau sand, $\phi' = 38$ degrees, $c' = 9$ kPa).

1. The first criterion that corresponds to an internal failure by pullout depends on the interface frictional resistance q_s

$$T_n \leq q_s \pi D L_a \tag{1}$$

where

T_n = axial force,
q_s = interface frictional resistance,
D = diameter of nail, and
L_a = length of nail behind the failure surface.

2. The second criterion corresponds to the failure of the soil below a nail. The pressure of a nail on the soil below it is limited by the bearing capacity pressure p_u. The failure of the soil below a nail can be defined when p_u is reached at one point (the point of maximum shear force in the nail), which yields the following criterion:

$$T_c \leq l_o p_u D/2 \tag{2}$$

where l_o is the transfer length (elastic analysis).

3. The third criterion corresponds to the failure of the nail by breakage. The combination of (T_n, T_c) that occurs in a nail at failure can be represented by the following simple criterion proposed by Anthoine (*6*), which is somewhat more conservative than other proposed criteria (*7,8*):

$$(T_n/R_m)^2 + (T_c/R_c)^2 + |M/M_o| \leq 1 \tag{3}$$

where

T_c = shear force in a nail,
M = bending moment in a nail,
R_n = maximum tensile force,
R_c = maximum shear force, and
M_o = maximum bending moment in pure bending.

This third criterion is represented by an ellipse in the plane (T_c, T_n).

4. The nail can fail on two other points, however: the points of maximum moment. Those points are at a distance $l_s/2$ of the shear plane. The distance l_s can be considered as the width of the shear band that develops around the shear plane. At the present time, there is no available method to calculate l_s with reasonable precision. The only available information about l_s is that it is equal to $\pi l_o/2$ when the nail first starts to plastify at two points by bending moment (elastic analysis). After formation, the two plastic hinges move with the progressive plastification of the soil under the nail. In the absence of more practical information about l_s, a simple assumption can be made: l_s is constant and equal to its initial value $\pi l_o/2$. Assuming, then, that the two plastic hinges at the points of maximum moment are fixed, the following criterion (C_4) can be defined.

$$T_c \leq b\,(M_o/l_o)[1 - (T_n/R_n)^2] + cDl_o(p_u - p_o) \tag{4}$$

where b and c are constants and R_n is the maximum axial force in simple tension.

The envelope of these four criteria in the (T_c, T_n) plane defines a domain of stability that is convex and in which the point (T_c, T_n) can be placed anywhere a priori. Figure 14 shows such a stability domain that represents the combination, called the multicriterion, of all four failure criteria. It is very important to note here that, depending on the soil type and on the nail-bending stiffness, the first criterion may play no role because it is above the second criterion in the presented case. At failure, the point (T_c, T_n) is on the border of the stability domain but its position is unknown a priori. A rule must be chosen. Schlosser proposed in 1982 and 1983 to use the rule of maximum work (*9,10*) as a particular case of the "normality rule." The position of the point (T_c, T_n) on the border is chosen to maximize the work of the nail in the considered potential failure mechanism. Once the displacement of the nail point at the intersection with the failure surface is known, (T_c, T_n) can be determined to maximize the dissipated work.

Numerical simulations of the failure of Wall 1 have been performed using the multicriterion (*11*). The wall failed after saturation of the soil behind the facing to a height of 4 to 5 m from the bottom. Before saturation, the soil had an apparent cohesion of about 3 kPa in its unsaturated state. Because of saturation, this apparent cohesion was reduced to zero. Two limiting cases of the soil properties have been thus considered (Figure 15): (a) the soil keeps its initial 3-kPa cohesion everywhere, which gives an upper bound of the height of water at failure; and (b) the soil loses its 3-kPa cohesion only in the zone in which it is saturated; this gives a lower bound.

SAFETY CONSIDERATIONS

Traditionally, safety is calculated in slope stability analyses by considering the ratio τ/τ_{max}, where τ is the tangential component of external forces and τ_{max}, the shear strength that can be mobilized along a potential failure surface. This ratio, which is usually called the global safety factor, is supposed to take into account many factors, including variability of properties, uncertainties on measures of material strengths, scat-

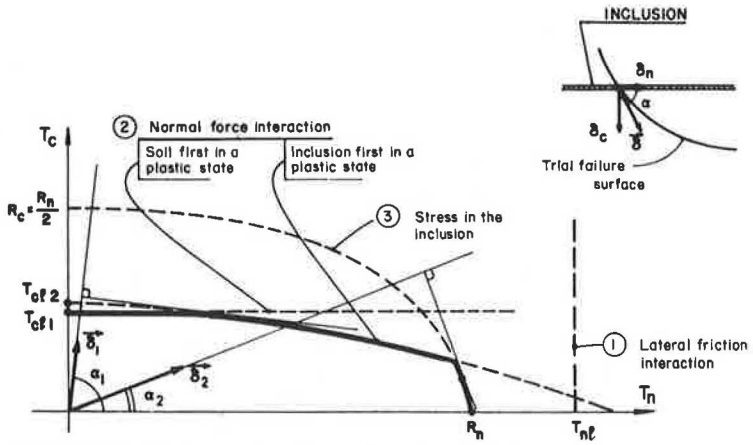

FIGURE 14 Various interaction mechanisms within normal force (T_n) and shear force (T_c) planes.

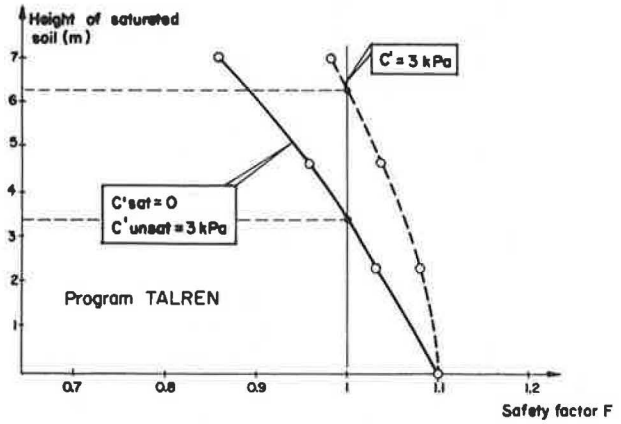

FIGURE 15 Evolution of safety factor in Wall 1.

tering of measures of material strengths, uncertainties on loading conditions, and errors inherent to the design method used. However, because all these factors are combined into one coefficient, they tend to be considered with equal importance. In the CLOUTERRE recommendations, a completely new formulation using different partial safety coefficients has been developed to separate clearly the factors described earlier.

The most probable values of the soil, nail, and soil-nail interaction parameters are determined by a geotechnician from the laboratory or in in situ testing with a sufficient number of samples. Then the variability and dispersion of these parameters are taken into account by defining characteristic values. These are calculated from the most probable values by using coefficients of scattering (*12*). Characteristic values of the material properties are then reduced with partial safety factors ($\Gamma_{m,c}$ = cohesion; $\Gamma_{m,\Phi}$ = friction). On the other hand, actions will be multiplied by weighting factors (Γ_Q = loads; Γ_G = gravity) to obtain calculation values (Table 1). Once calculation values have been determined, limit equilibrium methods are used to determine the ratio τ_{max}/τ, which is required to be greater than Γ_{s3}, called the method coefficient.

$$\Gamma_{s3}\tau \leq \tau_{max} \qquad (5)$$

TABLE 1 EXAMPLE OF PARTIAL SAFETY FACTORS

FUNDAMENTAL	FUNDAMENTAL COMBINATION	ACCIDENTAL COMBINATION
SOIL		
$\tan \phi^*$	1.65	1
c^*	1.2	1
SOIL-NAIL INTERACTION		
q_s	1.6 (correlations) 1.3 (pull-out tests)	1.4 (correlations) 1.2 (pull-out tests)

This coefficient takes into account the errors inherent in the methods. For limit equilibrium methods using the multicriterion and searching circular potential failure surfaces, Γ_{s3} is chosen to be 1.125 for a fundamental combination and 1.0 for an accidental combination. A design will be acceptable according to the present status of knowledge if the inequality is respected.

FACING DESIGN

The facing may have several functions in a nailed soil structure: it provides a lateral confinement for the soil between the nails, and it carries external loads such as decorative panels. However, hereafter only the first function will be considered because it is the most important one. Locally between each nail, soil must be retained.

Two soil-nailing techniques exist in France. The first and oldest one, called "Hurpinoise" after its inventor, consists of short nails, with a length of about 0.5 to 0.7 H, that are driven with or without vibrations. Usually, it uses one or two nails per square meter. The second one uses grouted nails in drilled holes with a length of 0.8 to 1.2 H. The number of nails per unit surface is about 0.15 to 0.4, which is almost one order of magnitude smaller. Because of these different densities of the nails, the facing tends to be very thin for the first technique and much thicker for the second one.

The density of the nails is a major factor, but other factors, including the rigidity of the facing itself, play a role. The facing

is in equilibrium by balancing the earth pressures and the forces applied by the nails. It is usual for design purposes to assume that these earth pressures are uniformly distributed. As a result, they are known as soon as the tension T_o is known. T_o is the tension in a nail at the facing when it is in a limit state while the rest of the structure (soil and nails) is in service. The ratio of T_o/T_{max}, T_{max} being the nail tension on the locus of maximum tensions, can be estimated from instrumented full-scale nailed soil walls. This ratio depends on many factors. However, as observed earlier, the nail spacing is the most important factor to the earth pressures, which are directly related to T_o. The ratio T_o/T_{max} can thus be estimated as a function of S_v and S_h, which are, respectively, the vertical and the horizontal spacing. On the basis of the experimental results, CLOUTERRE recommendations propose the following:

$$T_o/T_{max} = 0.5 + (S - 0.5)/S \quad \text{for } 1 \le S \le 3 \text{ m} \tag{6}$$

$$T_o/T_{max} = 0.6 \quad \text{for } S \le 1 \text{ m} \tag{7}$$

$$T_o/T_{max} = 1.0 \quad \text{for } S \ge 3 \text{ m} \tag{8}$$

where

S = max(S_v,S_h) (m),
S_v = vertical nail spacing, and
S_h = horizontal nail spacing.

Once the ratio T_o/T_{max} is known, one must estimate T_{max} to have T_o. A conservative approach is to calculate T_{max} from T_{lim}, maximum tension in the nails on the most critical failure surface, because the latter is a conservative value of T_{max}. Once the forces T_o and earth pressures acting on the facing are known, the facing can be designed like any similar concrete structure, typically, a floor carried by a great number of piles.

PULLOUT TESTS

One of the most important parameters in the design is q_s, the interface frictional resistance. For a given soil and nail type, q_s is independent of depth. Therefore, q_s can be calculated from the soil, nail, and soil-nail interface properties. Practically, q_s will be determined from the in situ testing measurements. Figure 8 shows such a correlation between q_s and p_l, the limit pressuremeter pressure. One can note the great amount of scatter in this figure, in which data on all types of soils are shown. One of the major contributions of CLOUTERRE has been to collect more than 450 results from pullout tests with the corresponding in situ pressuremeter test results. The processing of these data by type of soil and nail has allowed the development of correlation curves that will be useful for design. However, because of the great variability of q_s measurements, CLOUTERRE recommendations require that q_s be measured in the field in the soil and with the nails that will be used for construction using displacement-controlled pullout tests.

DURABILITY

Durability was of major concern in CLOUTERRE because one of the initial objectives was to promote soil nailing for permanent retaining structures. Most nailed soil structures are built with steel nails. Therefore, corrosion must be taken into account for structures with an expected service life of more than 18 months. Three types of provision can be taken to protect steel nails from corrosion: (a) increase of the nail sections, (b) protection with coatings, and (c) protection with barriers.

The most frequently used technique in soil nailing and in other reinforcement techniques such as reinforced earth is to use nails with thicker cross sections. This technique is efficient only if the type of steel used for the nails undergoes generalized corrosion and not punctual corrosion. The sections are calculated so that at the end of the expected service life the remaining noncorroded steel sections are thick enough. In the recommendations, a global index is defined to take into account the type of soil, its resistivity, its moisture content, and other parameters. Extra thicknesses of steel are then provided for each type of structure as a function of the global index (Table 2). Other techniques using special coatings, which may be painting or galvanization, can be used to slow steel corrosion. The last type of technique uses barriers that can be made with plastic to prevent corrosion. These barriers do not play any mechanical function. These types of techniques are used more and more because these types of nail are patented by the companies that develop and promote them.

LIMITATIONS OF SOIL NAILING

Despite its many advantages, the most important being its easy adaptation to any kind of site, soil nailing is a technique that has a few limitations. Most of them can be prevented by making construction or design provisions; however, these provisions may make soil nailing more expensive and thus less attractive. In nailed soil walls, displacements inherent to the technique occur. They are limited to about 0.003 the height of the wall, but this may still be too much for some urban sites. Different types of provisions can be chosen. One solution is to use bracings at the top of the nailed soil wall. Another solution is to install one or two rows of tiebacks in the upper part of the wall. This solution is often chosen especially for very high nailed soil walls (Figure 16). Because of the construction procedure for a nailed soil wall, it must be built above the water table level; it may be built below it only if the groundwater table can be lowered sufficiently for the construction duration. The last type of limitation concerns the in-place soils that can be nailed. Sandy soils without any apparent cohesion cannot be excavated over a sufficient depth

TABLE 2 EXTRA THICKNESSES RECOMMENDED FOR CORROSION PROTECTION

Class	Structures Expected Life ≤ 18 months	Structures Expected Life 1,5 to 30 years	Permanent Structures 30 to 100 years
IV	0	2 mm	4 mm
III	0	4 mm	8 mm
II	2 mm	8 mm	plastic barrier
I	Compulsory plastic barrier		

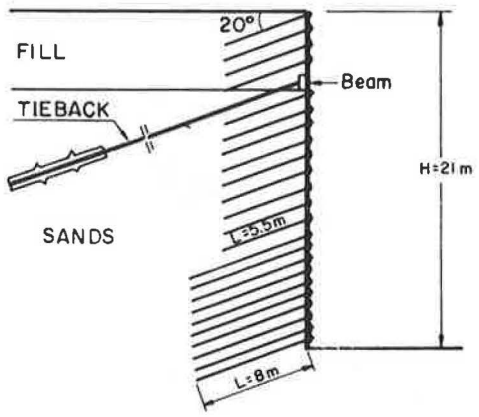

FIGURE 16 21-m-high nailed soil wall.

without protection. Clayey soils must be nailed with precautions; they may become saturated after construction and suffer a resulting significant decrease in the soil-nail interface frictional resistance.

CONCLUSIONS

CLOUTERRE, thanks to its 4 years of theoretical, numerical, and experimental research and its three full-scale experimental walls, has significantly increased the status of knowledge on soil nailing for temporary and permanent retaining structures in excavation.

The knowledge in seven topics has been improved: (a) behavior of nailed soil walls, (b) multicriterion design method, (c) partial safety coefficients, (d) design of the facing, (e) correlations for (q_s, p_l) based on 450 pullout tests, (f) corrosion provisions for steel nails, and (g) construction and design provisions.

CLOUTERRE recommendations will be a milestone in soil nailing because they will allow soil nailing to be used in more and more temporary and permanent structures. Every year new nailed soil walls are built in more difficult sites and with more difficult soils. The world record in height is 21 m. The limits of soil nailing have not yet been reached.

ACKNOWLEDGMENTS

The authors wish to thank the French Ministry of Transport and the 21 organizations that have contributed to CLOUTERRE.

REFERENCES

1. F. Schlosser and H. Vidal. La Terre Armée. *Bulletin de Liaison Laboratoire Routiers Ponts et Chaussées*, No. 41, 1969, pp. 101–144.
2. F. Schlosser and V. Elias. Friction in Reinforced Earth. *Proc., Symposium for Earth Reinforcement*, ASCE, Pittsburgh, Pa., 1978, pp. 735–763.
3. G. Cartier and J. P. Gigan. Experiments and Observations on Soil Nailing Structures. *Proc., 8th European Conference on Soil Mechanics and Foundation Engineering*, Vol. 2, Helsinki, Finland, 1983, pp. 473–476.
4. *Interaction sol-clou*. Étude en laboratoire. CLOUTERRE, Centre d'Enseignement et de Recherche en Mécanique des Sols, Dec. 1989.
5. J. Marchal. Reinforcement des sols par clouage—Etude expérimentale en laboratoire. *Proc., International Conference on In Situ Soil and Rock Reinforcement*, Paris, France, 1984, pp. 275–278.
6. A. Anthoine. Stabilité d'une fouille renforcée par clouage. *Proc., 4th Franco-Polish Conference on Applications of Soil Mechanics*, Grenoble, France, 1987.
7. Z. Sobotka. *Theory of Plasticity*, Vol. I and II, Ceskoslovenska Akademie Ved, Prague, 1954–1955.
8. B. G. Neal. The Effect of Shear and Normal Forces on the Fully Plastic Moment of a Beam of Rectangular Cross Section. *Journal of Applied Mechanics*, No. 269, June 1961.
9. F. Schlosser. Behaviour and Design of Soil Nailing. *Proc., Symposium for Recent Developments in Ground Improvement Techniques*, Bangkok, Thailand, 1978, pp. 399–413.
10. F. Schlosser. Analogies et différences dans le comportement et le calcul des ouvrages de soutènement en Terre Armée et par clouage des sols. *Annales ITBTP*, No. 418, 1983, Série Sols et Fondations, 184.
11. F. Blondeau, M. Christiansen, A. Guilloux, and F. Schlosser. TALREN: Méthode de calcul des ouvrages en terre renforcée. *Proc., International Conference on In Situ Soil and Rock Reinforcement*, Paris, France, 1984, pp. 219–224.
12. *Recommendations CLOUTERRE 1990*. Preliminary draft. Presses de l'Ecole Nationale des Ponts et Chaussées, Paris, France, 1990.
13. S. Rabejac and P. Toudic. Construction d'un mur de soutènement entre Versailles-Chantiers et Versailles-Matelots. *Revue Générale des Chemins de Fer*, Vol. 93, 1974, pp. 232–237.

Publication of this paper sponsored by Committee on Mechanics of Earth Masses and Layered Systems.

Three Full-Scale Experiments of French Project on Soil Nailing: CLOUTERRE

C. PLUMELLE AND F. SCHLOSSER

CLOUTERRE, a national research project on soil nailing, was performed in France during 1986–1990 to study the behavior of nailed soil retaining walls, develop design methods, and publish a French code of practice for building temporary and permanent nailed soil walls. Three full-scale experiments are described: a nailed soil wall pushed to failure, a wall built to study its stability during the excavation stages, and a simulation of failure due to the lack of adhesion on the bars. The nails, soil, and wall facing were instrumented to measure the displacements, forces, and stresses generated in the soil and reinforcements.

Soil nailing, invented in France, is a technique of in situ soil reinforcement using steel rods that interact with the soil. It is equivalent to reinforced earth for soils in a cut (*1*). Recent important developments in the soil-nailing technique have resulted in a research project called CLOUTERRE. Industrial laboratories, universities, consulting engineers, and major contractors participated in this project; their aim was to complete a major test and study program and propose a code of practice for building temporary and permanent nailed soil walls. The code was to be published in 1991.

Several job sites were instrumented and monitored, and three full-scale experiments were conducted to study the three types of failure shown in Figures 1–3. This paper describes the significant results of these three experiments.

SITE PREPARATION

The experiments were conducted at the Centre Expérimental du Bâtiment et des Travaux Publics (CEBTP) in Saint-Rémy-Les-Chevreuse, near Paris.

The backfill sand was of uniform gradation; it is referred to as Fontainebleau sand. The minimum and maximum densities of this sand were 1.31 kN/m^3 and 1.69 kN/m^3, respectively. The density after compaction in 20-cm-thick layers was 1.51 kN/m^3, equivalent to a medium-dense sand with an index density of 0.6. At this relative density, the sand had a dilatant behavior. The static pressure transducer (SPT) results (Figure 4) ranged from 8 blows per 0.3 m at a depth of 1 m to 15 blows per 0.3 m at a depth of 5 m; the limit pressure (p_l) and the modulus (E_m) measured by the Menard pressuremeter are also given in Figure 4. The sand's strength characteristics established in the laboratory were $\phi' = 38$ degrees and $c' = 3$ kPa. In comparison, $\phi' = 34$ degrees and $c' = 0$ were obtained by a phicometer (*2*) at a depth of 1.5 m.

C. Plumelle, Centre Expérimental du Bâtiment et des Travaux Publics, Domaine de St Paul, 78470 St-Rémy-Les-Chevreuse, France. F. Schlosser, TERRASOL, Tour Horizon, 52 quai de Dion Bouton, 92806 Puteaux Cédex, France.

WALL 1: FAILURE BY BREAKAGE OF BARS

Before construction of the nailed wall, a soil mass 7 m high was created. The soil was excavated and the wall built in layers, meter by meter. The vertical distance between the nails was 1 m, and the horizontal spacing was 1.15 m (Figure 5).

The characteristics of the nails were chosen so that the nails would fail by breakage or large deformations and not by pull-out (*3*). These characteristics required a design safety factor of 1.1 against the breakage of the bars.

The nailed sand mass was instrumented to follow the movements of the facing and the soil and to determine the strengths at the head and along the nails during construction of the nailed wall and during collapse.

Figure 6 indicates that the ratio T_o/T_{max} between the tensile force at the head (at the facing) and the maximum tensile force decreased as construction progressed. At the beginning of construction the ratio was about 1 and at the end it was about 0.7.

When the wall was finished, the nailed soil mass was progressively flooded with water from the top to increase its density and decrease its cohesion. This kind of failure was chosen to simulate the stresses that develop during a flood, major precipitation, or snowmelt in northern countries or mountains.

The flooding did not completely destroy the structure. The nailed wall, however, subsided 27 cm from its previous level. It advanced 8 cm at the top and 19 cm at the foot (*3,4*). During construction, knowledge of inclinometer displacements and the maximum tensile force line allowed the prediction of the failure zone (Figure 7). This conclusion is important because it shows that the failure design methods of TALREN (*5,6*) type are correct; thus, they will be adopted by the code of practice.

After failure, the nailed soil zone was excavated. The nails had suffered large bending deformations, and some of them were broken. Measured positions of the bands of black sand permitted reconstruction of the failure zone (Figure 8). One can note that the maximum tensile force line lies within the failure zone (Figure 9).

During construction, the tensile force in the nail was the first resisting force to be mobilized. However, before failure and under large deformations, the bending stiffness of the nails was also mobilized (Figure 10).

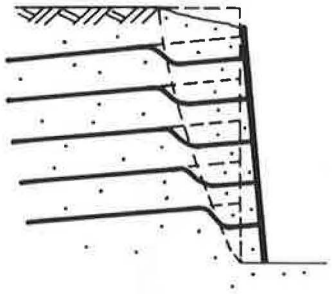

FIGURE 1 Failure of nailed soil mass due to breakage of bars.

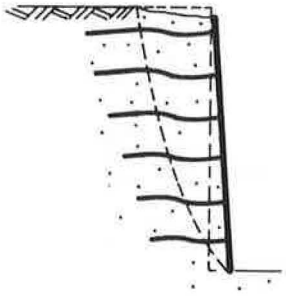

FIGURE 2 Failure of nailed soil mass during excavation.

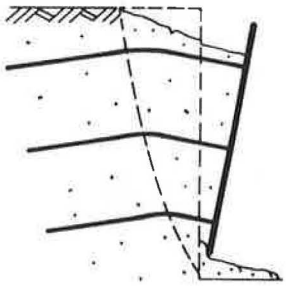

FIGURE 3 Failure of nailed soil mass due to lack of adhesion on bars.

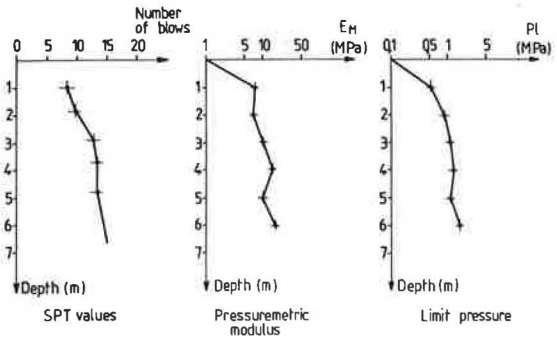

FIGURE 4 Results from SPT and pressuremeter tests.

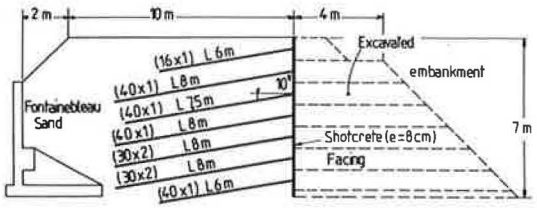

FIGURE 5 Layout of full-scale experiment, Wall 1.

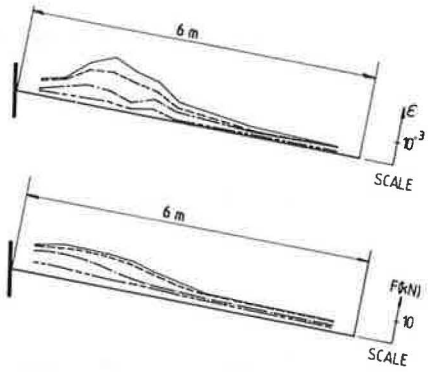

FIGURE 6 Distributions of strains and strengths, Nail 3, Phases 4 to 7.

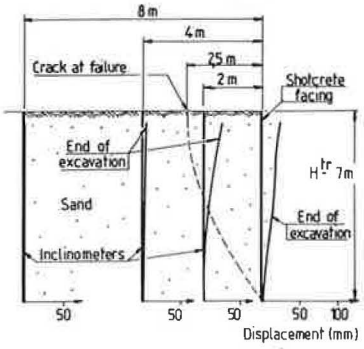

FIGURE 7 Horizontal displacements and failure zone, Wall 1.

WALL 2: FAILURE DURING EXCAVATION

Description of Experimental and Lateral Walls

The sand mass, 6 m high and 2 m wide, was constructed inside two walls made of boards. The boards were constrained by two lateral walls made of formworks and anchored by bolted rods on UAP embedded in the soil (Figure 11).

During backfilling, the sand mass was buttressed by metallic panels braced on a frame made of twin HEBs. Starting from the bottom, there were three removable panels 1 m high (Panels 1, 2, and 3) and a fixed panel that was to be nailed 3 m high (Panel 4). The sand was put on both sides of the board walls simultaneously to create an experimental sand

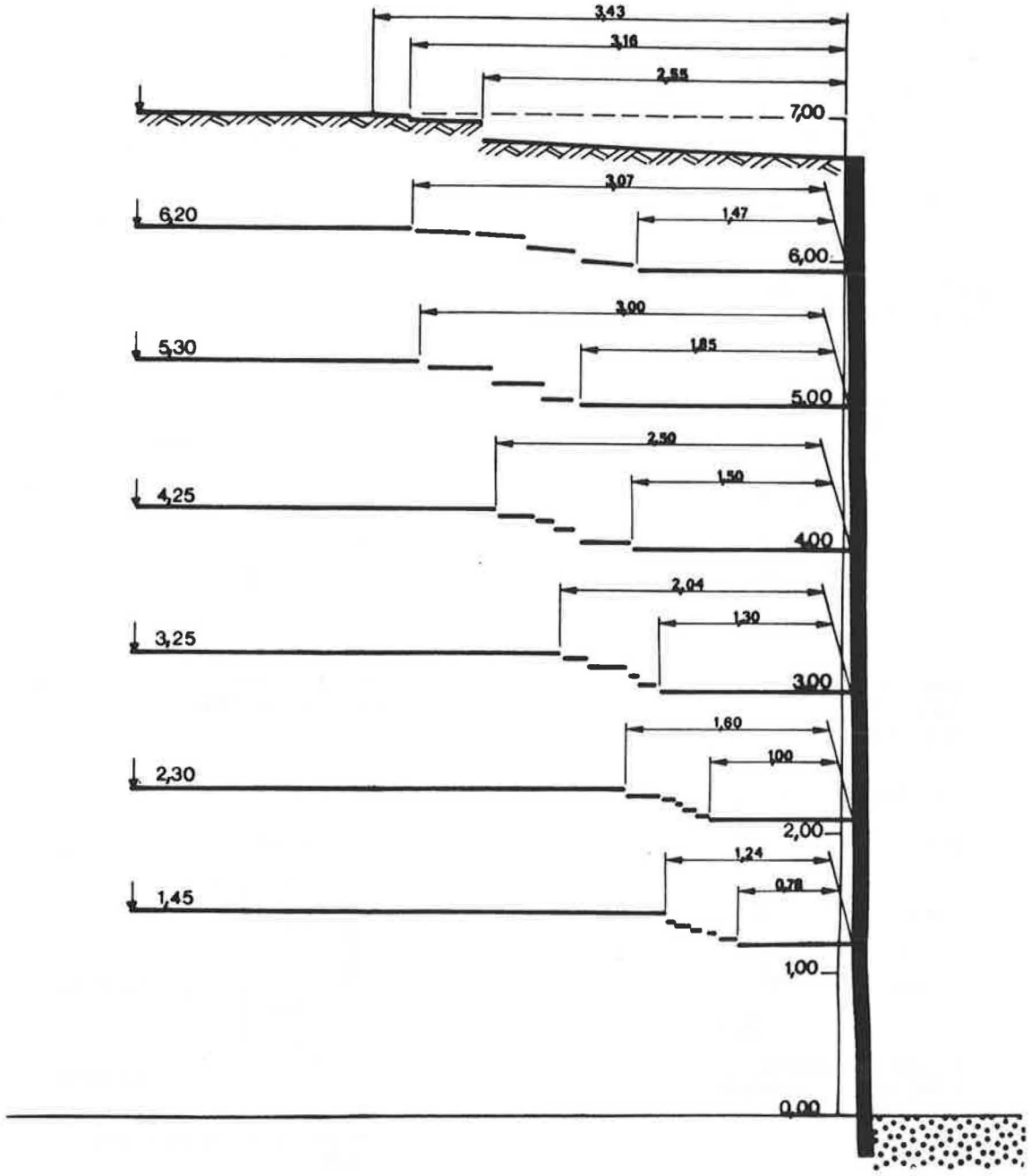

FIGURE 8 Displacements of bands of black sand after failure of nailed mass.

mass and two laterals walls. The board walls were covered inside with a greased double layer of plastic to prevent friction on the sides and to enforce plane strain conditions (Figure 11).

Nailing of Fixed Panel

Panel 4 was nailed with six nails made of aluminum tube (40-mm diameter, 1-mm wall thickness) and sealed with liquid cement in a 63-mm-diameter borehole. Each nail was 6 m long (Figure 11).

Instrumentation of Facing and Nailed Mass

At each phase the horizontal and vertical movements of the shotcrete facing were followed by microtriangulation.

The six nails were equipped with an electrical dynamometer to measure strengths at the head, and one nail per layer was instrumented with seven pairs of strain gages. The calibration of one identical nail under tensile force during the experiment on Wall 1 allowed the forces to be taken from the strains. Finally, during the construction of the sand mass, a horizontal band of black sand was placed at every meter along the axis of the wall.

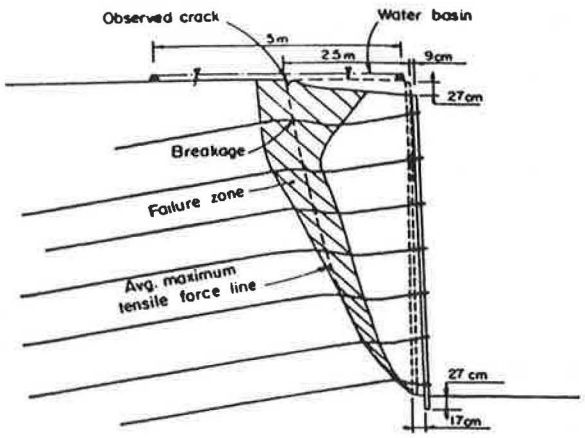

FIGURE 9 Failure zone developed in nailed soil wall.

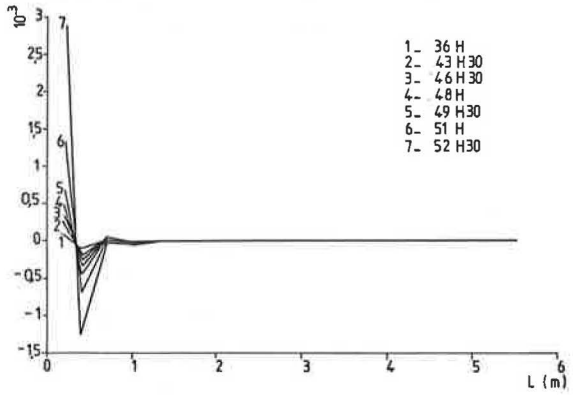

FIGURE 10 Bending moment strains just before failure.

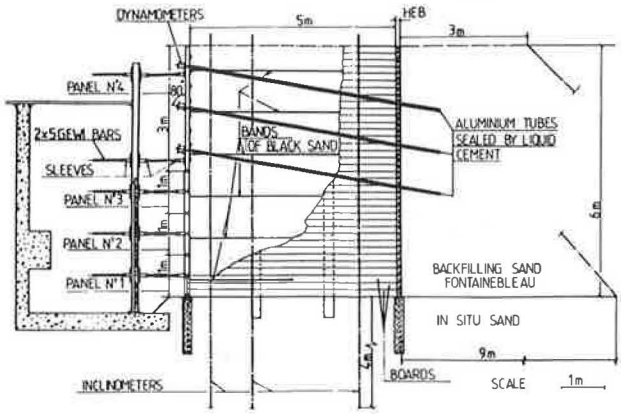

FIGURE 11 Layout of full-scale experiment, Wall 2.

Execution of Experiment

Aims

The aim of the experiment was to find, as the depth of excavation increases, the development of

- Stable excavation,
- Local instability, and
- Global instability.

In this study Panel 4 simulated a nailed wall that would be 3 m high, and Panels 3, 2, and 1 simulated excavation phases of 1, 2, and 3 m, respectively. During the experimental phases the behavior of the nailed mass was recorded as the displacements of Panel 4 and the strengths at the head and along the nails were measured.

Removal of Panel 4

To remove Panel 4 from its bars, the sleeves were unscrewed, putting the six nails under tensile stress.

Removal of Panel 3

To remove Panel 3 from the frame (Figure 12), two jacks were fixed on two HEBs of the frame and the sleeves that overtightened it were unscrewed simultaneously. The soil was intact and showed no cracks.

Removal of Panel 2

Panel 2 was removed in the same manner as Panel 3. When this panel was removed, a crack appeared under Panel 4. This crack grew until the sand fell and created a soil arch (Figure 13). This arch remained stable during the 24 hr preceding the last phase.

Removal of Panel 1

In the beginning of the last phase, the arch began to crack. The failure occurred for a 45-mm removal of the panel. When

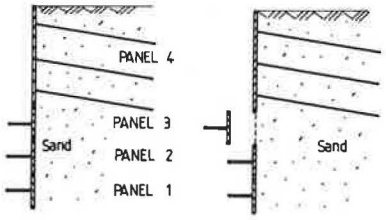

FIGURE 12 Test layout.

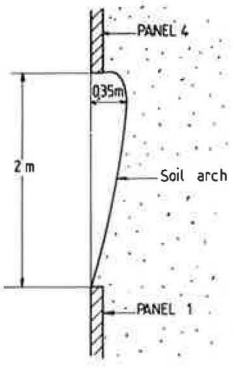

FIGURE 13 Cross section of soil arch.

the arch cracked, it induced a global instability in a few seconds. The nailed panel subsided 1.4 m but remained attached to the six nails, which did not break (Figure 14).

The excavation of the nailed sand mass allowed the discovery of the nail deformations and the reconstruction of the profile of the sand zone that had slipped.

MEASUREMENT RESULTS

Displacements of Panel 4

The displacements of the panel were in the same range as Wall 1, which had a 3-mm horizontal displacement of the facing in the third phase.

Evolution of Strength at Head

Figure 15 shows the evolution of the force at the head of the nails during each phase. Notice during Phase 1 of panel removal that mainly the first layer of nails was under stress; the bottom of the nailed panel was lying on Panel 3.

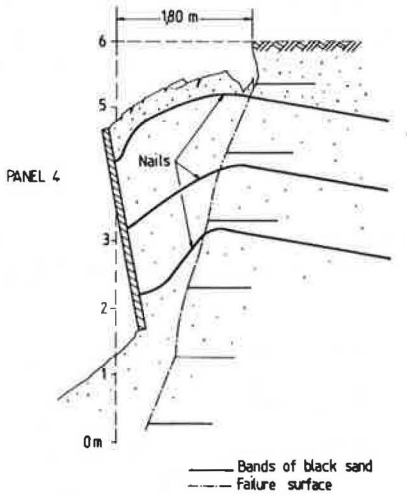

FIGURE 14 Cross section of failure.

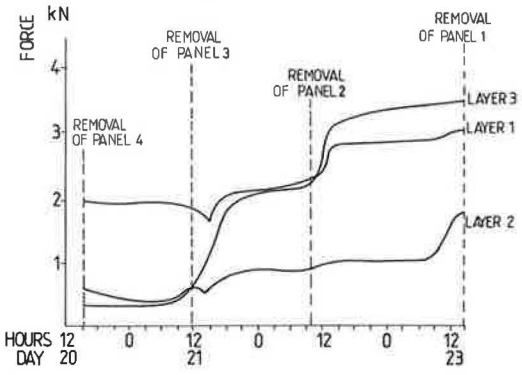

FIGURE 15 Evolution of strength at head for each phase.

During Phase 2, which simulated 1-m-deep excavation, forces on the first layer of nails did not significantly increase, but the nails of the third layer were rapidly put under stress.

The creation of the arch during Phase 3 with a 2-m-deep excavation insignificantly increased forces, but forces did increase in the third layer as it responded to the arch pressure.

Distribution of Forces Along Nails

Figures 16–18 synthesize the evolution of the tensile forces along the nails of the three layers versus phases. The third phase represents the last stage before failure. Note that the creation of the arch involved an increase of the tensile force only in the first layer.

The maximum tensile force points were the same as they were in the first nailed wall. They were located in the back of the facing; before the failure they were 2 m from the facing for the first layer and 0.7 m for the last layer.

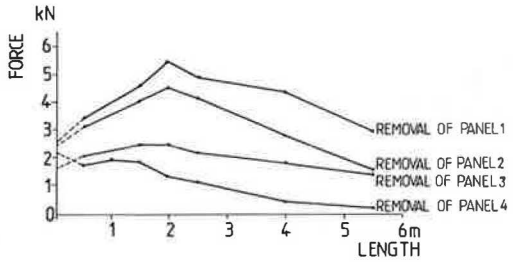

FIGURE 16 Load distribution along Nail 1 for each phase.

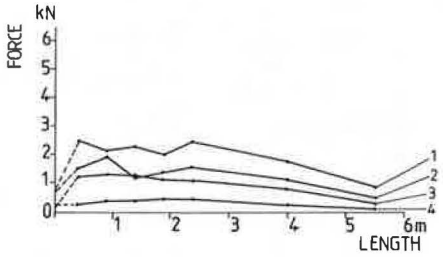

FIGURE 17 Load distribution along Nail 3 for each phase.

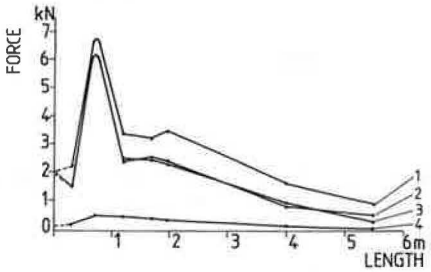

FIGURE 18 Load distribution along Nail 5 for each phase.

WALL 3: FAILURE FROM LACK OF ADHESION ON BARS

Description of Experimental and Lateral Walls

Construction of the sand mass backfilling, 6 m high and 2 m wide, was similar to that of Wall 2. Starting from the bottom, there were six removable panels 1 m high (Figure 19).

Construction of Nailed Wall

The wall was nailed by telescopic nails made of bars (50-mm diameter) inside tubes (71-mm diameter) driven into the sand, as shown in Figure 20.

Displacements of Nailed Mass

Displacements plotted on Figure 21 were measured at the end of the construction of the nailed wall and at the 12th stage of shortening of nails (4 stages before failure), for which nails

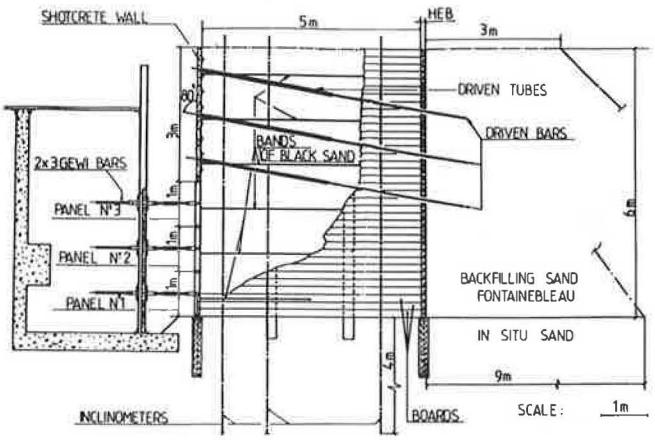

FIGURE 19 Layout of Wall 2 at end of Phase 3.

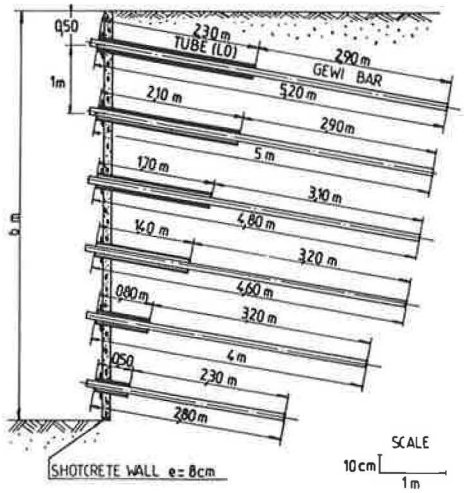

FIGURE 20 Scheme of Wall 3 at end of construction.

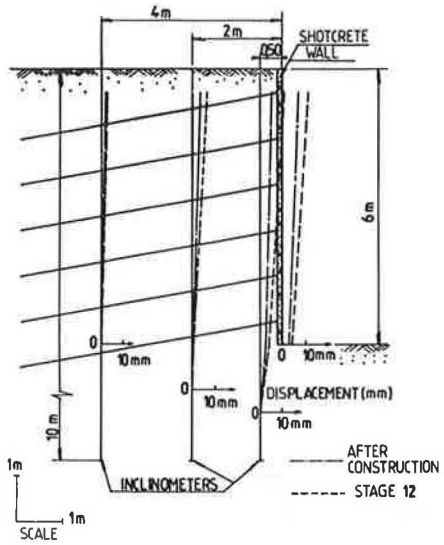

FIGURE 21 Measurements of horizontal displacements.

of the first layer were 2.3 m long; those of the second layer, 2.1 m; and those of four others, 1.8 m. These displacements were displacements of sand just behind the facing measured during excavation by inclinometers and displacements of facing after its construction. These measurements complete those carried out during execution of the Wall 1, during which only displacements of facing had been recorded.

For Wall 3, it should be noted that a horizontal displacement at the end of the construction, with a safety factor larger than 3, was 0.12 percent of total height of the nailed wall. Otherwise, significant displacements of mass of the sand beneath the foot of the facing were recorded.

Forces in Nails

Forces in nails at the end of the nailed wall construction were small but comparable with those recorded during the Wall 1 experiment. The maximum forces, 9 kN, were recorded on nails near the middle of the wall.

FAILURE BY SHORTENING NAILS

The initial length of the nails gave great stability to this nailed mass in the beginning. During the experiment in which the nails were shortened, with the same length of 2.4 m, stability was still maintained. Failure of the sand mass reinforced with tubes of decreasing length with depth occurred not because of the lack of adhesion, but because of the sliding of a block limited by the facing and a surface situated behind the ends of the nails. This block dropped 0.4 m, and the facing subsided 0.3 m beneath its previous level (Figure 22).

CONCLUSIONS

The three full-scale experiments performed by CEBTP focused on failure due to breakage of the bars, failure during

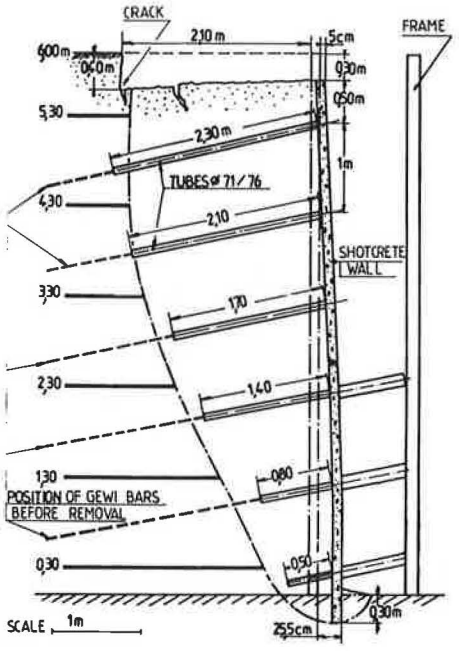

FIGURE 22 Scheme of failure for Wall 3.

a deep excavation phase, and failure due to shortening of the nails. The main conclusions from these tests are

- The maximum tensile force is not located at the front of the wall but at some distance from the facing; the ratio T_o/T_{max} decreases as the excavation progresses.
- The line of maximum tensile forces lies within the failure zone.
- The first resisting force to be mobilized is the tensile force in the nail. Before failure the bending stiffness gives an additional safety factor and prevents a sudden collapse.
- These results demonstrate that the TALREN method (*5*) is capable of accurately predicting the behavior of a nailed soil wall taken to failure.
- The excavation phases are difficult stages during the construction. If the depth of the cut is too great, a soil arch develops and the displacements of the soil above remain small. For a deeper excavation the soil arch becomes unstable and a sudden failure occurs.
- The horizontal and vertical displacements are the same at the head of the facing. The range is between 0.1 and 0.3 percent of the total height of the wall. The displacements depend on the safety factor, and they decrease as the safety factor increases.
- Significant displacements appear beneath the foot of the facing as the excavation progresses.
- Nails having great inertia give stability to the soil mass. In this case the slip surface for shortened nails occurred behind the nails.

REFERENCES

1. F. Schlosser. Analogie et différence dans le comportement et le calcul des ouvrages de soutènement en terre armée et par clouage du sol. *Annales de l'Institut Technique du Bâtiment et des Travaux Publics*, No. 418, 1983, pp. 8–23.
2. G. Philipponnat. Le Phicomètre. Essai de cisaillement in situ. *Revue française de Géotechnique*, No. 35, 1986.
3. C. Plumelle. Expérimentation en vraie grandeur d'une paroi clouée. *Revue française de Géotechnique*, 1987.
4. C. Plumelle et al. Expérimentations du projet national français sur le clouage des sols. *Proc., 12th International Conference on Soil Mechanics and Foundation Engineering*, Balkema, Rotterdam, the Netherlands, 1989.
5. F. Schlosser. Behavior and Design of Soil Nailing. *Proc., Symposium on Recent Developments in Ground Improvement Techniques*, Bangkok, Thailand, 1982, pp. 399–413.
6. F. Schlosser, H. M. Jacobsen, and I. Juran. Soil Reinforcement, General Report-Speciality Session 5. *Proc., 8th International Conference on Soil Mechanics and Foundation Engineering*, Helsinki, Finland, 1983, pp. 1,159–1,180.

Publication of this paper sponsored by Committee on Mechanics of Earth Masses and Layered Systems.

Construction of a Geogrid- and Geocomposite-Faced Soil-Nailed Slope Reinforcement Project in Eastern Canada

COLIN ALSTON

A case history of a project involving the installation of soil nails with a connected protective membrane facing as a slope-reinforcement technique is presented. The project involved the reshaping of a naturally stable hillside in Cambridge, Ontario. This slope is formed of very dense glacial till material that was resting at a gradient of 1v:2h, before construction; project requirements necessitated developing the slope at a grade of about 3v:1h. The construction involved the installation of a soil nail reinforcement system to permit the development of an 18-m-high slope. At the highest point, the upper 12 m of this slope is permanent; the lower 6 m was a temporary slope excavated to permit basement construction to proceed. Three slope facing systems were used. In one system a facing of nonwoven geotextile restrained by geogrids tied to the soil nails was applied; a sand, topsoil, and water slurry was injected behind the facing to serve as a void filler and to tension the membrane. In another portion of the slope a geocomposite wall was constructed in front of the soil nail-reinforced slope, and this was tied to the soil nails using geogrid. The third system, which was applied to the temporary slope, consisted of a single membrane of woven geotextile tied to the soil nails with anchor blocks. The reinforced slope has proved to be satisfactory through two winters and two spring thaws. Selection of the soil nail support system for the project was based on economic considerations, and the selection resulted in considerable cost savings for the owner.

A case history of soil nail design and installation is presented for a site in Cambridge, Ontario, that has been developed to permit construction of a highrise condominium. The site is on the side of a relatively steeply sloping river valley, such that the development required considerable encroachment into the slope of the valley side.

The original concept for supporting the excavation was to construct two separate retaining structures: a soldier pile and lagging wall was to have served as temporary support for the basement levels; the upper slope, which extends from the main floor level to the crest of the slope, was to have been supported permanently by a reinforced concrete gravity retaining wall. The maximum supported slope height was to be about 18 m, to be reduced to 12 m after completion of the basement structure. However, it was found that this original earth retention concept could not be constructed without temporary mechanical support because it would have required encroaching into land not owned by the developer, and the adjacent land owners were not willing to permit any construction within their properties. The original concept was therefore impractical.

At this stage, the author reviewed the geotechnical design of the project, and as a result of this review an alternative was proposed in which a system of soil nailing would be installed to support the reprofiled slope. The soil nails were to be designed to replace both the upper permanent reinforced concrete retaining wall and the lower temporary soldier pile and lagging wall. The principle virtues of the new (soil nail) concept to the developer were that (a) no negotiations were required with the adjacent property owners for excavation easements because the reprofiled slope could be constructed from the top down (starting at the intersection of the cut slope with the crest) rather than from the more conventional bottom up, and (b) there would be a substantial cost saving to the project.

SITE AND SUBSURFACE CONDITIONS

The Cambridge condominium site is located on the north bank of the Eramosa River valley. At this location, the slope has developed naturally to a gradient of about 1v:2h. The subsurface conditions at the site consist of a compact, rapidly becoming very dense till stratum overlying bedrock. Although principally silty in character, the composition of the till is somewhat variable, ranging in gradation from silty clay to silty fine sand. Much of the soil deposit is highly susceptible to frost, and it is also susceptible to piping in the event that seepage from the slope were to be unrestrained. The compact condition of the soil is represented by standard penetration test *N*-values ranging from 30 to more than 100 and typically more than 60 below a depth of 3 m. The more clayey zones of the deposit are concentrated in lenses, and the soil immediately above most of the clayey lenses was found to be saturated; thus, several perched water tables are present within the slope. Another consideration of the variable moisture condition of the soils exposed in the slope is that free water is available as a source for ice lensing under freezing conditions in the highly frost-susceptible silt soils that predominate in the slope.

Observations of cuts made into the hillside at an early stage in construction indicated that the native soil was able to stand unsupported at a nearly vertical inclination for 1 to 2 weeks before deterioration began to affect the stability of the cut face.

Geo-Canada Ltd., 90 Nolan Court, Unit 17, Markham, Ontario L3R 4L9, Canada.

DESIGN CONSIDERATIONS

The project required the design of the slope stabilization system to take into account that the upper portion of the reprofiled slope would be permanent and exposed, whereas the lower portion of the slope was to be temporary, required only for the duration of basement wall construction.

At the design stage, it was expected that the temporary slope would be required only to provide support for a maximum of 2 months in fall and that all the elements of the substructure would be complete before the onset of winter. There was, therefore, no perceived need to design the facing to the temporary slope to withstand freezing forces or heavy lateral pressures resulting from temporary loss of soil strength during the thaw. The (permanent) retained slope carried a trunk water main at its crest that had to remain in service and could not be interrupted or relocated. However, no superimposed loads were expected to be applied to the tableland at the crest.

As noted, the native soils at the site are susceptible to frost. Hence, it was required that the external sheeting membrane to be applied to the permanently exposed slopes be designed to accommodate continuing cyclic soil volume changes and corresponding load variations without rupturing. The membrane would also be required to facilitate drainage from saturated zones in the slope face and prevent the occurrence of piping.

The other consideration at the site was aesthetic: the condominium development was geared to the upper end of the market, so engineering design was to make allowance for the wishes of the project's landscape architect. This was achieved by constructing the slope in a series of terraces, each being about 3 m high, and with a bench about 1.2 m wide. These terraces were designed to extend over the entire height of the permanent slope (see Figure 1). Planters were to be placed on each of the terraces.

SLOPE DESIGN

General

In plan, the excavation entailed removing from the hillside a prism of ground that had a triangular footprint. The height of the excavation was a maximum of about 18 m at the intersection of the two faces of the wedge, and this tapered out with distance away from this intersection. Typical cross sections that illustrate high and low areas of reinforced slope are given in Figure 1, which also shows the relationship of the permanent to temporary slope heights. The west and north excavation faces were approximately 90 and 80 m long, respectively.

Soil Nail Design

The design of the soil nail system was based on the method given in the *NCHRP Report 290* (*1*), and it relied on tensile forces in the soil nails only; no benefit for the shear resistance of the nails across a potential sliding surface was allowed. A straight failure plane was assumed for stability analyses, and only a nominal surcharge loading was allowed on the tableland at the crest of the slope. In the absence of a Canadian code of practice, the design was prepared to conform with safety standards recommended by Stocker et al. (*2*). The specified nail was a "Dywidag" threaded steel bar with a guaranteed minimum yield stress of 415 MPa and diameters of 22 or 25 mm (depending on slope height); they were installed in 100-mm-diameter drilled holes. The bars were grouted into the drill holes with a cement–fly ash grout with a water/cement ratio of 0.4 and a compressive strength of 25 MPa. The design of the nail system was carried out using an angle of internal friction of the very dense till of 38 degrees and a unit weight of 22.5 kN/m^3.

The nails were installed on a 1.8- × 1.5-m grid, in all sections of the slope. The nail lengths for various sections of slope are given in Table 1.

As described, the project requirements dictated two slope conditions: a permanent slope of variable height and a lower temporary slope that increased the total height of retained soil by 6 m. Thus, the stresses in the soil nails in the short term were significantly larger than in the long term. Taking into account the lower long-term stresses, the tensile strength of the installed soil nails is not fully used. Thus, by comparing the forces applied over a reduced area to allow for corrosion, an approach now confirmed by Schlosser and Unterreiner in a paper in this Record, there was found to be no need to encapsulate the steel tendon with a plastic sheath. The outer 2 m of the nail was given two coatings of zinc paint as corrosion protection.

The prepared soil nail design was compared with published case histories of successful installations and design charts before being made final (*3–5*).

Design of Facing Membranes

Considerable attention was given to the selection of the slope face membranes. As noted, it was believed necessary to provide a surface membrane that would retain its strength properties through cyclic loading caused by soil expansion due to seasonal freezing in the permanent section of the slope. Furthermore, in view of the several perched water tables found in the slope and the frost-susceptible character of the native soils, it would be a significant advantage to apply a facing membrane with good drainage characteristics. This would then limit the supply of free water to fuel the growth of ice lenses, in turn reducing tension loads on the soil nails under winter conditions. It was also necessary for the membrane to conform to the terraced slope profile design that was acceptable to the landscape architect. Because of aesthetics, the owner was unwilling to accept a shotcrete facing membrane; a shotcrete facing was also expected to be inefficient at permitting drainage through the membrane as well as to be intolerant to soil movement caused by the formation of ice lenses in the retained soil.

The initially selected membrane system was a combination of geogrid and geotextile. The geotextile was used to permit the exit of groundwater from the slope but at the same time retain soil, thereby eliminating the risk of piping. The grid was used to transfer earth pressures to the soil nails by spanning between levels of soil nails. A system of 65- × 65-mm

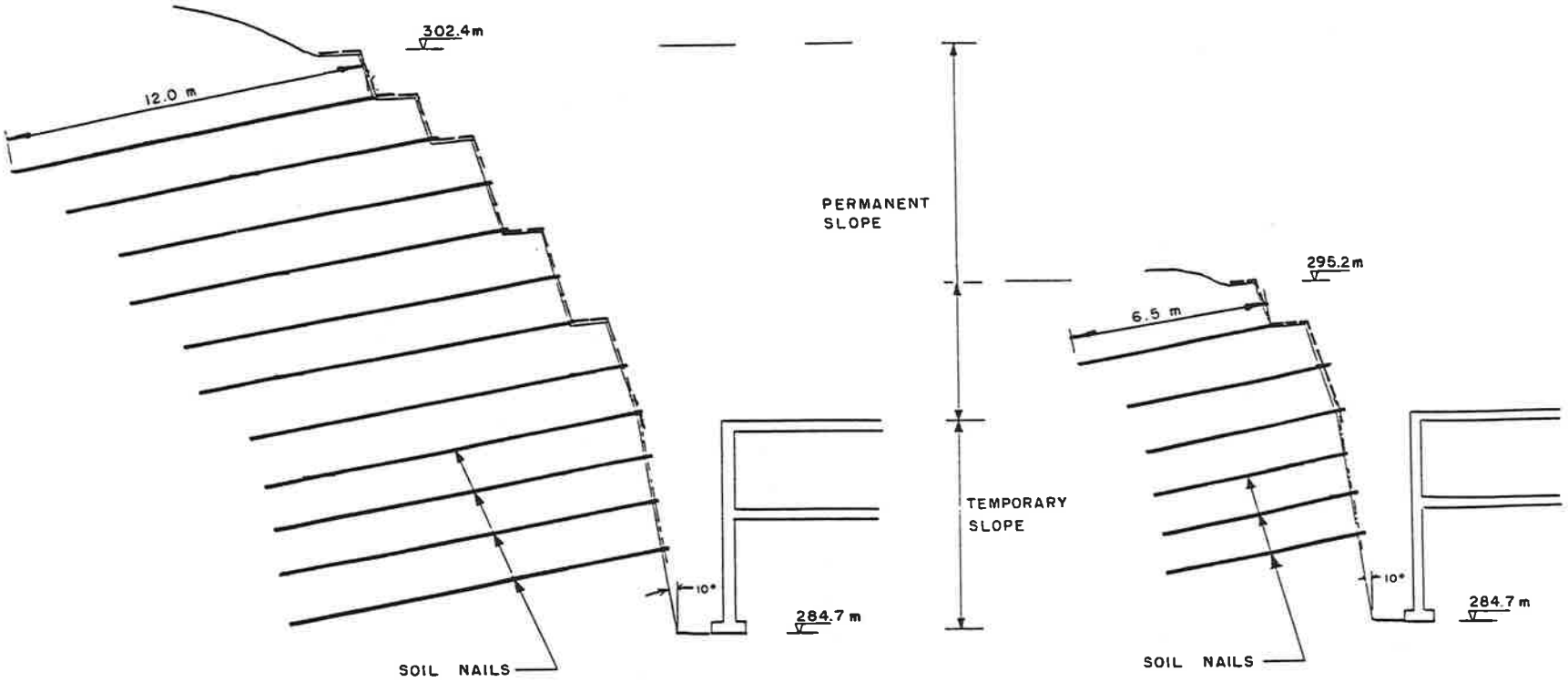

FIGURE 1 Typical cross sections through soil nail reinforced slope.

TABLE 1 SOIL NAIL LENGTHS FOR VARIOUS SLOPE HEIGHTS

Height of Slope		Length of Soil Nail (m)
Permanent (m)	Temporary & Permanent (m)	
4.5	10.5	6.5
8	14	8.8
12	18	12.0

angle bars was used to pick up the earth pressure loads from the geogrid membrane and to span between adjacent soil nails in the horizontal direction (Figure 2). The membrane chosen to provide the strength properties was an unequal bidirectional geogrid in which the prime reinforcement was aligned vertically and the secondary reinforcement horizontally. To accommodate the expected cyclic movement of soil in the face and to protect the reinforcing strands from atmospheric degradation, a grid with multiple polyester strands enclosed in polyolefin with a long-term allowable design load (LTADL) (i.e., design tensile capacity) of 40 kN/m width was selected. Beneath this geogrid, the nonwoven geotextile was used to keep the soil fines from escaping and to prevent surface erosion.

The geotextile was constructed of polyester fibers; it had a mass of 375 g/m^2 and an EOS of 75 μm. The geotextile-geogrid membrane was connected to the soil nails with a system of angle bars that span horizontally between adjacent nails. The angle bars were coated with zinc primer paint and compatible overcoatings of corrosion protection. Application of the membrane consisted of draping the geotextile and then the geogrid over the profiled face of the slope. The angle bars were then placed on top of the membrane and connected to the nails.

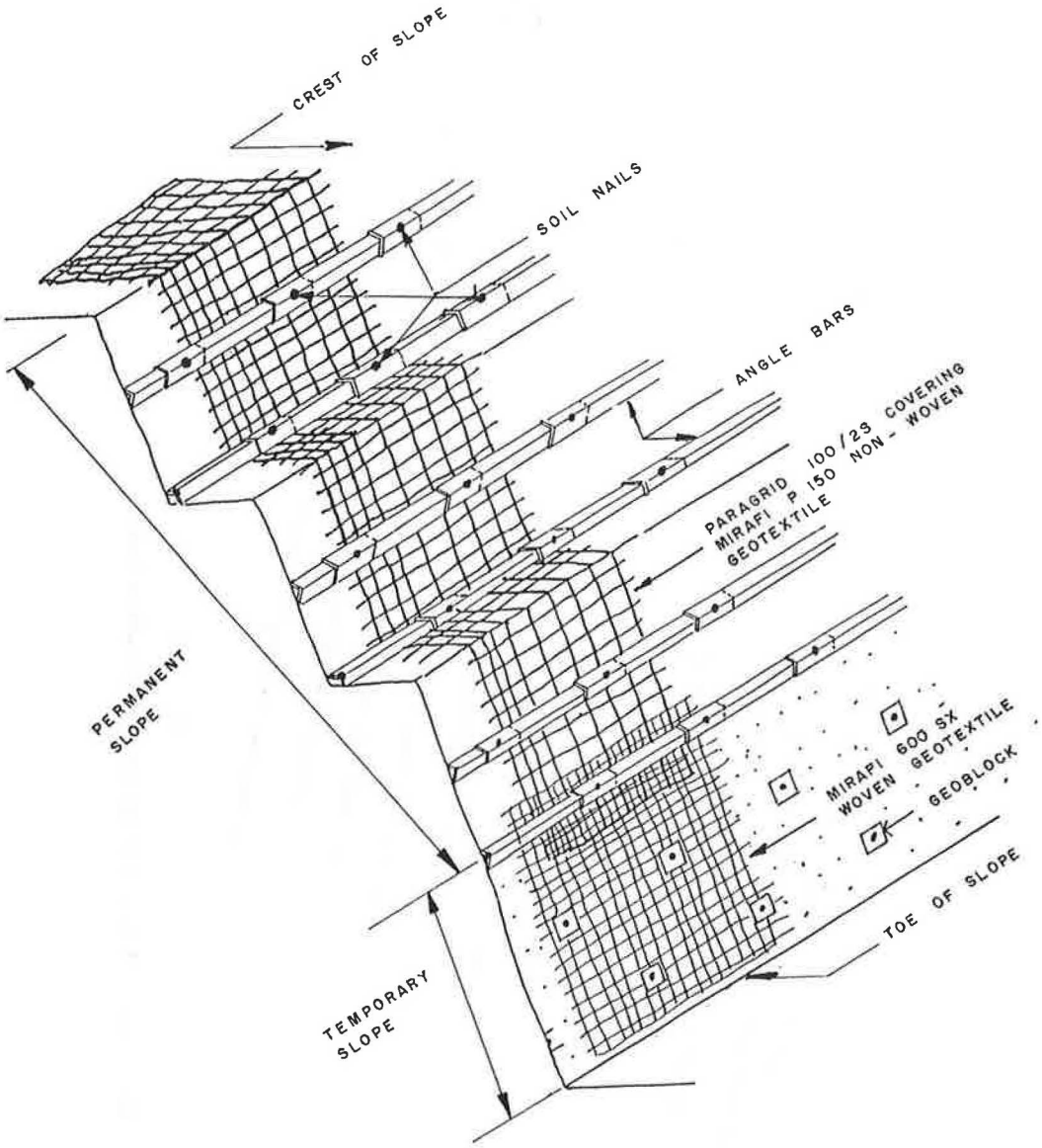

FIGURE 2 Schematic illustration of geotextile-geogrid surface covering of permanent and temporary slopes.

The action of drawing the angle bars to the face of the slope was used to tension the membrane and bring it into contact with the profiled slope. The loads in the membrane and angle bars were determined using the method given in *NCHRP Report 290* (*1*).

After the geogrid-geotextile complex was installed and tensioned, a sand, topsoil, and water slurry mixed in approximately 1.5:1:1 proportions was injected between the geotextile and the native soil as a void filler. The mixture was injected using a gravity-fed funnel and tubing arrangement with pressure being applied with a 1.5-m head of slurry. This method was adopted after trials using a slurry pump to inject the mixture found the pump to be much less effective than was hoped.

Circumstances necessitated a change in facing membrane design over part of the length of the retained slope. A wet area in the slope face (later found to be a consequence of a leak in the water main buried in the crest of the slope) collapsed continually and progressively, and winter came before the area could be stabilized. The face of this portion of the slope remained unrestrained throughout the winter. The winter of 1988–1989 was severe on the incomplete structure in that there were many freeze-thaw cycles and heavy rains alternated with snow. As a consequence, the completely unprotected portion of the "terraced" slope deteriorated and the face slumped to expose a succession of steep scarp slopes. To reduce additional deterioration of the partly slumped slope through the main spring thaw, a restraining membrane of nonwoven geotextile held in place by a timber grillage connected to the soil nails through the angle bars was applied to the soil face. In the spring, a new face had to be constructed and connected to the soil nail reinforcing system.

The face design selected for reconstruction of the deteriorated area of slope featured a facing of geocomposite (Geoweb infilled with sand) with a geogrid-reinforced granular infill placed between the geocomposite and the face of the scarp slope. The design of this section of face was developed on the presumptions that soil nails stabilized the retained slope and that the geocomposite would be required to support the forces developed in the active wedge of soil; these forces were transferred from the face into a reinforced backfill, and to the nails, with horizontally laid sheets of geogrid. The tensile forces in the geogrid and the active pressure were calculated using the method described by Jones for a sloping reinforced structure (*6*).

The Geoweb material was manufactured from 200-mm-wide strips of high-density polyethylene ultransonically welded together to give an open-cell construction having a cell diameter of 200 mm. The concept behind the use of this material in earth works is that when the Geoweb is expanded and infilled with granular material, the cells of the web laterally confine the soil to provide a stable soil-geosynthetic composite. For slope works, the cell structure effectively confines the infill soils so that raveling or sloughing of the slope face is prevented. The Geoweb fascia was also chosen because it is easy to form, it facilitates longitudinal wall contours, and it can be placed rapidly by unskilled labor with a minimum of training; in addition, the exposed cells in the structure can be vegetated (*7*). The geogrid reinforcement for the reconstructed portion of the slope was provided using an uniaxial geogrid, also of multistrand polyester construction, with an LTADL of 15 kN/m. The grid was installed at 0.6-m vertical spacings, and every other grid sheet (or every third, depending on vertical positioning) was tied back to the angle bars, which were in turn attached to the soil nails, thereby connecting the geocomposite facing to the soil nail reinforcement system. Pullout resistance of the geogrid at the geocomposite facing was attained by frictional forces (Figure 3).

In the temporary portion of the slope, the purposes of the surface membrane were to control surface erosion and to retain any minor dislodgements that might occur in the face of the slope. This slope was constructed without any architectural features, at an inclination of 10 degrees to the vertical. For the stated purposes a woven geotextile constructed of polypropylene material was thought to be acceptable for the 2-month design lifespan of the surfacing membrane, and a woven geotextile with a tensile strength of 1350 N was applied (Figure 2). This geotextile was secured to the soil nails with 300-mm² blocks ("Geoblocks") attached to the nails by nuts threaded onto the soil nails. Void filler was not injected behind this temporary membrane because of the expected limited design lifetime of this section and the presumption that it would not be exposed to freezing conditions.

CONSTRUCTION OF SOIL NAIL SYSTEM

The threaded steel bar soil nails were installed in 100-mm-diameter predrilled holes at the design locations in the slope. It was found that in the "dry" areas of the face, the drill holes would stay open without collapse for a few hours. This was long enough to allow several holes to be drilled successively, the threaded bars to be installed in the drilled holes (positions maintained with centralizers), and the bars to be grouted into position by pumping the grout through a 25-mm-diameter tube taped to the bars. The tubes fed the grout to the in-ground end of the nail. The grout was pumped in at low pressure and filled the annulus between the bar and the enclosing soil from the in-ground end outward. Grouting of the annulus was judged complete when uncontaminated grout exited freely at the face of the slope; then the tube was withdrawn.

Where the drill holes intercepted one (or more) of the perched water tables, the unsupported hole collapsed when conventional air drilling methods were used, and soil and groundwater would flow out of the face. At these locations, the drill hole would remain temporarily stable when the drilling was carried out using a venturi bit that injected a flushing air and water mixture both backward and forward. These drill holes were grouted immediately on completion, before the next installation was begun. Several times it was necessary to redrill a hole because of collapse, but never more than once.

At the design stage, the adhesion between the soil nail and the enclosing soil was evaluated using an adhesion factor applied to the overburden pressure (*8*). To verify the tensile capacity of the installed nails, cyclic loading tests were carried out on four specially installed test nails. The results for these tests are presented in Figure 4. Tests were carried out more than 7 days after nail installation. The ultimate tensile load capacity of these nails was estimated using the method developed by Chin (*9*) for evaluating the ultimate load-carrying capacity of a piled foundation that has not been taken to

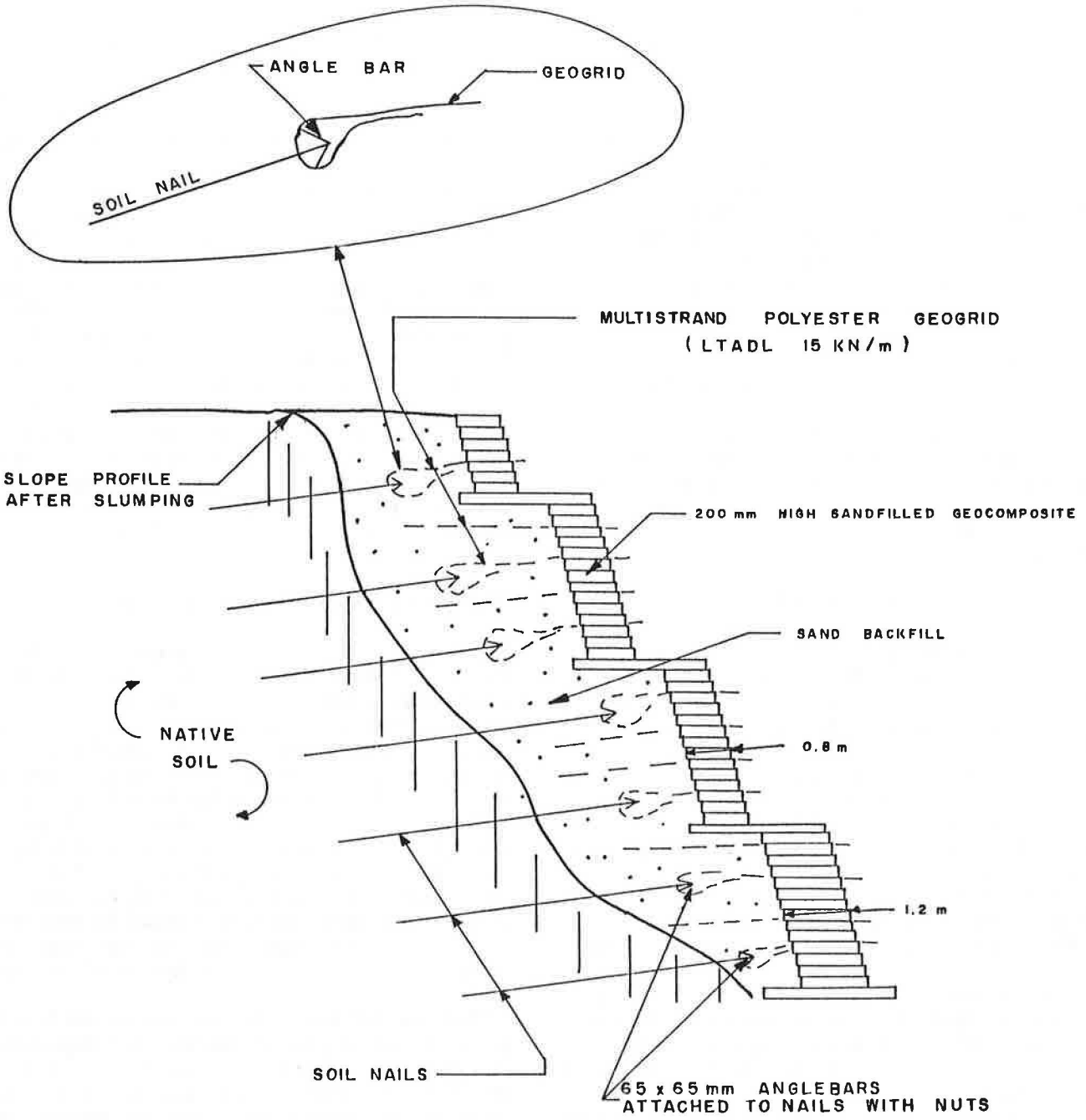

FIGURE 3 Schematic illustration of slope facing construction using geocomposite.

failure. For this analysis, the behavior of the nail was plotted using deflection normalized against tensile load versus deflection of the nail head (Figure 5). The failure load was evaluated from the inverse slope of the plot, and the test results were interpreted to give ultimate adhesions between the grout and the enclosing soil ranging from 225 to 700 kPa. The depth of each of the test nails below the crest and a qualitative estimate of the moisture condition of the soil are given in Table 2. These results illustrate the influence of the moisture condition of the soil on the available adhesion. They also indicate that for the heavily overconsolidated soils found at the subject site, this factor was of greater influence than the overburden pressure.

PERFORMANCE OF STRUCTURES

The performance of the soil nail retaining structure at the site has been generally satisfactory through two winters. The unforeseen major delay that occurred during construction of the building substructure resulted in the temporary slope's having to remain operational well beyond its design lifespan. The

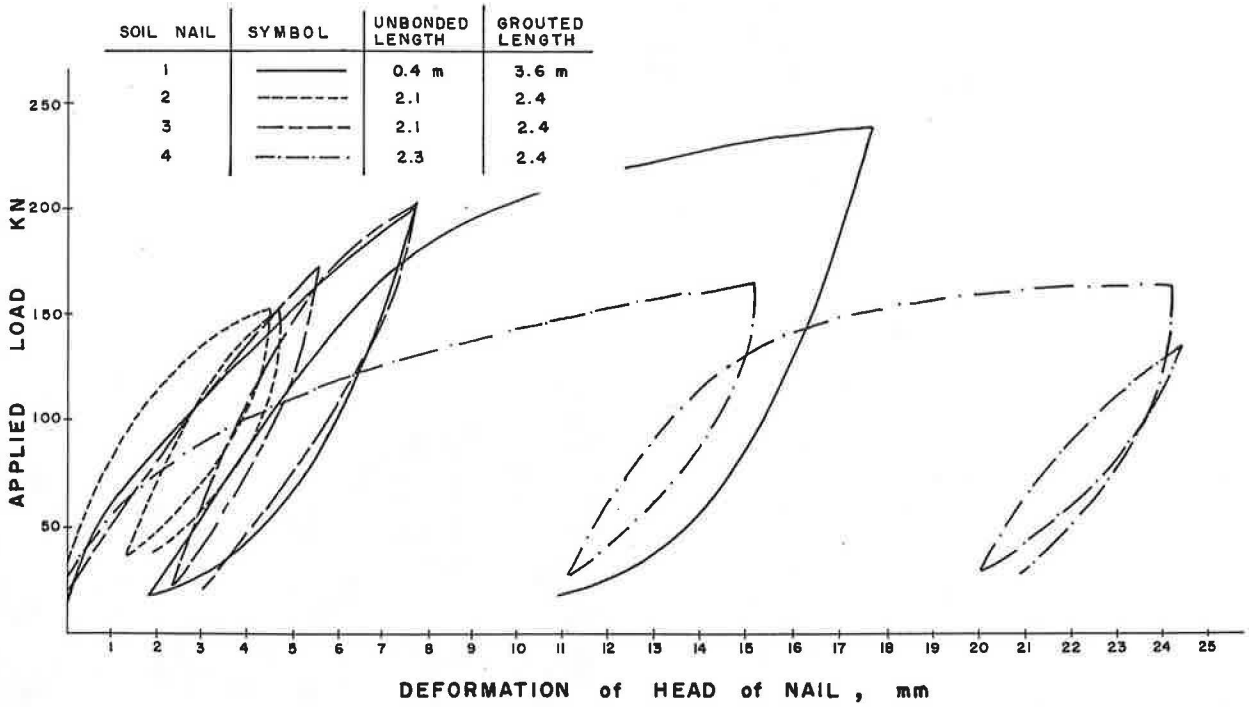

FIGURE 4 Tensile test results for soil nails.

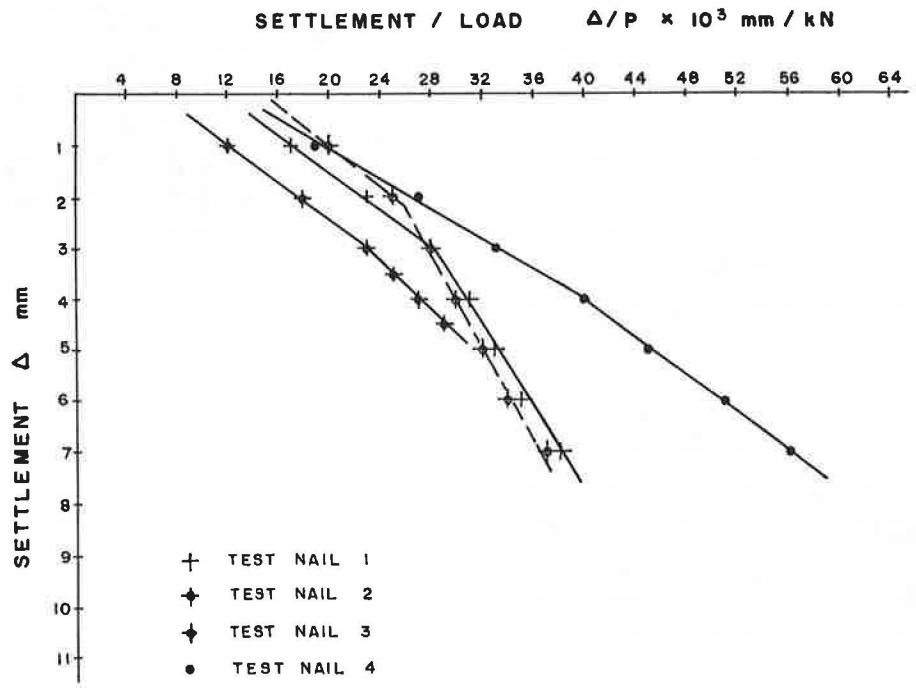

FIGURE 5 Summary of tensile test results for soil nails.

TABLE 2 TENSILE TEST RESULTS FOR TEST NAILS

Test Nail No.	Depth Below Crest of Slope (m)	Moisture Condition of Soil	Representative 'N'-value (blows/0.3 m)	Unbonded Length (m)	Grouted Length (m)	Measured Ultimate Adhesion (kPa)
1	3.0	moist	50	0.4	3.6	700
2	9.0	moist	100	2.1	2.4	475
3	12.0	moist	100	2.1	2.4	600
4	12.0	wet	100	2.3	2.4	255

consequence of this delay was that the temporary slope, including the relatively weak woven geotextile surface membrane, was required to remain in service throughout the entire winter season and spring thaw. During this time, some relatively large slabs of soil dislodged from the soil face, primarily as a consequence of freezing and thawing, and these slabs were too heavy for the woven geotextile surface retention membrane; this resulted in tearing of the geotextile and detachment of the membrane from the restraining blocks that had secured it to the soil nails. Additional support to the temporary slope covering membrane was supplied with a timber grillage in areas where the service life of this slope support system had to be prolonged (Figure 6), and this application was successful.

The unfaced portion of the permanent slope suffered surface deterioration and slumping, and the surface profiling was lost through a succession of minor slumps in the face. This necessitated the rebuilding of the face using the geocomposite wall described previously. There was some loss of the design shape in the portion of the terraced slope that had been covered with geogrid and geotextile, but which had not had the void-filling slurry injected beneath the surfacing membrane before the onset of winter.

The permanent slope at the Cambridge site is now structurally complete; it is being vegetated with creeping vines as visual screening. Photographs of the geogrid-surfaced and geocomposite-faced areas of the slope are presented in Figures 7 and 8. Since the void filler was injected under the geotextile-geogrid surface area of the slope, there has been no further deterioration, and the slope support is satisfactory.

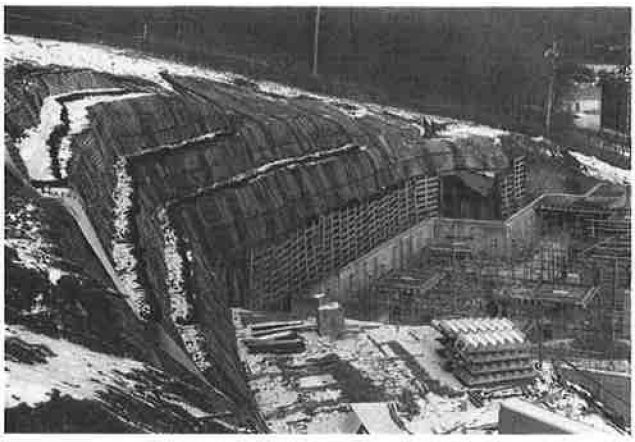

FIGURE 6 Geotextile-geogrid–faced permanent slope and geotextile-timber-grillage–faced temporary slope.

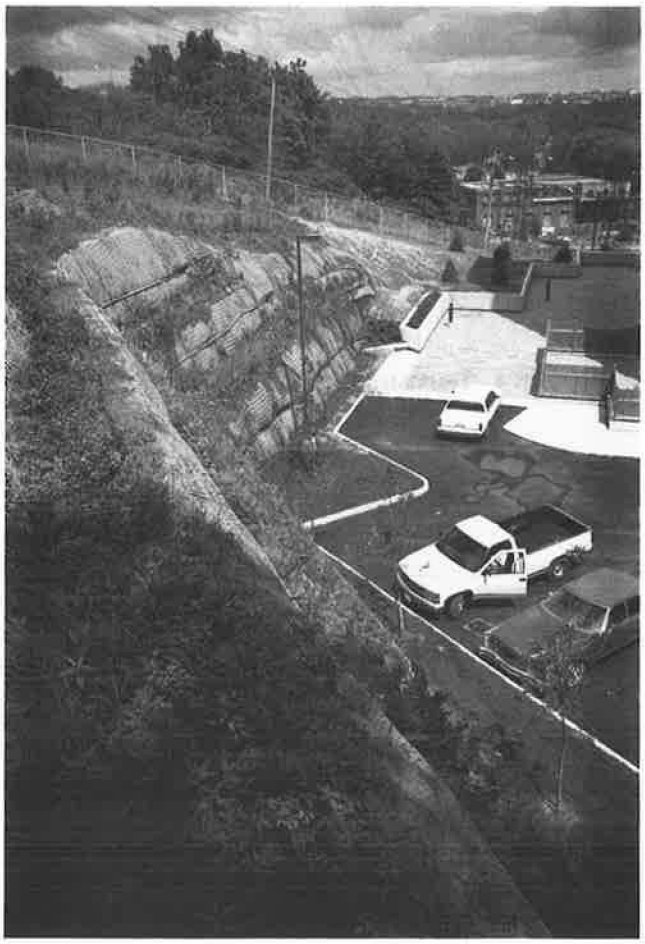

FIGURE 7 Completed slope in area of Figure 6.

The geocomposite facing has not experienced any problems. Both facing systems permit free drainage of wet areas of the face.

The postconstruction monitoring program for the nailed wall consists of two detailed visual inspections of the slope each year: after the spring thaw and before the onset of winter.

CONCLUDING REMARKS

At the subject site, the adoption of a soil nail solution enabled the project to proceed without surface intrusion into neighboring lands. The cost of the soil nail structure was 40 percent

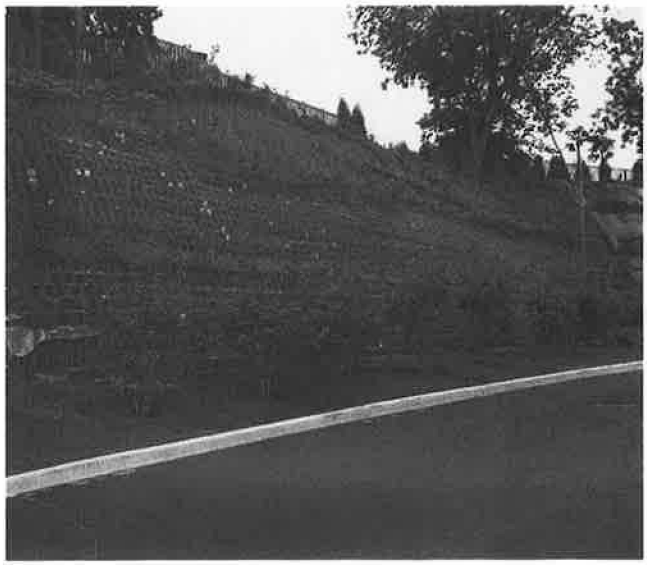

FIGURE 8 Geocomposite-faced slope.

less than the estimated cost of construction of the permanent reinforced concrete and temporary soldier pile and lagging retaining walls that were first envisaged for the site. The adoption of the soil nail solution has thus given the owner a substantial cost saving and a solution less visually obtrusive than the originally proposed retaining wall.

ACKNOWLEDGMENTS

The owner of the Cambridge, Ontario, project is Kressview Springs, Inc. Its project manager, M. Laundon, was very supportive in encouraging the design and implementation of this new slope support system at the site. Its permission to publish details of this project is gratefully acknowledged. The design and supervision of the installation of the soil nail slope support system was carried out by Dominion Soil Investigation, Inc. Detail design and project management were undertaken by Eric Chung of Kitchener-Waterloo. The soil nails at this site were installed by Groundation Engineering Contractors of Georgetown, Ontario. Associated Geotechnical Systems of Milton, Ontario, assisted in the selection of the slope covering materials and supplied and applied the geogrid, geotextile, and geocomposite products. R. Bathurst made many helpful comments during the preparation of this paper, and his input is appreciated.

REFERENCES

1. J. K. Mitchell and W. C. B. Villet. *NCHRP Report 290: Reinforcement of Earth Slopes and Embankments*. TRB, National Research Council, Washington, D.C., 1987.
2. M. F. Stocker, G. W. Kerber, G. Gassler, and G. Gudehus. Soil Nailing. *Proc., International Conference on Soil Reinforcement*, Vol. 2, Paris, France, March 1979, pp. 469–474.
3. D. A. Bruce and R. A. Jewell. Soil Nailing: Applications and Practise, Parts 1 and 2. *Ground Engineering*, Vol. 19, No. 6, and Vol. 20, No. 1, 1986.
4. G. Gassler and G. Gudehus. Soil Nailing—Some Aspects of a New Technique. *Proc., 10th International Conference on Soil Mechanics and Foundation Engineering*, Vol. 3, Stockholm, Sweden, 1981, pp. 665–670.
5. A. Gilloux, G. Notte, and H. Gonin. Experiences and Retaining Structure by Nailing in Moraine Soils. *Proc., 8th European Conference on Soil Mechanics and Foundation Engineering*, Helsinki, Finland, 1983, pp. 499–502.
6. C. J. F. P. Jones. *Earth Reinforcement and Soil Structures*. Butterworths, Stoneham, Mass., 1985.
7. R. E. Crowe, R. J. Bathurst, and C. Alston. Design and Construction of a Road Embankment Using Geosynthetics. *Proc., 42nd Canadian Geotechnics Conference*, Winnipeg, 1989, pp. 266–271.
8. T. H. Hanna. *Foundations in Tension—Ground Anchors*. McGraw-Hill, New York, N.Y., 1982.
9. F. K. Chin. Diagnosis of Pile Condition. *Geotechnical Engineering*, Vol. 9, 1978, pp. 85–104.

Publication of this paper was sponsored by Committee on Mechanics of Earth Masses and Layered Systems.